

THE INTERSTELLAR MEDIUM OF CENTAURUS A AND M51

**UNLOCKING THE PROPERTIES OF THE INTERSTELLAR MEDIUM  
OF CENTAURUS A AND M51**

By  
Tara Jill Parkin, B.Sc., M.Sc.

A Thesis  
Submitted to the School of Graduate Studies  
in Partial Fulfillment of the Requirements  
for the Degree of

Doctor of Philosophy

McMaster University

© Tara Jill Parkin, B.Sc., M.Sc., November 2013

**DOCTOR OF PHILOSOPHY (2013)**  
**(Physics and Astronomy)**

**McMaster University**  
**Hamilton, Ontario**

**TITLE:** Searching for Local Variations in the Interstellar Medium of Nearby Galaxies

**AUTHOR:** Tara Jill Parkin, B.Sc. (University of Western Ontario), M.Sc. (Queen's University)

**SUPERVISOR:** Dr. Christine Wilson

**NUMBER OF PAGES:** xx, 198

---

# Abstract

I investigate the interstellar medium (ISM) of two nearby, resolved galaxies, M51 (NGC 5194) and Centaurus A (Cen A; NGC 5128) using spectroscopic and photometric data from the *Herschel Space Observatory* to search for local variations of the characteristics of the ISM. I find that the average characteristics of the ISM in Cen A, a giant elliptical galaxy, are similar to those typically found in normal star forming galaxies, despite its unique morphology and classification as a radio galaxy with an active galactic nucleus (AGN). Using *Herschel* photometry I find radial trends in the dust temperature, the dust mass, and unexpectedly, the gas-to-dust mass ratio. I hypothesise that the AGN is removing nearby dust grains via dust sputtering or expulsion via jets. A comparison of *Herschel* spectroscopy of important cooling lines to a photon dominated region (PDR) model reveals the strength of the far-ultraviolet radiation field,  $G_0$ , and the hydrogen gas density,  $n$ , in the PDR gas within Cen A are consistent with values found in other nearby galaxies. I do not observe any obvious radial trend in these characteristics and conclude that the high inclination of Cen A may be inhibiting the identification of any impact the AGN is having on the surrounding gas.

An investigation of the gas in M51 using a similar spectroscopic dataset as with Cen A shows for the first time that a large fraction of the observed [C II](158  $\mu\text{m}$ ) emission in the centre of M51 originates in diffuse ionised gas. This fraction falls off with radius out to the arm and interarm regions. I also find via PDR modelling that there is a decreasing radial trend in the values of  $G_0$  and  $n$ , and that in the arm and interarm regions they are the same. Thus, there appears to be no difference in the physical properties of the molecular clouds in the arm and interarm regions of the galaxy. The results of this thesis contribute to further understanding the characteristics of the ISM of nearby galaxies, as well as the evolution of the ISM in galaxies containing an AGN.



*For Mom and Dad*

---

# Co-Authorship

Chapters 2, 3, and 4 of this thesis contain original scientific research written by myself, Tara Jill Parkin. Chapter 2 has been published as a peer-reviewed journal article in the Monthly Notices of the Royal Astronomical Society (MNRAS). The reference to this work is:

*Parkin, T. J., Wilson, C. D., Foyle, K., Baes, M., Bendo, G. J., Boselli, A., Boquien, M., Cooray, A., Cormier, D., Davies, J. I., Eales, S. A., Galametz, M., Gomez, H. L., Lebouteiller, V., Madden, S., Mentuch, E., Page, M. J., Pohlen, M., Remy, A., Roussel, H., Sauvage, M., Smith, M. W. L., Spinoglio, L., 2012, MNRAS, Volume 422, Issue 3, pp. 2291–2301.*

My supervisor, Dr. Christine Wilson, is the second author. Dr. Kelly Foyle ran my photometry through her dust spectral energy distribution code for the purposes of evaluating the impact of having two free parameters versus one on my results; however, we used my model for the full analysis. Dr. Foyle also provided general comments on the paper. Dr. Marc Sauvage, Dr. Helen Roussel, Dr. Michael Pohlen, and Matthew W. L. Smith processed the *Herschel* PACS and SPIRE photometric maps for Cen A, and Dr. George Bendo provided the convolution kernels for the PACS photometry. It is the policy of the SPIRE Special Astronomy Group 2 (SAG2) collaboration, of which I am a member, to circulate drafts of articles to be submitted for publication to other members for an internal peer-review process. Any member that provides comments on a circulated draft is automatically added to the list of authors on that paper. Thus, the remaining co-authors of this paper are members of the SAG2 that provided me with comments and suggestions to improve the draft prior to submission, but contributed nothing further to the primary analysis.

At the time of my final thesis submission to the School of Graduate Studies, the work presented in Chapter 3 has been accepted for publication by the peer-reviewed Astrophysical Journal (ApJ); however, it has not yet been published and thus does not yet have a full bibliographic reference. The author list is as follows:  
*T. J. Parkin, C. D. Wilson, M. R. P. Schirm, M. Baes, M. Boquien, A. Boselli, A. Cooray, D. Cormier, K. Foyle, O. Ł. Karczewski, V. Lebouteiller, I. de Looze, S. C.*

*Madden, H. Roussel, M. Sauvage and L. Spinoglio.*

Again, Dr. Christine Wilson is second author. Maximilien Schirm processed the SPIRE FTS spectroscopic observations and produced the [N II](205  $\mu$ m) map of M51 for use in my analysis. Dr. Marc Sauvage and Dr. Helen Roussel processed the PACS photometry I used as part of my analysis. Dr. Diane Cormier and Dr. Vianney Lebouteiller provided me with the code PACSman, which I used to process the PACS spectroscopy. The remaining co-authors are members of SAG2 who provided comments upon circulating a draft of the paper and obtained co-authorship as described above.

The research presented in Chapter 4 is in preparation to be submitted to ApJ. It has been circulated to the SAG2 for comments but they have not been incorporated into the work as of the time of final submission. The author list is as follows:

*T. J. Parkin, C. D. Wilson, M. R. P. Schirm, M. Baes, M. Boquien, A. Boselli, D. Cormier, M. Galametz, O. L. Karczewski, V. Lebouteiller, S. Madden, H. Roussel, M. W. L. Smith, and L. Spinoglio*

Dr. Christine Wilson is my supervisor and is second author. Maximilien Schirm processed the SPIRE FTS spectroscopy and produced the [N II](205  $\mu$ m) map for Cen A. Dr. Helen Roussel processed the PACS photometry I used for my analysis. Dr. Diane Cormier and Dr. Vianney Lebouteiller provided me with PACSman, and the remaining co-authors are members of SAG2 who provided comments upon circulating a draft of the paper and obtained co-authorship as described above.

All previously published material has been reformatted to conform to the required thesis style. I grant an irrevocable, non-exclusive license to McMaster University and the National Library of Canada to reproduce this material as part of this thesis.

---

# Acknowledgements

Over the past five years I have relied upon the friendship, guidance and support of many people to get me to this point and I would like to extend my gratitude toward them here.

First, a huge thank you to my supervisor, Dr. Christine Wilson. I have had an amazing experience working with you and I am grateful for everything you have given me. For your encouragement, ideas, knowledge and support. For the many conversations we shared, both scientific and otherwise. For giving me the opportunity to work with observations from Herschel, my dream dataset. And for sending me to numerous places to share this work with others, and to the top of Mauna Kea! No matter what lies ahead for me, I will always treasure my time here at McMaster, and all of the things I've learned along the way.

I would also like thank the numerous collaborators that have also helped me along the way. To Dr. Suzanne Madden, my “European Mom”. It’s been six years since I first met you as a Master’s student and now I’ve finally made it to the finish line! Thank you for introducing me to Herschel and for keeping tabs on me after all these years. Your friendship and support mean so much to me.

Thank you to Dr. Diane Cormier and Dr. Vianney Lebouteiller for showing me the ropes on PACS data processing and PACSman, to Dr. Kelly Foyle for your scientific help and advice, and to the rest of the Herschel SAG2 for helping me do the best science possible. And many thanks to my supervisory committee members, Dr. Laura Parker and Dr. James Wadsley, for keeping me on track and for your suggestions and guidance on improving my research.

Tina, Cheryl, Rose and Mara. You guys are the greatest secretaries a graduate student could ask for! You are awesome! I will always be thankful for the many conversations we’ve shared when I needed a break, as well as all of things you’ve done for me over the years.

I will be forever grateful for the friends I’ve made along the way. To Rachel Ward-Maxwell, Aaron Maxwell, David Kirsh, Maximilien Schirm, Eliz-

abek Tasker, Damien Robertson, Jonathan Newton, Kevin Sooley and Leo Van Nierop. You are all such amazing people and I can think of no other people I would have wanted to share the highs and lows of graduate school with. I would be lost without your kindness, jokes, advice, support and friendship. I will definitely miss our many crazy conversations over lunch!

I especially want to thank my parents for being there with me along this journey. You have always been there for me, no matter what, and for that I will be eternally grateful. I love you both so much! And Lee, you are the best brother a sister could ask for! You always put up with my craziness and lend an ear when I need one.

Lastly, to Kazimierz Sliwa. Kaz, the past three years have been amazing and I am so thankful that I met you. You have always believed in me, even when I didn't believe in myself, and I could not have made it without your love and support. And now it's my turn to be there for you while you finish your own degree. I love you!

"If we knew what it was we were doing, it would not be called research,  
would it?"

---

ALBERT EINSTEIN (1879-1955)

“If you wish to make an apple pie from scratch, you must first invent the universe.”

---

CARL SAGAN (1934-1996)

“All our dreams can come true, if we have the courage to pursue them.”

---

WALT DISNEY (1901-1966)

“Nothing is impossible, the word itself says ‘I’m possible’!”

---

AUDREY HEPBURN (1929-1993)

“Two roads diverged in a wood, and I, I took the one less traveled by, and  
that has made all the difference.”

---

*The Road Not Taken*

ROBERT FROST (1874-1963)



# Table of Contents

<b>Abstract</b>	<b>iii</b>
<b>Co-Authorship</b>	<b>vi</b>
<b>Acknowledgments</b>	<b>viii</b>
<b>List of Figures</b>	<b>xvi</b>
<b>List of Tables</b>	<b>xviii</b>
<b>List of Acronyms</b>	<b>xix</b>
<b>Chapter 1</b>	
<b>Introduction</b>	<b>1</b>
1.1 The Interstellar Medium . . . . .	4
1.1.1 Interstellar Gas . . . . .	5
1.1.2 Important Gas Tracers . . . . .	7
1.1.2.1 Cold Gas . . . . .	8
1.1.2.2 H II regions and PDRs . . . . .	9
1.1.3 Interstellar Dust . . . . .	11
1.2 The Interstellar Medium of Galaxies . . . . .	15
1.2.1 Spiral Galaxies . . . . .	15
1.2.1.1 M51 . . . . .	17
1.2.2 Elliptical Galaxies . . . . .	18
1.2.2.1 Centaurus A . . . . .	19
1.3 The Herschel Space Observatory . . . . .	20
1.3.1 Herschel Science Highlights . . . . .	25
1.4 PACS Spectroscopy and Processing . . . . .	27

1.5 This Thesis . . . . .	30
---------------------------	----

## Chapter 2

<b>The gas-to-dust mass ratio of Centaurus A as seen by Herschel</b>	<b>42</b>
2.1 Introduction . . . . .	42
2.2 Observations . . . . .	46
2.2.1 <i>Herschel</i> Observations . . . . .	46
2.2.1.1 PACS Observations . . . . .	48
2.2.1.2 SPIRE Observations . . . . .	49
2.2.1.3 Noise and Uncertainties . . . . .	50
2.2.2 JCMT Observations . . . . .	53
2.2.3 Ancillary Data . . . . .	55
2.3 Results . . . . .	56
2.3.1 SED Fitting . . . . .	56
2.3.2 Dust Mass . . . . .	60
2.3.3 Gas Mass . . . . .	62
2.3.4 The Gas-to-Dust Mass Ratio . . . . .	64
2.4 Discussion . . . . .	65
2.5 Conclusions . . . . .	70

## Chapter 3

<b>Regional variations in the dense gas heating and cooling in M51 from <i>Herschel</i> far-infrared spectroscopy</b>	<b>79</b>
3.1 Introduction . . . . .	80
3.2 <i>Herschel</i> Observations . . . . .	84
3.2.1 PACS Observations . . . . .	84
3.2.2 SPIRE Observations . . . . .	87
3.2.3 Ancillary Data . . . . .	88
3.2.4 Data Treatment for Analysis . . . . .	89
3.3 Physical characteristics of the gas . . . . .	91
3.3.1 Line Emission Morphology . . . . .	91
3.3.2 Line Deficits . . . . .	100
3.3.3 Heating and Cooling . . . . .	104
3.3.4 Ionized Gas . . . . .	110
3.3.4.1 Ionized Gas Contribution to [C II] Emission . . . . .	110
3.3.4.2 Ionized Gas Characteristics . . . . .	114
3.4 PDR Modeling of Observations . . . . .	117
3.4.1 Adjustments to the [C II] and [O I]63 Lines . . . . .	122
3.4.2 Possible Contamination from the Seyfert Nucleus . . . . .	123
3.4.3 Implications of PDR Model Results . . . . .	125
3.5 Conclusions . . . . .	129

<b>Chapter 4</b>	
<b>Searching for radial variations in the physical characteristics of the gas in the disk of Centaurus A using the <i>Herschel Space Observatory</i></b>	<b>138</b>
4.1 Introduction . . . . .	139
4.2 <i>Herschel</i> Observations . . . . .	142
4.2.1 PACS spectroscopy . . . . .	142
4.2.2 SPIRE spectroscopy . . . . .	146
4.2.3 Ancillary Data . . . . .	146
4.2.4 Final Steps for Analysis . . . . .	147
4.3 Results . . . . .	147
4.3.1 Morphological Properties . . . . .	147
4.3.2 Line Ratio Diagnostics . . . . .	155
4.3.2.1 [C II], [O I] <sub>63</sub> and $F_{\text{TIR}}$ . . . . .	155
4.3.2.2 Molecular Gas Cooling . . . . .	159
4.3.2.3 Ionized Gas Source . . . . .	162
4.3.3 The contribution of ionized gas to the [C II] emission . . . . .	164
4.4 PDR modelling . . . . .	167
4.5 Discussion . . . . .	172
4.5.1 Inferred Physical Conditions from PDR Modelling . . . . .	176
4.5.2 Potential Non-PDR contributions to observed lines . . . . .	177
4.5.3 Comparison to M51 . . . . .	178
4.6 Conclusions . . . . .	182
<b>Chapter 5</b>	
<b>Summary &amp; Future Work</b>	<b>191</b>
5.0.1 Future Work . . . . .	194

# List of Figures

1.1	Spectral energy distribution of the centre of M51 . . . . .	3
1.2	Atmospheric transmission as a function of frequency at the summit of Mauna Kea . . . . .	5
1.3	A cartoon of a molecular cloud . . . . .	8
1.4	A cartoon of the cooling process via the [C II](158 $\mu\text{m}$ ) fine struc- ture line . . . . .	10
1.5	Raw data cloud of a PACS [C II](158 $\mu\text{m}$ ) observation for M51 . .	28
1.6	Best line fit to a spaxel from PACS [C II](158 $\mu\text{m}$ ) observations of M51 . . . . .	29
2.1	<i>Herschel</i> photometric maps of Centaurus A at their native resolution	51
2.2	HI map of the disc region of Cen A overlaid with CO $J = 3 - 2$ contours . . . . .	56
2.3	Spectral energy distributions modelled by a modified blackbody for a typical pixel and the entire disc in Centaurus A . . . . .	59
2.4	Temperature map of the dust disc of Centaurus A . . . . .	60
2.5	Dust mass map of the disc of Centaurus A . . . . .	62
2.6	The total gas mass distribution of the disc of Centaurus A . . . . .	64
2.7	Gas-to-dust mass ratio of Centaurus A . . . . .	65
2.8	A radial plot of the average gas-to-dust mass ratio along the major axis of Centaurus A . . . . .	66
3.1	Total infrared flux of M51 . . . . .	90
3.2	<i>Herschel</i> spectroscopic maps of M51 at their native resolution . . .	93
3.3	Maps of important line ratios in M51 . . . . .	101
3.4	Heating efficiency as a function of the $70\mu\text{m}/160\mu\text{m}$ color in M51 .	108
3.5	Comparison of the average observed line ratio to the theoretical curves for each of the four regions we probe in M51 . . . . .	112
3.6	Schematic of the four regions into which we divide M51 for our analysis. . . . .	118

3.7	Comparisons of observed line ratios in M51 with a PDR model grid using the uncorrected and corrected observations . . . . .	121
4.1	A map of the total infrared flux for Centaurus A . . . . .	143
4.2	<i>Herschel</i> spectroscopic observations of Centaurus A at their native resolution . . . . .	149
4.3	Maps of important cooling line ratios of Centaurus A . . . . .	157
4.4	Heating efficiency as a function of dust temperature for Centaurus A	161
4.5	$[C\,II]/F_{TIR}$ and $[O\,III]/F_{TIR}$ line ratios as a function of $L_{TIR}/M_{H_2}$ for Centaurus A . . . . .	163
4.6	A comparison of the $[O\,III]_{88}/[N\,II]_{122}$ line ratio for Centaurus A to H II region and narrow line region AGN models . . . . .	165
4.7	The fraction of $[C\,II]_{158}$ emission originating from ionized gas for the eastern half of the disk of Centaurus A. . . . .	167
4.8	Observed line ratios for Centaurus A compared to the parameter space of a PDR model using uncorrected and corrected observations	170
4.9	Observed line ratios in Centaurus A and M51 compared to the parameter space of a PDR model . . . . .	181

# List of Tables

1.1	A comparison of <i>Herschel</i> to previous space observatories . . . . .	23
1.1	A comparison of <i>Herschel</i> to previous space observatories . . . . .	24
2.1	Observational details of <i>Herschel</i> photometry of Centaurus A . . . . .	47
3.1	Properties of our <i>Herschel</i> Observations . . . . .	86
3.2	Comparison to Previous Measurements of M51 . . . . .	99
3.3	Line to Total Infrared Flux Ratio in M51 . . . . .	100
3.4	Line/ $F_{\text{TIR}}$ Ratios in M51 Compared to Previous Global Surveys . .	105
3.5	[N II] Line Ratios and Ionized Fraction of [C II] . . . . .	113
3.6	Average Intensity of Fine-structure lines by Region . . . . .	119
3.7	Properties of the Gas Derived from the PDR Model . . . . .	124
3.8	Properties of the Gas from the PDR Model and Mean Line Ratios .	126
3.9	Comparison of the PDR Characteristics Measured in M51 to Previous Studies . . . . .	127
4.1	Basic details of the <i>Herschel</i> spectroscopic observations of Centaurus A . . . . .	145
4.2	Total integrated flux for the PACS cooling lines in Cen A. . . . .	155
4.3	Properties of the gas derived from the PDR model . . . . .	171

---

# List of Acronyms

<b>AGN</b>	Active Galactic Nucleus
<b>ALMA</b>	Atacama Large Millimetre Array
<b>ESA</b>	European Space Agency
<b>FIR</b>	Far Infrared
<b>FTS</b>	Fourier Transform Spectrometer
<b>FUV</b>	Far Ultra-Violet
<b>FWHM</b>	Full-Width at Half-Maximum
<b>HIFI</b>	Heterodyne Instrument for the Far Infrared
<b>HIPE</b>	Herschel Interactive Processing Environment
<b>IRAC</b>	Infrared Array Camera
<b>IRAS</b>	Infrared Astronomical Satellite
<b>IRS</b>	Infrared Spectrograph
<b>ISM</b>	Interstellar Medium
<b>ISRF</b>	Interstellar Radiation Field
<b>ISO</b>	Infrared Space Observatory

<b>ISOCAM</b>	Infrared Space Observatory CAMera
<b>ISOPHOT</b>	Infrared Space Observatory Photo-polarimeter
<b>JCMT</b>	James Clerk Maxwell Telescope
<b>KAO</b>	Kuiper Airborne Observatory
<b>LMC</b>	Large Magellanic Cloud
<b>MIPS</b>	Multiband Imaging Photometer for <i>Spitzer</i>
<b>NASA</b>	National Aeronautics and Space Administration
<b>PACS</b>	Photodetector Array Camera and Spectrometer
<b>PAH</b>	Polycyclic Aromatic Hydrocarbon
<b>PDR</b>	Photodissociation (Photon dominated) Region
<b>SCUBA-2</b>	Submillimetre Common User Bolometer Array 2
<b>SED</b>	Spectral Energy Distribution
<b>SINGS</b>	Spitzer Infrared Nearby Galaxy Survey
<b>SFR</b>	Star Formation Rate
<b>SFRD</b>	Star Formation Rate Density
<b>SMC</b>	Small Magellanic Cloud
<b>SPIRE</b>	Spectral and Photometric Imaging REceiver
<b>TIR</b>	Total Infrared
<b>ULIRG</b>	Ultra Luminous Infrared Galaxy
<b>VNGS</b>	Very Nearby Galaxies Survey

A rectangular box with a black border. On the left side, the word "Chapter" is written vertically. In the center, the number "1" is large and bold. The rest of the box is empty.

Chapter **1**

# Introduction

The night sky is full of stars, the moon and planets, galaxies and a variety of other galactic objects. Historically, our perspective of these objects was limited to what we could see with our eyes or through an optical telescope, which covers a small range of the electromagnetic spectrum. But our perspective changed in the 1930s when Karl G. Jansky discovered radio emission originating in the centre of the Milky Way Galaxy (Jansky, 1933), thus opening the door to radio astronomy and a new part of the electromagnetic spectrum. Since then, numerous ground- and spaced-based observatories have been built to probe the sky across the entire electromagnetic spectrum, and we have come to the realisation that the Universe and the objects within it are much more complex, rich and diverse than might have been suggested by optical observations alone. Thus, to fully understand the physics behind the phenomena we observe, it is necessary to conduct a multiwavelength study of each object.

Galaxies themselves are extremely rich objects. They are large gravitationally bound systems that fall into three broad morphological types: spiral/disk galaxies, elliptical galaxies and irregular types. Each galaxy is enriched with dark matter,

stars and the stuff between them, which we call the interstellar medium (ISM). The ISM comprises gas and dust in a variety of phases, such as molecular clouds, regions of ionised gas known as H II regions, or diffuse gas, and is the location of many physical processes including star formation, dust grain formation, metal enrichment, and energy transport, all of which rely on the evolution of stars and stellar systems (Tielens, 1995).

An important wavelength regime to utilise for probing the ISM is that of the infrared and submillimetre, which traces thermal emission at dust temperatures typically less than  $\sim 100$  K and gas temperatures of less than  $10^3$  K (Tielens, 2005). Ranging from approximately  $2\ \mu\text{m}$  to 1 mm, a significant fraction of a star-forming galaxy's total flux is emitted at these wavelengths, as shown by the spectral energy distribution (SED) for the centre of M51 in Figure 1.1. At near-infrared wavelengths, the continuum emission is dominated by older stellar populations. In the mid-infrared wavebands a small amount of radiation comes from the tail end of the stellar SEDs, while the rest of the emission comes from stochastically heated hot dust grains (continuum), as well as polycyclic aromatic hydrocarbons (PAHs) and a number of atomic and molecular fine structure lines (spectral line emission) (e.g. Draine & Li, 2007). Between the mid-infrared and the submillimetre the SED comprises emission primarily from dust grains. However, a significant fraction of emission at these wavelengths also comes from atomic and molecular fine structure lines tracing the cool gas (Kaufman et al., 1999). Comparing observations of the dust and gas emission at these wavelengths with models of dust SEDs (e.g. Dale et al., 2001; Galliano et al., 2003; Draine et al., 2007; Galliano et al., 2011) and photon dominated region (PDR) models (e.g. Tielens & Hollenbach, 1985; Wolfire et al., 1990; Hollenbach et al., 1991; Kaufman et al., 1999, 2006; Röllig et al., 2006) gives us insight into the physical properties of the ISM and star formation.

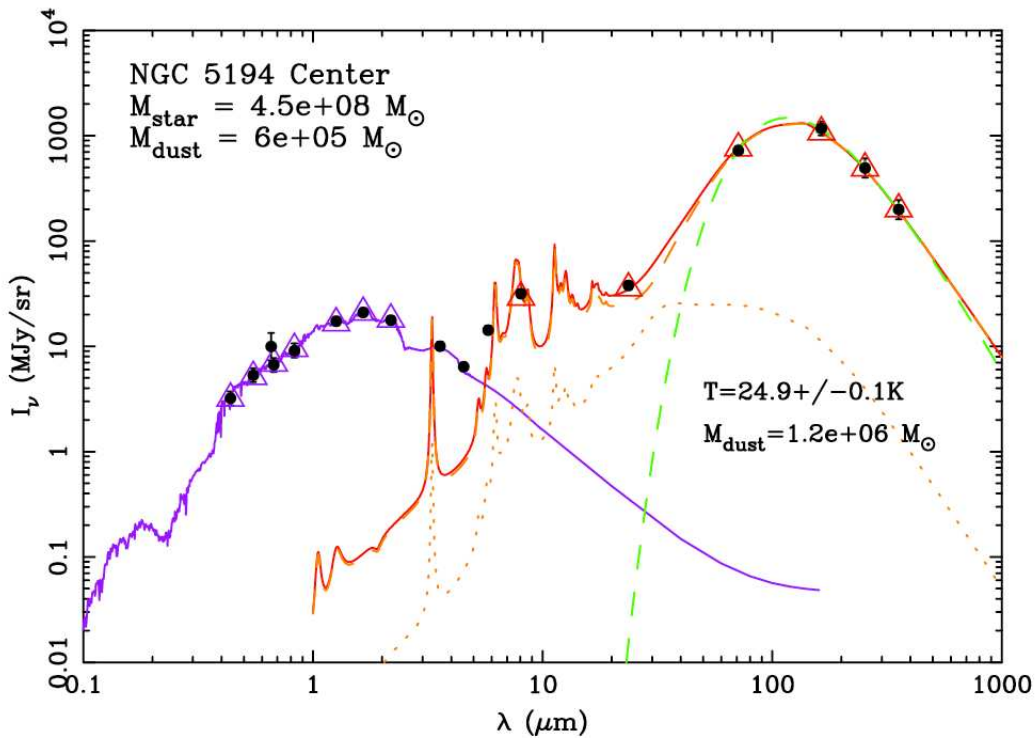


Figure 1.1: The spectral energy distribution for the centre of M51. Observed data are represented by the black dots while the best-fitting SED model flux at each corresponding waveband is shown by the open triangles. The best-fitting stellar SED model is represented by the purple curve and the best-fitting dust SED model is shown in red. The dust SED model is further subdivided into a PDR component and an underlying component shown as the orange dotted and dashed lines, respectively. The green dashed line is a modified blackbody fit. *Image credit: Adapted from Figure 4 of Mentuch Cooper, E. et al., 2012, "Spatially resolved stellar, dust, and gas properties of the post-interacting Whirlpool system", The Astrophysical Journal, Volume 755, Issue 2, Article ID 165, 23pp. Reproduced by permission of the American Astronomical Society.*

The one major caveat of observing the sky in these wavebands is that they suffer from atmospheric effects, meaning much of the radiation is absorbed before it can be observed on the ground (e.g. Holland et al., 2013). Ground-based observatories located at high altitudes and in dry climates, such as the James Clerk Maxwell Telescope (JCMT) and the Atacama Large Millimetre Array (ALMA), can partially observe the sky within select windows. In Figure 1.2 we show the atmo-

spheric transmission of submillimetre radiation as a function of wavelength (grey solid line) at the JCMT site at the summit of Mauna Kea, roughly 4000 m above sea level. Also shown are the filter shapes of the two bands observed by the Sub-millimetre Common User Bolometer Array 2 (SCUBA-2) instrument mounted on the JCMT, 450  $\mu\text{m}$  (blue) and 850  $\mu\text{m}$  (red). What is striking about this plot is that at wavelengths of less than about 600  $\mu\text{m}$ , there are only two observable windows, where at most only about half of the radiation at these wavelengths is observed; emission at wavelengths in between these windows is completely unobservable by the JCMT. The best solution to this problem is to build space-based observatories, which are capable of accessing emission across all wavelengths, or airborne observatories mounted on airplanes that are a compromise between ground-based and space-based observatories.

## 1.1 The Interstellar Medium

The interstellar medium (ISM) of a galaxy is a complex, multiphase environment, comprised primarily of gas and dust components and permeated by radiation at energies across much of the electromagnetic spectrum. Its evolution with time is driven by the dynamics of the galaxy, and more importantly for the purposes of this thesis, star formation and subsequent feedback (Tielens, 2005). Young star clusters rich in young, massive O and B stars provide a source of strong stellar winds and an outward flux of ionising radiation directed toward the surrounding gas and dust, impacting the physical characteristics of these components (Zinnecker & Yorke, 2007). Furthermore, the violent death of these high-mass stars in supernova explosions deposits mechanical energy and material back into the ISM, which in turn recycles this matter into the next generation of stars. We summarise the gas

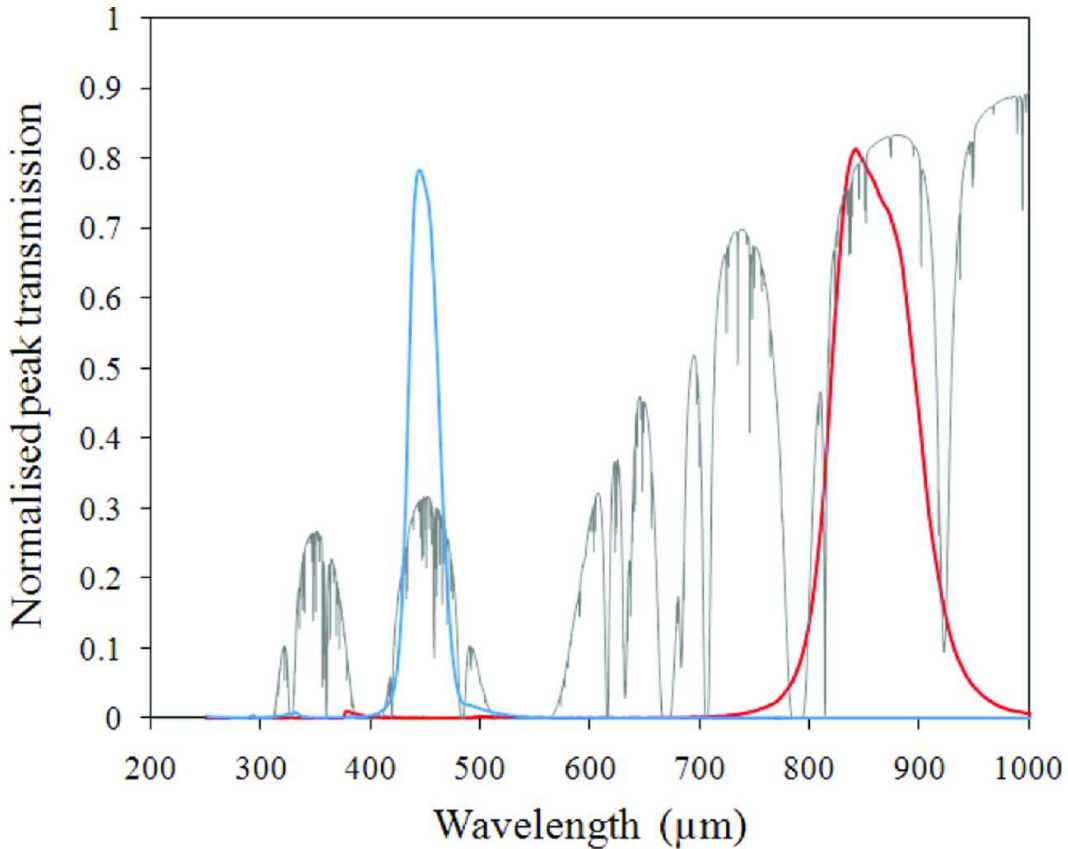


Figure 1.2: A plot of the fraction of submillimetre emission that passes through the atmosphere as a function of wavelength at the summit of Mauna Kea, Hawaii (altitude approximately 4000 m). The blue and red curves show the filter profiles of the 450 and 850  $\mu\text{m}$  bands, respectively, of the SCUBA-2 instrument mounted on the JCMT. *Image credit: Figure 3 from Holland, W. S. et al., 2013, "SCUBA-2: The 10000 pixel bolometer camera on the James Clerk Maxwell Telescope", Monthly Notices of the Royal Astronomical Society, Volume 430, Issue 4, Pages 2513-2533. Reproduced with permission from the Monthly Notices of the Royal Astronomical Society and Oxford University Press.*

and dust components relevant to this thesis below.

### 1.1.1 Interstellar Gas

Interstellar gas permeates a galaxy and exists in a number of phases with a broad range of temperatures, and densities, and can be in both neutral and ionised states.

The bulk of the mass of a star-forming galaxy comprises hydrogen, both atomic ( $H\ I$ ) and molecular ( $H_2$ ), though the relative contributions of each varies from galaxy to galaxy (Young & Knezek, 1989; Boselli et al., 2002; Obreschkow & Rawlings, 2009). A wealth of atomic and molecular species make up the remaining fraction of gas. Here we briefly describe the major components of the ISM and the typical ways to observe them.

The coldest gas is located within molecular clouds, the sites of star formation. The temperature in these regions is very cold, typically 10 K (Young & Scoville, 1991), and the typical gas density is of the order  $10^2\ cm^{-3}$  (Scoville, 2012), which allows for the formation of molecules. Molecular hydrogen comprises the majority of the gas in these clouds, followed by carbon monoxide (CO), the second most common molecule (e.g. Frerking et al., 1982). In the densest regions other common molecular constituents include HCN, CS,  $HCO^+$  and  $NH_3$  (Tielens, 2005; Bergin & Tafalla, 2007; Scoville, 2012). Star formation occurs in embedded cores within these clouds, where the conditions are different than the rest of the cloud.

Immediately surrounding regions of star formation are low density, ionised environments called  $H\ II$  regions. The harsh radiation field emanating from the central stars gives rise to hot gas temperatures of approximately  $10^4\ K$  (Rubin, 1985; Tielens, 2005) and densities spanning from tens to  $10^4\ \text{particles}\ cm^{-3}$  (Tielens, 2005). A large fraction of photons from these hot, young stars are emitted in the ultraviolet waveband, and a smaller fraction emit in the X-ray regime, giving rise to the production of numerous ions with ionisation potentials greater than that of hydrogen (13.6 eV) including  $N^+$ ,  $O^{++}$ , and  $H^+$  (Tielens, 2005).

At increasingly larger distances from the star forming region, the radiation field is not as strong and the  $H\ II$  region transitions to a photon-dominated region (PDR). Originally, a PDR was coined a photodissociation region by Tielens & Hol-

lenbach (1985) and was classically described to be the region adjacent to an H II region. However, PDRs can encompass a wider range of environments and thus now a PDR is considered to be any region where far-ultraviolet photons (wavelength  $\lambda = 912 \text{ \AA} - 2000 \text{ \AA}$  or energy  $E = 6-13.6 \text{ eV}$ ) dominate the chemistry in the gas (Tielens & Hollenbach, 1985; Hollenbach et al., 1991). In fact, with this definition much of a galaxy's ISM exists in PDRs, and thus they are an important regime to study and understand in order to characterise the conditions within the ISM (Tielens & Hollenbach, 1985).

Temperatures within a PDR range from less than 100 K to upwards of a few thousand K (Tielens & Hollenbach, 1985), while densities can range from  $10^1 \text{ cm}^{-3}$  to  $10^6 \text{ cm}^{-3}$ . This diverse range of physical conditions in the gas within a PDR can be diagnosed by the presence of various atoms and ions. Figure 1.3 shows a cartoon representation of a molecular cloud with an embedded H II region and surrounding PDR. In reality, the various environments are not so simply segregated, but this provides a basic description of conditions inside a molecular cloud.

### 1.1.2 Important Gas Tracers

Determining the physical conditions of the gas within the ISM involves observations of various atoms, ions and molecules and subsequent comparison of these observations with a theoretical model representing the ISM phase of interest. Here we describe some of the most important gas tracers, how they are produced and how we observe them.

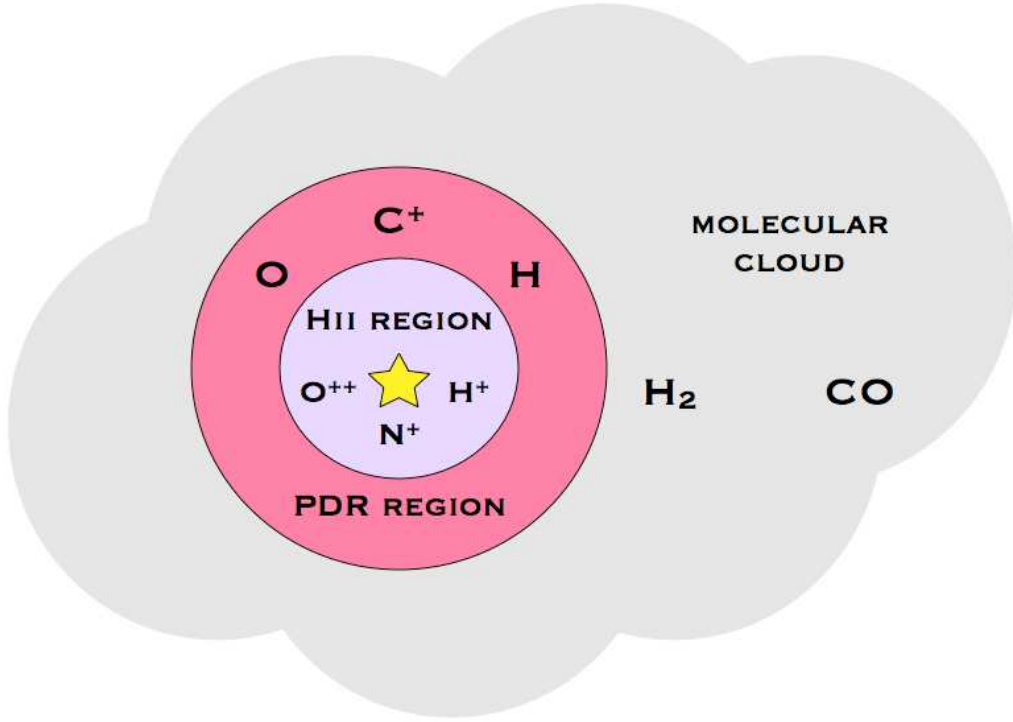


Figure 1.3: A cartoon schematic of a molecular with an embedded stellar cluster and surrounding H II and PDR regions.

### 1.1.2.1 Cold Gas

As stated above, the majority of a star forming galaxy's mass is found in neutral atomic and molecular hydrogen. Atomic hydrogen is probed via the “21 cm” line using radio telescopes, and some of the earliest reports of observations of this line in our Milky Way are summarised by van de Hulst (1951). Studies of the H I 21 cm line emission show that the atomic hydrogen distribution in galaxies is more extended than the optical disk (e.g. Broeils & Rhee, 1997; Thornley et al., 2010). The ubiquity of the atomic gas lends support to the importance of atomic hydrogen in understanding the properties of the ISM and the dynamics of a galaxy. A morphological exception is early type galaxies (ellipticals and lenticulars), which

often show few detections in atomic gas (e.g. Knapp et al., 1985; Knapp, 1987; Huchtmeier et al., 1995; Oosterloo et al., 2010).

Molecular gas is a more direct tracer of star formation than atomic gas, as star formation occurs in molecular clouds. Observing molecular hydrogen ( $\text{H}_2$ ) in its ground state is very difficult because it does not have an electric dipole moment (Young & Scoville, 1991). Thus, we trace it indirectly using observations of the  $J = 1 - 0$  rotational transition of carbon monoxide (CO) and an empirically determined relation between the column density of  $\text{H}_2$  and the integrated intensity of CO, the “CO-to- $\text{H}_2$  conversion factor”,  $X_{\text{CO}}$  (e.g. Young & Scoville, 1991). The typical value of this conversion factor is  $2 \times 10^{20} \text{ cm}^{-2} (\text{K km s}^{-1})^{-1}$  (Strong et al., 1988), although this value is different in ultra luminous infrared galaxies (Downes & Solomon, 1998), and can vary with radius and metallicity (e.g. Bolatto et al., 2013, and references therein). Higher level rotational transitions are useful tracers of warmer molecular gas (Wilson et al., 2009). One way to observe molecular hydrogen directly is through its quadrupole moment rotational transitions, which produce spectral lines in the infrared (Young & Scoville, 1991), accessible through observatories such as *Spitzer*. It is also possible to observe  $\text{H}_2$  directly via vibrational transitions of an electronically excited molecule, giving rise to spectral lines at around  $2 \mu\text{m}$  (Tielens, 2005). Lastly, one can observe  $\text{H}_2$  absorption lines in the ultraviolet Lyman-Werner bands, which indicate upward electronic transitions (Tielens, 2005).

### 1.1.2.2 H II regions and PDRs

Atomic fine structure lines are the most important spectral lines for tracing hot ionised gas in H II regions and the cool neutral gas in PDRs. These lines contribute to the total cooling of the gas in their respective environments by removing ther-

mal energy from the gas. Gas heating occurs when radiation (usually FUV) from nearby stars provides photons which eject electrons from dust grains or polycyclic aromatic hydrocarbons (PAHs) via the photoelectric effect (Tielens & Hollenbach, 1985; Hollenbach et al., 1991). These free electrons subsequently contribute to the thermal energy of the gas. Depending on the temperature of the gas, certain atoms and ions can be collisionally excited, and if the density of the gas is less than the critical density, which is the ratio of the spontaneous emission coefficient  $A_{ij}$  divided by the collisional rate coefficient  $\gamma_{ij}$ , these excited atoms will most often emit a photon via a fine structure transition rather than collisionally de-excite, as shown in Figure 1.4 (Tielens, 2005).

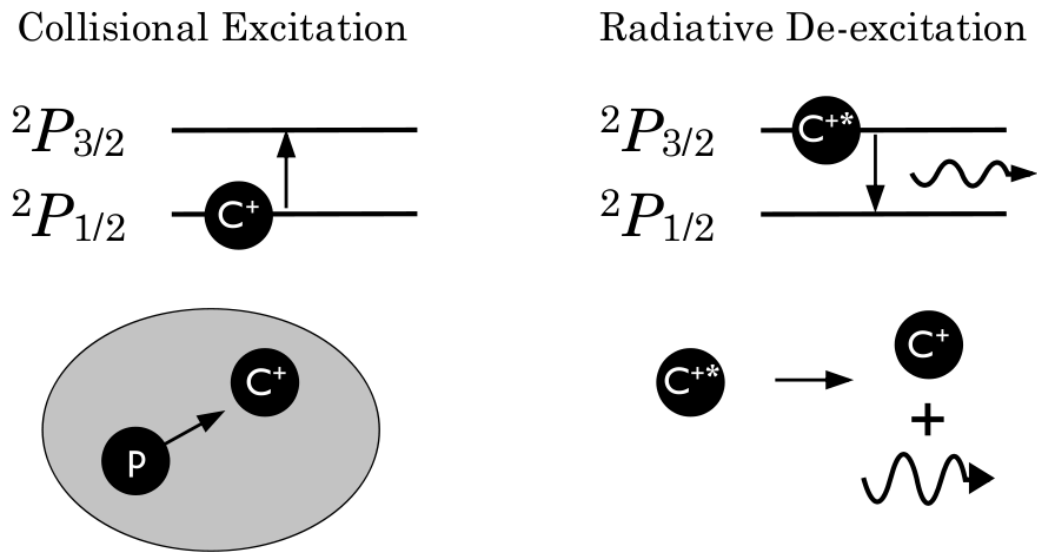


Figure 1.4: A cartoon schematic of the collisional excitation and subsequent radiative de-excitation of a  $\text{C}^+$  atom via the  $[\text{C II}](158 \mu\text{m})$  transition. The  $\text{C}^+$  atom is collisionally excited by a collision with a particle such as a proton or electron and makes an upward transition from the  $^2\text{P}_{1/2}$  state to the  $^2\text{P}_{3/2}$  state. The excited carbon ion,  $\text{C}^{+*}$ , then returns to the ground state by emitting a photon, thus removing thermal energy from the gas.

In an H II region the radiation field is hard enough to ionise atoms or ions

with ionisation potentials greater than 13.6 eV, such as N<sup>+</sup>, N<sup>++</sup> and O<sup>++</sup>. Among the brightest mid- and far-infrared cooling lines in these regimes are the [N II] lines at 122 and 205  $\mu\text{m}$ , the [O III] line at 88  $\mu\text{m}$ , and the [N III] line at 57  $\mu\text{m}$ , although there are many more cooling lines that contribute to the overall energy balance of the ionized gas (e.g. Hunter et al., 2001; Cormier et al., 2012; Lebouteiller et al., 2012).

In the neutral gas within PDRs the excited atoms have ionisation potentials less than 13.6 eV. Here, species such as C, C<sup>+</sup>, O and CO are the important coolants. The [C II] fine structure line at 158  $\mu\text{m}$  dominates the cooling in this environment in most normal galaxies, contributing roughly 1 % of the total cooling budget of a galaxy (Crawford et al., 1985; Stacey et al., 1991; Malhotra et al., 2001); however, it can be suppressed in ultraluminous infrared galaxies (e.g. Luhman et al., 1998, 2003). Other important PDR diagnostics include the [O I] lines at 63 and 145  $\mu\text{m}$ , and the various CO rotational transitions (Malhotra et al., 2001; Negishi et al., 2001).

### 1.1.3 Interstellar Dust

Dust is ubiquitous throughout the ISM and its thermal emission produces about half of the infrared continuum radiation observed in galaxies (Pilbratt et al., 2010). It is an important component of the ISM and molecular clouds in particular, as it shields strong radiation emitted by hot stars from penetrating deep into the cloud. Dust also acts as a catalyst for the formation of H<sub>2</sub>, polycyclic aromatic hydrocarbons (PAHs), and other molecules (Tielens, 2005).

The exact composition of dust grains is still debated in the literature but in general there is agreement that they fall into two broad categories, carbons and

silicates (or other heavier non-carbon based grains), although a mixture of the two has also been put forth by some models. Another important component, though not strictly dust grains but rather large molecules, is polycyclic aromatic hydrocarbons. These are large planar molecules comprising carbon atom chains arranged in a hexagonal pattern with hydrogen atoms bonded to the outermost atoms, and their vibrational modes produce spectral lines at mid-infrared wavelengths (Allamandola et al., 1985).

One of the pioneering dust models was put forth by Mathis et al. (1977) to model the observed interstellar extinction curve, who proposed that the grain population comprised a mix of naked graphite particles plus particles of a different material such as silicates or iron-based particles. They found that the observations were best matched by a model with a range in size of the dust grains between  $0.005 \mu\text{m}$  to  $1 \mu\text{m}$  for the graphites and  $0.025$  to  $0.25 \mu\text{m}$  for the other grains, following a power law distribution. Several later models have either adopted the size distribution of Mathis et al. (1977) or further investigated the composition of the dust using only the graphite and silicate type dust grains (e.g. Draine & Lee, 1984; Kim et al., 1994). Li & Draine (2001) expanded the graphite and silicate model by adding a PAH component, represented by extending the grains down in size to as small as a few Angstroms in diameter and attributing to the very small carbonaceous grains the properties of PAHs. One of the most recent models from this class is by Draine & Li (2007), which is now commonly used by observers (see below).

Other dust modellers have attempted to fit observations with alternative types of dust grains. For example, some authors such as Mathis & Whiffen (1989) consider ‘fluffy’ dust grains that are a combination of amorphous carbon, graphite and silicate particles loosely stuck together, as well as particles comprising just

graphite. Later, Mathis (1996) proposed a dust model of purely graphite, purely silicate, and fluffy composite grains of a mix of carbon, silicates and other elements. Zubko et al. (2004) consider a dust model with different sets of dust grain compositions (such as that of Li & Draine (2001), one testing the effects of including amorphous carbon instead of graphite, one including other heavier composite grains, and even one with only PAHs and no large carbon-based grains) to reproduce several observational constraints, and find that multiple models adequately fit the observations, emphasising the difficulty in establishing the exact nature of the dust grains. Lastly, a third model has been suggested that consists of dust grains with a silicate centre surrounded by a carbon-based coating, in addition to PAHs and carbon dominated very small grains (e.g. Desert et al., 1990).

As the dust grain modelling implies, grain sizes span a large range from small grains approximately 5 Å in diameter up to very large grains of approximately 1 μm. Large grains are in thermodynamic equilibrium with their environment and emit radiation in the far-infrared and submillimetre wavebands, corresponding to temperatures of roughly 20 K (Draine, 2003). Smaller dust grains tend to be out of equilibrium with their surroundings and are stochastically heated due to their small size. A single photon can significantly increase the temperature of a small dust grain, which then slowly re-radiates away that energy, thus producing a significant fraction of the radiation at wavelengths shorter than about 50 μm (Draine, 2003).

Modelling the observed spectral energy distribution of a galaxy or region within a galaxy can reveal properties of the dust grains such as composition, temperature and approximate size, depending on the type of model one uses. The simplest approach is to fit a modified blackbody (graybody) function, described by

$$I(\nu, T) = C\nu^\beta B(\nu, T), \quad (1.1)$$

to observed photometry at far-infrared to submillimetre wavelengths. Here,  $B(\nu, T)$  is the Planck function,  $\nu^\beta$  is from the empirical equation for the dust opacity,  $\kappa_\nu = \kappa_0(\nu/\nu_0)^\beta$ , with  $\beta$  the dust emissivity, and  $C$  is a scaling constant encompassing the distance to the source, the dust mass, and the factor  $\kappa_0/\nu_0^\beta$  from the dust opacity function. From a theoretical perspective,  $\kappa$  and  $\beta$  are functions of the properties of the dust grains (e.g. Draine & Lee, 1984) and thus  $\kappa_0$  may be calculated using a dust grain model for  $\nu_0$  (Li & Draine, 2001). The factor  $\beta$  is often left as a free parameter when fitting observations, but a value of  $\beta = 2.0$  is a common result (e.g. Reach et al., 1995; Bendo et al., 2003; Boselli et al., 2012; Foyle et al., 2012). Thus,  $\beta$  can also be fixed at 2.0 when modelling observations.

The other common way to model the dust SED of a galaxy is to incorporate a more sophisticated dust model into the fitting. The most commonly used of these models is that of Draine & Li (2007), which updates some of the properties of the dust grain models of Li & Draine (2001) and Weingartner & Draine (2001). This model considers dust grains comprised of silicates, carbonaceous grains, and PAHs and parameterises the radiation field the dust is exposed to by a parameter  $U$ , which is a dimensionless quantity such that  $u_\nu = U u_\nu^{\text{MW}}$  is the energy density of the field and  $u_\nu^{\text{MW}}$  is the energy density in the Solar neighbourhood from Mathis et al. (1983). The bulk of the interstellar dust (represented by a fraction  $(1 - \gamma)$ ) is exposed to a radiation field with a scaling factor of  $U_{\min}$ , while dust in the vicinity of PDRs (represented by a fraction  $\gamma$ ) is exposed to an effective radiation field represented by a power-law distribution of radiation fields with scaling factors between  $U_{\min}$  and  $U_{\max}$ . Fitting the model to observed photometry can produce a best-fitting model spectrum and return information on several free parameters, namely  $U_{\min}$ ,  $\gamma$  and the fractional abundance of PAHs,  $q_{\text{PAH}}$ , which in turn can be used to calculate secondary information such as the total dust mass.

Another dust SED model in the literature is that of Desert et al. (1990). It too considers silicate, carbonaceous and PAH grains, although in this model the silicate grains are coated or mixed with carbonaceous material, rather than being purely silicate as is the case for the Draine & Li (2007). This model has three components that are allowed to vary to best fit the observed spectrum, namely the PAH spectrum, the very small grain (carbon dominated grains) spectrum, and the big grain (silicate-carbon composite) spectrum. However, it requires that the radiation field be first calculated then entered as an input parameter, rather than being integrated into the code itself. This work became the basis for the model of Dale et al. (2001), who first introduced the parameterisation of the radiation field with  $U$ , and more recently that of Galliano et al. (2011), although that particular model was designed to work with low-metallicity environments.

## 1.2 The Interstellar Medium of Galaxies

Galaxies come in a wide variety of morphological shapes and sizes, presenting us with a wealth of environments to study. Based on their optical appearances they are classified loosely as either spiral galaxies, elliptical and lenticular galaxies, and in some cases, irregular galaxies (Hubble, 1926). Here we discuss briefly the basic properties of galaxies in each of the two major categories and give some details for the individual galaxies M51 and Centaurus A, which are the particular focus of this thesis.

### 1.2.1 Spiral Galaxies

Spiral or disk galaxies each consist of a disk, a central bulge, and a halo (Binney & Merrifield, 1998), and vary in total mass between  $10^9$  and  $10^{12} \text{ M}_\odot$  (Carroll &

Ostlie, 2006). The disk is rich in gas (atomic and molecular) and dust and can extend as large as 50 kpc in radius (Carroll & Ostlie, 2006). The disk typically shows a spiral structure with arms extending outward from the centre or central bar; these arms appear more luminous at numerous wavelengths than the interarm regions due to an increase in ISM density and star formation. These arms can vary in prominence from the grand-design style consisting of two distinct, symmetric arms, to flocculent, patchy arms (e.g. Hubble, 1926; Elmegreen & Elmegreen, 1982, 1987; Binney & Merrifield, 1998). The disk also contains a young stellar population in contrast to the bulge, which contains an older stellar population (e.g. Baade, 1944). The bulge is a spheroidal shape extending above and below the plane and can vary in size relative to the disk, often characterized by the bulge-to-disk ratio. At the very centre of the bulge in most spiral galaxies are supermassive black holes, and some of these power active galactic nuclei, which expel energy outward via jets, radiation or wind (Fabian, 2012). Lastly, the halo is a low density spheroidal region in which the disk sits. It contains a population of globular clusters, old stars and dark matter (Kent, 1987; Binney & Merrifield, 1998). However, it is worthwhile noting that most galaxies are dark matter dominated everywhere, not just in the halo.

A number of surveys over the past decade have extensively studied the properties of the ISM in extragalactic sources. In spiral galaxies there is a broad range of characteristics. Atomic and molecular gas masses can range anywhere from  $1 \times 10^7$ – $1.4 \times 10^{10} M_{\odot}$  and  $7 \times 10^6$ – $6 \times 10^9 M_{\odot}$ , respectively, in nearby galaxies (e.g. Walter et al., 2008; Leroy et al., 2009). There is also a wide range in temperatures for the dust populations. Galametz et al. (2012) investigated two dust components, a warm one and a cold one, and found a range of cold dust temperatures between 19 and 25.2 K, and a range of warm dust temperatures between 56 and 63 K. The total dust mass in spiral type galaxies ranges from  $10^{6.39}$ – $10^{8.57}$  as

found by the *Spitzer* Infrared Nearby Galaxy Survey (Draine et al., 2007), while the dust-to-gas mass ratio is on average about 0.007 (corresponding to a gas-to-dust ratio of roughly 140). More recently, Galametz et al. (2012) report dust masses in spirals between  $\sim 5 \times 10^6$  and  $1.4 \times 10^8 M_{\odot}$  via fitting the dust spectral energy distribution with a modified blackbody. Thus, spiral galaxies encompass a vast set of characteristics for their ISM properties.

### 1.2.1.1 M51

M51 (NGC 5194), also known as the Whirlpool Galaxy is an excellent example of a grand design, spiral galaxy and is located roughly 9.9 Mpc away (Tikhonov et al., 2009). Its optical disk is approximately  $11.2' \times 6.9'$  ( $32.3$  kpc  $\times$   $19.9$  kpc) in size at the  $25^{th}$  magnitude surface brightness level,  $D_{25}$  (Kennicutt et al., 2003), while its disk as observed in H I extends  $\sim 12.4' \times 10.0'$  ( $35.7$  kpc  $\times$   $28.8$  kpc) with a total mass of  $2.54 \times 10^9 M_{\odot}$  (Walter et al., 2008). The molecular hydrogen, H<sub>2</sub>, has a total mass of  $2 \times 10^9 M_{\odot}$  covering roughly  $9' \times 6'$  and well traces the H I emission. However, the ratio of atomic-to-neutral gas varies from 0.1 in the centre to 20 at the edges (Schuster et al., 2007) indicating that the centre of the galaxy is molecular gas dominated but transitions to atomic gas dominated with increasing radius (Schuster et al., 2007). Studies of H $\alpha$  and Pa $\alpha$  emission show over 1000 H II regions and a star formation rate of roughly  $4 M_{\odot} \text{ yr}^{-1}$  (Scoville et al., 2001). The galaxy also has a weak Seyfert 2 nucleus (Ho et al., 1997).

The dust content in M51 has been studied extensively at infrared wavelengths. Calzetti et al. (2005) first presented the *Spitzer* photometry from the *Spitzer* Infrared Nearby Galaxy Survey (SINGS; Kennicutt et al., 2003) at 3.6, 4.5, 5.8, 8.0, 24, 70 and 160  $\mu\text{m}$ . They find that the spiral arms are well defined at infrared wavelengths, tracing PAH emission and warm dust. Combining the infrared data with

ultraviolet and optical maps they determine that the  $24\text{ }\mu\text{m}$  emission can be used as a local tracer of the star formation rate in M51 and determine a star formation rate surface density of  $0.015\text{ M}_\odot\text{ yr}^{-1}\text{ kpc}^{-2}$ . Kennicutt et al. (2007) complemented this study by also making use of the *Spitzer* infrared data to study the star formation rate law. They find a strong linear correlation in log-log space between the star formation rate surface density and the total hydrogen gas mass surface density, with a slope ranging from 1.37–1.56, consistent with that of the Kennicutt-Schmidt law (which has a slope of  $1.4 \pm 0.15$ ; Kennicutt, 1998). More recently, Mentuch Cooper et al. (2012) utilized previously obtained infrared observations with *Herschel* photometry at 70, 160, 250, 350 and  $500\text{ }\mu\text{m}$  to carry out a detailed study of the dust via spectral energy distribution modelling. They found dust temperatures varying between 20 and 25 K, and a total dust mass of  $1.2 \times 10^8\text{ M}_\odot$ . The average gas-to-dust mass ratio is  $94 \pm 17$ , close to the average Galactic value of roughly 160 (Zubko et al., 2004). In the same study, it was determined that the most recent starburst episode in M51 was less than 500 Myr ago. Merger interactions between galaxies often trigger star formation, as demonstrated by numerical simulations (e.g. Mihos & Hernquist, 1996), and in M51, observations of the stellar population reveal that blue supergiants are found along the tidal tail between M51 and its companion (Tikhonov et al., 2009), supporting this theory.

### 1.2.2 Elliptical Galaxies

Unlike spiral galaxies, elliptical galaxies generally do not have an obvious disk and instead are spheroidal in shape with a wide range of masses, between  $10^7$  and  $10^{13}\text{ M}_\odot$  and sizes from 0.1 kpc to over 100 kpc across (Carroll & Ostlie, 2006). Elliptical galaxies contain large amounts of dark matter with mass-to-light ratios of

upwards of  $100 \text{ L}_\odot \text{ M}_\odot^{-1}$  (Carroll & Ostlie, 2006) and may contain many globular cluster systems. They also follow a characteristic surface brightness profile that falls off as  $\text{radius}^{1/4}$  in optical bands (de Vaucouleurs, 1948), and generally contain smaller amounts of cold gas and dust than spiral galaxies (e.g. Xilouris et al., 2004; Welch et al., 2010; Young et al., 2011; Smith et al., 2012).

Once thought to contain very little ISM, we now know that a significant fraction of early type galaxies do, in fact, contain gas and dust. The ATLAS<sup>3D</sup> survey (Young et al., 2011), consisting of a sample of 260 early type galaxies with a median stellar mass of  $3 \times 10^{10} \text{ M}_\odot$ , found a 20% detection rate in CO emission, implying the presence of molecular gas. Of those galaxies with molecular mass, the amount ranges between  $10^7$  and  $10^{9.3} \text{ M}_\odot$ . The *Herschel* Reference Survey (Boselli et al., 2010) determined that dust was present in 50% of their sample using the  $250 \mu\text{m}$  waveband as an indicator (Smith et al., 2012). Typical dust temperatures in early type galaxies range between 16 and 32 K, while dust masses are approximately  $10^{4.5}\text{--}10^7 \text{ M}_\odot$  (Bregman et al., 1998; Smith et al., 2012).

### 1.2.2.1 Centaurus A

Centaurus A is a giant elliptical galaxy with a prominent dust lane running through the centre of the galaxy, located 3.8 Mpc away (Harris et al., 2010). It has a tri-axial morphology implying no preferred axis of rotation and is approximately  $20'$  (22.1 kpc) in diameter as seen in optical wavebands (Israel, 1998). The galaxy is also rich in globular clusters, with over 400 confirmed (Woodley et al., 2007, 2010). It is believed that the galaxy underwent a merger with a small spiral galaxy at some point during its past, resulting in the warped disk and peculiar overall appearance (Baade, 1944; Quillen et al., 1993).

The disk is rich in both atomic and molecular gas (e.g. Eckart et al., 1990;

van Gorkom et al., 1990; Quillen et al., 1992; Struve et al., 2010) with a total H I mass of  $\sim 4 \times 10^8 M_\odot$ , and total H<sub>2</sub> mass of  $\sim 4 \times 10^8 M_\odot$  (Morganti, 2010). There have been shells detected in the outskirts of the galaxy (as far as 15' (16.6 kpc) from the centre) in H I, which strengthen the merger model (Schiminovich et al., 1994). Infrared studies using *Spitzer* IRAC observations by Quillen et al. (2006) reveal a ring that resembles a parallelogram as seen in the 3.6, 4.5, 5.8 and 8.0  $\mu\text{m}$  wavebands. It is modelled as a set of concentric rings at various inclinations giving rise to the warped disk morphology.

Cen A also has a set of very large radio lobes powered by an active galactic nucleus. The total area covered by the radio emission is roughly  $8^\circ \times 4^\circ$  (530.6 kpc  $\times$  265.3 kpc) (Combi & Romero, 1997), though the prominent bubble shaped lobes extend roughly 5 kpc outward from the nucleus (Israel, 1998). The compact jets near the nucleus extend only about 1 pc from the centre (Israel, 1998). There is also a large amount of X-ray emission from Cen A, spatially coincident with the nucleus, jets and lobes (e.g. Turner et al., 1997; Kraft et al., 2009).

### 1.3 The Herschel Space Observatory

The first space observatory designed to observe the sky at mid- and far-infrared wavelengths was the *Infrared Astronomical Satellite* (IRAS), which carried out an all-sky survey in 1983 at four wavelengths, 12, 25, 60 and 100  $\mu\text{m}$  (Neugebauer et al., 1984). This survey produced a number of catalogs containing upwards of  $2.7 \times 10^5$  point sources and extended sources, as well as hundreds of spectra of select objects (IRAS Explanatory Supplement, 1988). Following the success of IRAS, the *Infrared Space Observatory* (ISO), capable of both photometric and spectroscopic observations between 2.5 and 240  $\mu\text{m}$ , was launched in 1995 (Kessler et al., 1996).

ISO had numerous advantages over IRAS, including the ability for the observing community to propose for time on the telescope for their own projects. During the same era as IRAS and ISO the *Kuiper Airborne Observatory*, which started flying in 1975 (e.g. Harvey, 1979, and references therein), complemented the space-based observations by conducting regular flights observing the sky at high altitudes using a variety of instruments over its roughly 20 year lifetime.

Striving to produce increasingly higher resolution images of everything from embedded young stellar objects to high-redshift sources, the National Aeronautics and Space Administration (NASA) created the *Spitzer Space Telescope* (hereafter *Spitzer*; Werner et al., 2004), launched in 2003. *Spitzer* has a primary mirror with a diameter of 85 cm (Werner et al., 2004), and two photometers and a spectrometer on board. The Infrared Array Camera (IRAC) conducted photometry at 3.6, 4.5, 5.8 and 8  $\mu\text{m}$  (Fazio et al., 2004) and is still observing today at the two shortest wavelengths. The Multiband Imaging Photometer for *Spitzer* (MIPS) also conducted photometry, but at the mid- to far-infrared wavelengths 24, 70 and 160  $\mu\text{m}$  (Rieke et al., 2004), spanning the peak dust continuum emission. Lastly, the Infrared Spectrograph (IRS) could obtain spectra between 5.3 and 38  $\mu\text{m}$  (Houck et al., 2004). *Spitzer* ran out of the cryogen that kept the telescope at just a few degrees above absolute zero in 2009 (Carey et al., 2010), thus beginning the warm mission. The end of *Spitzer*'s cold mission paved the way for the next set of far-infrared observatories. In May of 2009, the *Herschel Space Observatory* (hereafter *Herschel*; Pilbratt et al., 2010) was launched by the European Space Agency (ESA) with some involvement by NASA, while the joint NASA and German Aerospace Center (DLR) flying *Stratospheric Observatory for Infrared Astronomy* (SOFIA) was also inaugurated in 2010 (Young et al., 2012). The majority of data acquired for this thesis come from *Herschel*, thus taking advantage of the best far-infrared data currently

available for analysis.

The *Herschel Space Observatory* has revolutionised our view of the Universe in the regime of the far-infrared and submillimetre astronomy. The primary mirror is currently the largest in space at 3.5 m in diameter (Pilbratt et al., 2010), and the observatory has three instruments capable of photometric and spectroscopic observations on board: the Photodetector Array Camera and Spectrometer (PACS; Poglitsch et al., 2010), the Spectral and Photometric Imaging REceiver (SPIRE; Griffin et al., 2010), and the Heterodyne Instrument for the Far Infrared (HIFI; de Graauw et al., 2010). A summary of the major properties of each instrument in comparison to previous observatories is presented in Table 1.1. PACS covers similar wavelength ranges to both *Spitzer* and ISO, but at much higher angular resolution (see Table 1.1). SPIRE’s wavelength range covers longer wavelengths than have been observed before by a space observatory, and in some cases, for the first time ever. Furthermore, the SPIRE Fourier Transform Spectrometer (FTS) has the major advantage of being able to obtain the complete spectrum of a target, rather than discrete parts of the spectrum centred on select spectral lines or wavelength ranges. In contrast to both the PACS spectrometer and the SPIRE FTS, HIFI makes use of heterodyne receivers to collect continuous spectra between 157 and 213  $\mu\text{m}$ , and 240 and 625  $\mu\text{m}$  using seven bands. A selection of some of the most interesting scientific discoveries *Herschel* has made, focusing on those most relevant to this thesis, are discussed below.

Table 1.1. A comparison of *Herschel* to previous space observatories

Property	Observatory			
	<i>Herschel</i> <sup>a</sup>	<i>Spitzer</i> <sup>b</sup>	ISO <sup>c</sup>	IRAS <sup>d</sup>
Primary Mirror diameter (m)	3.5	0.85	0.6	0.6
Photometric Wavebands ( $\mu\text{m}$ )	70, 100, 160 (PACS) 250, 350, 500 (SPIRE)	3.6, 4.5, 5.8, 8 (IRAC) 24, 70, 160 (MIPS)	2.5–5.5, 4–18 (ISOCAM) 3–120, 50–240 (ISOPHOT)	12, 25, 60, 100
Spectroscopic Wavelength ( $\mu\text{m}$ )	55–210 (PACS) 157–625 (HIFI) 194–671 (SPIRE)	5.3–38 (IRS)	2.4–45.2 (SWS) 43–197 (LWS)	8–13, 11–23
Photometric FWHM ('')				
of select wavelengths:				
~24–25 $\mu\text{m}$	—	6	23	240–360
60 or 70 $\mu\text{m}$	5.5 $\times$ 5.8	18	50–60	240–360
100 $\mu\text{m}$	6.7 $\times$ 6.9	—	~ 80	240–360

Table 1.1 (cont'd)

Property	Observatory			
	<i>Herschel</i> <sup>a</sup>	<i>Spitzer</i> <sup>b</sup>	ISO <sup>c</sup>	IRAS <sup>d</sup>
160 $\mu\text{m}$	10.5 $\times$ 12.0	40	134	—

<sup>a</sup>PACS: Poglitsch et al. (2010), SPIRE: Poglitsch et al. (2010), HIFI: de Graauw et al. (2010); PACS FWHM from the PACS OM (2011), SPIRE FWHM from the SPIRE OM (2011)

<sup>b</sup>IRAC: Fazio et al. (2004), MIPS: Rieke et al. (2004), IRS: Houck et al. (2004)

<sup>c</sup>ISOCAM: Cesarsky et al. (1996), SWS: de Graauw et al. (1996), LWS: Clegg et al. (1996); FWHM values from The ISO Handbook (Kessler et al., 2003).

<sup>d</sup>IRAS Explanatory Supplement (IRAS Explanatory Supplement, 1988)

### 1.3.1 Herschel Science Highlights

There were many goals across various categories within astronomy set for *Herschel* before it was launched, and it has certainly met and arguably exceeded a number of them already. The mission has just come to an end, but many more results are still to come as the data become fully exploited by the astronomy community. Advances and discoveries have been made in a number of areas from young embedded stellar objects to the distant Universe. For example, Acke et al. (2012) presented *Herschel* observations of a debris disk around the star Fomalhaut that indicate that the star's disk is active in producing fluffy dust grains via collisions, giving us insight into the dynamics of exoplanetary systems. On slightly larger scales, *Herschel* observations are revealing more clues about star formation. Initial analysis of two subregions of the Herschel Infrared GALactic plane survey (Hi-Gal; Molinari et al., 2010b,a) by Elia et al. (2010) found a total of almost 1000 embedded cores, and SED modelling of a subset of these objects indicates a large fraction of them are forming high-mass stars despite possessing lower than critical core gas mass surface densities. This critical threshold is a theoretical value for the surface density of the gas that cores must surpass in order to form massive stars, and is derived to be  $1 \text{ g cm}^{-2}$  (Krumholz & McKee, 2008). *Herschel*'s high resolution photometry has also revealed that molecular clouds are filled with a cobweb-like structure of filaments, which possess a characteristic width of 0.1 pc that likely stems from the dissipation of turbulence (Arzoumanian et al., 2011). These filamentary structures also appear to be the primary hosts of star-forming regions within a molecular cloud.

*Herschel* has also produced some spectacular observations of many well-known galaxies. The HERschel Inventory of The Agents of Galaxy Evolution (HERITAGE; Meixner et al., 2010) team is investigating the Small and Large

Magellanic Clouds (SMC and LMC, respectively) in search of understanding the evolution of the ISM in a low-metallicity environment, one that might mimic primordial galaxies at high redshift. Meixner et al. (2010) presented early science results for the LMC and determined that the dust grains are likely composed of amorphous carbon and silicates rather than graphite and silicates. One interesting result that stemmed from the *Herschel* photometry of the LMC is the first far-infrared and submillimetre detection of Supernova 1987A. An investigation of this emission showed that the dust coincident with the location of the remnant has been produced by the supernova ejecta, indicating quick processing of material post-event (Matsuura et al., 2011). A study of the ultra-luminous infrared galaxy (ULIRG) Arp 220 by Rangwala et al. (2011) using the SPIRE Fourier Transform Spectrometer (FTS) revealed that this extreme environment hosts an X-ray luminous active galactic nucleus (AGN) at its centre and a wealth of molecules in various energy states in its gas component. Furthermore, the mechanical energy of the merger in this galaxy is affecting this molecular gas. The *Herschel* Virgo Cluster Survey has presented numerous results thus far, one of which focuses on the dust-to-gas ratio of the spatially resolved members of the Virgo Cluster (Pappalardo et al., 2012). These authors find among other things a radially increasing or flat trend in the dust-to-gas ratio with increasing radius for galaxies deficient in atomic gas, and they conclude that the cluster environment is having an effect on the molecular gas and dust distributions within individual galaxy members. The observations of the *Herschel* Multi-tiered Extragalactic Survey have even revealed gravitationally lensed submillimetre galaxies, some of which would normally have fluxes too weak to be detected by SPIRE at 500  $\mu\text{m}$  (Wardlow et al., 2013).

These are just a few of the many important and inspiring results published to date and there will be many more to come. In this thesis, we focus on a unique

set of observations from the PACS and SPIRE instruments, adding to the rich and diverse science produced with *Herschel*.

## 1.4 PACS Spectroscopy and Processing

A large portion of this thesis is spent analysing spectroscopy from the *Herschel* PACS instrument; thus, it is useful to describe the data processing steps in more detail here than it appears in Chapters 3 and 4. We refrain from detailing the PACS and SPIRE photometry reduction process further, as it is a more simple process and it is described sufficiently in Chapter 2.

The PACS spectrometer consists of 25 spatial pixels (spaxels) arranged in a  $5 \times 5$  grid, with each spaxel covering a field of view on the sky of  $9.4'' \times 9.4''$  (PACS OM, 2011). The spectral dimension in each spaxel is subdivided into 16 pixels, producing a spectral resolution of between approximately 75 and 300 km s<sup>-1</sup> (PACS OM, 2011). All of our PACS spectroscopic observations were carried out using the Line Spectroscopy mode, meaning we centred each observation on the spectral line we intended to target and the total wavelength range seen by the instrument was narrow, ranging from  $\sim 0.35\text{--}1.8 \mu\text{m}$ . This wavelength range is stepped through by the instrument's grating during an observation such that each spaxel contains many individual spectra covering slightly different overlapping wavelength ranges, with the centre of the line being sampled by the most steps. An example of these overlapping spectra for our [C II](158  $\mu\text{m}$ ) observations of the centre of M51 is shown in Figure 1.5.

The spectroscopic observations from the *Herschel* PACS are initially processed using the Herschel Interactive Processing Environment (HIPE; Ott, 2010) and Flexible Image Transport System (FITS) files holding the final spectral data are

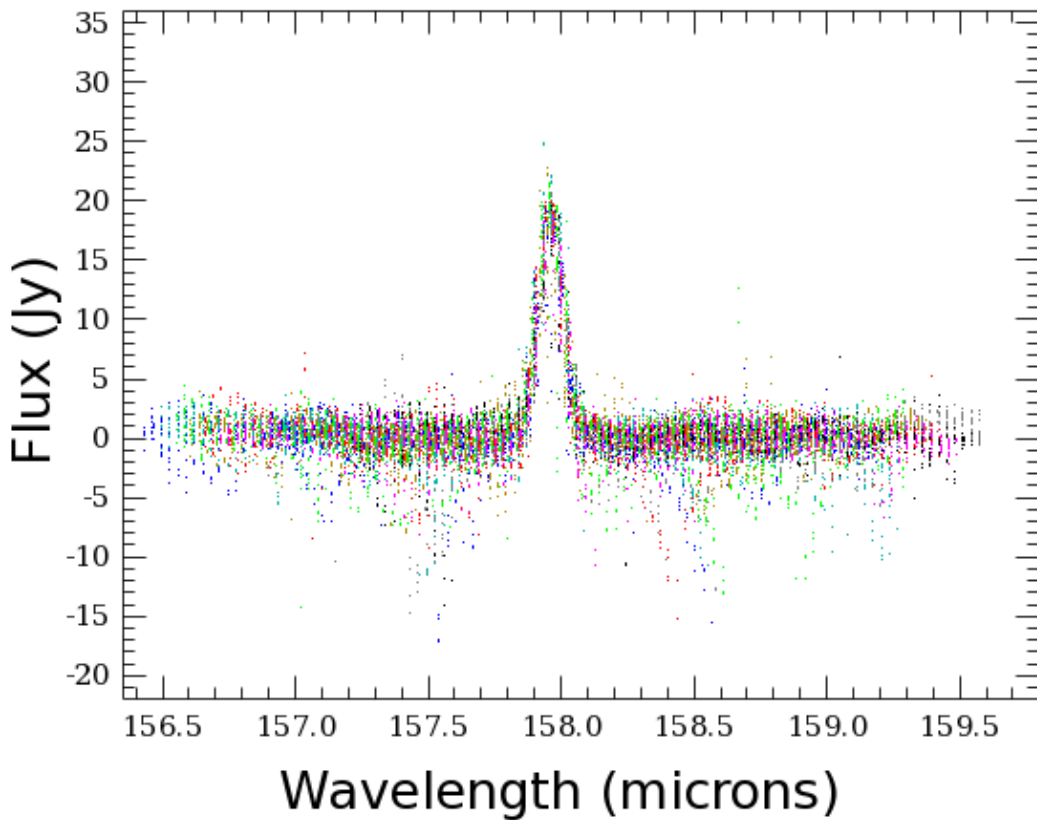


Figure 1.5: An example of a PACS spectroscopic observation in its raw data form. Shown is the spectrum of the [C II]( $158 \mu\text{m}$ ) line in the central spaxel of one of the rasters of M51.

produced. The line fitting and map making are done in a program called PACSman (Lebouteiller et al., 2012), which is an Interactive Data Language (IDL) package.

The line fitting iterates through each of the 25 spaxels comprising a single raster, and then through each raster if there is more than one, as is the case for both M51 (see Chapter 3) and Centaurus A (see Chapter 4). The fitting is carried out on the raw data produced in HIPE, prior to any rebinning, so as to obtain the best fit possible. The continuum is fit first using a polynomial of up to a maximum of five orders, at the choice of the user. For our observations, a second order polynomial was sufficient for the baseline fitting. Next, the line is fit using a Gaussian function

with the option of adding a broadening component for broader lines. The parameters of the best fitting function, as well as the integrated flux, velocity information, full-width at half-maximum (FWHM) of the line, and continuum information are saved for the last step, map making. An example of a [C II](158  $\mu\text{m}$ ) spectrum for M51 and its best fit are shown in Figure 1.6.

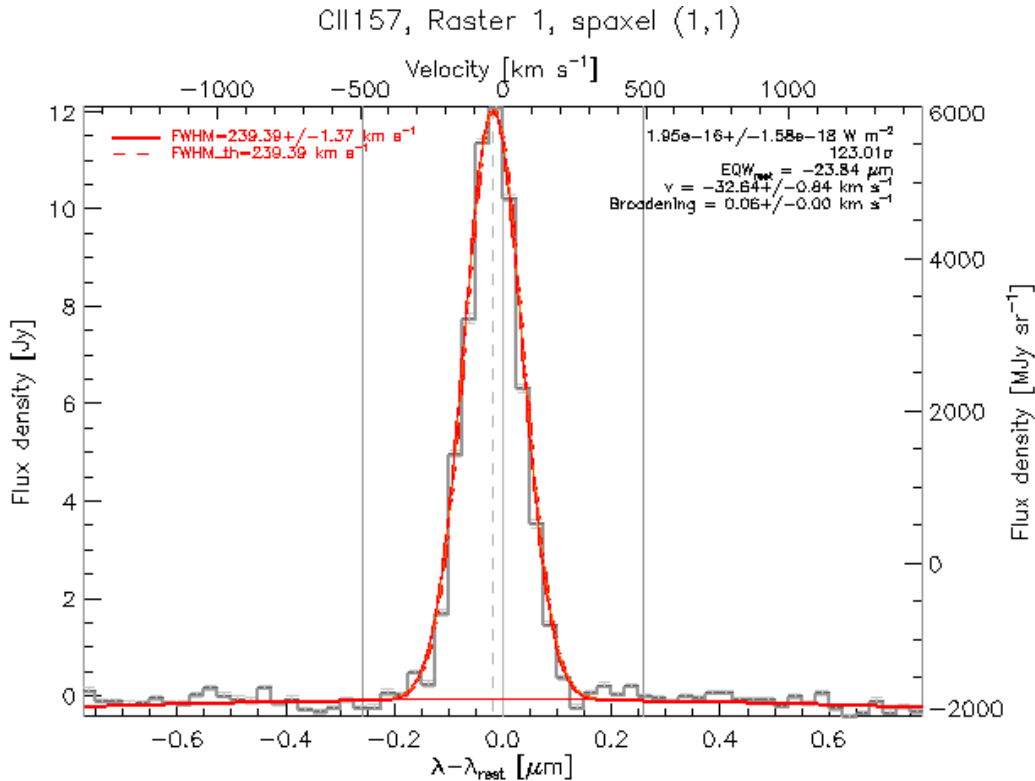


Figure 1.6: An example of a line fit to a [C II](158  $\mu\text{m}$ ) spectrum of M51 using PACSman. The rebinned spectrum is shown in gray, the thin red line shows the best fit to the continuum, and the thick red line shows the best fit to the line. The vertical gray lines mark the predicted line centre, and the two boundaries of the line component. The vertical dashed line marks the observed line centre.

The maps are constructed by first laying down a grid with a pixel scale of 9.4''/3, corresponding to one-third of the original pixel scale of a raster (i.e. each pixel is subdivided into nine pixels at the new scale). For each pixel in the final grid, the code iterates through all rasters searching for all contributing pixels. Each

contributing pixel is rotated through the appropriate position angle to align it to the final grid. Next, the area of each original pixel that coincides with the selected final pixel is calculated as the weight for that pixel. Finally, the weighted mean of the values of the contributing pixels is calculated and stored in the new pixel. This process is completed for the flux, velocity, FWHM and continuum data and the new maps are stored as fits files for full analysis, along with their associated error maps.

## 1.5 This Thesis

As described above, the infrared and submillimetre wavelength regime is important for probing the cold ISM. With the unprecedented resolution of *Herschel* we can now investigate the evolution of the cold regions of the ISM and the impact of star formation on not only molecular clouds in our own Milky Way, but in nearby galaxies as well. Resolving details on scales of a few hundred parsecs in other galaxies gives us additional insight into the characteristics of the ISM and we can search for variations in these important properties within a single galaxy. Extragalactic studies also allow us to look at each galaxy as a whole to broaden our understanding, something that can be difficult to exploit in our own Galaxy, depending on the wavelength regime being used. Thus, we can also compare and contrast ISM properties between galaxies of different morphologies to see how environment impacts the local ISM.

The *Herschel* Very Nearby Galaxies Survey (VNGS; P.I. Christine Wilson) is a diverse sample of 13 galaxies located closer than roughly 80 Mpc away. Centaurus A (Cen A; NGC 5128) and M51 (NGC 5194) are both sources that are a part of this survey. M51 is classified as a grand-design, late-type spiral, SAbc (de Vaucouleurs et al., 1991), and is oriented almost face-on to our line of sight. Cen A

is classified as a peculiar S0 giant elliptical galaxy (de Vaucouleurs et al., 1991) and contains an embedded, edge-on disk. Thus, at first glance they are quite different in morphology; however, both have active nuclei (CenA is a proper AGN and M51 is a low luminosity AGN) and have been affected by merger events. Investigating the ISM in each galaxy affords us the ability to both search for regional variations as well as global morphological influence on the ISM. In particular, we can compare and contrast the molecular cloud properties of the two galaxies and evaluate the possible influence of an active nucleus, a merger event, or spiral arms on the evolution and properties of the ISM.

In this thesis, we utilise observational data obtained from the James Clerk Maxwell Telescope and the *Herschel* Space Observatory to investigate the gas and dust components of the ISM in Cen A and M51. Both observatories target wavelengths in the far-infrared and submillimetre regimes, key wavebands to study to enrich our understanding of the ISM. Photometry from *Herschel* allows us to model the observed spectral energy distribution (SED) on smaller scales, as well as at longer wavelengths than other space observatories. *Herschel*'s spectroscopic instruments have improved sensitivity and resolution over observatories such as ISO, allowing us to detect weaker far-infrared cooling lines that may have been previously undetected, in addition to better observations of the strongest lines. Furthermore, the JCMT's HARP-B instrument allows us to probe the CO( $J = 3 - 2$ ) transition, adding additional information about the gas to our investigation. Thus, we will study these two objects with the best data available to satisfy our scientific goals of contributing to the understanding of the evolution of the ISM.

This thesis is organised in the following manner. In Chapter 2 we present an investigation of the gas-to-dust ratio in Cen A using *Herschel* PACS and SPIRE photometry, as well as spectroscopy from the JCMT. In Chapter 3 we present an

investigation of the molecular cloud properties of the inner region of M51 using photodissociation (photon dominated) region modelling of PACS spectroscopy, and in Chapter 4 we carry out photodissociation region modelling on a radial strip of the disk of Cen A. We summarise the achievements of this work and discuss future directions in Chapter 5.

# Bibliography

- Acke, B., Min, M., Dominik, C., et al. 2012, A&A, 540, A125
- Allamandola, L. J., Tielens, A. G. G. M., & Barker, J. R. 1985, ApJ, 290, L25
- Arzoumanian, D., André, P., Didelon, P., et al. 2011, A&A, 529, L6
- Baade, W. 1944, ApJ, 100, 147
- Bendo, G. J., Joseph, R. D., Wells, M., et al. 2003, AJ, 125, 2361
- Bergin, E. A., & Tafalla, M. 2007, ARA&A, 45, 339
- Binney, J., & Merrifield, M. 1998, Galactic Astronomy, Princeton Series in Astrophysics (Princeton, NJ: Princeton University Press)
- Bolatto, A. D., Wolfire, M., & Leroy, A. K. 2013, ArXiv e-prints
- Boselli, A., Lequeux, J., & Gavazzi, G. 2002, A&A, 384, 33
- Boselli, A., Eales, S., Cortese, L., et al. 2010, PASP, 122, 261
- Boselli, A., Ciesla, L., Cortese, L., et al. 2012, A&A, 540, A54
- Bregman, J. N., Snider, B. A., Grego, L., & Cox, C. V. 1998, ApJ, 499, 670

- Broeils, A. H., & Rhee, M.-H. 1997, A&A, 324, 877
- Calzetti, D., Kennicutt, Jr., R. C., Bianchi, L., et al. 2005, ApJ, 633, 871
- Carey, S. J., Surace, J. A., Glaccum, W. J., et al. 2010, in Society of Photo-Optical Instrumentation Engineers (SPIE) Conference Series, Vol. 7731, Society of Photo-Optical Instrumentation Engineers (SPIE) Conference Series
- Carroll, B. W., & Ostlie, D. A. 2006, An Introduction to Modern Astrophysics, 2nd edn. (Addison-Wesley)
- Cesarsky, C. J., Abergel, A., Agnese, P., et al. 1996, A&A, 315, L32
- Clegg, P. E., Ade, P. A. R., Armand, C., et al. 1996, A&A, 315, L38
- Combi, J. A., & Romero, G. E. 1997, A&AS, 121, 11
- Cormier, D., Lebouteiller, V., Madden, S. C., et al. 2012, A&A, 548, A20
- Crawford, M. K., Genzel, R., Townes, C. H., & Watson, D. M. 1985, ApJ, 291, 755
- Dale, D. A., Helou, G., Contursi, A., Silbermann, N. A., & Kolhatkar, S. 2001, ApJ, 549, 215
- de Graauw, T., Haser, L. N., Beintema, D. A., et al. 1996, A&A, 315, L49
- de Graauw, T., Helmich, F. P., Phillips, T. G., et al. 2010, A&A, 518, L6
- de Vaucouleurs, G. 1948, Annales d'Astrophysique, 11, 247
- de Vaucouleurs, G., de Vaucouleurs, A., Corwin, Jr., H. G., et al. 1991, Third Reference Catalogue of Bright Galaxies (Springer-Verlag, New York)
- Desert, F.-X., Boulanger, F., & Puget, J. L. 1990, A&A, 237, 215

Downes, D., & Solomon, P. M. 1998, ApJ, 507, 615

Draine, B. T. 2003, ARA&A, 41, 241

Draine, B. T., & Lee, H. M. 1984, ApJ, 285, 89

Draine, B. T., & Li, A. 2007, ApJ, 657, 810

Draine, B. T., Dale, D. A., Bendo, G., et al. 2007, ApJ, 663, 866

Eckart, A., Cameron, M., Rothermel, H., et al. 1990, ApJ, 363, 451

Elia, D., Schisano, E., Molinari, S., et al. 2010, A&A, 518, L97

Elmegreen, D. M., & Elmegreen, B. G. 1982, MNRAS, 201, 1021

—. 1987, ApJ, 314, 3

Fabian, A. C. 2012, ARA&A, 50, 455

Fazio, G. G., Hora, J. L., Allen, L. E., et al. 2004, ApJS, 154, 10

Foyle, K., Wilson, C. D., Mentuch, E., et al. 2012, MNRAS, 421, 2917

Frerking, M. A., Langer, W. D., & Wilson, R. W. 1982, ApJ, 262, 590

Galametz, M., Kennicutt, R. C., Albrecht, M., et al. 2012, MNRAS, 425, 763

Galliano, F., Madden, S. C., Jones, A. P., et al. 2003, A&A, 407, 159

Galliano, F., Hony, S., Bernard, J.-P., et al. 2011, A&A, 536, A88

Griffin, M. J., Abergel, A., Abreu, A., et al. 2010, A&A, 518, L3

Harris, G. L. H., Rejkuba, M., & Harris, W. E. 2010, PASA, 27, 457

Harvey, P. M. 1979, PASP, 91, 143

Ho, L. C., Filippenko, A. V., & Sargent, W. L. W. 1997, ApJS, 112, 315

Holland, W. S., Bintley, D., Chapin, E. L., et al. 2013, MNRAS, 430, 2513

Hollenbach, D. J., Takahashi, T., & Tielens, A. G. G. M. 1991, ApJ, 377, 192

Houck, J. R., Roellig, T. L., van Cleve, J., et al. 2004, ApJS, 154, 18

Hubble, E. P. 1926, ApJ, 64, 321

Huchtmeier, W. K., Sage, L. J., & Henkel, C. 1995, A&A, 300, 675

Hunter, D. A., Kaufman, M., Hollenbach, D. J., et al. 2001, ApJ, 553, 121

IRAS Catalogs and Atlases: Explanatory Supplement, 1988, ed. C. A. Beichman,  
G. Neugebauer, H. J. Habing, P. E. Clegg and T. J. Chester, Washington, DC.:  
GPO, <http://irsa.ipac.caltech.edu/IRASdocs/exp.sup/>

Israel, F. P. 1998, A&A Rev., 8, 237

Jansky, K. G. 1933, Nature, 132, 66

Kaufman, M. J., Wolfire, M. G., & Hollenbach, D. J. 2006, ApJ, 644, 283

Kaufman, M. J., Wolfire, M. G., Hollenbach, D. J., & Luhman, M. L. 1999, ApJ,  
527, 795

Kennicutt, Jr., R. C. 1998, ApJ, 498, 541

Kennicutt, Jr., R. C., Armus, L., Bendo, G., et al. 2003, PASP, 115, 928

Kennicutt, Jr., R. C., Calzetti, D., Walter, F., et al. 2007, ApJ, 671, 333

Kent, S. M. 1987, AJ, 93, 816

Kessler, M. F., Steinz, J. A., Anderegg, M. E., et al. 1996, A&A, 315, L27

Kessler, M. F., Müller, T. G., Leech, K., et al. 2003, The ISO Handbook. Volume I: ISO - Mission & Satellite Overview, version 2.0 edn., European Space Agency

Kim, S.-H., Martin, P. G., & Hendry, P. D. 1994, ApJ, 422, 164

Knapp, G. R. 1987, in IAU Symposium, Vol. 127, Structure and Dynamics of Elliptical Galaxies, ed. P. T. de Zeeuw & S. D. Tremaine, 145–153

Knapp, G. R., Turner, E. L., & Cunniffe, P. E. 1985, AJ, 90, 454

Kraft, R. P., Forman, W. R., Hardcastle, M. J., et al. 2009, ApJ, 698, 2036

Krumholz, M. R., & McKee, C. F. 2008, Nature, 451, 1082

Lebouteiller, V., Cormier, D., Madden, S. C., et al. 2012, A&A, 548, A91

Leroy, A. K., Walter, F., Bigiel, F., et al. 2009, AJ, 137, 4670

Li, A., & Draine, B. T. 2001, ApJ, 554, 778

Luhman, M. L., Satyapal, S., Fischer, J., et al. 2003, ApJ, 594, 758

—. 1998, ApJ, 504, L11

Malhotra, S., Kaufman, M. J., Hollenbach, D., et al. 2001, ApJ, 561, 766

Mathis, J. S. 1996, ApJ, 472, 643

Mathis, J. S., Mezger, P. G., & Panagia, N. 1983, A&A, 128, 212

Mathis, J. S., Rumpl, W., & Nordsieck, K. H. 1977, ApJ, 217, 425

Mathis, J. S., & Whiffen, G. 1989, ApJ, 341, 808

Matsuura, M., Dwek, E., Meixner, M., et al. 2011, Science, 333, 1258

Meixner, M., Galliano, F., Hony, S., et al. 2010, A&A, 518, L71

Mentuch Cooper, E., Wilson, C. D., Foyle, K., et al. 2012, ApJ, 755, 165

Mihos, J. C., & Hernquist, L. 1996, ApJ, 464, 641

Molinari, S., Swinyard, B., Bally, J., et al. 2010a, A&A, 518, L100

—. 2010b, PASP, 122, 314

Morganti, R. 2010, PASA, 27, 463

Negishi, T., Onaka, T., Chan, K.-W., & Roellig, T. L. 2001, A&A, 375, 566

Neugebauer, G., Habing, H. J., van Duinen, R., et al. 1984, ApJ, 278, L1

Obreschkow, D., & Rawlings, S. 2009, MNRAS, 394, 1857

Oosterloo, T., Morganti, R., Crocker, A., et al. 2010, MNRAS, 409, 500

Ott, S. 2010, in Astronomical Society of the Pacific Conference Series, Vol. 434, Astronomical Data Analysis Software and Systems XIX, ed. Y. Mizumoto, K.-I. Morita, & M. Ohishi, 139–+

PACS Observer's Manual, 2011, HERSCHEL-HSC-DOC-0832, v2.4, available from the ESA *Herschel* Science Centre

Pappalardo, C., Bianchi, S., Corbelli, E., et al. 2012, A&A, 545, A75

Pilbratt, G. L., Riedinger, J. R., Passvogel, T., et al. 2010, A&A, 518, L1

Poglitsch, A., Waelkens, C., Geis, N., et al. 2010, A&A, 518, L2

- Quillen, A. C., Brookes, M. H., Keene, J., et al. 2006, ApJ, 645, 1092
- Quillen, A. C., de Zeeuw, P. T., Phinney, E. S., & Phillips, T. G. 1992, ApJ, 391, 121
- Quillen, A. C., Graham, J. R., & Frogel, J. A. 1993, ApJ, 412, 550
- Rangwala, N., Maloney, P. R., Glenn, J., et al. 2011, ApJ, 743, 94
- Reach, W. T., Dwek, E., Fixsen, D. J., et al. 1995, ApJ, 451, 188
- Rieke, G. H., Young, E. T., Engelbracht, C. W., et al. 2004, ApJS, 154, 25
- Röllig, M., Ossenkopf, V., Jeyakumar, S., Stutzki, J., & Sternberg, A. 2006, A&A, 451, 917
- Rubin, R. H. 1985, ApJS, 57, 349
- Schiminovich, D., van Gorkom, J. H., van der Hulst, J. M., & Kasow, S. 1994, ApJ, 423, L101+
- Schuster, K. F., Kramer, C., Hitschfeld, M., Garcia-Burillo, S., & Mookerjea, B. 2007, A&A, 461, 143
- Scoville, N. Z. 2012, ArXiv e-prints
- Scoville, N. Z., Polletta, M., Ewald, S., et al. 2001, AJ, 122, 3017
- Smith, M. W. L., Gomez, H. L., Eales, S. A., et al. 2012, ApJ, 748, 123
- SPIRE Observers' Manual, 2011, HERSCHEL-HSC-DOC-0798, v2.4, available from the ESA *Herschel* Science Centre
- Stacey, G. J., Geis, N., Genzel, R., et al. 1991, ApJ, 373, 423

- Strong, A. W., Bloemen, J. B. G. M., Dame, T. M., et al. 1988, *A&A*, 207, 1
- Struve, C., Oosterloo, T. A., Morganti, R., & Saripalli, L. 2010, *A&A*, 515, A67+
- Thornley, M. D., Leroy, A. K., Schruba, A., et al. 2010, in Astronomical Society of the Pacific Conference Series, Vol. 438, Astronomical Society of the Pacific Conference Series, ed. R. Kishes, T. L. Landecker, & A. G. Willis, 3
- Tielens, A. G. G. M. 1995, in Astronomical Society of the Pacific Conference Series, Vol. 73, From Gas to Stars to Dust, ed. M. R. Haas, J. A. Davidson, & E. F. Erickson, 3–22
- Tielens, A. G. G. M. 2005, *The Physics and Chemistry of the Interstellar Medium* (Cambridge: Cambridge University Press)
- Tielens, A. G. G. M., & Hollenbach, D. 1985, *ApJ*, 291, 722
- Tikhonov, N. A., Galazutdinova, O. A., & Tikhonov, E. N. 2009, *Astronomy Letters*, 35, 599
- Turner, T. J., George, I. M., Mushotzky, R. F., & Nandra, K. 1997, *ApJ*, 475, 118
- van de Hulst, H. C. 1951, *AJ*, 56, 144
- van Gorkom, J. H., van der Hulst, J. M., Haschick, A. D., & Tubbs, A. D. 1990, *AJ*, 99, 1781
- Walter, F., Brinks, E., de Blok, W. J. G., et al. 2008, *AJ*, 136, 2563
- Wardlow, J. L., Cooray, A., De Bernardis, F., et al. 2013, *ApJ*, 762, 59
- Weingartner, J. C., & Draine, B. T. 2001, *ApJ*, 548, 296
- Welch, G. A., Sage, L. J., & Young, L. M. 2010, *ApJ*, 725, 100

- Werner, M. W., Roellig, T. L., Low, F. J., et al. 2004, ApJS, 154, 1
- Wilson, C. D., Warren, B. E., Israel, F. P., et al. 2009, ApJ, 693, 1736
- Wolfire, M. G., Tielens, A. G. G. M., & Hollenbach, D. 1990, ApJ, 358, 116
- Woodley, K. A., Harris, W. E., Beasley, M. A., et al. 2007, AJ, 134, 494
- Woodley, K. A., Harris, W. E., Puzia, T. H., et al. 2010, ApJ, 708, 1335
- Xilouris, E. M., Madden, S. C., Galliano, F., Vigroux, L., & Sauvage, M. 2004, A&A, 416, 41
- Young, E. T., Becklin, E. E., Marcum, P. M., et al. 2012, ApJ, 749, L17
- Young, J. S., & Knezek, P. M. 1989, ApJ, 347, L55
- Young, J. S., & Scoville, N. Z. 1991, ARA&A, 29, 581
- Young, L. M., Bureau, M., Davis, T. A., et al. 2011, MNRAS, 414, 940
- Zinnecker, H., & Yorke, H. W. 2007, ARA&A, 45, 481
- Zubko, V., Dwek, E., & Arendt, R. G. 2004, ApJS, 152, 211

Chapter **2**

# The gas-to-dust mass ratio of Centaurus A as seen by Herschel

T. J. Parkin, C. D. Wilson, K. Foyle, M. Baes, G. J. Bendo, A. Boselli, M. Bouquin, A. Cooray, D. Cormier, J. I. Davies, S. A. Eales, M. Galametz, H. L. Gomez, V. Lebouteiller, S. Madden, E. Mentuch, M. J. Page, M. Pohlen, A. Remy, H. Roussel, M. Sauvage, M. W. L. Smith, and L. Spinoglio

2012, *The Monthly Notices of the Royal Astronomical Society*, Volume 422, Issue 3, pp. 2291–2301, DOI: 10.1111/j.1365-2966.2012.20778.x. Reproduced with permission from the *Monthly Notices of the Royal Astronomical Society* and Oxford University Press.

## 2.1 Introduction

Elliptical galaxies were long thought to be gas and dust poor, but in the past few decades, several observational surveys have shown that a significant fraction of

these galaxies contain a rich interstellar medium (ISM). Detections of cold dust (temperatures of  $\sim 30$  K) in non-peculiar early type galaxies using data from IRAS could only be made in about 12 percent of the sample (e.g. Bregman et al., 1998); with improvements in our ability to detect the cold dust component of the ISM, we are finding more evidence for dust within early-types (e.g. Temi et al., 2004; Xilouris et al., 2004; Leeuw et al., 2008; Young et al., 2009; Smith et al., 2012). Other studies suggest there is a relationship between a detection of cold dust in these galaxies and the likelihood of a radio source at the core (e.g. Walsh et al., 1989). Cold gas has also been found in elliptical galaxies, both molecular (i.e. Thronson et al., 1989; Wiklind et al., 1995; Welch & Sage, 2003; Young et al., 2011), and atomic (e.g. Knapp et al., 1985; Bregman et al., 1992; Huchtmeier, 1994; Huchtmeier et al., 1995; Morganti et al., 1999, 2006; Welch et al., 2010).

Centaurus A (Cen A; NGC 5128) is the closest example of a giant elliptical galaxy, located at a distance of  $3.8 \pm 0.1$  Mpc (Harris et al., 2010). It has a warped disc, likely the result of a past merger event, which contains an abundance of both gas and dust, and has a central active galactic nucleus (AGN) with radio jets extending out to large distances in both directions. Thus, Cen A is an ideal laboratory for studying variations in the ISM at high-resolution and to look for effects the AGN might have on the neighbouring disc. Note that while these interesting traits do make Cen A a somewhat peculiar elliptical galaxy, some studies show that overall Cen A is still a normal elliptical on global scales, and that its proximity is what gives us insight to its peculiarity (e.g. Harris, 2010).

Cen A has been observed extensively in the past over a wide range of wavelengths. For a comprehensive review of the numerous physical characteristics of Cen A, see Israel (1998) and Morganti (2010). Observations of H I covering a large area of the sky surrounding Cen A (e.g van Gorkom et al., 1990; Schiminovich

et al., 1994; Morganti et al., 2008; Struve et al., 2010) reveal emission throughout the disc and in shells at large distances from the disc, supporting the merger scenario. The central core itself shows both blueshifted and redshifted HI absorption (Morganti et al., 2008; Struve et al., 2010), consistent with a circumnuclear disc.

Due to its low latitude in the southern sky ( $13^{\text{h}}25^{\text{m}}27.6^{\text{s}}$ ,  $-43^{\circ}01'09''$ ), only a small number of telescopes are capable of observing Cen A in CO, such as the Swedish-ESO Submillimeter Telescope (SEST; e.g. Phillips et al., 1987; Eckart et al., 1990; Quillen et al., 1992; Rydbeck et al., 1993). Detections in the  $J = 1 - 0$  transition by Eckart et al. (1990) show that the emission primarily traces the optical disc, but drops off significantly beyond about 90 arcsec on either side of the centre of the disc. In addition, Eckart et al. (1990) and Eckart et al. (1990b) report detections of the  $^{12}\text{CO}$  and  $^{13}\text{CO}$   $J = 1 - 0$  line in absorption against the nuclear non-thermal continuum, and suggest the same molecular clouds are responsible for both the emission and absorption features.

*Spitzer Space Observatory* IRAC observations of Cen A (Quillen et al., 2006) reveal a prominent parallelogram-shaped ring of dusty material in the central disc at higher resolution than earlier mid-infrared observations of Cen A using ISOCAM on the *Infrared Space Observatory* (ISO; Mirabel et al., 1999). Observations of Cen A at 450 and 850  $\mu\text{m}$  with SCUBA and 870  $\mu\text{m}$  with LABOCA show a warped ‘S’-shaped structure close to the nucleus spanning approximately 5 arcmin across, similar to the mid-infrared observations (Leeuw et al., 2002; Weiß et al., 2008). Less-defined, fainter emission surrounds this structure and extends over much of the optical dust lane. To explain the ‘S’-shaped disc, Quillen et al. (2006) model the warped morphology of the inner infrared/submm disc using a ‘tilted-ring’ model, consisting of a series of concentric rings. The IRAS measurements of Eckart et al. (1990) reveal an average dust temperature of about 42 K,

with the temperature decreasing towards the edge of the disc. Leeuw et al. (2002) also find a temperature of  $\sim 40$  K in the disc that decreases outward. Furthermore, Weiß et al. (2008) show the first detections at submm wavelengths of non-thermal emission from the radio lobes. Studying the thermal emission within the disc, their two-component dust model shows the dust has temperatures of 30 and 20 K (warm and cold components, respectively), but no decreasing trend at larger radii. Lastly, a complementary study to this paper by Auld et al. (2012) analyses the dust properties of the remains of the smaller merger component in Cen A at large radii from the centre, using data from the *Herschel Space Observatory* (Pilbratt et al., 2010).

In spite of the number of observations of the disc of Cen A in both the dust and gas components, there are few published values of the gas-to-dust mass ratio in this galaxy. Stickel et al. (2004) report a ratio of  $\sim 300$  in a region north of the disc using data taken with ISOPHOT on ISO, and Israel (1998) suggests an upper limit of 450. Even for other early-type galaxies, only a small number of surveys report gas-to-dust mass ratios. The *Spitzer* Infrared Nearby Galaxies Survey (SINGS) survey found ratios similar to that of the Milky Way (Draine et al., 2007), while Leeuw et al. (2008) found a range of values between  $\sim 230$  and 400 for the inner H<sub>2</sub>-dominated regions of seven ellipticals. In comparison the typical value for the Milky Way is  $\sim 160$  (e.g. Zubko et al., 2004). With *Herschel* we have the capability to study the gas-to-dust mass ratio for the disc of Cen A at unprecedented resolution, and we can investigate how this ratio varies throughout the galaxy including regions near the AGN, and try to understand how the AGN affects the structure of the ISM. *Herschel* also gives us increased sensitivity compared to ground based observatories, and extends coverage to longer wavelengths than previous space missions, which are crucial to measuring the dust content of the ISM.

Here we present a detailed analysis of the gas-to-dust mass ratio of Cen A

through the central disc. We use photometric observations with both the Photodetector Array Camera and Spectrometer (PACS; Poglitsch et al., 2010) and the Spectral and Photometric Imaging Receiver (SPIRE; Griffin et al., 2010) on *Herschel*, as well as observations with the HARP-B receiver mounted on the James Clerk Maxwell Telescope (JCMT). In Section 2.2 we present the observations and data reduction process. In Section 2.3 we present our *Herschel* and JCMT photometry, our spectral energy distribution (SED) model and maps of the best-fitting dust temperatures, dust and gas masses, and the gas-to-dust mass ratio across the disc. In Section 2.4 we discuss the possible mechanisms that might explain the characteristics of our maps, and we conclude in Section 2.5.

## 2.2 Observations

### 2.2.1 *Herschel* Observations

We have obtained PACS photometry at 70 and 160  $\mu\text{m}$  (OBSIDs 1342188855 and 1342188856), and SPIRE photometry at 250, 350 and 500  $\mu\text{m}$  (OBSID 1342188663) as part of the Very Nearby Galaxies Survey (VNGS; P.I.: Christine Wilson), which is a *Herschel* Guaranteed Time program. All of these images cover a  $37' \times 37'$  area on the sky centred on Cen A. In Table 2.1 we summarise the basic characteristics of the original *Herschel* maps, which are shown in Figure 2.1.

Table 2.1: A summary of the *Herschel* observation information as well as the pixel noise and calibration uncertainty values. The measurement uncertainty is pixel-dependent (see Section 2.2.1.3 for details) and thus values are not presented here.

Wavelength ( $\mu\text{m}$ )	Beam Size (arcsec)	Pixel Size (arcsec)	Colour Correction <sup>a</sup>	Pixel Noise <sup>b</sup> ( $\text{mJy pix}^{-1}$ )	Calibration Uncertainty <sup>c</sup> (percent)
70	5.76	2	1.043	0.009	3
160	12.13	4	1.029	0.060	5
250	18.2	6	0.9836	0.147	7
350	24.5	8	0.9821	0.114	7
500	36.0	12	0.9880	0.110	7

<sup>a</sup>PACS values are divisive and SPIRE values are multiplicative.

<sup>b</sup>These uncertainties are for the pixels at their native pixel scale, as listed in this table.

<sup>c</sup>We have ignored the fact that the SPIRE calibration errors are correlated between all three bands and our total 7 percent error comprises 5 percent correlated error and 5 percent un-correlated error.

### 2.2.1.1 PACS Observations

The PACS 70 and 160  $\mu\text{m}$  observations were obtained simultaneously in scan-map mode at the ‘medium’ scan speed of 20 arcsec  $\text{s}^{-1}$ . The scans were carried out in orthogonal directions to produce a square map with homogenous coverage, with a scan-leg length of 37.0 arcmin. The observations were then processed using a pipeline that has been modified from the official one released with the *Herschel* Interactive Processing Environment (HIPE, version 4.0; Ott, 2010), using calibration file set (FM,v4). Reduction steps include protecting the data against possible cross-talk effects between bolometers in the array, and deglitching only at the second level. This involves comparing the signal detected within all of the pixels in the data cube that cover the same location in the sky, and flagging any pixels that are outliers as glitches. In addition, flat-field corrections were applied to the images, and the signal was converted to units of  $\text{Jy pix}^{-1}$ . We also applied correction factors of 1.119 and 1.174 to the 70 and 160  $\mu\text{m}$  maps, respectively, to update the images with the most recent set of calibration files. Once these steps were done in HIPE, the final map-making was done in SCANAMORPHOS<sup>1</sup> (version 6.0) (Roussel, 2013) using standard settings and pixel sizes of 2.0 and 4.0 arcsec for the 70 and 160  $\mu\text{m}$  images, respectively. We applied a colour correction to each map to accommodate the non-monochromatic nature of the galaxy’s spectral energy distribution (SED) through each of the PACS filters. To do so, we first measure the slope of the spectral energy distribution (SED) at 70 and 160  $\mu\text{m}$  using our one-component blackbody fit (see Section 2.3.1 for details), and applied the colour corrections for those slopes. Then we re-calculate the slope of the SED for the corrected fluxes and check for any change in the slope. We find slopes of -3 and +1 at 70 and 160  $\mu\text{m}$ ,

---

<sup>1</sup><http://www2.iap.fr/users/roussel/herschel/>

respectively, and thus we divide these images by correction factors of 1.043 and 1.029 (Müller et al., 2011). Lastly, we determine the mean sky value within numerous apertures overlaid onto off-target regions surrounding the galaxy at each wavelength, and then determine the average mean across all apertures. We take this mean as our background contribution and subtract it from each PACS image.

The final 70 and 160  $\mu\text{m}$  images have been convolved with appropriate kernels (see Bendo et al. (2012) for details) to match the 36 arcsec resolution of the 500  $\mu\text{m}$  image, and then regridded to a 12 arcsec pixel scale, again to match the 500  $\mu\text{m}$  image.

### 2.2.1.2 SPIRE Observations

The SPIRE observations were done in large scan-map mode with the nominal scan speed of 30 arcsec  $\text{s}^{-1}$  and the cross-scanning method. Data reduction was carried out in HIPE using a pipeline that has been altered from the standard one, in which the custom algorithm for temperature drift corrections, *BRight Galaxy ADaptive Element* (BRI $G$ ADE), was used in lieu of the standard algorithm. A description of the data processing including how BRI $G$ ADE applies this correction is given in Auld et al. (2012), Smith et al. (2012) and Smith et al. (in preparation). The final maps were made using HIPE’s map-making tool, and are in units  $\text{Jy beam}^{-1}$  with pixel scales of 6, 8 and 12 arcsec at 250, 350 and 500  $\mu\text{m}$ , respectively. However, we converted the units from  $\text{Jy beam}^{-1}$  to  $\text{Jy pix}^{-1}$  for consistency with the PACS images using beam areas for this conversion of 423, 751 and 1587 arcsec $^2$  for the 250, 350 and 500  $\mu\text{m}$  images, respectively (SPIRE Observers’ Manual, 2011). We calibrated the flux to correct for the extended nature of Cen A, using multiplicative K4 correction factors of 0.9828, 0.9834 and 0.9710 for the 250-, 350- and 500  $\mu\text{m}$  images, respectively (SPIRE Observers’ Manual, 2011). Lastly, we applied a colour

correction to each image using the same method as for the PACS images (see Table 2.1 for specific values), as well as a background subtraction. The five *Herschel* images are presented in Figure 2.1 in their original resolutions.

For analysis purposes, we have convolved the 250 and 350  $\mu\text{m}$  images with a Gaussian beam to match the 36 arcsec resolution of the 500  $\mu\text{m}$  image. The point-spread function of the SPIRE beam is well-represented by a Gaussian function down to about three percent of the peak in all three wavebands (Griffin et al., 2010), justifying our use of a Gaussian kernel. Next, these maps were regridded such that they all had the pixel scale of the 500  $\mu\text{m}$  image, 12 arcsec.

### 2.2.1.3 Noise and Uncertainties

There are three sources of noise and uncertainty that we take into account for the *Herschel* images. The dominant uncertainty for all images is the calibration uncertainty. For the PACS 70 and 160  $\mu\text{m}$  images, the calibration uncertainties are 3 and 5 percent, respectively (PACS Observer’s Manual, 2011). For the 250, 350 and 500  $\mu\text{m}$  images, the calibration uncertainties are taken to be 7 percent (SPIRE Observers’ Manual, 2011). There is also an underlying measurement uncertainty associated with the flux values in each pixel, and a map with these uncertainties is produced as part of the general reduction. Finally, there is a contribution to the error in each pixel from the background subtraction. To calculate this noise, we first find the mean value within a number of apertures overlaid on the convolved and regridded images, just as we did for the background subtraction. Then we find the average mean across all apertures (at each wavelength), and then determine the standard error, given by the standard deviation of the individual aperture mean values divided by the square root of the number of apertures. Note that we have not accounted for the confusion noise in individual pixels in the SPIRE maps (see

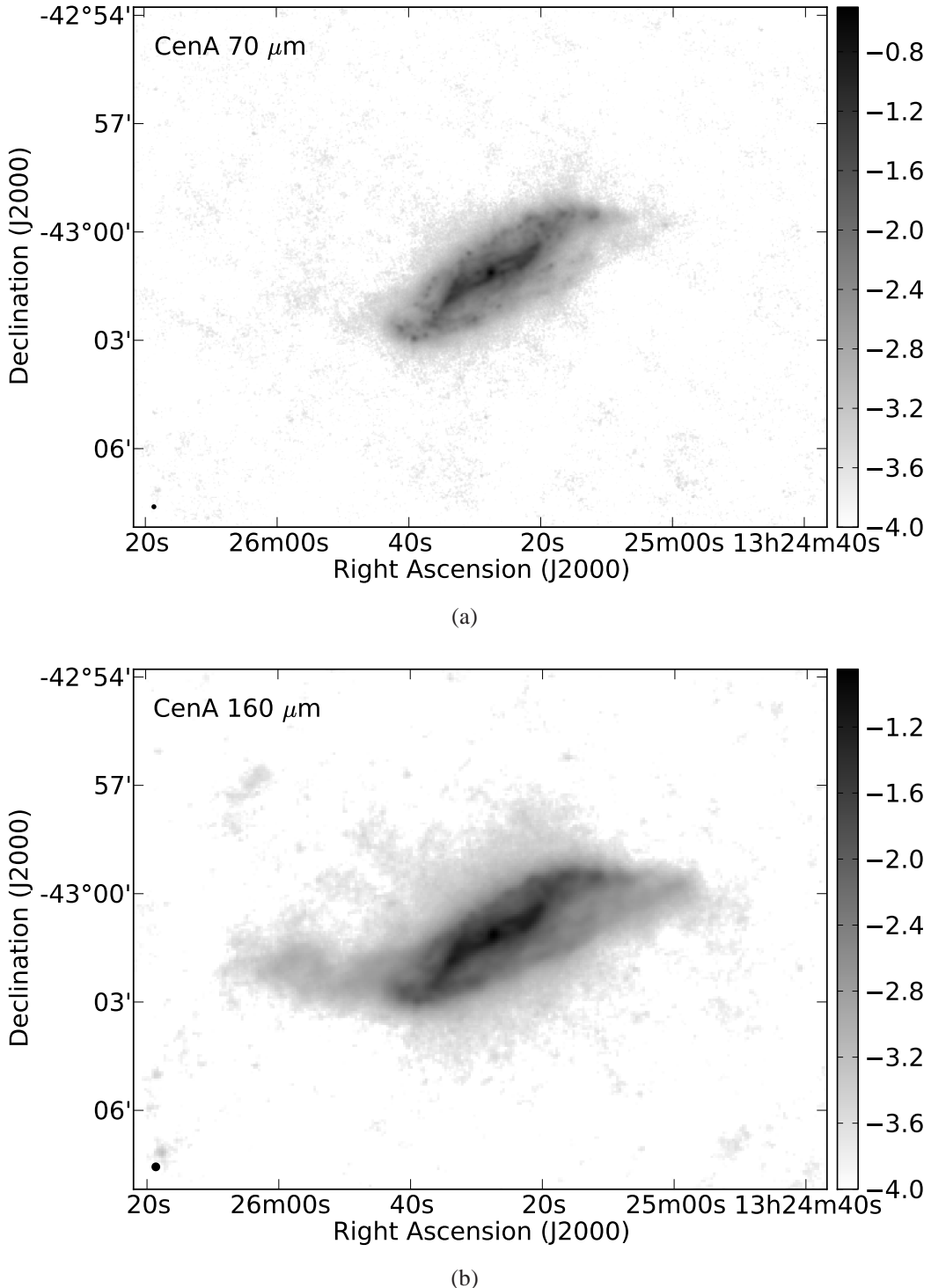
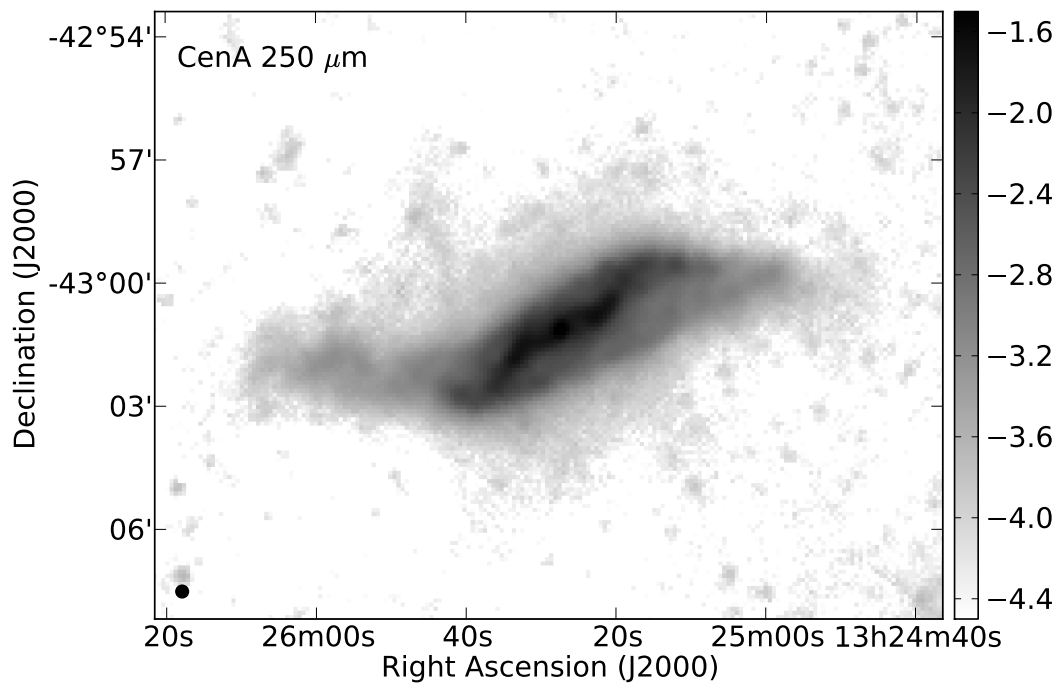
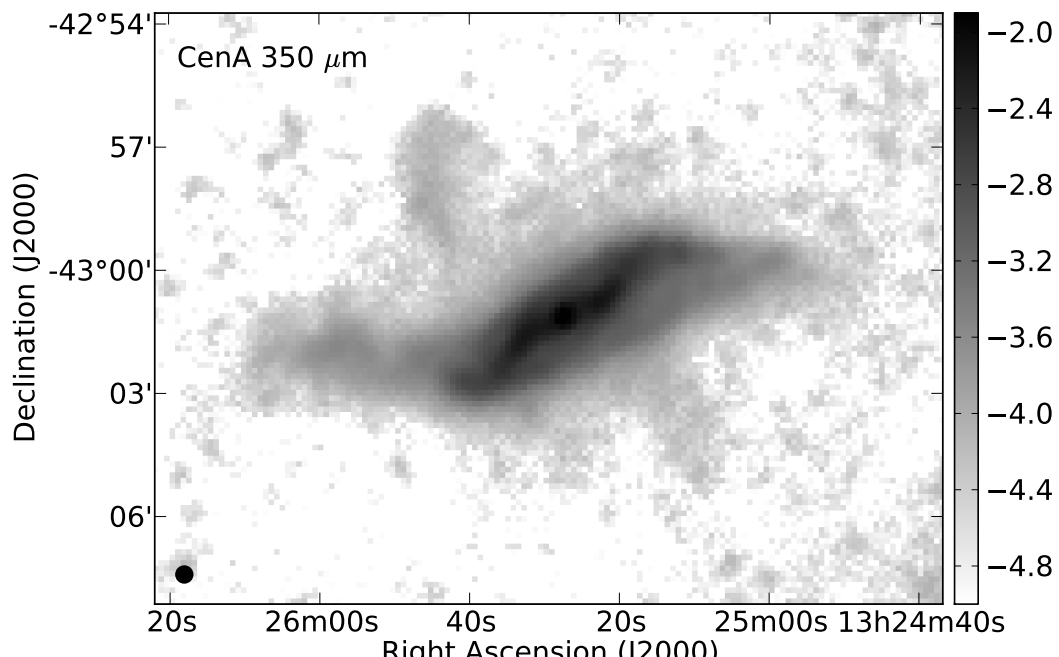


Figure 2.1: The five *Herschel* images at their native resolutions. The colour scale units are  $\log(\text{Jy arcsec}^{-2})$ , and the beam size is in the lower left corner of each image. Note that the radio jets become more prominent at 350 and 500  $\mu\text{m}$  due to synchrotron radiation.

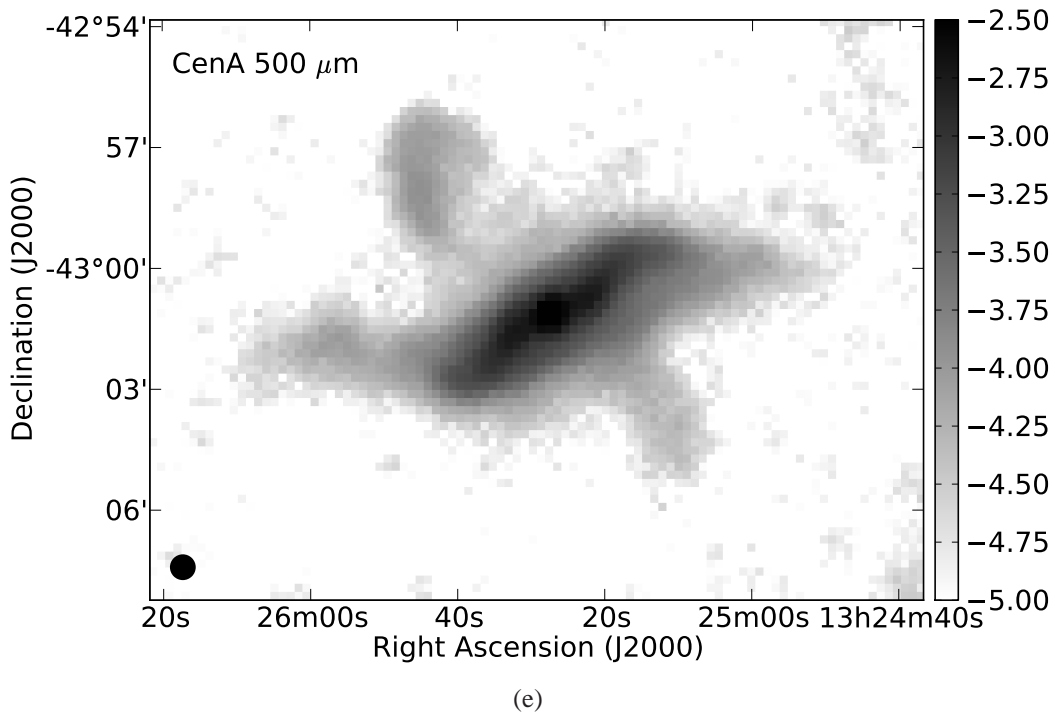


(c)



(d)

Figure 2.1: *continued*

Figure 2.1: *continued*

Nguyen et al., 2010); however, we expect it to be trivial except perhaps in the extreme outer disc, and the global average of the confusion noise has been removed with the background subtraction. A summary of the pixel errors from background subtraction and calibration uncertainties is presented in Table 2.1.

### 2.2.2 JCMT Observations

The  $^{12}\text{CO}$   $J = 3 - 2$  transition at a rest frequency of 345.79 GHz was mapped using the HARP-B instrument on the JCMT, located on Mauna Kea in Hawaii. These observations were taken over the nights of 2010 January 24–26 as part of project M09BC05 (P.I.: Tara Parkin), with a telescope beam size of 14.5 arcsec. We combined nine overlapping jiggle-maps (each with an integration time of 50 s) instead of creating a raster map due to the low elevation of Cen A from the location

of the JCMT. The maps were observed using beam-switching with a chop throw of 150 arcsec perpendicular to the major axis of Cen A. Each jiggle-map covers a 2 arcmin  $\times$  2 arcmin area on the sky, and our final map covers an area of 10 arcmin  $\times$  2 arcmin, to observe the dust lane out to  $D_{25}/2$ , which is half the distance from the centre of the galaxy to where the optical magnitude falls to 25. The backend receiver, the Auto-Correlation Spectrometer Imaging System (ACSiS), was set to a bandwidth of 1 GHz with 2048 channels, giving us a resolution of 488 kHz or  $0.43 \text{ km s}^{-1}$ .

The data were reduced using the STARLINK<sup>2</sup> software package (Currie et al., 2008), maintained by the Joint Astronomy Centre. We first flagged the data for any bad pixels in the raw data, and then built a cube (two spatial dimensions and one in frequency) with 7.5 arcsec pixels combining all of our observations. Next, we masked out detections of the  $^{12}\text{CO}$   $J = 3 - 2$  line in our cube using an automated fitting routine, then fit a third order polynomial to the baseline in order to remove it from the cube. We then binned this cube to a resolution of  $20 \text{ km s}^{-1}$  to measure the average rms in the line free regions, which we determined to be  $T_A^* = 16 \text{ mK}$ .

The first three moment maps (integrated intensity, integrated velocity and velocity dispersion) were created using the routine ‘findclump’ (part of STARLINK), which looks for detections of greater than  $2\sigma$ . We first convolve the unbinned cube with a Gaussian beam to match the 36 arcsec resolution of the *Herschel* SPIRE 500  $\mu\text{m}$  map. Next, we determine the average rms within the line free regions of the spectrum and expand the two-dimensional noise map into a cube. Then we create a signal-to-noise cube by dividing the convolved cube by the noise cube and apply ‘findclump’ to it. This method allows us to make detections of low-level emission better than just applying ‘findclump’ to our image cube. The routine creates a mask

---

<sup>2</sup>The STARLINK package is available for download at <http://starlink.jach.hawaii.edu>.

of the detections in a smoothed version of the cube and then multiplies this mask by the signal-to-noise cube to obtain a cube containing only detections above several different  $\sigma$  cutoffs. Then this cube is collapsed along the velocity axis to create the three moment maps in terms of the signal-to-noise. Finally, the integrated intensity-to-noise map is multiplied by the two-dimensional noise map to obtain the true integrated intensity map. For a more detailed description of our reduction method see Warren et al. (2010).

To evaluate the uncertainty in the integrated intensity map, we make use of the following equation:

$$\Delta I = \left[ \Delta v \sigma \sqrt{N_{\text{line}}} \right] \sqrt{1 + \frac{N_{\text{line}}}{N_{\text{base}}}}, \quad (2.1)$$

where  $\Delta v$  is the width of each channel in  $\text{km s}^{-1}$ ,  $\sigma$  is the noise in units of Kelvin,  $N_{\text{line}}$  is the total number of channels within the spectral line itself, and  $N_{\text{base}}$  is the number of channels used for fitting the baseline. Several calibration sources measured during these observations were compared to standard spectra, and from these we estimate the calibration uncertainty to be 10 percent. The integrated intensity map is presented as contours in Figure 2.2.

### 2.2.3 Ancillary Data

The H I map of Cen A was kindly provided to us by Tom Oosterloo and previously published in Struve et al. (2010). This map has a resolution of 19 arcsec and units of  $10^{19} \text{ cm}^{-2}$ , with a pixel scale of 4 arcsec. We smoothed the image to a resolution of 36 arcsec using a Gaussian beam to match the resolution of the SPIRE 500  $\mu\text{m}$  image, and regridded the image to match the 12 arcsec pixel size.

We also have a map of the radio continuum at 1.425 GHz, originally pub-

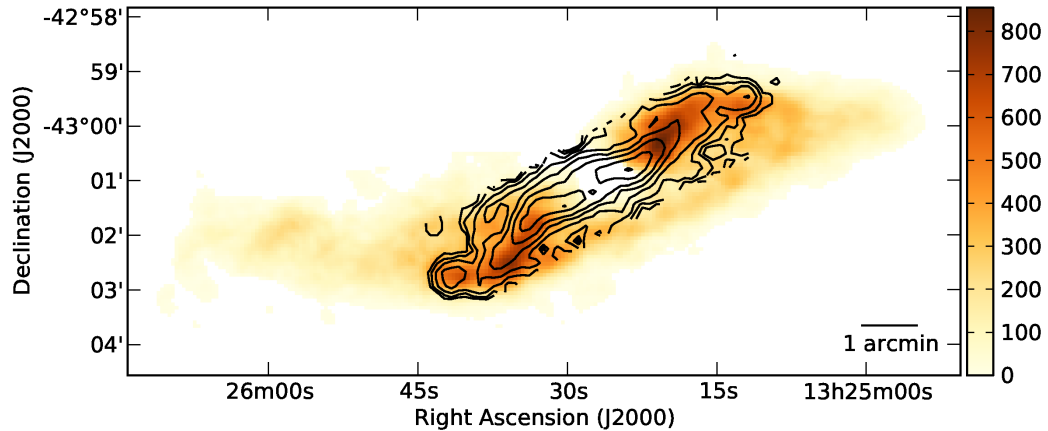


Figure 2.2: HI map of the disc region of Cen A in units of  $10^{19} \text{ cm}^{-2}$  from Struve et al. (2010); colourscale), with a beam of 19 arcsec. JCMT CO  $J = 3 - 2$  contours with a resolution of 14.5 arcsec are overlaid in black. CO contour levels are 0.4, 0.8, 1.6, 3.2, ..., 25.6 and  $38.4 \text{ K km s}^{-1}$ , where the temperature units are  $T_A^*$ .

lished as part of the *IRAS* Bright Galaxy Atlas (Condon et al., 1996), and retrieved from the NASA Extragalactic Database (NED). This map allows us to trace the jets extending out from the central AGN. We convolved this radio image with a Gaussian beam and then regridded it to match the SPIRE 500  $\mu\text{m}$  image.

## 2.3 Results

### 2.3.1 SED Fitting

To determine the dust temperatures within the disc of Cen A, we fit the far-infrared and submm part of the spectral energy distribution (SED; 70 – 500  $\mu\text{m}$ ) with a simple modified blackbody with  $\beta = 2$ ,

$$I(\nu, T) = C \times \nu^\beta \times B(\nu, T), \quad (2.2)$$

where  $C$  is a scaling constant to match the model to our observed fluxes. The parameter  $\beta$  originates from the dust emissivity function,  $\kappa_\nu = \kappa_0(\nu/\nu_0)^\beta$ .

To constrain our modified blackbody fits, we created uncertainty maps for each wavelength that are a combination of the measurement uncertainty in the flux value of each pixel, the background noise in each pixel, and the calibration uncertainties for both PACS and SPIRE (see Section 2.2.1.3 for details), added in quadrature. The value in each pixel of the resulting map is taken to be the total uncertainty for the equivalent pixel at a given wavelength.

For each pixel in the images that has a  $S/N \geq 10$  at all five *Herschel* wavelengths, we fit Equation 2.2 to our flux measurements to determine the best-fitting temperature  $T$  and constant  $C$  for that pixel. An example of a SED fit for a typical pixel is shown in Figure 2.3, and the pixel location is shown with a cross in Figure 2.4. We also show the global SED that was obtained by summing the flux at each wavelength within all of the pixels with good fits in Figure 2.3, and fitting the resulting totals. Note that we tested the effect of removing the  $70\text{ }\mu\text{m}$  data point from our SED fit to ensure it was not forcing the curve to peak at shorter wavelengths, and that it was not from a separate thermal component of the dust (Smith et al., 2010; Bendo et al., 2010a, 2012). We found that the  $70\text{ }\mu\text{m}$  flux falls on the best-fit curves within uncertainties for these tests and thus we use all five wavelengths in our fitting routine. We then create a map of the dust temperature where pixels with poor chi-squared fits at the 95 percent confidence level have been masked out. In general the pixels with poor fits coincide with those where non-thermal radiation is making a significant contribution to the flux at  $500\text{ }\mu\text{m}$ . The temperature map is presented in Figure 2.4, with  $500\text{ }\mu\text{m}$  contours overlaid to point out the location of the non-thermal emission. The temperature is about 30 K near the central AGN region, and then smoothly falls off to about 20 K in the outer disc, and the average

temperature throughout the entire region is approximately  $(21.8 \pm 0.3)$  K.

We have also tried allowing both  $\beta$  and temperature to vary in Equation 2.2, to investigate if the model fits to our data improve. While there is some small variation in  $\beta$  throughout the disc, these deviations are small and the average value of  $\beta$  is  $2.07 \pm 0.07$ . Furthermore, there are no obvious trends in the variation of  $\beta$  with radius. Thus, the results of our test are consistent with our one parameter fit, giving us confidence in our fixed  $\beta$  fits.

We evaluated the uncertainty on the dust temperature by implementing a monte carlo algorithm on our modified blackbody fitting routine. For each wavelength, an artificial flux value lying within the uncertainty bounds of our observed measured flux value is generated randomly using a Gaussian number generator. Then we run the modified blackbody fitting routine on the simulated dataset and extract the temperature and constant for the best fitting function corresponding to that dataset. This process of creating artificial data and then fitting a function to them to determine the temperature is repeated 800 times for each pixel. We take the standard deviation of the temperature distribution for each pixel to be the uncertainty in the temperature. This uncertainty varies throughout the map, with an average of about 1 percent per pixel. The highest uncertainties are 5 percent around the very edge of our map, where the signal to noise is lower for the flux maps, and we note that these uncertainties exclude the uncertainties arising from our assumed value for  $\beta$  and thus emissivity.

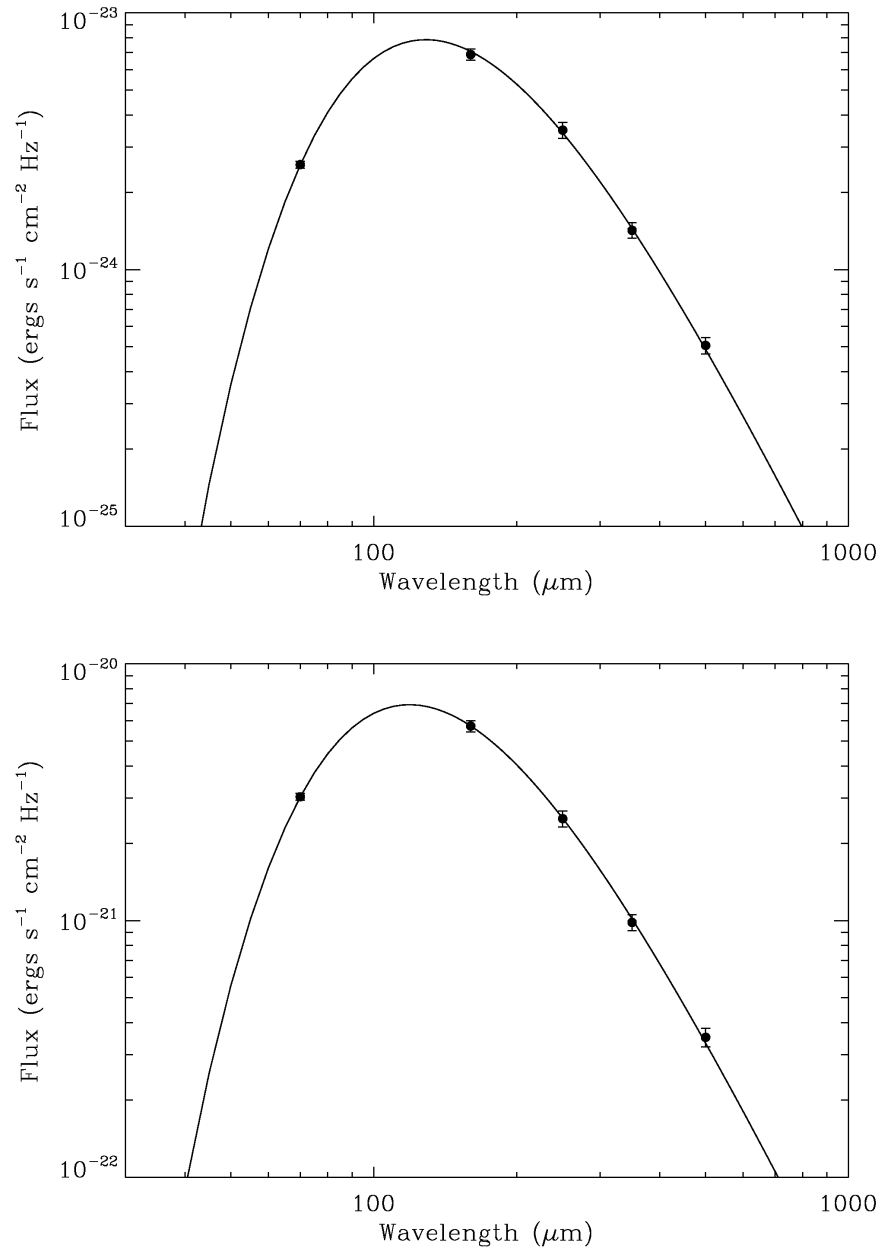


Figure 2.3: Top: the SED for a typical pixel (pixel location shown as a cross in Figure 2.4). The best-fitting modified blackbody is shown as a solid line, while our measured flux values are represented by the data points. Bottom: a global SED for the entire disc, consisting of all pixels contributing to the total dust mass (see Section 2.3.2).

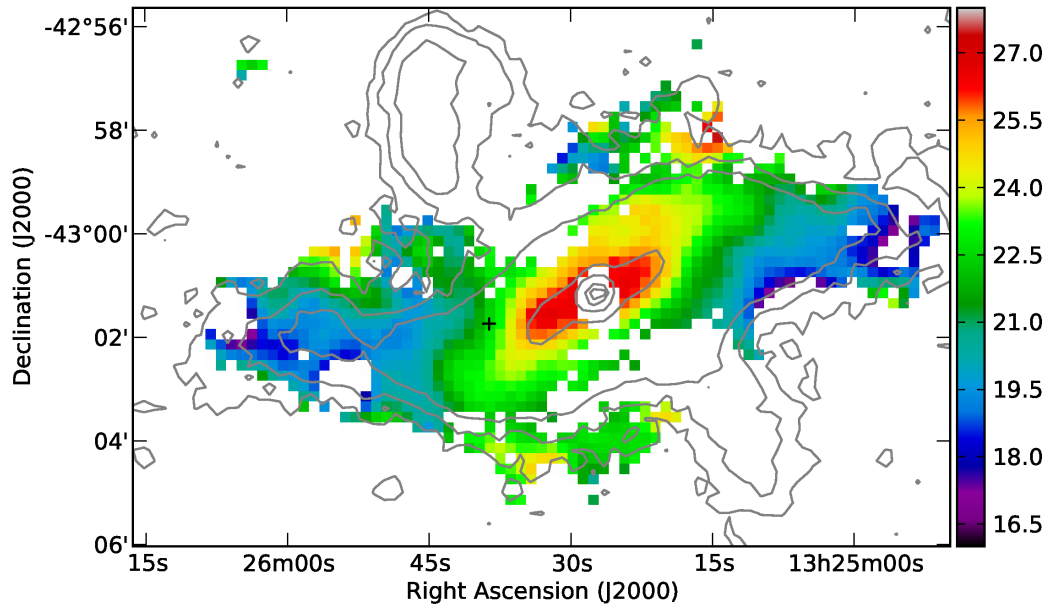


Figure 2.4: Temperature map of the dust disc of Cen A (colour scale), in units of degrees Kelvin. Contours of the 500  $\mu\text{m}$  SPIRE map are shown in grey for reference. The contours for the 500  $\mu\text{m}$  image are 0.0139, 0.0347, 0.0694, 0.347, 0.694, 1.39, 2.78, 4.17 and 4.86 mJy arcsec<sup>-2</sup>. The black cross is the location of the pixel for which the best-fitting SED is shown in Figure 2.3. Note that the central region does not have any reasonable fits due to the non-thermal emission present in the 350 and 500  $\mu\text{m}$  maps.

### 2.3.2 Dust Mass

The equation we use to evaluate the dust mass at a specific frequency is

$$M_{\text{dust}} = \frac{S_\nu D^2}{\kappa_\nu B(\nu, T)}, \quad (2.3)$$

when the monochromatic flux is optically thin. In this expression,  $S_\nu$  is the flux from the source,  $D$  is the distance to the source,  $B(\nu, T)$  is the equation for a black-body and  $\kappa_\nu$  is the dust emissivity. Here we adopt a value for the dust emissivity at 250  $\mu\text{m}$ ,  $\kappa_{250}$ , of 3.98 cm<sup>2</sup> g<sup>-1</sup> from the dust model of Draine (2003)<sup>3</sup>. Substituting

<sup>3</sup>These data are also available at <http://www.astro.princeton.edu/draine/dust/dustmix.html>

$\kappa_{250}$  into Equation 2.3, the dust mass becomes

$$M_{\text{dust}} = 5.258 \times 10^3 S_{250} (e^{(57.58 \text{ K}/T)} - 1) M_{\odot}. \quad (2.4)$$

We checked that the SED of Cen A is optically thin by assuming that the pixel with the highest flux at  $70 \mu\text{m}$  is a worst-case scenario in terms of optical depth  $\tau$ , and measured the flux in the same pixel at  $250 \mu\text{m}$ . Using the results from our SED fitting we calculate the dust mass within that pixel using Equation 2.4, and convert the dust mass to a dust mass surface density  $\Sigma$  using the area of one  $12 \text{ arcsec}$  pixel. The optical depth at  $250 \mu\text{m}$  can be calculated as  $\tau_{250} = \Sigma \kappa_{250}$ . Using this method we find that  $\tau_{250} \ll 1$ , thus we can assume the galaxy is optically thin at  $250 \mu\text{m}$ . This method can be repeated for the other wavelengths as well.

Substituting our temperature and the SPIRE  $250 \mu\text{m}$  fluxes returned by our model SED fits into Equation 2.4, we obtain a pixel-by-pixel map of the dust mass, which is shown in Figure 2.5. The dust mass distribution peaks toward the centre, and falls off in the outer regions. Uncertainties range from about 3 to 30 percent with the lower uncertainties corresponding to pixels closer to the centre of the disc. The typical uncertainty in each pixel is  $\sim 5$  percent. Summing up the individual dust masses within each pixel leads to a total dust mass in the disc of  $(1.59 \pm 0.05) \times 10^7 M_{\odot}$ . As a check, we also evaluated the total dust mass using the global SED fit results, and obtain a total of  $1.47 \times 10^7 M_{\odot}$ .

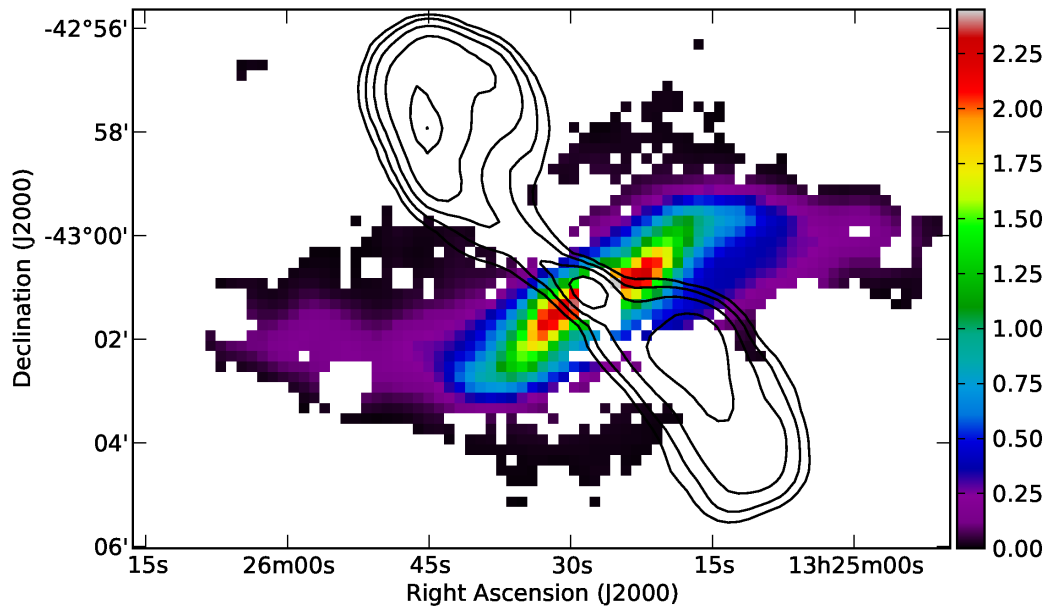


Figure 2.5: Dust mass map of Centaurus A. Units of the colour scale are  $M_{\odot} \text{ pc}^{-2}$ . Contours of the 1.425 GHz radio continuum are overlaid in black to show the regions where synchrotron radiation is present.

### 2.3.3 Gas Mass

We convert our CO  $J = 3 - 2$  integrated intensity map to a column density of molecular hydrogen using the following equation:

$$N_{\text{H}_2} = \frac{X_{\text{CO}} I_{\text{CO}(3-2)}}{\eta_{\text{mb}}} \left( \frac{I_{\text{CO}(3-2)}}{I_{\text{CO}(1-0)}} \right)^{-1}, \quad (2.5)$$

where  $X_{\text{CO}}$  is the CO( $J = 1 - 0$ )-H<sub>2</sub> conversion factor,  $I_{\text{CO}(3-2)}$  is the integrated intensity of the CO  $J = 3 - 2$  emission,  $\eta_{\text{mb}} = 0.6$  is the conversion factor from an antenna temperature  $T_A^*$  to a main beam temperature  $T_{\text{mb}}$  for the JCMT, and the factor within the brackets is the ratio of the CO  $J = 3 - 2$  line intensity to the CO  $J = 1 - 0$  line intensity. Despite the additional uncertainty introduced by this line intensity ratio, we choose to use our CO  $J = 3 - 2$  map in this analysis because of its better intrinsic resolution (14.5 arcsec) and sensitivity compared to

the CO  $J = 1 - 0$  of Eckart et al. (1990). We assume a  $X_{\text{CO}}$  factor of  $(2 \pm 1) \times 10^{20} \text{ cm}^{-2} (\text{K km s}^{-1})^{-1}$ , typical for the Milky Way (Strong et al., 1988), and a CO  $J = 3 - 2/\text{CO } J = 1 - 0$  ratio of 0.3, which is a suitable ratio for the diffuse ISM as found by the JCMT Nearby Galaxies Legacy Survey (NGLS; Wilson et al., 2009). We note here that Wilson et al. (2009) and other groups from the NGLS have seen ratio variations within other galaxies by up to a factor of 2–3, which may increase our molecular gas mass uncertainties (see Section 2.4 for further discussion).

Next, we convert our column density to a molecular gas mass map via

$$M_{\text{H}_2} = A_{\text{pix}} N_{\text{H}_2} m_{\text{H}_2} \quad (2.6)$$

with  $A_{\text{pix}}$  the area of one pixel ( $12 \text{ arcsec} \times 12 \text{ arcsec}$ ) at the distance of Cen A, and  $m_{\text{H}_2}$  the mass of one molecular hydrogen atom. The total mass of molecular hydrogen, over the entire coverage of our map, is  $(1.42 \pm 0.15) \times 10^9 \text{ M}_{\odot}$ , where we have excluded uncertainty contributions from the assumed CO  $J = 3 - 2/\text{CO } J = 1 - 0$  ratio.

Following the same method we also convert the units of the HI map (Figure 2.2) to units of mass. Then the molecular gas mass and atomic gas mass maps are combined in such a way that in regions where we have coverage for both HI and H<sub>2</sub>, the total gas mass is a sum of the two, and for the remaining regions the mass is from HI or H<sub>2</sub> alone. We then multiply the resulting map by 1.36 to obtain the total gas mass, including helium. Summing over all pixels, we find a total gas mass of  $(2.7 \pm 0.2) \times 10^9 \text{ M}_{\odot}$ . Our map of the total gas is presented in Figure 2.6, and covers about half of the area for which we have dust mass measurements.

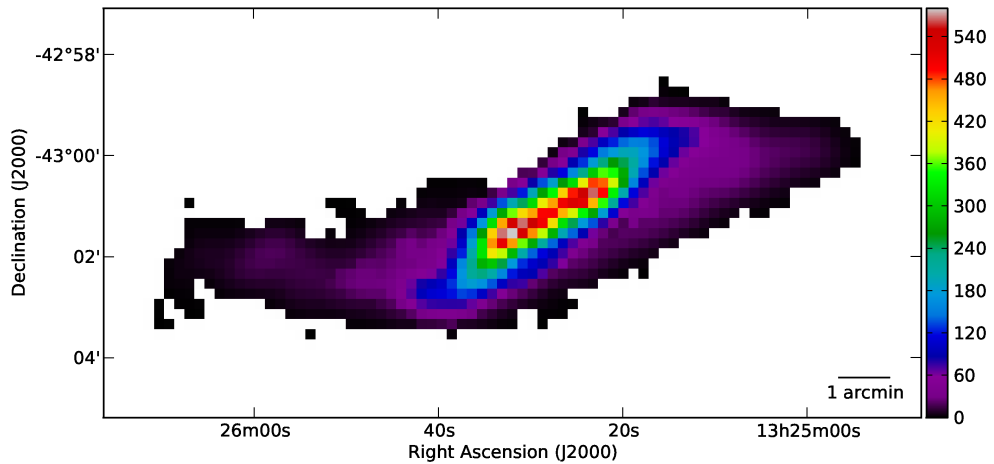


Figure 2.6: The total gas mass distribution of the disc of Cen A. This map includes both the HI mass distribution, as well as the H<sub>2</sub> mass, where we have coverage for it, and has been multiplied by 1.36 to account for helium as well. Units for the colour scale are  $M_{\odot} \text{ pc}^{-2}$ .

### 2.3.4 The Gas-to-Dust Mass Ratio

We present the gas-to-dust mass ratio in Figure 2.7, which covers all pixels for which we have both a gas mass and a dust mass. The box outlined in black shows the region that has coverage both in HI and H<sub>2</sub>, which is 10 arcmin  $\times$  2 arcmin in area. As is seen in this figure, the majority of the disc has a gas-to-dust mass ratio similar to that of the Galaxy with an average value of  $103 \pm 8$ ; the Galactic value varies from about 120 (Li & Draine, 2001) to  $\sim 160$  (Zubko et al., 2004) to  $\sim 180$  (Draine et al., 2007, and references therein). Interestingly, the gas-to-dust mass ratio increases to a significantly higher value of almost 300 in regions closest to the AGN. Typical uncertainties in this ratio are about 10 percent. We also present the average gas-to-dust mass ratio as a function of distance from the centre of Cen A along a position angle of 30 deg north of west in Figure 2.8. This plot emphasizes the radial trend of the gas-to-dust mass ratio along the disc. In other galaxies such

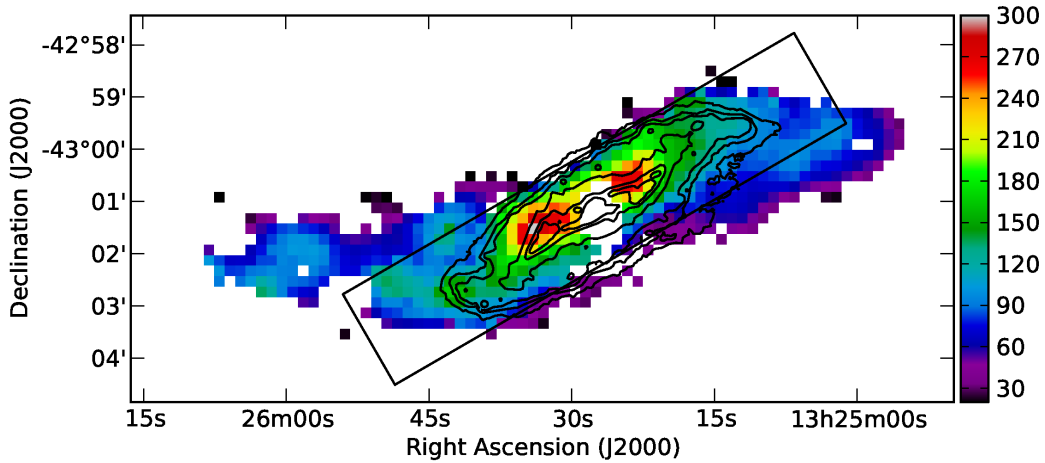


Figure 2.7: Gas-to-dust mass ratio of Centaurus A (colourscale), with PACS  $70\ \mu\text{m}$  contours (at original resolution) overlaid in black. Contour levels are 0.75, 1.5, 2.5, 7.5, 20, and  $37.5\ \text{mJy arcsec}^{-2}$ . The box shown in black highlights the region in the disc for which the gas contribution is from HI and H<sub>2</sub>, and is  $10\ \text{arcmin} \times 2\ \text{arcmin}$  in size.

as those from the SINGS survey, the gas-to-dust mass ratio varies from  $\sim 136$  to  $\sim 453$  (Draine et al., 2007). We discuss the possible origin of this high central gas-to-dust mass ratio below.

## 2.4 Discussion

Our total dust mass of  $(1.59 \pm 0.05) \times 10^7\ M_{\odot}$  is comparable to other published numbers for Cen A in the literature; however, we note that this value is likely a lower limit as regions where non-thermal emission contaminates the dust continuum had poor model fits. Several publications have used two-component modified blackbody modelling combined with far-infrared and submm observations to derive a dust mass for Cen A. Leeuw et al. (2002) used a wavelength range of  $60\text{--}850\ \mu\text{m}$  for their SED fit and found a total mass of  $2.6 \times 10^6\ M_{\odot}$  (adjusting for our distance) within an elliptical region  $120\ \text{arcsec} \times 450\ \text{arcsec}$  in size, but excluding the unre-

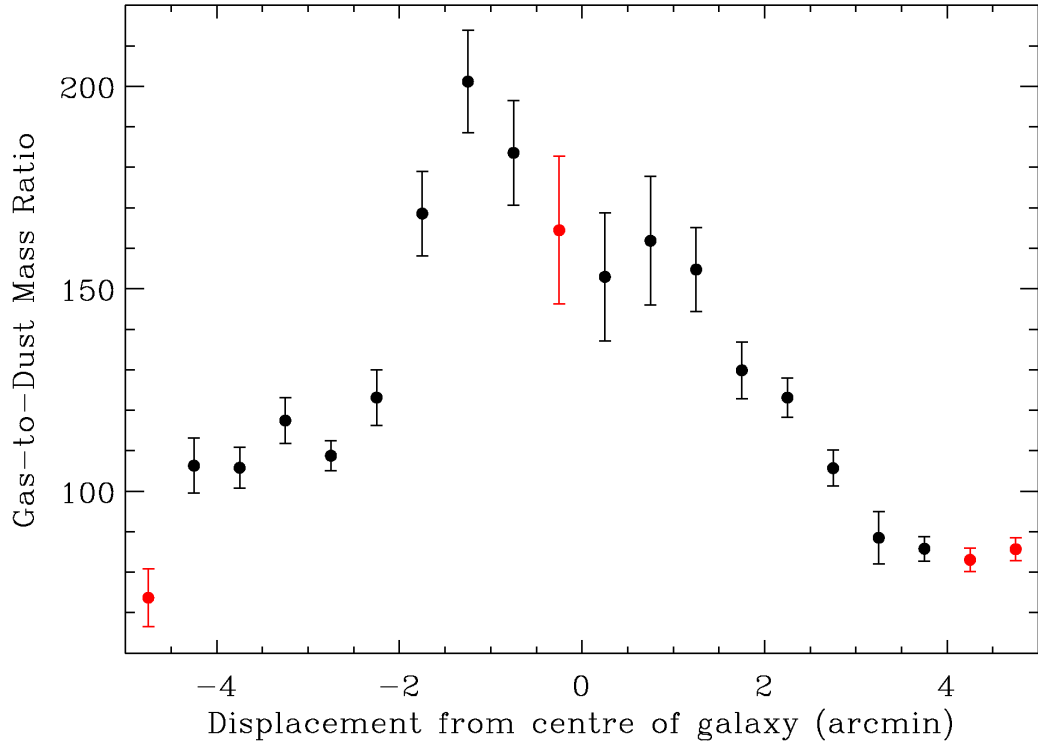


Figure 2.8: A radial plot of the average gas-to-dust mass ratio along the major axis of Cen A with a position angle of 30 deg north of west. We measured the average gas-to-dust mass ratio value within 20 bins along this position-angle, each measuring 2 arcmin  $\times$  0.5 arcmin in size. The red data points represent the bins in which we had at most 10 good pixels out of a possible 25, and therefore are not as well sampled as those shown in black.

solved core at the centre. Since this ellipse covers a similar area to our observations, the discrepancy is likely due to an inadequate chop throw in the Leeuw et al. (2002) 850  $\mu\text{m}$  dataset, leading to difficulties quantifying the background. Our observations show faint emission at 500  $\mu\text{m}$  extending beyond the 120 arcsec chop throw the authors used, and oversubtracting the background will lead to a lower dust mass estimate. Wei\ss{} et al. (2008) studied the submm continuum using LABOCA 870  $\mu\text{m}$  data and combining these data with fluxes spanning 25–870  $\mu\text{m}$  they found a higher mass of  $2.2 \times 10^7 \text{ M}_\odot$ . They subtract the flux contribution of the unresolved core from the total flux prior to estimating the dust, but do caution that they may not

have removed all of the non-thermal emission arising from the radio jet.

The gas mass we have obtained from our H<sub>2</sub> map alone is  $(1.42 \pm 0.15) \times 10^9 M_{\odot}$ , including the central region which we masked out for our dust fitting. Eckart et al. (1990) determined a molecular gas mass of  $1.9 \times 10^8 M_{\odot}$ , after we adjust their result for our assumed X<sub>CO</sub> factor and distance. In addition, Morganti (2010) suggests the total molecular gas mass is  $4 \times 10^8 M_{\odot}$  based on observations of Eckart et al. (1990) and Quillen et al. (1992). Our molecular gas mass is thus higher than those values previously published; this is likely due to the improved sensitivity of our observations. The molecular gas mass is about twice the atomic mass of  $4.9 \times 10^8 M_{\odot}$  (Struve et al., 2010).

The high gas-to-dust mass ratio towards the central AGN is a most interesting result. Several studies of spiral galaxies have found that the gas-to-dust mass ratio is not constant throughout the disc, but rather decreases with decreasing distance from the centre of the galaxy (e.g. Muñoz-Mateos et al., 2009; Bendo et al., 2010b; Magrini et al., 2011), in contrast to what we have found here. We have made a rough estimate of the CO  $J = 3 - 2$ /CO  $J = 1 - 0$  ratio throughout the central disc using the CO  $J = 1 - 0$  map of Eckart et al. (1990) to check if our assumption of 0.3 for this ratio is valid in the centremost regions of the disc. Our calculations show an average value of 0.35, and more importantly, they show no significant variation with radius. Furthermore, looking at Figure 2.7 we see that there is a smooth transition of the gas-to-dust mass ratio between the H<sub>2</sub>-dominated region to the H<sub>i</sub>-dominated region in the outer disc, which also suggests CO excitation is not the primary cause of the high gas-to-dust mass ratio.

The X<sub>CO</sub> factor is one variable that might affect the gas-to-dust mass ratio if it is not constant throughout the disc. We have assumed the Galactic value for our calculations; however, studies have shown that this conversion factor can vary with

metallicity (Wilson, 1995; Israel, 1997, 2000; Barone et al., 2000; Israel et al., 2003; Strong et al., 2004; Israel, 2005; Leroy et al., 2011). If the metallicity decreases as a function of radius within Cen A, we would require a larger conversion factor at larger radii, which in turn would increase the gas-to-dust mass ratio farther out in the disc, potentially bringing it up to a similar value as that in the centre. Alternatively, the  $X_{CO}$  factor can be smaller by up to a factor of  $\sim 4$  for starbursting galaxies (Downes & Solomon, 1998). This effect could reduce the gas-to-dust mass ratio in regions of strong star forming activity; however, the total far-infrared luminosity for Cen A is  $\leq 10^{10} L_\odot$ , while the  $X_{CO}$  conversion factor is typically affected at luminosities greater than  $\sim 10^{11} L_\odot$  (e.g. Downes, Solomon & Radford, 1993; Solomon et al., 1997).

One possibility is that dust is being destroyed by the jets extending out in either direction from the AGN. It is plausible that some of the dust grains are being destroyed by the AGN either through dust sputtering or through shocks. The total X-ray luminosity of the AGN of Cen A is  $8 \times 10^{42} \text{ erg s}^{-1}$  (Rothschild et al., 2011), which is comparable in X-ray luminosity to the AGN found in M87 (Werner et al., 2006). It might be possible for these photons to deplete the dust in the surrounding ISM. In support of this scenario, Baes et al. (2010) did not detect thermal dust emission in M87, which also contains a jet.

It is also possible that the dust is entrained in the jets of Cen A. Roussel et al. (2010) found a dusty halo surrounding the starbursting galaxy M82 using *Herschel* observations. They considered entrainment by a galactic wind as a possible explanation even though they finally concluded that the origin was likely due to tidal interactions. We cannot rule out entrainment by galactic winds as a possibility for Cen A. Unfortunately, we cannot probe close enough to the jets to further investigate this assumption due to our limited resolution and the non-thermal emission

component.

Alternatively, a larger gas reservoir in the centre could also increase the gas-to-dust mass ratio. This would require dust-poor gas falling onto the disc and being funneled toward the centre. However, if this was the case, we would likely have found a high gas-to-dust mass ratio throughout the disc and not concentrated toward the innermost part of the disc. It also does not seem plausible for the gas to be migrating through the disc faster than the dust.

Interestingly, there is a large ring of material that is seen in the mid- and far-infrared close to the regions in which we see a high gas-to-dust mass ratio. Mirabel et al. (1999) first noticed the ‘S’ shaped structure with ISOCAM observations at 7 and 15  $\mu\text{m}$ , and postulated that this structure was a bar at the centre of the galaxy. Later, observations (Leeuw et al., 2002; Quillen et al., 2006) supported a tilted ring scenario to explain the structure observed. Our *Herschel* observations at 70  $\mu\text{m}$  also show emission from this ring (Figure 2.1), and in fact, the high gas-to-dust mass ratio appears to correspond with the 70  $\mu\text{m}$  contours of the ring, as shown in Figure 2.7. The models by Quillen et al. (2006) suggest that there is a deficit in the dust distribution at radii less than about 50 arcsec ( $\sim 920 \text{ pc}$ ). This is at a similar radius to our observed high gas-to-dust mass ratio. A dust deficit throughout  $r \leq 50 \text{ arcsec}$  might seem less likely to be related to the AGN and is perhaps better related to star formation activity. Observations probing closer to the nucleus are necessary to determine if the gas-to-dust mass ratio remains high or increases further as we approach the AGN.

## 2.5 Conclusions

We have presented new observations of the dust continuum from the PACS and SPIRE instruments on board the *Herchel Space Observatory* at 70, 160, 250, 350 and 500  $\mu\text{m}$ . In addition, we present new data tracing the CO  $J = 3 - 2$  transition taken with the HARP-B instrument mounted on the JCMT. We have used these data to probe the interstellar medium within the disc of Centaurus A on a pixel-by-pixel basis. We observe the ring of emission at 70  $\mu\text{m}$  previously reported at infrared and submm wavelengths, while our 500  $\mu\text{m}$  (and to some extent the 350  $\mu\text{m}$ ) images show detections of the non-thermal continuum emission previously reported at 870  $\mu\text{m}$  by Wei\ss et al. (2008).

We model the dust spectral energy distribution using a single component modified blackbody, and find temperatures of  $\leq 30$  K in the centre that decrease with radius. Using the temperature map, we find the total dust mass to be  $(1.59 \pm 0.05) \times 10^7 \text{ M}_\odot$ . The total gas mass is  $(2.7 \pm 0.2) \times 10^9 \text{ M}_\odot$ , and combining the dust and gas masses we have produced a gas-to-dust mass ratio map. The average gas-to-dust mass ratio is approximately  $103 \pm 8$ , similar to that of the Milky Way, with an interesting peak to about 275 towards the centre of the galaxy. After exploring several possible scenarios to explain the high gas-to-dust mass ratio, the most appealing one is that of a correspondance between the high gas-to-dust mass ratio and the ring about 1 kpc in size, which is best fit by a warped tilted ring model by Quillen et al. (2006) that consists of a deficit of dusty material inwards of the ring. The deficit of dust may be due to X-ray emission from the central AGN destroying the dust grains or due to the jets removing dust from the centre of the galaxy.

## Acknowledgments

The research of C. D. W. is supported by the Natural Sciences and Engineering Research Council of Canada and the Canadian Space Agency. PACS has been developed by a consortium of institutes led by MPE (Germany) and including UVIE (Austria); KU Leuven, CSL, IMEC (Belgium); CEA, LAM (France); MPIA (Germany); INAF-IFSI/OAA/OAP/OAT, LENS, SISSA (Italy); IAC (Spain). This development has been supported by the funding agencies BMVIT (Austria), ESA-PRODEX (Belgium), CEA/CNES (France), DLR (Germany), ASI/INAF (Italy), and CICYT/MCYT (Spain). SPIRE has been developed by a consortium of institutes led by Cardiff University (UK) and including Univ. Lethbridge (Canada); NAOC (China); CEA, LAM (France); IFSI, Univ. Padua (Italy); IAC (Spain); Stockholm Observatory (Sweden); Imperial College London, RAL, UCL-MSSL, UKATC, Univ. Sussex (UK); and Caltech, JPL, NHSC, Univ. Colorado (USA). This development has been supported by national funding agencies: CSA (Canada); NAOC (China); CEA, CNES, CNRS (France); ASI (Italy); MCINN (Spain); SNSB (Sweden); STFC and UKSA (UK); and NASA (USA). HIPE is a joint development by the Herschel Science Ground Segment Consortium, consisting of ESA, the NASA Herschel Science Center, and the HIFI, PACS and SPIRE consortia. The James Clerk Maxwell Telescope is operated by The Joint Astronomy Centre on behalf of the Science and Technology Facilities Council of the United Kingdom, the Netherlands Organisation for Scientific Research, and the National Research Council of Canada. This research has made use of the NASA/IPAC Extragalactic Database (NED) which is operated by the Jet Propulsion Laboratory, California Institute of Technology, under contract with the National Aeronautics and Space Administration. This research made use of APLpy, an open-source plotting pack-

age for Python hosted at <http://aplpy.github.com>. T. J. P. thanks the anonymous referee for providing constructive feedback about this work.

# Bibliography

Auld R. et al., 2012, MNRAS, 420, 1882

Baes M. et al., 2010, A&A, 518, L53

Barone L. T., Heithausen A., Hüttemeister S., Fritz T., Klein U., 2000, MNRAS, 317, 649

Bendo G. J. et al., 2010a, A&A, 518, L65

Bendo G. J. et al., 2010b, MNRAS, 402, 1409

Bendo G. J. et al., 2012, MNRAS, 419, 1833

Bregman J. N., Hogg D. E., Roberts M. S., 1992, ApJ, 387, 484

Bregman J. N., Snider B. A., Grego L., Cox C. V., 1998, ApJ, 499, 670

Condon J. J., Helou G., Sanders D. B., Soifer B. T., 1996, ApJS, 103, 81

Currie M. J., Draper P. W., Berry D. S., Jenness T., Cavanagh B., Economou F., 2008, in Argyle R. W., Bunclark P. S., Lewis J. R., eds, ASP Conf. Ser. Vol. 394, Astronomical Data Analysis Software and Systems XVII, Astron. Soc. Pac., San Francisco, p. 650

Downes D., Solomon P. M., 1998, ApJ, 507, 615

Downes D., Solomon P. M., Radford, S. J. E., 1993, ApJ, 414, L13

Draine B. T., 2003, ARA&A, 41, 241

Draine B. T. et al., 2007, ApJ, 663, 866

Eckart A., Cameron M., Rothermel H., Wild W., Zinnecker H., Rydbeck G., Olberg M., Wiklind T., 1990a, ApJ, 363, 451

Eckart A., Cameron M., Genzel R., Jackson J. M., Rothermel H., Stutzki J., Rydbeck G., Wiklind T., 1990b, ApJ, 365, 522

Griffin M. J. et al., 2010, A&A, 518, L3

Harris G. L. H., 2010, PASA, 27, 475

Harris G. L. H., Rejkuba M., Harris W. E., 2010, PASA, 27, 457

Huchtmeier W. K., 1994, A&A, 286, 389

Huchtmeier W. K., Sage L. J., Henkel C., 1995, A&A, 300, 675

Israel F. P., 1997, A&A, 328, 471

Israel F. P., 1998, A&A Rev., 8, 237

Israel F. P., 2000, in Combes F., Pineau Des Forets G., eds, Cambridge Contemporary Astrophysics Vol. xix, Molecular Hydrogen in Space, Cambridge University Press, Cambridge, p. 293

Israel F. P., 2005, A&A, 438, 855

Israel F. P., Baas F., Rudy R. J., Skillman E. D., Woodward C. E., 2003, A&A, 397, 87

Knapp G. R., Turner E. L., Cunniffe P. E., 1985, AJ, 90, 454

Leeuw L. L., Hawarden T. G., Matthews H. E., Robson E. I., Eckart A., 2002, ApJ, 565, 131

Leeuw L. L., Davidson J., Dowell C. D., Matthews H. E., 2008, ApJ, 677, 249

Leroy A. K. et al., 2011, ApJ, 737, 12

Li A., Draine B. T., 2001, ApJ, 554, 778

Magrini L. et al., 2011, A&A, 535, 13

Mirabel I. F. et al., 1999, A&A, 341, 667

Morganti R., 2010, PASA, 27, 463

Morganti R., Oosterloo T., Sadler E. M., Vergani D., 1999, in Carral P., Cepa J., eds, ASP Conf. Ser. Vol. 163, Star Formation in Early Type Galaxies, Astron. Soc. Pac., San Francisco, p. 84

Morganti R. et al., 2006, MNRAS, 371, 157

Morganti R., Oosterloo T., Struve C., Saripalli L., 2008, A&A, 485, L5

Müller T., Okumura K., Klaas U., 2011, PICC-ME-TN-038, available from the ESA  
*Herschel* Science Centre

Muñoz-Mateos J. C. et al., 2009, ApJ, 701, 1965

Nguyen H. T. et al., 2010, A&A, 518, L5

Ott S., 2010, in Mizumoto Y., Morita K.-I., Ohishi M., eds, ASP Conf. Ser. Vol. 434, Astronomical Data Analysis Software and Systems XIX, Astron. Soc. Pac., San Francisco, p. 139

PACS Observer's Manual, 2011, HERSCHEL-HSC-DOC-0832, available from the  
ESA *Herschel* Science Centre

Phillips T. G. et al., 1987, ApJ, 322, L73

Pilbratt G. L. et al., 2010, A&A, 518, L1

Poglitsch A. et al., 2010, A&A, 518, L2

Quillen A. C., de Zeeuw P. T., Phinney E. S., Phillips T. G., 1992, ApJ, 391, 121

Quillen A. C., Brookes M. H., Keene J., Stern D., Lawrence C. R., Werner M. W.,  
2006, ApJ, 645, 1092

Rothschild R. E., Markowitz A., Rivers E., Suchy S., Pottschmidt K., Kadler M.,  
Müller C., Wilms J., 2011, ApJ, 733, 23

Roussel H., 2013, PASP, preprint (arXiv:1205.2576)

Roussel H. et al., 2010, A&A, 518, L66

Rydbeck G., Wiklind T., Cameron M., Wild W., Eckart A., Genzel R., Rothermel  
H., 1993, A&A, 270, L13

Schiminovich D., van Gorkom J. H., van der Hulst J. M., Kasow S., 1994, ApJ,  
423, L101

Smith M. W. L. et al., 2010, A&A, 518, L51

Smith M. W. L. et al., 2012, ApJ, 748, 123

Solomon P. M., Downes D., Radford S. J. E., Barrett J. W., 1997, ApJ, 478, 144

SPIRE Observers' Manual, 2011, HERSCHEL-HSC-DOC-0798, available from  
the ESA *Herschel* Science Centre

Stickel M., van der Hulst J. M., van Gorkom J. H., Schiminovich D., Carilli C. L.,  
2004, A&A, 415, 95

Strong A. W. et al., 1988, A&A, 207, 1

Strong A. W., Moskalenko I. V., Reimer O., Digel S., Diehl R., 2004, A&A, 422,  
L47

Struve C., Oosterloo T. A., Morganti R., Saripalli L., 2010, A&A, 515, A67

Temi P., Brighenti F., Mathews W. G., Bregman J. D., 2004, ApJS, 151, 237

Thronson Jr. H. A., Tacconi L., Kenney J., Greenhouse M. A., Margulis M.,  
Tacconi-Garman L., Young J. S., 1989, ApJ, 344, 747

van Gorkom J. H., van der Hulst J. M., Haschick A. D., Tubbs A. D., 1990, AJ, 99,  
1781

Walsh D. E. P., Knapp G. R., Wrobel J. M., Kim D.-W., 1989, ApJ, 337, 209

Warren B. E. et al., 2010, ApJ, 714, 571

Weiβ A., Kovács A., Güsten R., Menten K. M., Schuller F., Siringo G., Kreysa E.,  
2008, A&A, 490, 77

Welch G. A., Sage L. J., 2003, ApJ, 584, 260

Welch G. A., Sage L. J., Young L. M., 2010, ApJ, 725, 100

Werner N., Böhringer H., Kaastra J. S., de Plaa J., Simionescu A., Vink J., 2006,  
A&A, 459, 353

Wiklind T., Combes F., Henkel C., 1995, A&A, 297, 643

Wilson C. D., 1995, ApJ, 448, L97

Wilson C. D. et al., 2009, ApJ, 693, 1736

Xilouris E. M., Madden S. C., Galliano F., Vigroux L., Sauvage M., 2004, A&A,  
416, 41

Young L. M., Bendo G. J., Lucero D. M., 2009, AJ, 137, 3053

Young L. M. et al., 2011, MNRAS, 414, 940

Zubko V., Dwek E., Arendt R. G., 2004, ApJS, 152, 211

Chapter **3**

# **Regional variations in the dense gas heating and cooling in M51 from *Herschel* far-infrared spectroscopy**

T. J. Parkin, C. D. Wilson, M. R. P. Schirm, M. Baes, M. Boquien,, A. Boselli, A. Cooray, D. Cormier, K. Foyle, O. Ł. Karczewski, V. Lebouteiller, I. de Looze, S. C. Madden, H. Roussel, M. Sauvage, and L. Spinoglio

*This article has been accepted for publication in The Astrophysical Journal, but as of the time of submission of my final thesis it has not yet been assigned a bibliographic designation. Reproduced by permission of the American Astronomical Society.*

### 3.1 Introduction

The atomic fine-structure lines [C II](158  $\mu\text{m}$ ), [N II](122 and 205  $\mu\text{m}$ ), [O I](63 and 145  $\mu\text{m}$ ) and [O III](88  $\mu\text{m}$ ) are among the dominant cooling lines of the cold neutral and ionized regimes of the interstellar medium (ISM). The progenitor atoms of these lines are collisionally excited and then de-excite through forbidden transitions, emitting photons and thus removing thermal energy from the gas. The [O I] lines originate in the neutral regime of photon-dominated regions (PDRs; Tielens & Hollenbach, 1985) as atomic oxygen has an ionization potential greater than 13.6 eV, while [C II] emission, though considered a primary tracer of PDRs, can also trace ionized gas as the ionization potential of atomic carbon is only 11.26 eV. In contrast, the [N II] and [O III] lines only trace ionized gas, particularly in H II regions, because the ionization potentials of N and O<sup>+</sup> are 14.5 and 35 eV, respectively, requiring the presence of a hard radiation field. Thus, observations of these lines can tell us important characteristics about the gas in these components of the ISM.

Observationally, these cooling lines were first detectable with the Kuiper Airborne Observatory (KAO) and the *Infrared Space Observatory (ISO)* and are now observable with the *Herschel Space Observatory* (Pilbratt et al., 2010) at unprecedented resolution. Previous surveys studied [C II](158  $\mu\text{m}$ ), [N II](122  $\mu\text{m}$ ), and [O I](63  $\mu\text{m}$ ) on global scales in galaxies using *ISO* and found a decreasing ratio of  $L_{[\text{CII}]} / L_{\text{TIR}}$  with increasing infrared color,  $F_\nu(60\mu\text{m}) / F_\nu(100\mu\text{m})$ , as well as a correlation between  $L_{[\text{OI}63]} / L_{[\text{CII}]}$  and infrared color (e.g. Malhotra et al., 1997, 2001; Negishi et al., 2001; Brauher et al., 2008).  $L_{[\text{CII}]} / L_{\text{TIR}}$  is used as a probe of the photoelectric heating efficiency of the far-ultraviolet (FUV) radiation field, indicating the fraction of FUV photons that contribute to dust heating via absorption,

versus the fraction responsible for ejecting electrons from dust grains or polycyclic aromatic hydrocarbons (PAHs; Tielens & Hollenbach, 1985; Malhotra et al., 2001), which thermally heat the gas. The ratio  $F_\nu(60\mu\text{m})/F_\nu(100\mu\text{m})$  indicates dust temperatures, with higher temperatures indicating compact H II regions. These studies concluded that the trends seen indicate a decrease in this heating efficiency with increasing color.

More recently these cooling lines have been probed on galactic and spatially resolved scales in nearby galaxies with *Herschel* (e.g., Beirão et al., 2010, 2012; Graciá-Carpio et al., 2011; Mookerjea et al., 2011; Croxall et al., 2012; Braine et al., 2012; Lebouteiller et al., 2012; Contursi et al., 2013). Beirão et al. (2010, 2012), Mookerjea et al. (2011), and Lebouteiller et al. (2012) investigated the Seyfert 1 galaxy NGC 1097, M33, and the H II region LMC-N11, respectively, and found that  $L_{[\text{CII}]}/L_{\text{TIR}}$  varies on local scales as well. Furthermore, Croxall et al. (2012) and Lebouteiller et al. (2012) also see the same relationship between  $L_{[\text{CII}]+[\text{OI}]63}/L_{\text{TIR}}$  and infrared color that is seen on global scales. Interestingly, they also investigated the ratio  $L_{[\text{CII}]+[\text{OI}]63}/L_{\text{PAH}}$  as a function of color and found that there was a stronger correlation between these two parameters than between  $L_{[\text{CII}]+[\text{OI}]63}/L_{\text{TIR}}$  and color, implying that PAHs are likely a better indicator of heating efficiency than the total infrared luminosity within the gas. At the warmest colors,  $L_{[\text{CII}]+[\text{OI}]63}/L_{\text{PAH}}$  decreased slightly, and the authors attributed this to the PAHs becoming increasingly ionized, thus reducing their ability to eject photoelectrons.

Diagnosing the physical conditions of the gas in the ISM using these important cooling lines requires comparing the observed fluxes to those predicted by a PDR model. Tielens & Hollenbach (1985) presented a PDR model that characterizes the physical conditions in the PDR by two free variables, the hydrogen nucleus density,  $n$ , and the strength of the FUV radiation field in units of the Habing field,

$G_0 = 1.6 \times 10^{-3}$  erg cm $^{-2}$  s $^{-1}$  (Habing, 1968). They assume a slab geometry and include a complex chemical network, thermal balance, and radiative transfer. In successive papers, Wolfire et al. (1990) and Hollenbach et al. (1991) expanded this work to model ensembles of molecular clouds in diffuse environments as well as galactic nuclei and active galactic nuclei (AGNs). Kaufman et al. (1999, 2006) have further updated the model of Wolfire et al. (1990) and provide a set of diagnostic plots using ratios between cooling lines and the total infrared luminosity to determine  $n$  and  $G_0$ .<sup>1</sup> PDR models using different sets of observables have also been developed by van Dishoeck & Black (1986, 1988), Sternberg & Dalgarno (1989, 1995), Luhman et al. (1997), Störzer et al. (2000), and Le Petit et al. (2006). PDR models with a spherical geometry instead of the plane-parallel geometry also exist, such as Kosma  $\tau$  (e.g., Röllig et al., 2006). For a recent discussion and comparison of the different available PDR models see Röllig et al. (2007). A number of studies have compared observations to PDR models to determine the gas density, temperature, and strength of the FUV radiation field in numerous galaxies and Galactic PDRs. When they compared their observations to the PDR model of Kaufman et al. (1999), Malhotra et al. (2001) found that the FUV radiation field,  $G_0$ , scales as the hydrogen nucleus density,  $n$ , to the power 1.4, with  $10^2 \leq G_0 \leq 10^{4.5}$  and  $10^2 \text{ cm}^{-3} \leq n \leq 10^{4.5} \text{ cm}^{-3}$  for their sample of galaxies. Croxall et al. (2012) studied NGC 1097 and NGC 4559 and found  $10^{2.5} \text{ cm}^{-3} \leq n \leq 10^3 \text{ cm}^{-3}$  across both galactic disks, with  $50 \leq G_0 \leq 1000$ .

The goal of this paper is to investigate the gas component of the ISM in M51 with modeling of the far-infrared fine-structure lines. M51 ( $D = 9.9$  Mpc; Tikhonov et al., 2009) is a gas-rich, grand-design spiral galaxy with a smaller com-

---

<sup>1</sup> Also available for analysis using this model is the PDR Toolbox (Pound & Wolfire, 2008), found at <http://dustem.astro.umd.edu/pdrt>.

panion, NGC 5195, and is classified as a Seyfert 2 galaxy (Ho et al., 1997). The metallicity ( $12+\log(\text{O/H})$ ) of M51 is  $8.55 \pm 0.01$  on average and has a slight radial gradient (Moustakas et al., 2010), though it does not change significantly over the area covered in this work. M51 has been previously observed with the KAO and *ISO* to investigate the far-infrared cooling lines. Nikola et al. (2001) mapped the [C II](158  $\mu\text{m}$ ) line in the inner 6' of the galaxy with the far-infrared imaging Fabry–Perot interferometer on the KAO at 55'' resolution ( $\sim 2.6$  kpc at our adopted distance). Their comparison with PDR models revealed  $G_0 \sim 150\text{--}850$  and two density solutions,  $n \sim 10^2 \text{ cm}^{-3}$  and  $n \sim 5 \times 10^5 \text{ cm}^{-3}$ . Later, Kramer et al. (2005) used *ISO* to map M51 in [C II](158  $\mu\text{m}$ ), [O I](63  $\mu\text{m}$ ), and [N II](122  $\mu\text{m}$ ). This study focused on the nucleus and two selected positions in the spiral arms at a resolution of 80'' ( $\sim 3.8$  kpc at our adopted distance). Their comparison to PDR models revealed  $G_0 = 20\text{--}30$  and  $n \sim 10^4 \text{ cm}^{-3}$  within these regions. As part of the *Herschel* Guaranteed Time Key Project the Very Nearby Galaxies Survey (VNGS; PI: C. D. Wilson), Mentuch Cooper et al. (2012) presented a detailed analysis of the dust and gas of both M51 and NGC 5195 using *Herschel* Photodetector Array Camera and Spectrometer (PACS; Poglitsch et al., 2010) and Spectral and Photometric Imaging Receiver (SPIRE; Griffin et al., 2010) photometry, as well as the spectral energy distribution (SED) model of Draine & Li (2007). They find that there was a burst of star formation approximately 370–480 Myr ago, a gas-to-dust mass ratio of  $94 \pm 17$  (the Milky Way has a gas-to-dust mass ratio of  $\sim 160$  (; Zubko et al., 2004)), and an interstellar radiation field (ISRF) within the spiral arms of approximately 5–10 times the average value of the ambient ISRF in the solar neighborhood ( $G_0 \sim 6\text{--}12$ ).

The general goals of the VNGS are to investigate properties of the gas and dust in the ISM in an intentionally diverse sample of 13 nearby galaxies using *Her-*

*schel*. The galaxies represent a sample of different morphological types and have previously been observed in numerous other wavebands across the electromagnetic spectrum, thus allowing us to create a complete picture of the conditions in the ISM of these objects. Here we present new far-infrared spectroscopy of M51 from the PACS instrument, focusing on the [C II](158  $\mu\text{m}$ ), [N II](122  $\mu\text{m}$ ), [O I](63 and 145  $\mu\text{m}$ ), and [O III](88  $\mu\text{m}$ ) fine-structure lines at unprecedented resolution (better than  $\sim 12''$ , or roughly 600 pc). In addition, we present observations of the [N II](205  $\mu\text{m}$ ) line from the SPIRE Fourier Transform Spectrometer (FTS). We use these spectra to investigate the gas component of the galaxy by using the PDR model of Kaufman et al. (1999, 2006) to diagnose some of the physical characteristics of the ISM. In Section 3.2 we describe our method for processing the data. In Section 3.3 we describe the characteristics of the gas, and in Section 3.4 we compare our observations to theoretical PDR models. We conclude in Section 3.5.

## 3.2 *Herschel* Observations

### 3.2.1 PACS Observations

The PACS spectrometer covers a wavelength range of 51–220  $\mu\text{m}$  and comprises 25 spatial pixels (spaxels) arranged in a  $5 \times 5$  grid with a square field of view on the sky of  $47''$  on a side. Each spaxel records a separate spectrum from a  $9.''4$  field of view at a spectral resolution ranging from approximately  $75$ – $300$  km  $\text{s}^{-1}$ .<sup>2</sup> The FWHM of the beam varies from just over  $9''$  to about  $13''$ . More details about the spectrometer can be found in Poglitsch et al. (2010) or in the PACS OM.

All of our PACS spectroscopic observations of M51 were carried out as part

---

<sup>2</sup>PACS Observer's Manual (hereafter PACS OM; HERSCHEL-HSC-DOC-0832, 2011), available for download from the ESA *Herschel* Science Centre.

of the VNGS using the unchopped grating scan mode. We have raster maps covering the central  $2.^{\circ}5 \times 2.^{\circ}5$  of M51 in the [C II](158  $\mu\text{m}$ ), [N II](122  $\mu\text{m}$ ), and [O I](63  $\mu\text{m}$ ) lines (hereafter [C II], [N II]122, and [O I]63, respectively) and  $47'' \times 3.^{\circ}25$  raster strips extending from the center (for the [O I](145  $\mu\text{m}$ ) and [O III](88  $\mu\text{m}$ ) lines, hereafter [O I]145 and [O III], respectively) and  $47'' \times 2.^{\circ}25$  raster strips extending from the near center (for the [C II], [N II]122, and [O I]63 lines) of the galaxy out along a position angle of  $310^{\circ}$  counter clockwise from north. In Figure 3.1 we show the outline of our spectroscopic maps on the total infrared flux map (see Section 3.2.3 for details). For the central maps we use the recommended raster point step size of  $24''$  ( $16''$ ) and raster line step size of  $22''$  ( $14.^{\circ}5$ ) for full Nyquist sampling of the red (blue) wavebands (PACS OM). The strips have  $30''$  raster spacing along the orientation angle. The basic observational details are summarized in Table 3.1.

The PACS spectroscopic observations were processed using the Herschel Interactive Processing Environment (HIPE; Ott, 2010) developer's track 9.0 build 2634 using calibration version FM, 32. We follow the standard pipeline reduction steps for the unchopped observing mode from Level 0 to Level 2. The data were flagged again, and the unbinned spectral data fit with a second-order polynomial for the continuum and a Gaussian function for the spectral line using the PACSman package (Lebouteiller et al., 2012). Lastly, we combine the individual rasters to produce a final integrated flux mosaic map by projecting each raster onto an over-sampled grid, also using PACSman.

Table 3.1. Properties of our *Herschel* Observations

Line	Wavelength ( $\mu\text{m}$ )	OBSID	Date of Observation	Map Size ' $\times$ '	FWHM <sup>a</sup> ( $''$ )	Integration Time (s)
[O I]	63.184	1342211190	2010 Dec 14	$2.5 \times 2.5$	$\sim 9.3$	10735
		1342211195	2010 Dec 15	$0.72 \times 2.25$	$\sim 9.3$	1254
[O III]	88.356	1342211191	2010 Dec 14	$0.72 \times 3.25$	$\sim 9.3$	2791
[N II]	121.898	1342211189	2010 Dec 14	$2.5 \times 2.5$	$\sim 10$	10511
		1342211192	2010 Dec 15	$0.72 \times 2.25$	$\sim 10$	2005
[O I]	145.525	1342211194	2010 Dec 15	$0.72 \times 3.25$	$\sim 11$	5277
[C II]	157.741	1342211188	2010 Dec 14	$2.5 \times 2.5$	$\sim 11.5$	5597
		1342211193	2010 Dec 15	$0.72 \times 2.25$	$\sim 11.5$	1254
[N II]	205.178	1342201202	2010 Jul 25	$\sim 2'$ diameter circle	17	17603

<sup>a</sup>Values are from the PACS Observer's Manual and the SPIRE Observer's Manual.

### 3.2.2 SPIRE Observations

As characterized in Griffin et al. (2010) and the SPIRE Observer’s Manual<sup>3</sup>, the *Herschel* SPIRE FTS instrument consists of two bolometer arrays, the SPIRE Short Wavelength spectrometer array (SSW) covering the wavelength range 194–313  $\mu\text{m}$ , and the SPIRE Long Wavelength spectrometer array (SLW) covering the range 303–671  $\mu\text{m}$ , and has a field of view approximately 2' in diameter. Each array is arranged in a honeycomb pattern, with 37 (19) receivers in the SSW (SLW) with receiver beams spaced by 33'' (51'') on the sky, thus sampling different regions of the overall field of view. The spectral resolution ranges from approximately 1.2 GHz (highest attainable resolution) to upward of 25 GHz and is dependent on the maximum difference between path lengths,  $d$ , traveled by the radiation after it has passed through the interferometer’s beam splitter, as given by  $(2d)^{-1}$ . The FWHM of the beam varies as a function of wavelength between 17 and 21'' (29 and 42'') for the SSW (SLW) (Griffin et al., 2010; Swinyard et al., 2010).

The *Herschel* FTS observation of the [N II](205  $\mu\text{m}$ ) line (hereafter [N II]205) is also part of the VNGS, and its basic properties are listed in Table 3.1. The observations consist of a single pointing carried out with intermediate spatial sampling covering a circular area approximately 2' in diameter and the high spectral resolution (1.2 GHz) setting. The total integration time of the observation is  $\sim$ 5 hr, with 32 repetitions of the spectral scan pair at each of the four jiggle positions that produce an intermediately sampled map. The standard processing pipeline for intermediately sampled mapped observations using HIPE 9.0 and SPIRE calibration context v9.1 was used, starting with the Level 0.5 product. Basic standard processing steps include first-level deglitching and correcting the signal for the non-linearity

---

<sup>3</sup>Hereafter SPIRE OM. Document HERSCHEL-DOC-0798 version 2.4 (2011 June) is available from the ESA *Herschel* Science Centre.

of detector response, temperature drifts, saturation effects, and time domain phase delays. Next, Level 1 interferograms are created, and the baseline is subsequently fit and subtracted from the signal. The interferograms then undergo second-level deglitching, phase corrections, and a Fourier transform to produce the spectra. The spectra are then calibrated to convert units to flux, telescope and instrument emission is removed, and an extended source flux conversion is applied. One additional step is applied to our data at this stage that is not part of the standard pipeline for mapped observations. A point source flux calibration correction that is determined separately for each bolometer of the array is applied to the data because M51 does not uniformly fill the beam. Finally, two (one each for the SSW and SLW) spectral cubes containing the processed spectra are created.

The final spectra were fit with a polynomial and Sinc function for the baseline and line, respectively (see Schirm et al., 2013, for details). Given that the spatial sampling is intermediate, we created the final integrated flux map using a fine  $4''$  pixel scale such that the finite pixels are centered on each of the bolometers of the FTS array, while the remaining pixels are left blank. The calibration uncertainty for the [N II]205 map is better than 7% and stems from a comparison between a model spectrum of Uranus and observational and model spectra of Neptune, pointing uncertainties, and the accuracy of background signal removal (SPIRE OM).

### 3.2.3 Ancillary Data

We also make use of the PACS photometric maps at 70 and 160  $\mu\text{m}$  originally presented in Mentuch Cooper et al. (2012), as well as the MIPS 24  $\mu\text{m}$  map from the *Spitzer Space Telescope*, which was re-processed by Bendo et al. (2012) for the purposes of complementing the *Herschel* photometry in a couple of Guaranteed

Time programs, including the VNGS. We calculate the total infrared flux using the MIPS 24  $\mu\text{m}$  and PACS 70 and 160  $\mu\text{m}$  maps and the empirically determined equation for the total infrared flux (or luminosity) from Dale & Helou (2002),

$$\begin{aligned} F_{\text{TIR}} = & \xi_1 \nu F_\nu(24\mu\text{m}) + \xi_2 \nu F_\nu(70\mu\text{m}) \\ & + \xi_3 \nu F_\nu(160\mu\text{m}), \end{aligned} \quad (3.1)$$

where  $[\xi_1, \xi_2, \xi_3] = [1.559, 0.7686, 1.347]$  at a redshift of  $z = 0$ . The total infrared luminosity determined with this equation covers emission from 3 to 1100  $\mu\text{m}$ . The map of the total infrared flux,  $F_{\text{TIR}}$ , is presented in Figure 3.1, which also shows the spatial coverage of our PACS and SPIRE spectroscopic maps.

The *Spitzer* IRAC 8  $\mu\text{m}$  map of M51 was also obtained from the SINGS survey (Kennicutt et al., 2003) archive to be used as a proxy for PAH emission. We applied a color correction to the image following the method described in the *Spitzer* Data Analysis Cookbook<sup>4</sup>, and subtracted the stellar contribution to the map using the correction from Marble et al. (2010), which is adopted by Croxall et al. (2012) to be an estimate of the total PAH power when only the IRAC 8  $\mu\text{m}$  map is available (their Equation (2)).

### 3.2.4 Data Treatment for Analysis

All of our spectral maps have been convolved with a Gaussian function to a common resolution matching that of the PACS 160  $\mu\text{m}$  map, 12''. The MIPS 24  $\mu\text{m}$  and PACS 70  $\mu\text{m}$  maps were convolved with the appropriate kernels developed by Aniano et al. (2011). In addition, each map has been regridded to match the pixel size

---

<sup>4</sup>Available for download at <http://irsa.ipac.caltech.edu/data/SPITZER/docs/dataanalysis/tools/cookbook/>.

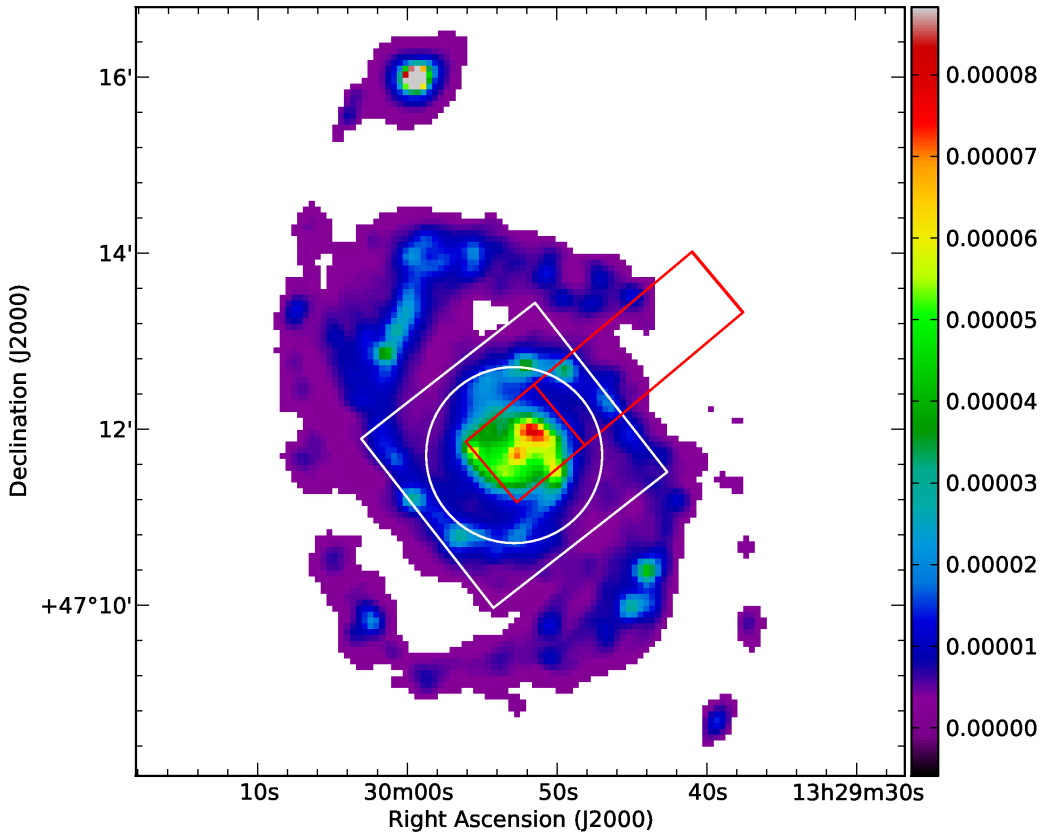


Figure 3.1: Total infrared flux,  $F_{\text{TIR}}$ , calculated using the MIPS 24  $\mu\text{m}$  and PACS 70  $\mu\text{m}$  and 160  $\mu\text{m}$  maps and Equation (3.1). The map is at the resolution of the PACS 160  $\mu\text{m}$  map, 12'', and has a plate scale of 4''. Units are  $\text{W m}^{-2} \text{sr}^{-1}$ . The white square and red rectangles outline the coverage of the PACS spectroscopic maps and strips, respectively. The white circle represents the footprint of the SPIRE FTS observations.

of the PACS 160  $\mu\text{m}$  map, 4''. For the comparison with the PDR models, we applied a  $5\sigma$  cut to our PACS spectroscopic maps to ensure we are considering robust detections in our ratio maps. Our quoted uncertainties throughout the paper take into account both measurement uncertainties, in calculating the line fluxes for our PACS spectroscopic maps, and calibration uncertainties, unless otherwise noted. We note here that the calibration uncertainties for the PACS spectroscopy are approximately 30% and are dominated by small offsets in pointing as well as drifting

of the detector response, while the calibration uncertainties for the photometry at 70 and 160  $\mu\text{m}$  are 3% and 5%, respectively (PACS OM).

### 3.3 Physical characteristics of the gas

#### 3.3.1 Line Emission Morphology

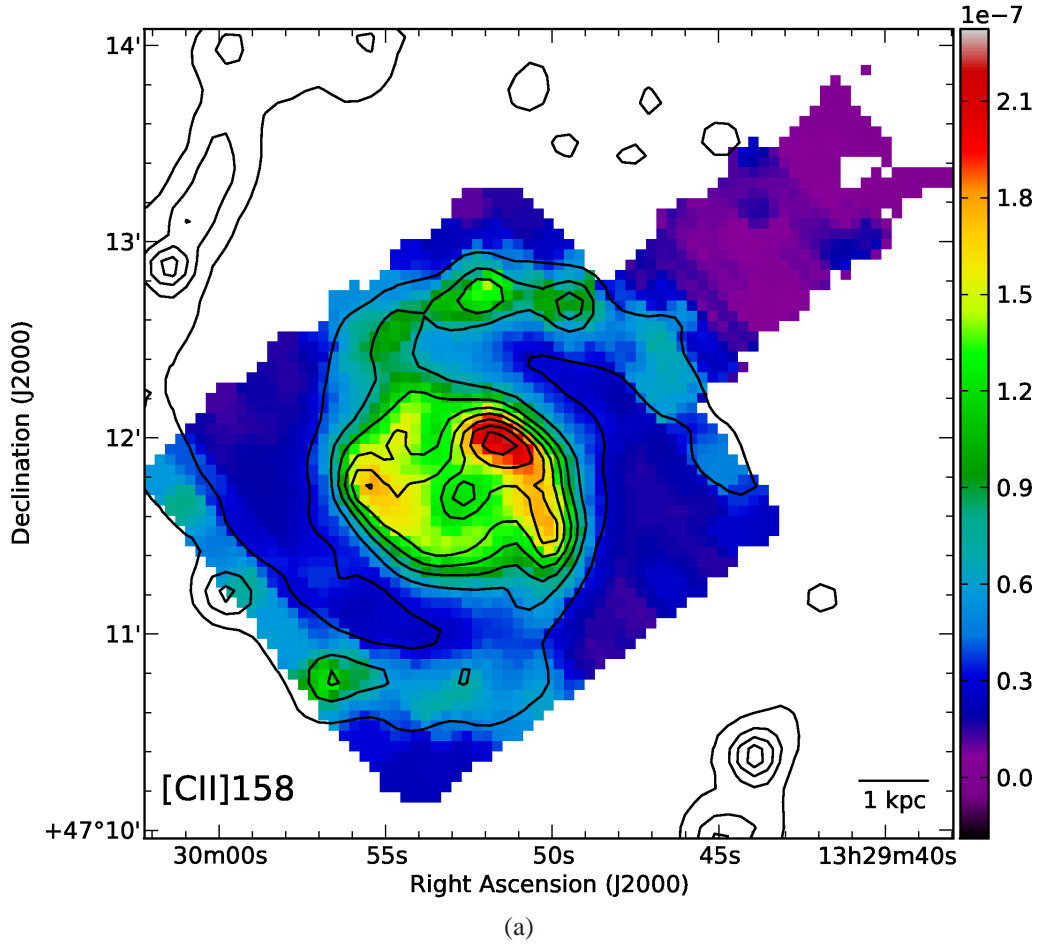
We present the final maps of the [C II], [N II]122, [O I]63, [O I]145, [O III], and [N II]205 lines at their native resolution with a  $3\sigma$  cut applied to the PACS maps in Figure 3.2. We note that the [C II] data were first presented by Schinnerer et al. (2013) using a different processing method, though it does not play a major role in their analysis. Both the [C II] and [N II]122 maps show similar distributions throughout the center of the galaxy. Overall there is strong emission in the central  $\sim 1.^{\prime}25$ , with the innermost sections of the spiral arms showing the strongest emission. The average signal to noise ratio (S/N) in the central region is  $\sim 200$  and 70 for the [C II] and [N II]122 maps, respectively. The peak in the inner northwestern arm is also present in other wavebands, including, the 24, 70, and 160  $\mu\text{m}$  images (combined in Figure 3.1), as well as other star formation tracers such as H $\alpha$  and Pa $\alpha$  (e.g., Kennicutt et al., 2003; Calzetti et al., 2005). The emission is a factor of  $\sim 1.5$  higher in this peak compared to the center of the galaxy in both [C II] and [N II]122. The spiral arms can be seen extending outward in weaker emission with a few stronger pockets.

The total [C II] emission in our map is  $(2.9 \pm 0.9) \times 10^{-14} \text{ W m}^{-2}$  covering an area of  $\sim 5.5 \times 10^{-7} \text{ sr}^{-1}$ . Nikola et al. (2001) mapped the [C II] emission over a  $6' \times 6'$  area of M51 with the KAO and found a peak intensity of  $(1.31 \pm 0.15) \times 10^{-4} \text{ erg s}^{-1} \text{ cm}^{-2} \text{ sr}^{-1}$  in the center of the galaxy. The integrated intensity of our

map over an aperture of approximately  $1'$  centered on the galaxy (to match the  $55''$  beam of the KAO) is  $\sim (1.4 \pm 0.4) \times 10^{-4} \text{ erg s}^{-1} \text{ cm}^{-2} \text{ sr}^{-1}$ , in good agreement with the KAO measurement. Kramer et al. (2005) and Negishi et al. (2001) both present *ISO* observations of M51 and found a [C II] integrated intensity at the center of  $4.41 \times 10^{-5} \text{ erg s}^{-1} \text{ cm}^{-2} \text{ sr}^{-1}$  and  $(9 \pm 2) \times 10^{-5} \text{ erg s}^{-1} \text{ cm}^{-2} \text{ sr}^{-1}$  within an  $80''$  beam, respectively, while in an aperture of the same size we measure an integrated intensity of  $(1.1 \pm 0.3) \times 10^{-4} \text{ erg s}^{-1} \text{ cm}^{-2} \text{ sr}^{-1}$ . Our results agree with those of Negishi et al. (2001) but are higher than those of Kramer et al. (2005) by about a factor of two. This discrepancy arises because Kramer et al. (2005) applied an extended source correction to their observations to obtain the integrated intensity within the *ISO* beam.

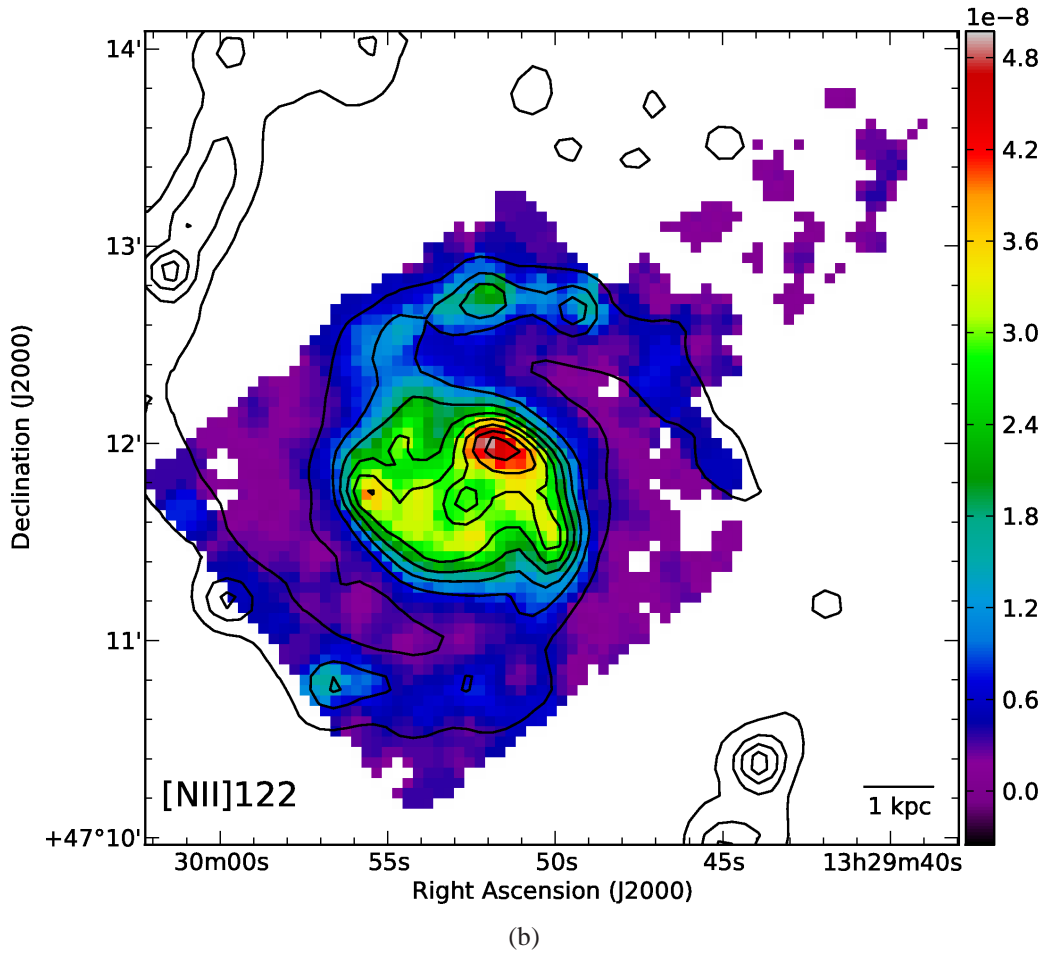
The [O I]63 map shows a strong spiral arm morphology in the innermost region (average S/N  $\sim 40$ ), with a similar peak in the northwest arm to that seen in [C II] and [N II]122. However, in contrast to the [C II] and [N II]122 emission, the [O I]63 emission peaks prominently in the center of the galaxy. M51 has been classified as a Seyfert 2 (Ho et al., 1997), and thus we believe that the peaked emission in the center may be due to a low-luminosity active nucleus. We measure a total [O I]63 flux within an  $80''$  beam of  $(3 \pm 1) \times 10^{-15} \text{ W m}^{-2}$ , in good agreement with the values obtained with *ISO* of  $(4.4 \pm 0.9) \times 10^{-15} \text{ W m}^{-2}$  (Negishi et al., 2001) and  $\sim 3.9 \times 10^{-15} \text{ W m}^{-2}$  (Kramer et al., 2005). Negishi et al. (2001) presented a survey of 34 galaxies, including those classified as AGNs, or Seyfert types. Comparison of our [O I]63 flux obtained for M51 with values from their survey for AGN and Seyfert galaxies shows agreement within a factor of  $\sim 2$  for most sources, suggesting that our results are typical for galaxies with active centers.

As we have only observed M51 along a strip in [O I]145 and [O III] emission, the maps cover much less area. [O III] emission is concentrated primarily in

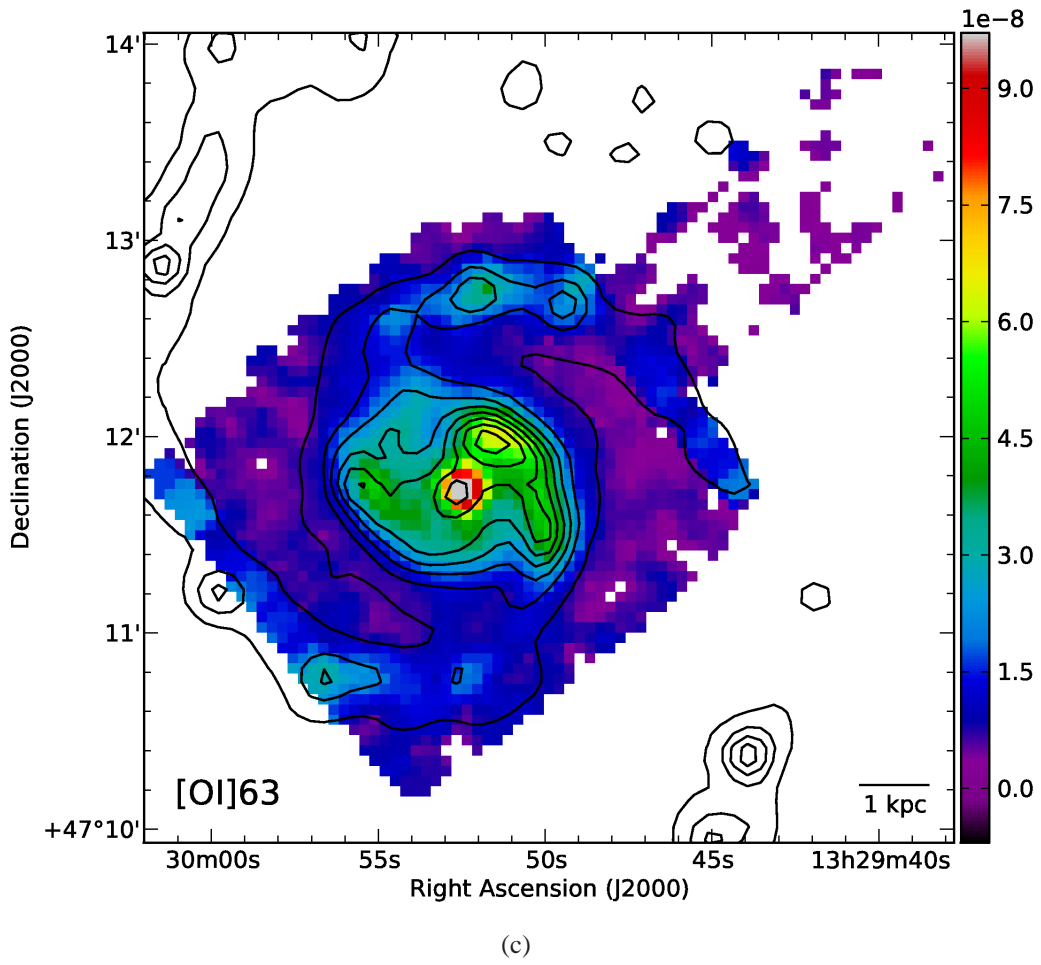


(a)

Figure 3.2: *Herschel* PACS and SPIRE spectroscopic maps of M51 of the six fine-structure lines at their native resolution and pixel scale. We have applied a  $3\sigma$  cutoff to all five PACS images, and the units are  $W\text{ m}^{-2}\text{ sr}^{-1}$ . Contours of the total infrared flux are overlaid to direct the eye to the major features of the inner galaxy. We note that the integrated intensity within each pixel of the [N II]205 map is actually the average surface brightness over the  $17''$  beam of each bolometer in the FTS array, and not the average over the  $4''$  pixel each bolometer is centered on.

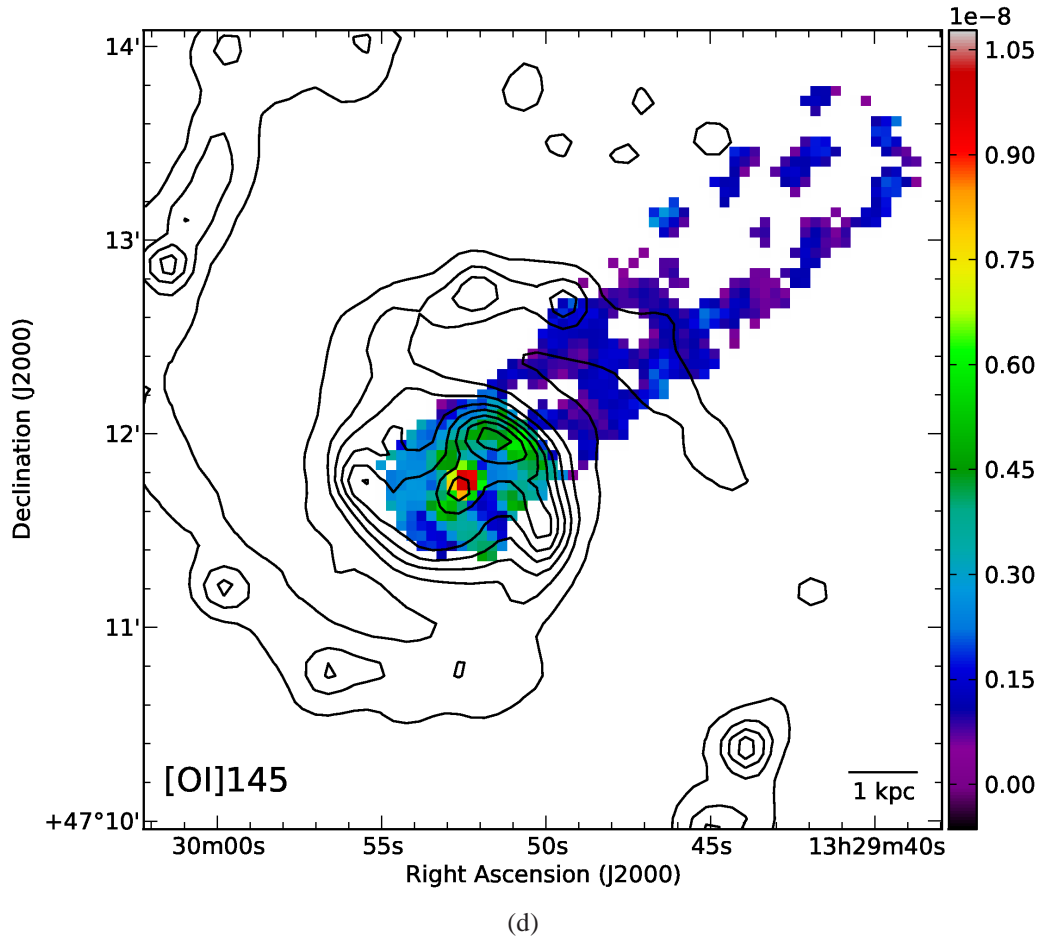
Figure 3.2: *continued*

the nuclear region with a peak in the very center and a slight enhancement in the northwestern inner region of the spiral arm. There is also a “stripe” extending from the center to the southeast that may indicate a bar-like structure. Overall, the flux in this line is weaker than in [C II], [N II]122, and [O I]63 emission, in part due to the fact that the line is intrinsically weak. However, there is also less sensitivity in the strips than the maps due to the raster spacing in the strips. The average S/N in the central part of the [C II] map is  $\sim 200$ , while it is only about 8 and 11 for the central footprint in the [O III] and [O I]145 strips, respectively. The morphology of the center of the [O I]145 strip looks very similar to the [O I]63 emission, only

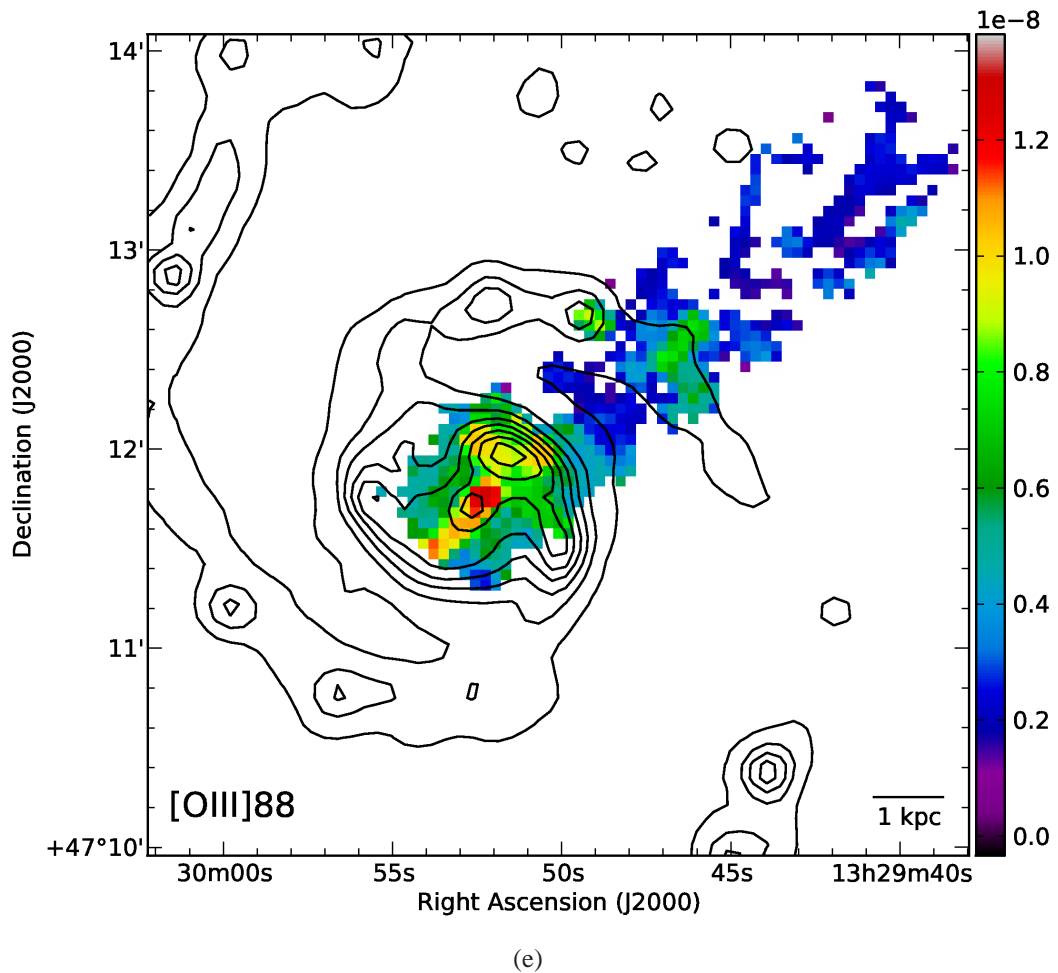
Figure 3.2: *continued*

weaker. We note here that Negishi et al. (2001) observed the [O I]145 line with *ISO* but did not detect it, while they measured a flux of  $(0.8 \pm 0.3) \times 10^{-15} \text{ W m}^{-2}$  for the [O III] line, twice as high as our measured value of  $(3 \pm 1) \times 10^{-16} \text{ W m}^{-2}$ . This is likely because we only observed a strip in this line and thus the  $80''$  aperture of Negishi et al. (2001) is larger than our observed region.

In Table 3.2 we compare the total flux of each line with previous work. In a region approximately  $2.^{\prime}7$  from the center of M51, centered on the HII region CCM 10, Garnett et al. (2004) used *ISO* to observe the same fine-structure lines as we present here. Kramer et al. (2005) also observed M51 with *ISO* in the center

Figure 3.2: *continued*

and two locations in the spiral arms, detecting [C II], [O I]63, and [N II]122, while Negishi et al. (2001) presented observations of the center taken with *ISO* and detected the same lines we have, with the exception of the [O I]145 line. To compare our results to these previous observations, we have calculated the flux within the central 80'' for each line to match the beam size of a single pointing with *ISO*. In general our measurements agree well with those of Negishi et al. (2001); however, our values are stronger than those of Garnett et al. (2004). This is a reasonable result given that CCM 10 is located in a region outside the central 80'' aperture and in fact falls outside our observed region entirely.

Figure 3.2: *continued*

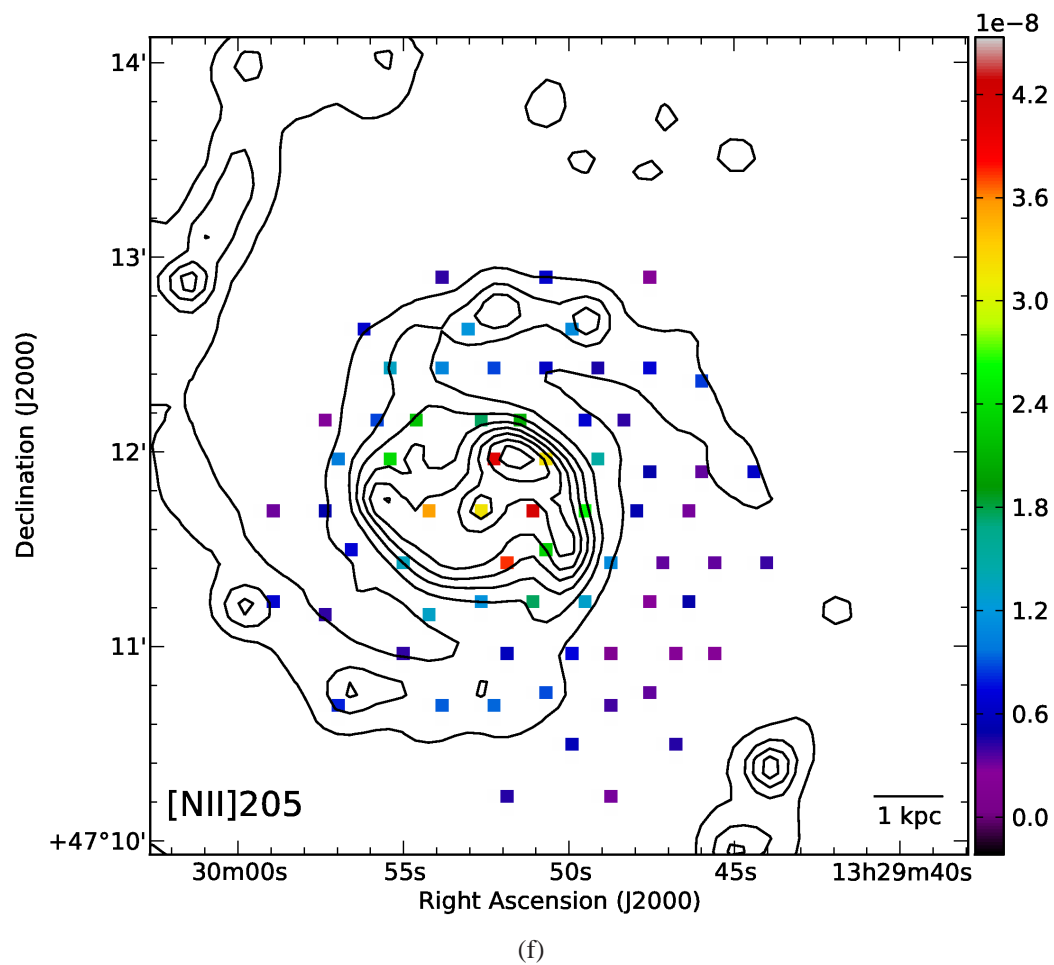
Figure 3.2: *continued*

Table 3.2. Comparison to Previous Measurements of M51

Line	Flux ( $10^{-16}$ W m $^{-2}$ )			
	This Work	Garnett et al. (2004)	Negishi et al. (2001)	Kramer et al. (2005)
	Central 80'' <sup>a</sup>	CCM 10 <sup>b</sup>	Center	Center <sup>c</sup>
[C II](158 $\mu$ m)	135 $\pm$ 40	39 $\pm$ 3	104 $\pm$ 21	52.92
[N II](122 $\mu$ m)	24 $\pm$ 7	3.3 $\pm$ 0.1	21 $\pm$ 4	14.76
[O I](63 $\mu$ m)	30 $\pm$ 10	14 $\pm$ 4	44 $\pm$ 9	38.64
[O I](145 $\mu$ m)	1.5 $\pm$ 0.4	0.8 $\pm$ 0.2	...	...
[O III](88 $\mu$ m)	3 $\pm$ 1	8 $\pm$ 2	8 $\pm$ 3	...

Note. — Total flux measured within an 80'' aperture centered on the nucleus of M51. The aperture matches the beam size of the *ISO* observations. Only pixels with a  $5\sigma$  detection or better within the aperture were included in calculating the total flux from our *Herschel* maps.

<sup>a</sup>The number of pixels with at least a  $5\sigma$  detection within the 80'' aperture varies between lines. The [C II], [N II], and [O I]63 lines are detected in all pixels within the aperture, covering a total solid angle of  $1.2 \times 10^{-7}$  sr. The solid angle covered by the [O I]145 emission within the aperture is  $4.6 \times 10^{-8}$  sr, and the solid angle covered by the [O III] emission within the aperture is  $4.9 \times 10^{-8}$  sr.

<sup>b</sup>CCM 10 is an H II region that lies outside the region discussed in this work.

<sup>c</sup>These are the same data as presented by Negishi et al. (2001); however, an extended source correction has been applied by Kramer et al. (2005) in calculating the integrated intensity, reducing its value.

Table 3.3. Line to Total Infrared Flux Ratio in M51

Line	$10^{-4}$ Line/ $F_{\text{TIR}}^{\text{a}}$	Area <sup>b</sup> ( $\square''$ )
[C II](158 $\mu\text{m}$ )	$40 \pm 10$	21360
[N II](122 $\mu\text{m}$ )	$5 \pm 1$	17536
[O I](63 $\mu\text{m}$ )	$9 \pm 3$	17472
[O I](145 $\mu\text{m}$ )	$1.0 \pm 0.7$	3008
[O III](88 $\mu\text{m}$ )	$2 \pm 1$	2976

<sup>a</sup>Average spectral line flux divided by the total infrared flux, as calculated using our  $5\sigma$ -cut maps for M51. The uncertainties shown are the standard deviations.

<sup>b</sup>The area over which each average is calculated. The variations reflect the size differences in our maps between different fine-structure lines.

### 3.3.2 Line Deficits

In Figure 3.3(a) we show the [C II]/ $F_{\text{TIR}}$  ratio, which varies between  $10 \times 10^{-4}$  and  $100 \times 10^{-4}$  with an average  $40 \times 10^{-4}$ . Typical measurement uncertainties (excluding calibration errors) in a given pixel are  $\sim 3\%$ , with the highest measurement uncertainties (and thus lowest S/N) of  $\sim 20\%$  found in the pixels on the outermost edges of the map. There are a few regions along the spiral arms in the north and southwest of the map where there is a small enhancement of the ratio, corresponding to peaks in the [C II] emission. In addition, we see a lower ratio in the center of the galaxy, corresponding to a slight deficit of [C II] emission. The average [C II]/ $F_{\text{TIR}}$  ratio, along with the line/ $F_{\text{TIR}}$  ratio for each of the other far-infrared lines, is shown in Table 3.3. Not surprisingly, the next strongest ratio after the [C II]/ $F_{\text{TIR}}$  ratio is the [O II]63/ $F_{\text{TIR}}$  ratio. The emission from these lines accounts for between 0.01% and 0.4% of the total infrared flux in this region of M51.

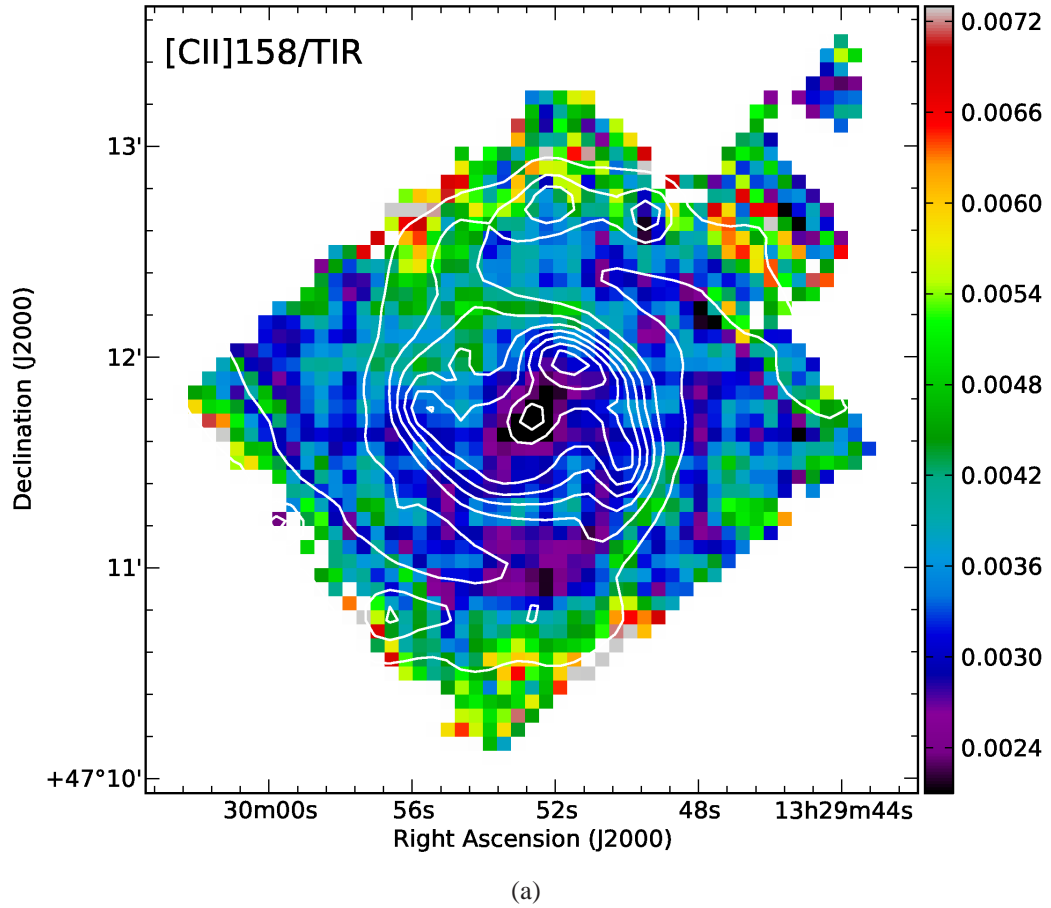
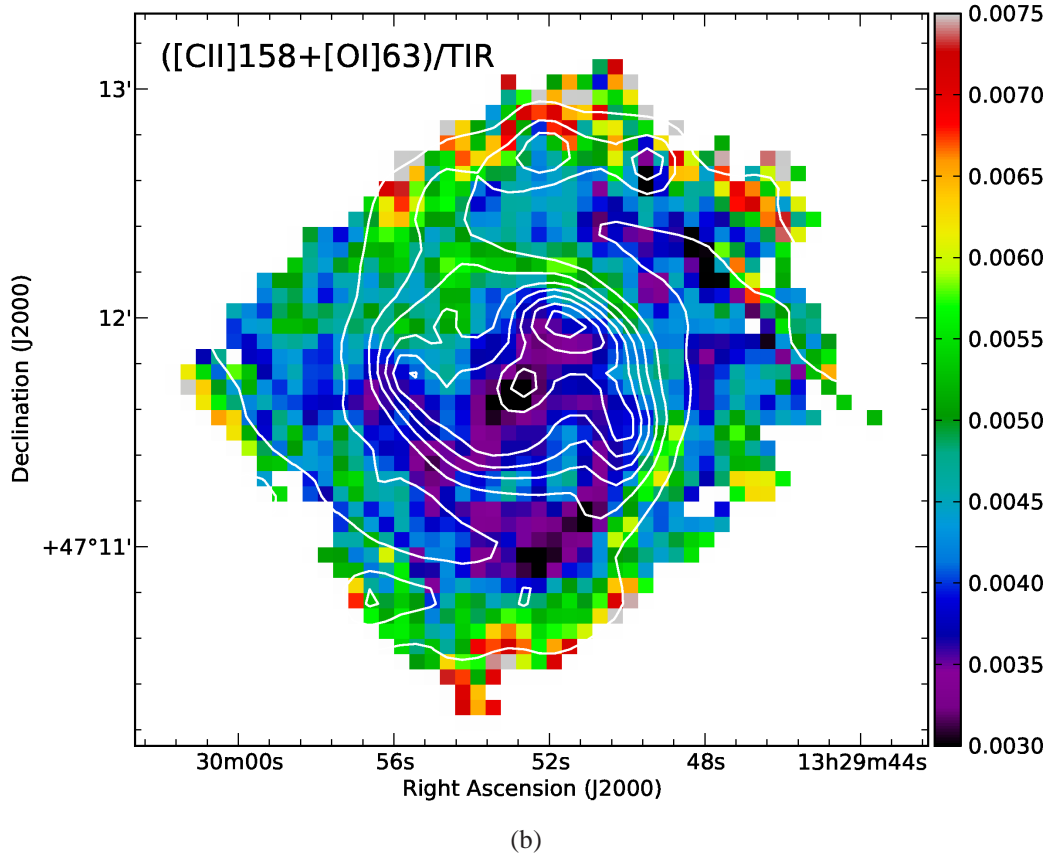
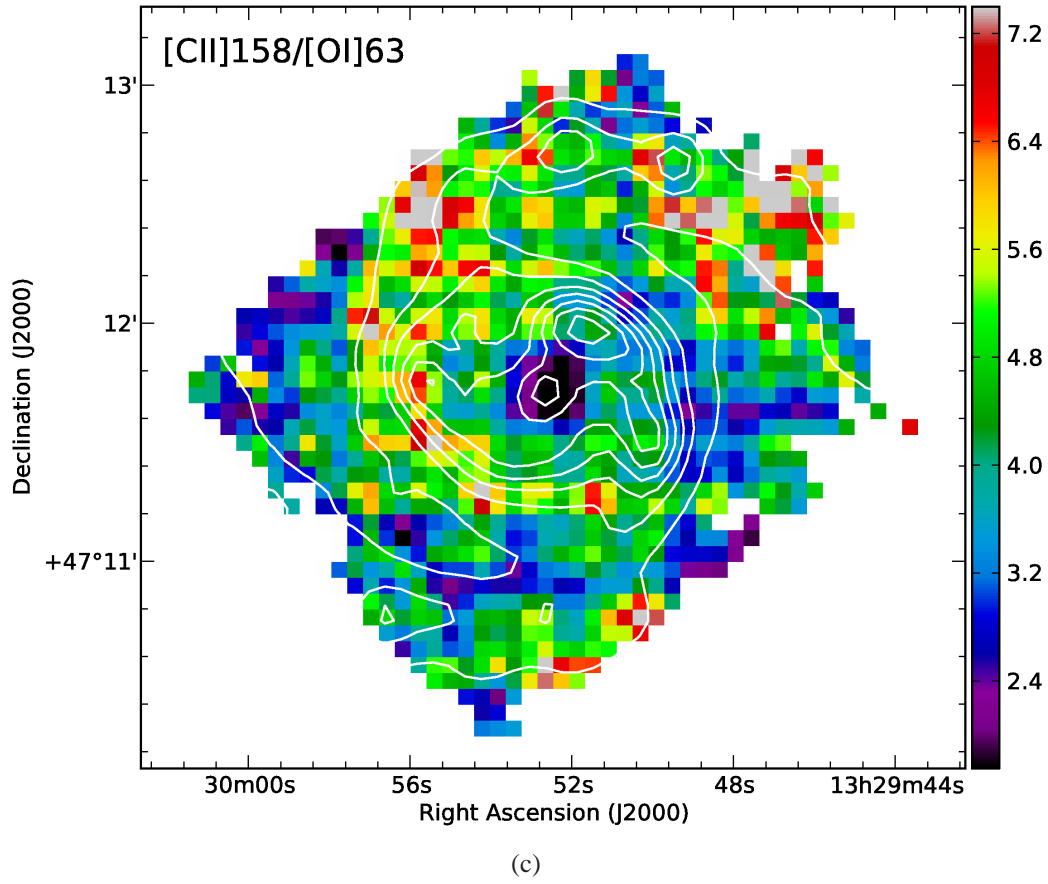


Figure 3.3: (a) The [C II] emission divided by the total infrared flux,  $F_{\text{TIR}}$ , in M51. (b) The sum of the [C II] and [O I]63 emission in M51 divided by the total infrared flux,  $F_{\text{TIR}}$ . (c) The [C II] emission in M51 divided by the [O I]63 emission. A  $5\sigma$  cutoff has been applied to all of the spectral line maps. Contours of  $F_{\text{TIR}}$  are overlaid on each ratio plot to highlight the major features of the galaxy.

Figure 3.3: *continued*

The global  $[\text{C II}]/F_{\text{TIR}}$  ratio has been measured by numerous surveys of both nearby galaxies and high-redshift sources to investigate the  $[\text{C II}]$  deficit. Studies of the  $[\text{C II}]/L_{\text{FIR}}$  ratio in ultra-luminous infrared galaxies (ULIRGs) show a deficit when compared to normal galaxies, with values of less than  $5 \times 10^{-4}$  (e.g., Luhman et al., 1998, 2003). This is the so-called  $[\text{C II}]$  deficit. Multiplying our  $[\text{C II}]/F_{\text{TIR}}$  ratio by a factor of 1.3 to convert  $F_{\text{TIR}}$  to  $F_{\text{FIR}}$  (Graciá-Carpio et al., 2008), we find that our  $[\text{C II}]/F_{\text{FIR}}$  range of  $13 \times 10^{-4}$  to  $130 \times 10^{-4}$  with an average  $52 \times 10^{-4}$  is in good agreement with previous studies of the  $[\text{C II}]/F_{\text{FIR}}$  ratio. Nikola et al. (2001) previously investigated M51 and found that this ratio varied between  $60 \times 10^{-4}$  and  $140 \times 10^{-4}$ . Stacey et al. (1985) found a global value for the  $[\text{C II}]/F_{\text{FIR}}$  ratio within

Figure 3.3: *continued*

the Milky Way of  $30 \times 10^{-4}$  and on smaller scales, Stacey et al. (1993) found the same value for the Orion molecular cloud. Crawford et al. (1985) conducted a study of six gas-rich galaxies, including M51, and found that the ratio is about  $50 \times 10^{-4}$  for this sample. Malhotra et al. (2001) found ratios of greater than  $20 \times 10^{-4}$  in two-thirds of their sample of 60 normal star-forming galaxies, and Graciá-Carpio et al. (2011) found a range of values between  $1 \times 10^{-4}$  and  $100 \times 10^{-4}$  for a sample of 44 AGN and starburst-type galaxies from the SHINING survey. On smaller scales, Contursi et al. (2002) investigated NGC 6946 and NGC 1313 and found that the ratio for these two galaxies is  $80 \times 10^{-4}$ , while Contursi et al. (2013) found that the  $[\text{C II}]/F_{\text{FIR}}$  ratio varies between roughly  $10 \times 10^{-4}$  and  $100 \times 10^{-4}$  for various

regions within the starburst M82. Kramer et al. (2013) recently discovered a radial trend in the [C II]/ $F_{\text{FIR}}$  ratio in M33, increasing from  $80 \times 10^{-4}$  in the inner galaxy to  $300 \times 10^{-4}$  at a distance of roughly 4.5 kpc from the center, and thus increasing with decreasing far-infrared flux.

We also compare our results to the empirically derived relation from Spinoglio et al. (2012) predicting the global [C II] luminosity given a galaxy's total infrared luminosity. Using our total-infrared luminosity of  $4.71 \times 10^{10} L_{\odot}$  and Equation (33) from Spinoglio et al. (2012), we calculate a global [C II] luminosity of  $7.5 \times 10^7 L_{\odot}$  and thus a [C II]/ $L_{\text{FIR}}$  ratio of  $16 \times 10^{-4}$ . This value is in agreement with the lower range of our observed values. Thus, we find that even though our [C II]/ $F_{\text{FIR}}$  ratio is smaller (by up to a factor of two) in the nucleus than in the rest of M51, it is not as extreme as the low values seen in ULIRGs.

Negishi et al. (2001) calculated the line/ $F_{\text{TIR}}$  ratio for the same far-infrared lines we measured here with PACS. Their sample of galaxies, including normal, starburst, and AGN types, shows line/ $F_{\text{TIR}}$  ratios consistent with those measured in M51. Furthermore, our results for M51 are also consistent with the results Malhotra et al. (2001) found for their sample of normal galaxies (note we have increased their far-infrared flux values by a factor of 1.3 to approximate the total infrared flux). We compare our results to both papers in Table 3.4. Our resolved average values for M51 fall within the range of ratios typically found in a variety of galaxy types on unresolved scales.

### 3.3.3 Heating and Cooling

In Figure 3.3(b) we show a map of  $([\text{C II}]+[\text{O I}]63)/F_{\text{TIR}}$ , which is considered a proxy for the total heating efficiency,  $\epsilon$  (Tielens & Hollenbach, 1985). The heating

Table 3.4. Line/ $F_{\text{TIR}}$  Ratios in M51 Compared to Previous Global Surveys

Line	$10^{-4}$ Line/ $F_{\text{TIR}}$		
	This Work <sup>a</sup>	Negishi et al. (2001)	Malhotra et al. (2001)
	Average	Range	
[C II](158 $\mu\text{m}$ )	$40 \pm 10$	9–100	7–50
[N II](122 $\mu\text{m}$ )	$5 \pm 1$	2–10	1–7
[O I](63 $\mu\text{m}$ )	$9 \pm 3$	4–30	4–40
[O I](145 $\mu\text{m}$ )	$1.0 \pm 0.7$	0.3–5	...
[O III](88 $\mu\text{m}$ )	$2 \pm 1$	0.9–8	1–10
			2–20

<sup>a</sup>Note that only  $5\sigma$  detections are included; global values for M51 are likely to be lower.

efficiency represents the fraction of energy from the interstellar FUV radiation field that is converted to gas heating through the photoelectric effect, divided by the fraction of its energy deposited in dust grains. This ratio represents the heating efficiency within the context of gas heating in PDR regimes (see, e.g., Tielens & Hollenbach, 1985). A comparison with the [C II]/ $F_{\text{TIR}}$  ratio shows that adding the [O I]63 emission enhances some of the structure in the spiral arms. We look at this ratio in more detail in Section 3.4.

The [C II]/[O I]63 ratio is also shown in Figure 3.3(c). Cooling via the [C II] line is more efficient in lower density, lower temperature regimes, while [O I]63 cooling dominates at higher densities and warmer temperatures (Tielens & Hollenbach, 1985). In this figure, the central region shows a ratio lower than the rest of the galaxy by a factor of  $\sim 2$ –4, corresponding to the strong [O I]63 emission in the center; however, the ratio remains greater than 1.0 everywhere. There is a visible increase in the ratio to upward of 6.0 along the inner part of the eastern spiral arm, spatially coincident with the decreasing [C II] emission at the outer edge of the nuclear region. The low ratio in the center of the galaxy might indicate that the gas is

warmer and/or more dense, and cooling by the [O I]63 line becomes more important. Typical measurement uncertainties are about 8% with the noisiest pixels lying around the edge of the map having uncertainties of up to  $\sim 24\%$ .

The ratio of the two [O I] lines, [O I]145/[O I]63, can probe the temperature in the range around  $\sim 300$  K for optically thin neutral gas because the excitation energies,  $\Delta E/k$ , are 228 K and 325 K above the ground state for the [O I]63 and [O I]145 lines, respectively (Tielens & Hollenbach, 1985; Kaufman et al., 1999; Malhotra et al., 2001; Liseau et al., 2006). However, the [O I]63 line can become optically thick at a lower column density than the [O I]145 line, boosting the ratio of the two [O I] lines for gas temperatures less than  $\sim 1000$  K (Tielens & Hollenbach, 1985). Using a  $5\sigma$  cutoff for both the [O I]63 and [O I]145 lines and noting that the [O I]145 was only mapped along a radial strip (see Figure 3.2), our measurements of the ratio reside primarily in the central region of the galaxy, along with a few pixels in the inner part of the northwestern spiral arm. In the center region the average ratio is 0.08 with typical measurement uncertainties of  $\sim 9\%$ . Taking the inverse of this value to obtain a [O I]63/[O I]145 ratio of  $12.5 \pm 5.3$  and comparing it with Figure 4 from Liseau et al. (2006), we find that the [O I]63 line is either optically thick with  $T \gtrsim 200$  K and  $n \gtrsim 10^3$  cm $^{-3}$  or optically thin and hot with  $T \sim 4000$  K and a density of approximately 10 $^3$  cm $^{-3}$ .

We can also investigate the diagnostic plots  $([\text{C II}]+[\text{O I}]63)/F_{\text{TIR}}$  or  $([\text{C II}]+[\text{O I}]63)/F_{\text{PAH}}$  versus far-infrared color to look at the heating efficiency in more depth. Here we take the far-infared color  $70\mu\text{m}/160\mu\text{m}$ , but typically the *IRAS* color  $60\mu\text{m}/100\mu\text{m}$  is used. Previous work has found a correlation between the heating efficiency and the infared color showing a decrease in heating efficiency with warmer colors, on both global and galactic scales (e.g., Malhotra et al., 2001; Croxall et al., 2012). This decrease has been attributed to warmer dust grains be-

coming increasingly positively charged when exposed to stronger radiation fields, thus lowering the efficiency of the photoelectric effect. It has also been shown that there is an even tighter correlation between heating efficiency and PAH emission, perhaps indicating that PAHs are the primary contributor to gas heating rather than dust grains in regions where [C II] and [O I]63 are the primary coolants (Croxall et al., 2012; Lebouteiller et al., 2012). In Figure 3.4 we plot  $([C\text{ II}]+[\text{O I}]63)/F_{\text{TIR}}$  as a function of  $70\mu\text{m}/160\mu\text{m}$  (top) and  $([C\text{ II}]+[\text{O I}]63)/F_{\text{PAH}}$  as a function of color (bottom). In both cases, each data point corresponds to one pixel in our images and the colors correspond to the four different regions we break the galaxy into for our PDR analysis (see Section 3.4 and Figure 3.6 for more details). We find that the heating efficiency as traced by  $([C\text{ II}]+[\text{O I}]63)/F_{\text{TIR}}$  decreases by about a factor of two with increasing color as found by previous studies, which corresponds to a lower heating efficiency in the center of the galaxy than in the arm and interarm regions. When we trace the heating efficiency by  $([C\text{ II}]+[\text{O I}]63)/F_{\text{PAH}}$ , we find a variation of approximately 30% across the color space, in agreement with general trends found by Lebouteiller et al. (2012) in LMC N11B and Croxall et al. (2012) in NGC 1097 and NGC 4559. However, this ratio does not vary significantly for the warmer dust, in contrast to the  $([C\text{ II}]+[\text{O I}]63)/F_{\text{TIR}}$  ratio.

Our value for the total heating efficiency within PDRs as measured by  $([C\text{ II}]+[\text{O I}]63)/F_{\text{TIR}}$  ranges between approximately  $2 \times 10^{-3}$  and  $5 \times 10^{-3}$ . The survey conducted by Malhotra et al. (2001) found a range of values between  $10^{-3}$  and  $10^{-2}$ . Croxall et al. (2012) looked at NGC 1097 and NGC 4559 and found that this proxy for the heating efficiency falls between approximately  $2 \times 10^{-3}$  to  $10^{-2}$ ; thus, our values for M51 fall within the lower range of their results. In slightly lower metallicity environments the ratio is about the same at  $2.77 \times 10^{-3}$  for NGC 4214 (metallicity of  $\log(\text{O/H})+12 = 8.2$ ; Cormier et al., 2010) and  $2 \times 10^{-3}$  in Haro 11

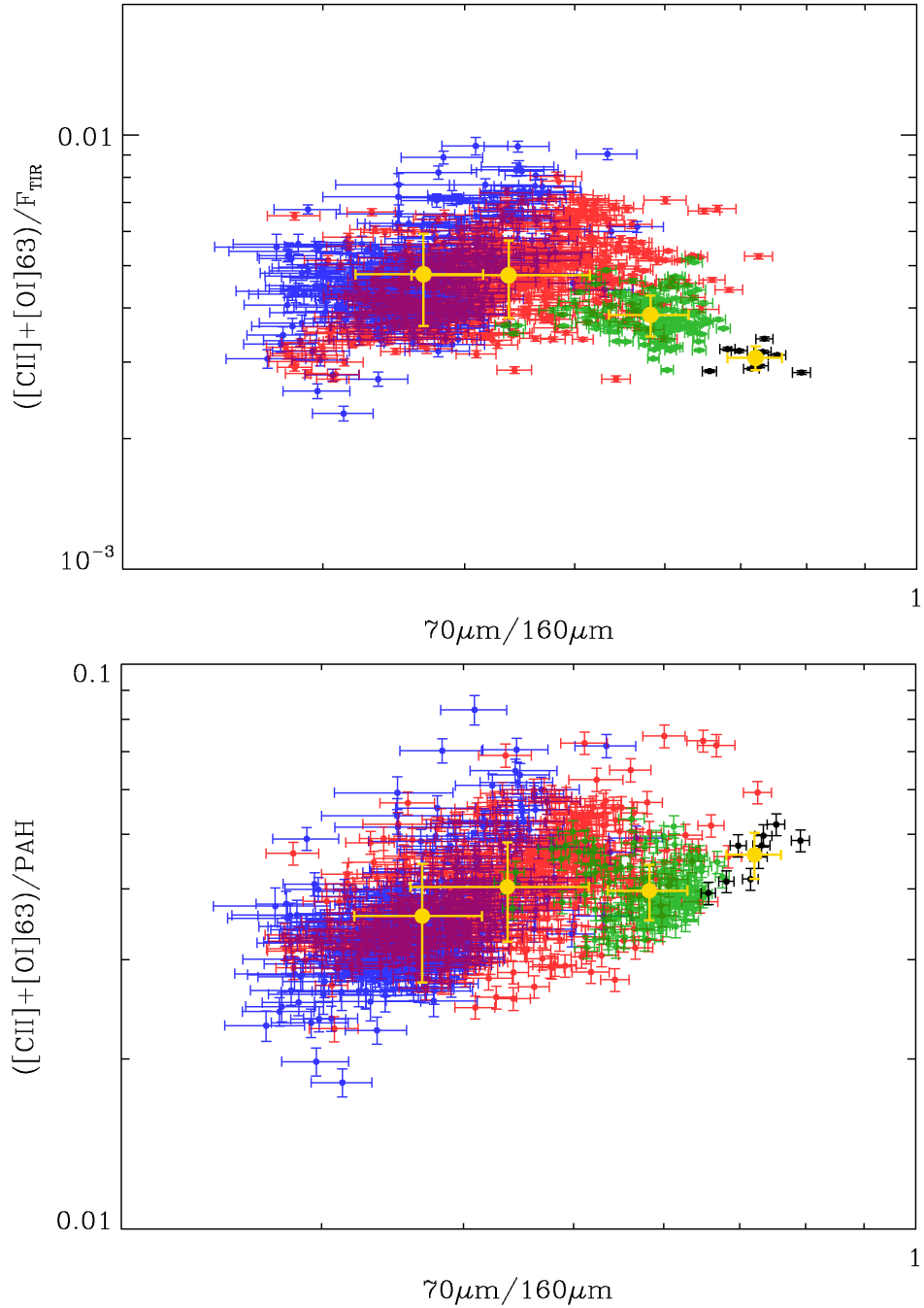


Figure 3.4: Top: total cooling ( $[\text{C II}]+[\text{O I}]63$ ) divided by the total infrared flux vs. the PACS  $70\mu\text{m}/160\mu\text{m}$  color. Bottom: total cooling ( $[\text{C II}]+[\text{O I}]63$ ) divided by the PAH emission, represented by the stellar subtracted IRAC  $8\mu\text{m}$  flux, vs. the PACS  $70\mu\text{m}/160\mu\text{m}$  color. In both cases, one data point represents one pixel. The pixels from the nucleus, center, arm, and interarm regions are shown in black, green, red and blue, respectively. The large yellow circles represent the mean for each region.

(metallicity 1/3 solar; Cormier et al., 2012). On small scales, Lebouteiller et al. (2012) investigated the H II region LMC-N11B (metallicity  $\sim$ 1/2 solar), and found an average value of  $\sim 5.5 \times 10^{-3}$  in PDRs, but the ratio decreased in regions dominated by ionized gas, a trend they attribute to contamination of the total infrared flux from the ionized gas where [C II] and [O I]63 do not primarily emit.

Looking at the ([C II]+[O I]63)/PAH ratio, we find an average of  $\sim 0.01$ , which is less than the value of 0.07 in LMC-N11B (Lebouteiller et al., 2012), as well as the range of 0.035–0.06 in NGC 1097 and NGC 4559 (Croxall et al., 2012). Beirão et al. (2012) find that the ([C II]+[O I]63)/PAH ratio varies from 0.03 to 0.1 and is approximately 50% lower in the ring of NGC 1097 than in the nucleus. However, Croxall et al. (2012) note that for NGC 1097 and NGC 4559, using the IRAC 8 $\mu$ m map as a proxy for the total PAH emission overestimates (by about 10%) the true total emission, estimated from running the *Spitzer* Infrared Spectrograph (IRS) spectrum through PAHfit (Smith et al., 2007). As a similar check for M51, we run the IRS spectrum for M51 produced by the SINGS team (Kennicutt et al., 2003), which is an average extracted from a region approximately 60''  $\times$  35'' centered on the nucleus, through PAHfit. We then measure the total PAH intensity from within the same region using the IRAC 8  $\mu$ m and compare it to the total calculated by PAHfit. We find that for the region covered by the IRS spectrum, the IRAC 8  $\mu$ m map overestimates the total PAH intensity by a factor of  $\sim 3.5$ . Applying this correction to the ([C II]+[O I]63)/PAH ratio in all four regions we investigate here will bring the data points in Figure 3.4 (bottom) up by a factor of 3.5, and thus in better agreement with the range of values determined by (Lebouteiller et al., 2012), Beirão et al. (2012), and (Croxall et al., 2012). We note that our PAH map has not been corrected for the underlying dust continuum, which may partially explain the discrepancy between the PAH intensity measured by PAHfit and that measured by

the IRAC 8  $\mu\text{m}$  map.

### 3.3.4 Ionized Gas

#### 3.3.4.1 Ionized Gas Contribution to [C II] Emission

To compare our [C II] map properly with the theoretical results of Kaufman et al. (1999, 2006), we need to correct for the fraction of [C II] emission arising from ionized gas, as [C II] emission can originate in both neutral and ionized gas. We follow the method of Oberst et al. (2006) and use the diagnostic capabilities of the [N II]122/[N II]205 and [C II]/[N II]205 line ratios. [N II] emission arises entirely from ionized gas because the ionization potential of N<sup>+</sup> is greater than 13.6 eV. In addition, the ratio of its two fine-structure lines is a sensitive probe of the gas density in H II regions. The critical densities of the [N II]122 and [N II]205 lines are 293 and 44 cm<sup>-3</sup>, respectively, when  $T_e = 8000$  K (commonly adopted for H II regions) (Oberst et al., 2006). Furthermore, at the same temperature, the [C II] line has a critical density of 46 cm<sup>-3</sup> for collisions with electrons (Oberst et al., 2006), and so the [C II]/[N II]205 ratio is primarily dependent on the abundances of C<sup>+</sup> and N<sup>+</sup>. A comparison of the theoretical ratio to the observed ratio at a specific electron density will determine the fraction of the [C II] flux coming from ionized gas. We compute the theoretical curves for the [N II]122/[N II]205 and [C II]/[N II]205 line ratios as a function of electron density using solar gas phase abundances of C/H =  $1.4 \times 10^{-4}$  and N/H =  $7.9 \times 10^{-5}$  (Savage & Sembach, 1996), collision strengths for the [N II] and [C II] lines from Hudson & Bell (2004) and Blum & Pradhan (1992), respectively, and Einstein coefficients from Galavis et al. (1997) and Galavis et al. (1998) for the [N II] and [C II] transitions, respectively. We choose to adopt solar abundances here because Garnett et al. (2004) showed

that the C and N abundances in M51 are consistent with the solar values within their uncertainties. We note that while M51 has a slightly higher metallicity than solar (Asplund et al., 2009) and has a slight decrease in metallicity with increasing radius (Moustakas et al., 2010; Mentuch Cooper et al., 2012), Garnett et al. (1999) showed that the C/N abundance ratio is not affected by metallicity gradients in two nearby spirals, M101 and NGC 2403. Thus, we believe that the metallicity gradient will not strongly affect our results.

To measure the observed  $[\text{N II}]122/[\text{N II}]205$  and  $[\text{C II}]/[\text{N II}]205$  line ratios, we convolved our  $[\text{C II}]$  and  $[\text{N II}]122$  maps to the resolution of the  $[\text{N II}]205$  map ( $\sim 17''$ ) and then calculated the ratios. Our  $[\text{N II}]205$  map only contains a small number of finite pixels; thus, the resulting ratio maps give us an estimate of  $[\text{N II}]122/[\text{N II}]205$  and  $[\text{C II}]/[\text{N II}]205$  (at positions observed in  $[\text{N II}]205$ ) that we can use to estimate the electron density and fraction of  $[\text{C II}]$  emission from ionized gas in each region. Comparing our observed ratios in each region to the theoretical curves (Figure 3.5) we find that the fraction of the  $[\text{C II}]$  emission in our observations coming from ionized gas is  $0.8 \pm 0.2$ ,  $0.7^{+0.3}_{-0.2}$ ,  $0.5^{+0.3}_{-0.2}$ , and  $0.5^{+0.2}_{-0.1}$  for the nucleus, center, arm and interarm regions, respectively (Table 3.5). Calibration uncertainties are included and have the effect of shifting all our ratios up or down, but the trend from region to region will remain the same.

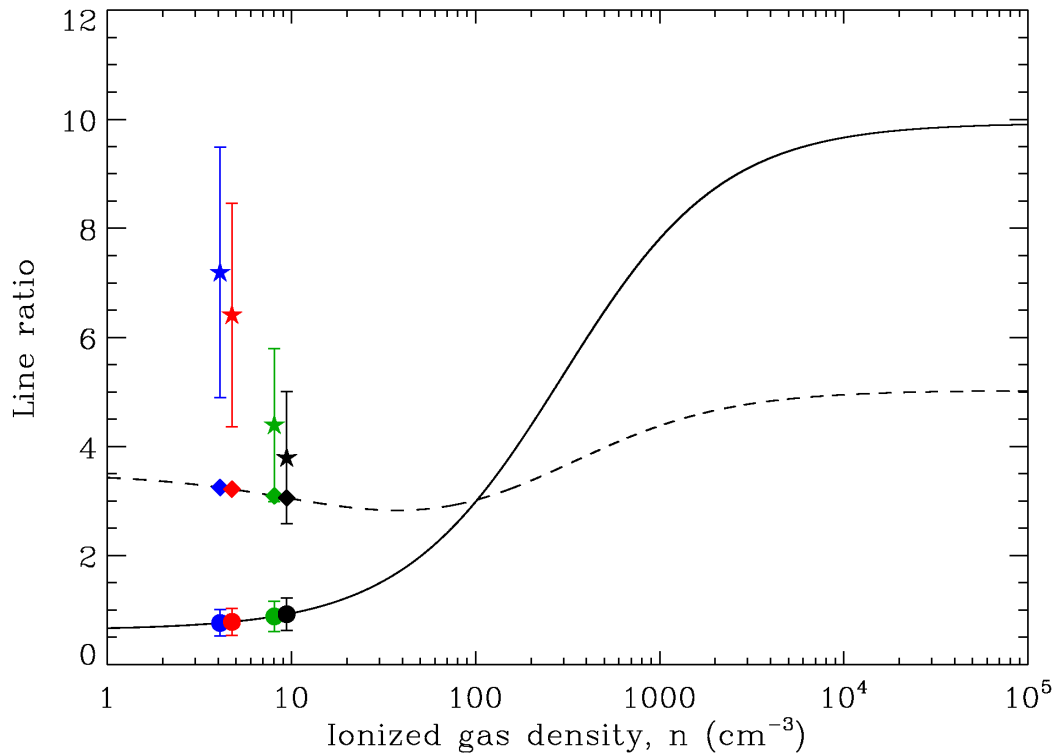


Figure 3.5: Comparison of the average observed line ratio to the theoretical curves for each of the four regions we probe in M51. The black solid line represents the theoretical curve for the  $[\text{N II}]122/[\text{N II}]205$  line ratio, while the black dashed line represents the theoretical curve for the  $[\text{C II}]/[\text{N II}]205$  line ratio. The pixels from the nucleus, center, arm, and interarm regions are shown in black, green, red, and blue, respectively. The solid dots show where the observed  $[\text{N II}]122/[\text{N II}]205$  line ratios for each region fall on the theoretical curve, thus allowing us to determine the ionized gas density. The diamonds (stars) show the theoretical (observed) values of the  $[\text{C II}]/[\text{N II}]205$  line ratio at the inferred ionized gas density. The error bars on the observed line ratios include calibration uncertainties.

Table 3.5. [N II] Line Ratios and Ionized Fraction of [C II]

Region	Observed [N II] <sub>122</sub> /[N II] <sub>205</sub>	$n_e$ <sup>a</sup> (cm <sup>-3</sup> )	Predicted [C II] <sub>158</sub> <sup>ionized</sup> /[N II] <sub>205</sub> <sup>b</sup>	Observed [C II] <sub>158</sub> /[N II] <sub>205</sub>	Ionized Fraction of [C II]
Nucleus	$0.9^{+0.3}_{-0.2}$	$9^{+10}_{-7}$	$3.1^{+0.3}_{-0.2}$	$4 \pm 1$	$0.8^{+0.2}_{-0.2}$
Center	$0.9^{+0.3}_{-0.2}$	$8^{+10}_{-6}$	$3.1^{+0.3}_{-0.2}$	$4 \pm 1$	$0.7^{+0.3}_{-0.2}$
Arm	$0.78^{+0.25}_{-0.08}$	$5^{+8}_{-3}$	$3.2^{+0.1}_{-0.2}$	$6 \pm 2$	$0.5^{+0.3}_{-0.2}$
Interarm	$0.76^{+0.24}_{-0.06}$	$4^{+8}_{-2}$	$3.2^{+0.1}_{-0.3}$	$7 \pm 2$	$0.5^{+0.2}_{-0.1}$

Note. — These are average values for each of the four regions, and calibration uncertainties are included.

<sup>a</sup>Derived from [N II]<sub>122</sub>/[N II]<sub>205</sub>; see text.

<sup>b</sup>Derived from  $n_e$  and theoretical prediction of [C II]/[N II]<sub>205</sub> ratio in ionized gas; see text.

### 3.3.4.2 Ionized Gas Characteristics

The fraction of N<sup>+</sup> originating from diffuse ionized gas versus that originating from HII regions has been discussed at length in the literature. A set of models for H II regions by Rubin (1985) and a later model by Rubin et al. (1994) show that the ratio between the two [N II] lines, [N II]122/[N II]205, varies from 3 for  $n_e \sim 100 \text{ cm}^{-3}$  to 10 for  $n_e \gtrsim 10^3 \text{ cm}^{-3}$ . When  $n_e \ll n_{\text{critical}}$ , the theoretical value for this ratio is 0.7 (Wright et al., 1991; Bennett et al., 1994). Observations of [N II]122 and [N II]205 in the Milky Way show that the [N II]122/[N II]205 falls between 1.0 and 1.6 (Wright et al., 1991). Comparison between the observed and theoretical ratios implies that between 60% and 87% of the [N II] emission in the Milky Way as measured with the *Cosmic Background Explorer* comes from diffuse gas while the remainder comes from H II regions with  $n_e \sim 100 \text{ cm}^{-3}$ . Bennett et al. (1994) re-examine the data presented in Wright et al. (1991) and find [N II]122/[N II]205 =  $0.9 \pm 0.1$  assuming a constant ratio, but also note that their data are better fit when the ratio is allowed to vary. Our observations show that [N II]122/[N II]205 ranges between  $0.76^{+0.24}_{-0.06}$  and  $0.92^{+0.3}_{-0.2}$ , thus approaching the theoretical lower limit of 0.7, implying that much of the ionized gas is diffuse. Nonetheless, our mean values of the [N II] line ratios are consistent with those of the Milky Way.

Our values for the fraction of [C II] emission coming from PDRs are lower than those determined in other nearby galaxies, as well as previous calculations for M51. Furthermore, a gradient in this fraction has not previously been observed in other galaxies and is an important result. Given that we believe that the Seyfert nucleus is not the major source of gas excitation in the center (see Section 3.4.2), the high fraction of ionized gas likely indicates that there are more massive stars per unit volume providing the ionizing photons.

The [N II]205 line is difficult to detect, and so it is often necessary to rely on the [C II]/[N II]122 line ratio to determine the ionized gas fraction in the [C II] emission. This ratio requires knowledge about the density of the gas, which can sometimes be difficult to obtain. However, in the absence of [N II]205 observations it is often the best way to estimate the ionized gas contribution to the observed [C II] emission. Malhotra et al. (2001) used the [C II]/[N II]122 emission and the Galactic value of the [N II]122/[N II]205 ratio to estimate that about 50% of the observed [C II] emission in their sample of galaxies originated in PDRs, in agreement with our results for the arm and interarm regions. However, Kramer et al. (2005) used a similar method to determine that 70%–85% of [C II] emission comes from PDRs in M51 and M83. This is a much higher value than what we determine using the [N II]205 line for M51, especially in the center and nuclear regions, where we find that a large fraction of [C II] emission is coming from ionized gas. In both cases the correction was applied globally, but our results demonstrate that this method may not accurately correct the observed [C II] emission and thus lead to incorrect results when comparing observations to PDR models.

The [O III] line can also be used to probe the ionized gas. One diagnostic used for high-redshift galaxies is the ratio [O III]/[N II]122. Ferkinhoff et al. (2011) showed that this ratio can constrain the hardness of the UV radiation field as the ionization potentials of N and O<sup>+</sup> are 14.5 and 35 eV, respectively, while the [N II]122 and [O III] lines have critical densities of 310 and 510 cm<sup>-3</sup>, respectively. This means that the line ratio is relatively constant as a function of gas density. If the emission arises from H II regions, then the ratio gives an indication of the effective stellar temperature of the ionizing source(s). If the emission comes from an AGN, particularly from the narrow-line region (NLR), the ratio indicates the value of the ionization parameter,  $U$ . This parameter represents the photon density of the

incident radiation field on a molecular cloud divided by the gas density of the cloud and gives an indication of the amount of dust absorbing the ionizing flux (Luhman et al., 2003; Abel et al., 2009).

In their Figure 1, Ferkinhoff et al. (2011) compare their observed  $[\text{O III}]/[\text{N II}]_{122}$  line ratio to that predicted for H II regions using the model of Rubin (1985), as well as the ratio predicted for an NLR within an AGN using the model of Groves et al. (2004). For their high-redshift galaxy, the ratio satisfies either model as well as a combination of the two. We find that for the nucleus region of M51, which represents the area covered by the PACS point-spread function, the  $[\text{O III}]/[\text{N II}]_{122}$  ratio is  $0.33 \pm 0.05$ , while for the somewhat larger ‘center’ region we measure  $0.23 \pm 0.05$ . Following the method of Ferkinhoff et al. (2011), we compare our observed ratios to model predictions. Assuming that the emission is from an H II region, our results suggest that the most luminous stars are B0 (Vacca et al., 1996) for both the nucleus and center regions. On the other hand, if we assume that the emission is from the AGN, our results imply a small ionization parameter of  $10^{-4}$  to  $10^{-3.5}$ , which means the incident ionizing flux is weak. A comparison of our average  $[\text{O III}]/F_{\text{TIR}}$  ratio to model predictions of the ratio for AGN and starburst galaxies from Abel et al. (2009) shows that our ratio of  $2 \pm 1$  is also consistent with a low value of  $U$ . Furthermore, Satyapal et al. (2004) conducted a survey of galaxies with low-luminosity nuclei using IRS LWS spectroscopy, including M51. They determined that the flux of the  $[\text{O IV}]$  line, which is only excited in AGNs due to the strong ionization potential of  $\text{O}^{++}$  (55 eV), is lower in the nucleus of M51 than in typical AGNs. This result also indicates weak activity in the nucleus of M51. Thus, we conclude that the Seyfert nucleus in M51 is not significantly affecting the excitation of the gas.

## 3.4 PDR Modeling of Observations

We compare our observed line ratios to the PDR model of Kaufman et al. (1999, 2006). This model probes PDRs with two free parameters, namely, the density of hydrogen nuclei,  $n$ , and the strength of the FUV radiation field incident on the PDR,  $G_0$ . Kaufman et al. (1999) consider a density range of  $10^1 \text{ cm}^{-3} \leq n \leq 10^7 \text{ cm}^{-3}$  and an FUV radiation field range of  $10^{-0.5} \leq G_0 \leq 10^{6.5}$ . Here we look at the inner part of M51 by carrying out a pixel-by-pixel comparison between the model and our observations and consider pixels within four regions, namely, the “nucleus”, the “center”, the “arm,” and the “interarm” regions. These regions were distinguished using flux cutoffs in our total infrared flux map (Figure 3.1) to isolate the nucleus from the rest of the center region and the spiral arms from the interarm regions. Breaking the galaxy down into four distinct subregions allows us to probe the gas in different environments within the galaxy. These regions are outlined in Figure 3.6 with cutoff maximum fluxes of  $9.6 \times 10^{-7}$  and  $3.7 \times 10^{-5} \text{ W m}^{-2} \text{ sr}^{-1}$  for the interarm and arm regions, respectively. The center region consists of everything above  $3.7 \times 10^{-5} \text{ W m}^{-2} \text{ sr}^{-1}$  except for the central nine pixels which comprise the nucleus. We note that with a pixel scale of  $4''$  in our maps, each pixel is not independent from its neighbors. In Table 3.6 we list the average integrated intensity measured in each region for each of the five far-infrared lines that we have observed.

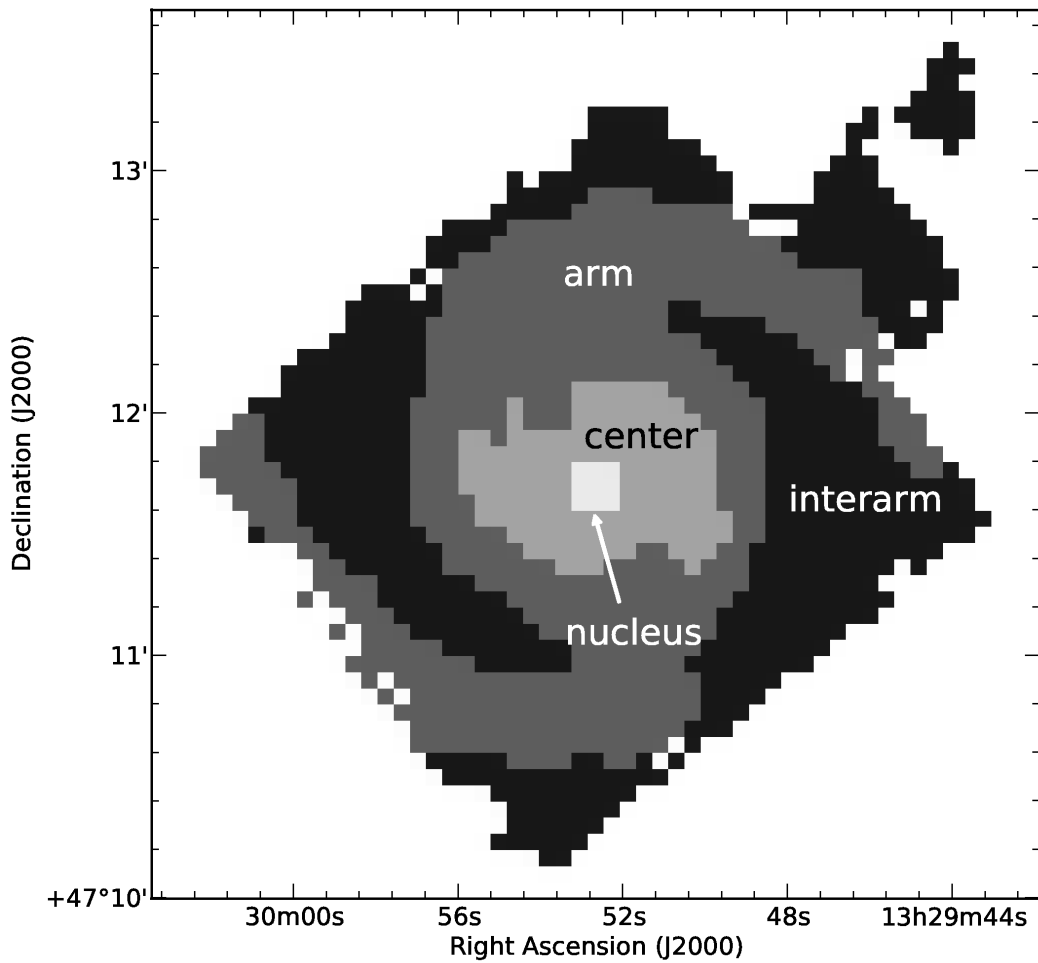


Figure 3.6: Schematic of the four regions into which we divide M51 for our analysis.

Table 3.6. Average Intensity of Fine-structure lines by Region

Region	Integrated Intensity ( $\text{W m}^{-2} \text{ sr}^{-1}$ )				
	[C II](158 $\mu\text{m}$ )	[N II](122 $\mu\text{m}$ )	[O I](63 $\mu\text{m}$ )	[O I](145 $\mu\text{m}$ )	[O III](88 $\mu\text{m}$ )
Nucleus <sup>a</sup>	$(1.4 \pm 0.1) \times 10^{-8}$	$(3.2 \pm 0.2) \times 10^{-9}$	$(8 \pm 1) \times 10^{-9}$	$(7 \pm 2) \times 10^{-10}$	$(1.0 \pm 0.1) \times 10^{-9}$
Center <sup>b</sup>	$(1.1 \pm 0.2) \times 10^{-9}$	$(1.7 \pm 0.4) \times 10^{-10}$	$(2.9 \pm 0.7) \times 10^{-10}$	$(3 \pm 1) \times 10^{-11}$	$(8 \pm 2) \times 10^{-11}$
Arms <sup>c</sup>	$(1.2 \pm 0.5) \times 10^{-10}$	$(1.4 \pm 0.9) \times 10^{-11}$	$(3 \pm 1) \times 10^{-11}$	$(4 \pm 1) \times 10^{-11}$	$(8 \pm 2) \times 10^{-11}$
Interarm <sup>d</sup>	$(5 \pm 2) \times 10^{-11}$	$(8 \pm 3) \times 10^{-12}$	$(1.8 \pm 0.5) \times 10^{-11}$	$(3.2 \pm 0.8) \times 10^{-11}$	$(1.7 \pm 0.4) \times 10^{-10}$

Note. — Average integrated intensity measured in the four different regions for each of the far-infrared fine-structure lines, using our maps with a  $5\sigma$  cut applied. The uncertainties shown are the standard deviations.

<sup>a</sup>The number of pixels included in this measurement is 9 for all five lines.

<sup>b</sup>The number of pixels included in this measurement is 136 for the [C II], [N II]122, and [O I]63 lines, 95 for the [O I]145 line, and 93 for the [O III] line.

<sup>c</sup>The number of pixels included in this measurement is 583, 560, 553, 46, and 61 for the [C II], [N II]122, [O I]63, [O I]145, and [O III] lines, respectively.

<sup>d</sup>The number of pixels included in this measurement is 607, 391, 394, 38, and 23 for the [C II], [N II]122, [O I]63, [O I]145, and [O III] lines, respectively.

In Figure 3.7(a) we show the  $[\text{C II}]/[\text{O I}]_{63}$  ratio versus the  $([\text{C II}]+[\text{O I}]_{63})/F_{\text{TIR}}$  ratio for M51 overlaid on the parameter space defined by lines of constant  $\log(n/\text{cm}^{-3})$  (dotted lines) and  $\log G_0$  (solid lines) adapted from plots in Kaufman et al. (1999). The authors of that paper note that for extragalactic sources it is recommended that the observed total infrared flux be reduced by a factor of two to account for the (optically thin) infrared continuum flux coming from both the front and back sides of the cloud, whereas the model assumes that emission is only coming from the front side of the cloud, just as the fine-structure lines do. Here we have applied this correction to our observed total infrared flux in order to compare it properly with the PDR model. However, in this plot we have not yet corrected for the fraction of  $[\text{C II}]$  emission arising from ionized gas (see Section 3.3.4 for details). We also note that the  $F_{\text{TIR}}$  we use for our comparison to the Kaufman et al. (1999) model is equivalent to their bolometric far-infrared flux.

With the exception of the nucleus, all of the data points tend to cluster around one locus and approximately one-third of the pixels fall outside of the parameter space covered by the models. The  $[\text{C II}]/[\text{O I}]_{63}$  versus  $([\text{C II}]+[\text{O I}]_{63})/F_{\text{TIR}}$  parameter space actually provides two possible model solutions. One is a low- $G_0$ , high- $n$  regime, and the other is a regime with more moderate values for both parameters. We do not display the low- $G_0$ , high- $n$  solutions as we can eliminate these solutions by considering the number of clouds emitting within our beam. When we compare the model-predicted  $[\text{C II}]$  emission based on the values of  $G_0$  and  $n$  to our observed  $[\text{C II}]$  emission, we find that we would require a filling factor (i.e., the number of PDRs) of upward of  $10^3$ , which is an unreasonably large number of clouds along the line of sight. This is the same reasoning used by Kramer et al. (2005) to eliminate the low- $G_0$ , high- $n$  solution. Thus, for the remaining discussion we consider only the moderate  $n$  and  $G_0$  solutions.

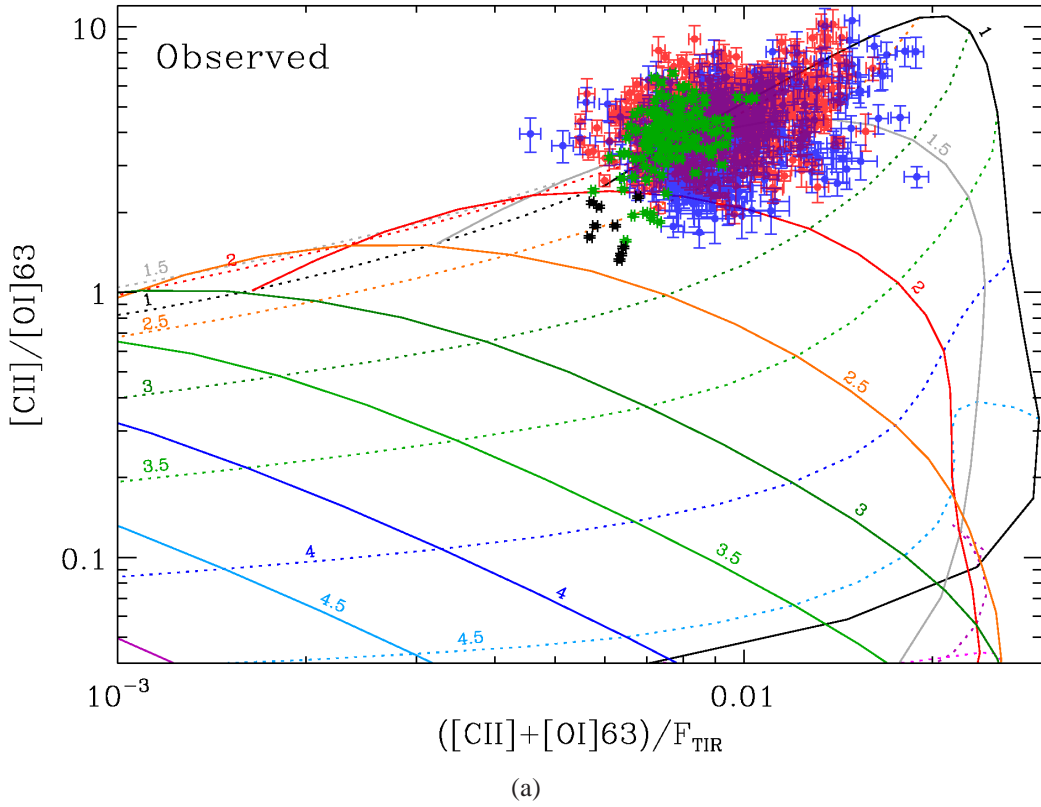
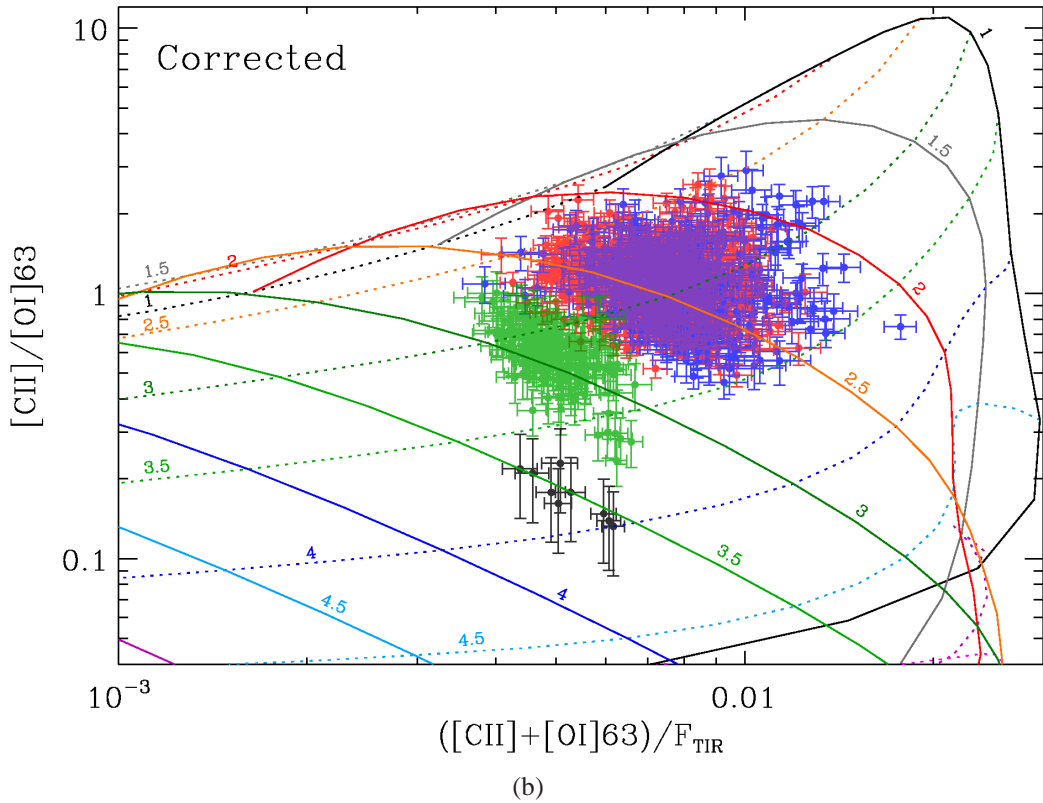


Figure 3.7: Our observed data are overlaid on the PDR model grid of lines of constant  $\log(n/\text{cm}^{-3})$  (dotted lines) and  $\log G_0$  (solid lines). One data point represents one pixel. The pixels from the nucleus, center, arm, and interarm regions are shown in black, green, red, and blue, respectively. (a)  $[\text{C II}]/[\text{O I}]63$  vs.  $([\text{C II}]+[\text{O I}]63)/F_{\text{TIR}}$  prior to removing the fraction of  $[\text{C II}]$  emission from ionized gas. (b)  $[\text{C II}]/[\text{O I}]63$  vs.  $([\text{C II}]+[\text{O I}]63)/F_{\text{TIR}}$  with the  $[\text{C II}]$  emission corrected to remove the fraction originating in ionized gas, and the  $[\text{O I}]63$  emission corrected for an ensemble of clouds (see text).

Figure 3.7: *continued*

### 3.4.1 Adjustments to the [C II] and [O I]63 Lines

A proper comparison to the PDR model of Kaufman et al. (1999) requires us to make two adjustments. The first is to remove the fraction of [C II] emission from ionized gas, as the model only applies to [C II] emission from PDRs. We use the results from Section 3.3.4.1 to correct our [C II] map.

The second correction is applied to the [O I]63 map. The Kaufman et al. (1999) model is a plane-parallel slab that only experiences an incident radiation field on one side, which is the same side from which we observe emission from the far-infrared cooling lines. In the case of M51, there are many clouds within a given PACS beam, and the irradiated side of an individual cloud is not always oriented such that it is facing us. Kaufman et al. (1999) caution that the velocity

dispersion for such an ensemble of clouds, combined with the assumption that the [O I]63 line will become optically thick much faster than either the [C II] line or the total infrared flux, means we observe only [O I]63 flux emitted from clouds with their front (lit) sides facing toward us, but we will observe [C II] and total infrared flux from all clouds. Thus, we only see about half of the total [O I]63 emission from all PDRs within our beam, and as a result we multiply the observed [O I]63 emission by a factor of two for comparison with the PDR model.

The resulting parameter space after the [C II] and [O I]63 results have been corrected is shown in Figure 3.7(b), and the values for  $n$  and  $G_0$  are presented in Table 3.7. Comparing the two panels of Figure 3.7, we can see that after applying the appropriate corrections to the [C II] and [O I]63 emission there is a general shift of pixels to lower values of  $([C\,II]+[O\,I]63)/F_{TIR}$ . In addition, pixels from the center and nuclear regions have decreased more in [C II]/[O I]63, as expected. Looking at Table 3.7, we see an increase in  $n$  by approximately an order of magnitude for all four regions after we apply our corrections. Likewise,  $\log G_0$  increases by  $\sim 1.5$ .

We use our derived values for  $n$  and  $G_0$  to determine the range in the surface temperature of the gas using Figure 1 from Kaufman et al. (1999). The temperatures for the uncorrected [C II] and [O I]63 observations, as well as for the full corrected case, are given in Table 3.7. In general, the cloud surface temperatures increase after the corrections are applied, while there is a decrease in temperature from the central region to the interarm region.

### 3.4.2 Possible Contamination from the Seyfert Nucleus

The [O I]63 emission peaks in the nucleus of M51, and as a result [C II]/[O I]63 is lower in the center than in the rest of the galaxy. In addition, the [O III] line is

Table 3.7. Properties of the Gas Derived from the PDR Model

Case	Region	$\log(n/\text{cm}^{-3})$	$\log G_0$	$T (\text{K})$
Uncorrected <sup>a</sup>	Nucleus	2.25–2.75	2.0–2.5	170–320
	Center	1.5–2.75	1.0–2.5	70–1070
	Arms	1.5–3.0	1.0–2.25	60–820
	Interarm	1.5–3.25	0.75–2.25	50–820
Corrected <sup>b</sup>	Nucleus	3.5–4.25	3.25–4.0	240–475
	Center	2.5–4.0	2.5–3.5	170–680
	Arms	2.0–3.75	1.75–3.0	100–760
	Interarm	2.25–3.75	1.5–3.0	80–550

<sup>a</sup>The uncorrected case includes all of the observed [C II] emission.

<sup>b</sup>The corrected case includes only [C II] emission from neutral gas, and the [O I]63 has been increased by a factor of two as described in Section 3.4.1.

also brightest in the nucleus and center regions, thus indicating higher densities and warmer temperatures in the center of the galaxy. This is consistent with the results of our PDR modeling, but it is also possible that some of the [O I]63 emission from the nucleus is not arising from starlight but rather from shock heating. Once the temperature of the gas behind a shock front has cooled down to below 5000 K, the [O I]63 line dominates the cooling for densities below  $10^5 \text{ cm}^{-3}$  (Hollenbach & McKee, 1989). If indeed some of the [O I]63 emission did arise from shocks rather than stellar radiation in PDRs, then this correction would mean that the [C II]/[O I]63 ratio attributable to PDRs would increase in the center of the galaxy. Thus, the data point(s) in Figure 3.7 would shift upward and to the left in the parameter space, thus decreasing the gas density, and possibly the value of  $G_0$  as well, although quantifying this effect would be difficult. As a result, the gradient we observe in density and radiation field due to PDRs would become less prominent. We also note here

that some of the total infrared flux may originate in non-PDRs such as HII regions. Reducing this flux would move our data points to the right in Figure 3.7.

### 3.4.3 Implications of PDR Model Results

The range of densities, temperatures, and FUV radiation field strengths presented in Table 3.7 agree with the range of temperatures that we obtain for the [O I]63/[O I]145 line ratio if the [O I]63 line is optically thick ( $T \gtrsim 200$  K). In calculating these results, we have assumed that the corrections we applied to our observations of the fine-structure lines (i.e., removing the [C II] emission originating from diffuse ionized gas and accounting for [O I]63 emission escaping away from our line of sight) and the total infrared flux (reducing the total observed flux by a factor of two to remove emission originating from the back side of or even beyond the cloud) are correct for comparing our observations to the PDR model. However, it is possible that some of the remaining  $F_{\text{TIR}}$  emission originates from regions other than PDRs (such as HII regions or the diffuse ISM), meaning less than half of the total observed flux comes from PDRs. In such a case, the data points in the “Corrected” panel of Figure 3.7 would shift to the right, thus resulting in lower values of  $G_0$  and higher densities. Looking at this figure, we see that we can only reduce the fraction of  $F_{\text{TIR}}$  originating in PDRs to approximately 1/8 of the total observed infrared flux before our data would no longer be consistent with the PDR model. Thus, our data and analysis are consistent with at least 12% and at most 50% of  $F_{\text{TIR}}$  arising from PDRs in M51.

Our values of  $n$  and  $G_0$  are in good agreement with previous extragalactic surveys. Furthermore, our results agree with resolved studies of individual galaxies. However, none of these studies show a decreasing trend with radius such as we show

Table 3.8. Properties of the Gas from the PDR Model and Mean Line Ratios

Region	Average <sup>a</sup> ([C II] + [O I](63 $\mu$ m))/ $F_{\text{TIR}}$	Average <sup>a</sup> [C II]/[O I](63 $\mu$ m)	$\log(n/\text{cm}^{-3})$	$\log G_0$
Nucleus	$(5.3 \pm 0.2) \times 10^{-3}$	$0.18 \pm 0.01$	3.75–4.0	3.25–3.75
Center	$(5.01 \pm 0.05) \times 10^{-3}$	$0.60 \pm 0.01$	3.0–3.25	2.75–3.0
Arms	$(7.35 \pm 0.06) \times 10^{-3}$	$1.18 \pm 0.01$	2.75–3.0	2.25–2.5
Interarm	$(8.10 \pm 0.09) \times 10^{-3}$	$1.14 \pm 0.02$	2.75–3.0	2.25–2.5

<sup>a</sup>Uncertainties are the standard error for the means. Calibration uncertainties are not included.

here, not only because of resolution constraints, but also because most previous work has not looked at variations with region within an individual galaxy. Kramer et al. (2005) searched within the center of M51, as well as two positions in the spiral arms with *ISO*; however, they were unable to resolve any differences between the three locations.

We see that the arm and interarm regions have approximately the same range of  $G_0$  and  $n$  despite lower star formation rate surface densities in the interarm region. This may indicate that molecular clouds and star formation are similar in the arm and interarm regions, but there are just fewer clouds per unit area in the interarm regions. To confirm this result, we have calculated the mean values of  $[\text{C II}]/[\text{O I}]63$  and  $([\text{C II}]+[\text{O I}]63)/F_{\text{TIR}}$  for each region and compared them to the PDR model. The results are summarized in Table 3.8. We also compare these results with surveys and individual galaxies in Table 3.9.

Finally, we compare our values for  $G_0$  with those determined using other approaches. First, assuming that all of our observed infrared flux has been converted from the impeded FUV flux by dust grains, we can compare the inferred values of  $G_0$  from the PDR model to the observed  $F_{\text{TIR}}$  in M51. To convert the observed

Table 3.9. Comparison of the PDR Characteristics Measured in M51 to Previous Studies

Paper	Source(s)	$\log(n/\text{cm}^{-3})$	$\log G_0$
This work	Nucleus	3.75–4.0	3.25–3.75
...	Center	3.0–3.25	2.75–3.0
...	Arms	2.75–3.0	2.25–2.5
...	Interarm	2.75–3.0	2.25–2.5
(1)	Normal galaxies	2.0–4.0	2.0–4.0
(2)	AGN, starbursts, normal	2.0–4.5	2.0–4.5
(3)	NGC 5713	4.2	2.8
(4)	NGC 4214	3.3–3.5	2.9–3.0
(5)	NGC 6946, NGC 1313	2.0–4.0	2.0–4.0
(6)	M83, M51	2.0–4.25	2.5–5.0
(7)	NGC 1097, NGC 4559	2.5–3.0	1.7–3.0
(8)	M33 (BCLMP 302)	2.5	1.5

References. — (1) Negishi et al. (2001); (2) Malhotra et al. (2001); (3) Lord et al. (1996); (4) Cormier et al. (2010); (5) Contursi et al. (2002); (6) Kramer et al. (2005); (7) Croxall et al. (2012); (8) Mookerjea et al. (2011).

integrated intensity of the TIR continuum we follow Kramer et al. (2005) and calculate  $G_0^{\text{obs}}$  as  $4\pi I_{\text{TIR}}^{\text{slab}}/2(1.6 \times 10^{-3} \text{ erg cm}^{-2} \text{ s}^{-1})$ , where  $I_{\text{TIR}}^{\text{slab}}$  is the observed total integrated intensity reduced by a factor of two, to consider only emission from the front side of the cloud, as described above. We find mean values for  $G_0^{\text{obs}}$  of 120, 100, 35, and 15 for the nucleus, center, arm, and interarm regions, respectively, in fairly good agreement with those determined by Kramer et al. (2005), who found values of roughly 76, 20, and 15 for the nucleus and two locations in the spiral arms of M51. The ratio of the observed radiation field to that from the PDR model,  $G_0^{\text{obs}}/G_0$ , gives us a filling factor for the clouds within each beam. We find filling factors of roughly 2%–7%, 10%–20%, 10%–20%, and 4%–8% for the nucleus,

center, arm, and interarm regions, respectively. The lower filling factor in the inter-arm region is consistent with our theory that there are fewer clouds in this region than in the spiral arms.

Next, we compare the model-predicted values of  $G_0$  to the value of the FUV field determined using dust SED modeling by Mentuch Cooper et al. (2012). They model the SED using the model of Draine & Li (2007), which parameterizes the ISRF with  $U$ , a scaling factor of the average Milky Way ISRF spectrum,  $U_{\text{MW}}$  from Mathis et al. (1983). We note here that the conversion between  $U$  and  $G_0$  is  $U = 0.88G_0$  (Draine et al., 2007). The ambient ISRF is represented in the dust SED model by  $U_{\text{min}}$ . In addition, the model has a “PDR” component that represents a stronger radiation field due to massive stars. This component comprises a sum of intensities with  $U$  scaling factors ranging between  $U_{\text{min}}$  and  $10^6U_{\text{MW}}$ . Mentuch Cooper et al. (2012) find that the typical ISRF in M51 is  $\sim$ 5 to 10 times that of the average value in the Milky Way, and their analysis covers the central region of the galaxy where we have mapped our fine-structure lines. They also determined that the PDR component contributes at most about 2% of the total radiation field within the same region.

Ideally, we would make a direct comparison between  $G_0$  measured in this work and the total strength of the radiation field measured within the PDR component as measured by the dust SED model. However, this value was not reported by Mentuch Cooper et al. (2012). But we do point out that the dust SED modeling suggests that only 2% of the dust content is exposed to the strong PDR component, whereas we find that at least 12% of the total dust continuum emission originates in PDRs. This difference may arise due to the different concept of a PDR in each model. The Kaufman et al. (1999) picture adopts a PDR as any region within the ISM where FUV photons have a significant effect on the chemistry in that region,

which can include regions with weak (i.e., ambient) values of  $G_0$  (Tielens & Hollenbach, 1985). On the other hand, the dust SED model of Draine & Li (2007) assumes that the PDR component is exposed to a radiation field above the ambient field, and thus may overlook some PDRs as defined by the Kaufman et al. (1999) model. Our models produce in some sense an average measure of  $G_0$  over all regions within a single PACS beam (including regions with both low and high FUV radiation field strengths), and so perhaps it is not surprising that our measured values of  $G_0$  are larger than the value of  $U_{\min}$ .

### 3.5 Conclusions

We present new *Herschel* PACS and SPIRE observations of the grand design spiral galaxy M51 of the important fine-structure lines [C II](158  $\mu\text{m}$ ), [N II](122 and 205  $\mu\text{m}$ ), [O I](63  $\mu\text{m}$ ), [O I](145  $\mu\text{m}$ ), and [O III](88  $\mu\text{m}$ ). We measure several diagnostic ratios, including  $[\text{C II}]/F_{\text{TIR}}$ ,  $([\text{C II}]+[\text{O I}]63)/F_{\text{TIR}}$ ,  $[\text{C II}]/[\text{O I}]63$ , and  $[\text{O I}]145/[\text{O I}]63$ . We find a  $[\text{C II}]/F_{\text{TIR}}$  ratio of  $4 \times 10^{-3}$  on average, consistent with previous results for M51, as well as other nearby galaxies in various surveys and resolved studies. Furthermore, we see a slight deficit in this ratio in the central region of M51 when compared to the surrounding environment, and the  $([\text{C II}]+[\text{O I}]63)/F_{\text{TIR}}$  ratio suggests reduced heating efficiency in these central regions. We also find that the [N II]122/[N II]205 ratio indicates that diffuse ionized gas dominates these emission lines.

We divide the disk of M51 into four regions to conduct a pixel-by-pixel analysis in each region to investigate possible variations within the properties of the interstellar gas. We determine that the fraction of ionized gas contributing to the total observed [C II] emission is approximately 80% in the nucleus of the galaxy

and decreases to 50% in the arm and interarm regions. The [O I]145/[O I]63 ratio indicates that the [O I]63 line is optically thick in the inner region of M51. We correct for both the [O I] optical depth and the ionized contribution to the [C II] emission in our analysis.

We compare our observed line ratios in each region to the PDR model of Kaufman et al. (1999) and find that the incident FUV fluxes are  $G_0 \sim 10^{3.25}-10^{4.0}$ ,  $10^{2.25}-10^{3.75}$ ,  $10^{1.5}-10^{3.0}$ , and  $10^{1.5}-10^{4.0}$  for the nucleus, center, arm, and interarm regions, respectively. The density of hydrogen nuclei,  $n$ , is  $10^{3.5}-10^{4.25}$ ,  $10^{2.5}-10^{4.0}$ ,  $10^{2.0}-10^{3.75}$ , and  $10^{2.25}-10^{4.25} \text{ cm}^{-3}$  for the nucleus, center, arm, and interarm regions, respectively. These derived values are similar to those previously seen in M51 on larger scales, as well as global results of numerous galaxies in surveys such as Malhotra et al. (2001).

We show for the first time that both  $G_0$  and  $n$  decrease with increasing radius within M51. Furthermore, we find that the arm and interarm regions, despite having different star formation rate surface densities and physical processes, show approximately the same incident FUV field and density within their molecular clouds. Finally, our data and analysis suggest that PDRs contribute between 12% and 50% of the total infrared emission in M51.

## Acknowledgments

T.J.P. would like to extend her thanks to the anonymous referee for his/her constructive comments, which have contributed to strengthening our work. The research of C.D.W. is supported by the Natural Sciences and Engineering Research Council of Canada and the Canadian Space Agency. The research of V.L. is supported by a CEA/Marie Curie Eurotalents fellowship. PACS has been developed by a con-

sortium of institutes led by MPE (Germany) and including UVIE (Austria); KU Leuven, CSL, IMEC (Belgium); CEA, LAM (France); MPIA (Germany); INAF-IFSI/OAA/OAP/OAT, LENS, SISSA (Italy); IAC (Spain). This development has been supported by the funding agencies BMVIT (Austria), ESA-PRODEX (Belgium), CEA/CNES (France), DLR (Germany), ASI/INAF (Italy), and CICYT/MCYT (Spain). SPIRE has been developed by a consortium of institutes led by Cardiff University (UK) and including Univ. Lethbridge (Canada); NAOC (China); CEA, LAM (France); IFSI, Univ. Padua (Italy); IAC (Spain); Stockholm Observatory (Sweden); Imperial College London, RAL, UCL-MSSL, UKATC, Univ. Sussex (UK); and Caltech, JPL, NHSC, Univ. Colorado (USA). This development has been supported by national funding agencies: CSA (Canada); NAOC (China); CEA, CNES, CNRS (France); ASI (Italy); MCINN (Spain); SNSB (Sweden); STFC and UKSA (UK); and NASA (USA). HIPE is a joint development by the Herschel Science Ground Segment Consortium, consisting of ESA, the NASA Herschel Science Center, and the HIFI, PACS and SPIRE consortia. The James Clerk Maxwell Telescope is operated by The Joint Astronomy Centre on behalf of the Science and Technology Facilities Council of the United Kingdom, the Netherlands Organisation for Scientific Research, and the National Research Council of Canada. This research has made use of the NASA/IPAC Extragalactic Database (NED), which is operated by the Jet Propulsion Laboratory, California Institute of Technology, under contract with the National Aeronautics and Space Administration. This research made use of APLpy, an open-source plotting package for Python hosted at <http://aplpy.github.com>.

# Bibliography

- Abel, N. P., Dudley, C., Fischer, J., Satyapal, S., & van Hoof, P. A. M. 2009, ApJ, 701, 1147
- Aniano, G., Draine, B. T., Gordon, K. D., & Sandstrom, K. 2011, PASP, 123, 1218
- Asplund, M., Grevesse, N., Sauval, A. J., & Scott, P. 2009, ARA&A, 47, 481
- Beirão, P., Armus, L., Appleton, P. N., et al. 2010, A&A, 518, L60
- Beirão, P., Armus, L., Helou, G., et al. 2012, ApJ, 751, 144
- Bendo, G. J., Galliano, F., & Madden, S. C. 2012, MNRAS, 423, 197
- Bennett, C. L., Fixsen, D. J., Hinshaw, G., et al. 1994, ApJ, 434, 587
- Blum, R. D., & Pradhan, A. K. 1992, ApJS, 80, 425
- Braine, J., Gratier, P., Kramer, C., et al. 2012, A&A, 544, A55
- Brauher, J. R., Dale, D. A., & Helou, G. 2008, ApJS, 178, 280
- Calzetti, D., Kennicutt, Jr., R. C., Bianchi, L., et al. 2005, ApJ, 633, 871
- Contursi, A., Kaufman, M. J., Helou, G., et al. 2002, AJ, 124, 751

Contursi, A., Poglitsch, A., Grácia Carpio, J., et al. 2013, A&A, 549, A118

Cormier, D., Madden, S. C., Hony, S., et al. 2010, A&A, 518, L57

Cormier, D., Lebouteiller, V., Madden, S. C., et al. 2012, A&A, 548, A20

Crawford, M. K., Genzel, R., Townes, C. H., & Watson, D. M. 1985, ApJ, 291, 755

Croxall, K. V., Smith, J. D., Wolfire, M. G., et al. 2012, ApJ, 747, 81

Dale, D. A., & Helou, G. 2002, ApJ, 576, 159

Draine, B. T., & Li, A. 2007, ApJ, 657, 810

Draine, B. T., et al. 2007, ApJ, 663, 866

Ferkinhoff, C., Brisbin, D., Nikola, T., et al. 2011, ApJ, 740, L29

Galavis, M. E., Mendoza, C., & Zeippen, C. J. 1997, A&AS, 123, 159

—. 1998, A&AS, 131, 499

Garnett, D. R., Edmunds, M. G., Henry, R. B. C., Pagel, B. E. J., & Skillman, E. D. 2004, AJ, 128, 2772

Garnett, D. R., Shields, G. A., Peimbert, M., et al. 1999, ApJ, 513, 168

Graciá-Carpio, J., García-Burillo, S., Planesas, P., Fuente, A., & Usero, A. 2008, A&A, 479, 703

Graciá-Carpio, J., Sturm, E., Hailey-Dunsheath, S., et al. 2011, ApJ, 728, L7

Griffin, M. J., et al. 2010, A&A, 518, L3

Groves, B. A., Dopita, M. A., & Sutherland, R. S. 2004, ApJS, 153, 9

- Habing, H. J. 1968, Bull. Astron. Inst. Netherlands, 19, 421
- Ho, L. C., Filippenko, A. V., & Sargent, W. L. W. 1997, ApJS, 112, 315
- Hollenbach, D., & McKee, C. F. 1989, ApJ, 342, 306
- Hollenbach, D. J., Takahashi, T., & Tielens, A. G. G. M. 1991, ApJ, 377, 192
- Hudson, C. E., & Bell, K. L. 2004, MNRAS, 348, 1275
- Kaufman, M. J., Wolfire, M. G., & Hollenbach, D. J. 2006, ApJ, 644, 283
- Kaufman, M. J., Wolfire, M. G., Hollenbach, D. J., & Luhman, M. L. 1999, ApJ, 527, 795
- Kennicutt, Jr., R. C., Armus, L., Bendo, G., et al. 2003, PASP, 115, 928
- Kramer, C., Mookerjea, B., Bayet, E., et al. 2005, A&A, 441, 961
- Kramer, C., Abreu-Vicente, J., García-Burillo, S., et al. 2013, A&A, 553, A114
- Le Petit, F., Nehmé, C., Le Bourlot, J., & Roueff, E. 2006, ApJS, 164, 506
- Lebouteiller, V., Cormier, D., Madden, S. C., et al. 2012, A&A, 548, A91
- Liseau, R., Justtanont, K., & Tielens, A. G. G. M. 2006, A&A, 446, 561
- Lord, S. D., Malhotra, S., Lim, T., et al. 1996, A&A, 315, L117
- Luhman, M. L., Jaffe, D. T., Sternberg, A., Herrmann, F., & Poglitsch, A. 1997, ApJ, 482, 298
- Luhman, M. L., Satyapal, S., Fischer, J., et al. 2003, ApJ, 594, 758
- . 1998, ApJ, 504, L11

Malhotra, S., Helou, G., Stacey, G., et al. 1997, ApJ, 491, L27

Malhotra, S., Kaufman, M. J., Hollenbach, D., et al. 2001, ApJ, 561, 766

Marble, A. R., Engelbracht, C. W., van Zee, L., et al. 2010, ApJ, 715, 506

Mathis, J. S., Mezger, P. G., & Panagia, N. 1983, A&A, 128, 212

Mentuch Cooper, E., Wilson, C. D., Foyle, K., et al. 2012, ApJ, 755, 165

Mookerjea, B., Kramer, C., Buchbender, C., et al. 2011, A&A, 532, A152

Moustakas, J., Kennicutt, Jr., R. C., Tremonti, C. A., et al. 2010, ApJS, 190, 233

Negishi, T., Onaka, T., Chan, K.-W., & Roellig, T. L. 2001, A&A, 375, 566

Nikola, T., Geis, N., Herrmann, F., et al. 2001, ApJ, 561, 203

Oberst, T. E., Parshley, S. C., Stacey, G. J., et al. 2006, ApJ, 652, L125

Ott, S. 2010, in Astronomical Society of the Pacific Conference Series, Vol. 434, Astronomical Data Analysis Software and Systems XIX, ed. Y. Mizumoto, K.-I. Morita, & M. Ohishi, 139—

Pilbratt, G. L., et al. 2010, A&A, 518, L1

Poglitsch, A., et al. 2010, A&A, 518, L2

Pound, M. W., & Wolfire, M. G. 2008, in Astronomical Society of the Pacific Conference Series, Vol. 394, Astronomical Data Analysis Software and Systems XVII, ed. R. W. Argyle, P. S. Bunclark, & J. R. Lewis, 654

Röllig, M., Ossenkopf, V., Jeyakumar, S., Stutzki, J., & Sternberg, A. 2006, A&A, 451, 917

Röllig, M., Abel, N. P., Bell, T., et al. 2007, A&A, 467, 187

Rubin, R. H. 1985, ApJS, 57, 349

Rubin, R. H., Simpson, J. P., Lord, S. D., et al. 1994, ApJ, 420, 772

Satyapal, S., Sambruna, R. M., & Dudik, R. P. 2004, A&A, 414, 825

Savage, B. D., & Sembach, K. R. 1996, ARA&A, 34, 279

Schinnerer, E., Meidt, S. E., Pety, J., et al. 2013, ArXiv e-prints

Schirm, M. R. P., Wilson, C. D., Parkin, T. J., et al. 2013, ApJ, submitted

Smith, J. D. T., Draine, B. T., Dale, D. A., et al. 2007, ApJ, 656, 770

Spinoglio, L., Dasyra, K. M., Franceschini, A., et al. 2012, ApJ, 745, 171

Stacey, G. J., Jaffe, D. T., Geis, N., et al. 1993, ApJ, 404, 219

Stacey, G. J., Viscuso, P. J., Fuller, C. E., & Kurtz, N. T. 1985, ApJ, 289, 803

Sternberg, A., & Dalgarno, A. 1989, ApJ, 338, 197

—. 1995, ApJS, 99, 565

Störzer, H., Zielinsky, M., Stutzki, J., & Sternberg, A. 2000, A&A, 358, 682

Swinyard, B. M., Ade, P., Baluteau, J.-P., et al. 2010, A&A, 518, L4

Tielens, A. G. G. M., & Hollenbach, D. 1985, ApJ, 291, 722

Tikhonov, N. A., Galazutdinova, O. A., & Tikhonov, E. N. 2009, Astronomy Letters, 35, 599

Vacca, W. D., Garmany, C. D., & Shull, J. M. 1996, ApJ, 460, 914

van Dishoeck, E. F., & Black, J. H. 1986, ApJS, 62, 109

—. 1988, ApJ, 334, 771

Wolfire, M. G., Tielens, A. G. G. M., & Hollenbach, D. 1990, ApJ, 358, 116

Wright, E. L., Mather, J. C., Bennett, C. L., et al. 1991, ApJ, 381, 200

Zubko, V., Dwek, E., & Arendt, R. G. 2004, ApJS, 152, 211

Chapter **4**

**Searching for radial variations in  
the physical characteristics of  
the gas in the disk of  
Centaurus A using the *Herschel*  
*Space Observatory***

T. J. Parkin, C. D. Wilson, M. R. P. Schirm, M. Baes, M. Boquien, A. Boselli, D. Cormier, M. Galametz, O. Ł. Karczewski, V. Lebouteiller, S. Madden, H. Roussel, M. W. L. Smith, and L. Spinoglio

*This article has been prepared for submission to The Astrophysical Journal.*

## 4.1 Introduction

A comprehensive understanding of the interstellar medium (ISM) of a galaxy requires a multiwavelength probe of both the gas and dust components, as well as knowledge of the morphological and dynamical features of the galaxy on a global scale. Galaxies that are nearby provide excellent laboratories to study the properties of the ISM because the current capabilities of infrared and submillimeter observatories allow us to study them on resolved scales, down to sub-kiloparsec (kpc) scales in some cases. Centaurus A (Cen A; NGC 5128) is an example of one such galaxy in which we can investigate the gas and dust components at scales of a few hundred parsecs, as it is only  $3.8 \pm 0.1$  Mpc away (Harris et al., 2010).

Cen A ( $13^{\text{h}}25^{\text{m}}27.6^{\text{s}}$ ,  $-43^{\circ}01'09''$ ) has a unique morphology as it is a giant elliptical that appears to have swallowed a smaller disk galaxy at some point during its past (e.g. Tubbs, 1980). The disk provides a prominent dust lane through the center, and shows a strong warp, giving it an ‘S’ like shape at infrared wavelengths (Leeuw et al., 2002; Quillen et al., 2006; Weiß et al., 2008; Parkin et al., 2012). Cen A is the closest galaxy with an active galactic nucleus (AGN) and associated radio jets extending approximately  $4^{\circ}$  in either direction (e.g. Combi & Romero, 1997; Israel, 1998). It is also rich in gas, both atomic (H I) and molecular (H<sub>2</sub>) hydrogen (Morganti et al., 2008; Struve et al., 2010) as well as carbon monoxide (CO) as observed in various rotational transitions (Phillips et al., 1987; Eckart et al., 1990; Quillen et al., 1992; Rydbeck et al., 1993; Parkin et al., 2012). For a detailed summary of the physical properties of the galaxy see Israel (1998) and Morganti (2010).

Recently, Parkin et al. (2012) presented new photometric observations at 70, 160, 250, 350 and 500  $\mu\text{m}$  using the Photodetector Array Camera and Spectrometer

(PACS; Poglitsch et al., 2010) and the Spectral and Photometric Imaging Receiver (SPIRE; Griffin et al., 2010) on the *Herschel Space Observatory* (Pilbratt et al., 2010). Through dust spectral energy distribution (SED) modelling they determined a radially decreasing trend in dust temperature from about 30 to 20 K, and combined the resulting dust map with a gas map (created with CO( $J = 3 - 2$ ) observations from the James Clerk Maxwell Telescope and an H I map (Struve et al., 2010)) to produce a gas-to-dust mass ratio map. This ratio also shows a radial trend from Galactic values of roughly 100 up to 275 near the center, a result attributed to local effects on the ISM from the AGN. Here, we extend the investigation of the disk of Cen A by combining the *Herschel* PACS photometry with new PACS spectroscopic observations of important atomic fine structure lines to probe the neutral and ionized gas.

Fine-structure lines such as [C II](158  $\mu\text{m}$ ), [N II](122 and 205  $\mu\text{m}$ ), [O I](63 and 145  $\mu\text{m}$ ) and [O III](88  $\mu\text{m}$ ) (hereafter [C II], [N II]<sub>122</sub>, [N II]<sub>205</sub>, [O I]<sub>63</sub>, [O I]<sub>145</sub> and [O III], respectively) play a crucial role in the thermal balance of the gas in the ISM by providing a means of gas cooling via photon emission rather than collisional de-excitation. The [C II] line is a tracer of both neutral and ionized gas as C<sup>+</sup> is produced by far-ultraviolet (FUV) photons with energy greater than 11.26 eV, and it is the dominant coolant of the aforementioned lines with a luminosity of roughly 0.1–1 % that of the far-infrared (FIR) luminosity in typical galaxies (e.g. Stacey et al., 1985, 1993; Malhotra et al., 2001; Graciá-Carpio et al., 2011; Parkin et al., 2013). Atomic oxygen has an ionization potential greater than that of hydrogen (13.6 eV), thus the two [O I] lines trace neutral gas, while the [N II] and [O III] lines trace ionized gas. These lines are predominantly found in photon dominated (photodissociation) regions (PDRs) and H II regions.

A commonly used diagnostic of the heating efficiency of the gas is the

( $[\text{C II}]+[\text{O I}]_{63}/F_{\text{FIR}}$ ) (or sometimes  $[\text{C II}]/F_{\text{FIR}}$ ) line ratio, which represents the relative contributions of the FUV flux to the heating of gas versus dust (Tielens & Hollenbach, 1985). Observations show that as infrared colour increases (thus dust temperature), the heating efficiency decreases because the dust grains and polycyclic aromatic hydrocarbons (PAHs) that provide free electrons for gas heating via the photoelectric effect, have become too positively charged to free more electrons (Malhotra et al., 2001; Brauher et al., 2008; Graciá-Carpio et al., 2011; Croxall et al., 2012; Braine et al., 2012; Lebouteiller et al., 2012; Contursi et al., 2013; Parkin et al., 2013). A similar trend called the “[C II] deficit” was originally observed in ultra-luminous infrared galaxies (ULIRGs), which is a decrease (compared to normal galaxies) in the  $[\text{CII}]/F_{\text{FIR}}$  to as low  $10^{-4}$  (e.g. Luhman et al., 1998, 2003).

To determine physical properties of the gas we need to compare ratios of our observed fine structure lines to those predicted by a PDR model. There are a number of models which explore the characteristics of PDRs such as van Dishoeck & Black (1986, 1988), Sternberg & Dalgarno (1989, 1995), Luhman et al. (1997), Störzer et al. (2000), Le Petit et al. (2006) and Röllig et al. (2006), but one of the most commonly used models was first developed by Tielens & Hollenbach (1985), consisting of a plane-parallel, semi-infinite slab PDR. The gas is characterized by two free parameters, the hydrogen nucleus density,  $n$ , and the strength of the FUV radiation field,  $G_0$ , normalized to the Habing Field,  $1.6 \times 10^{-3}$  erg cm $^{-2}$  s $^{-1}$  (Habing, 1968). This model has now been updated by Wolfire et al. (1990), Hollenbach et al. (1991), and Kaufman et al. (1999, 2006).

Probes of PDRs and cooling lines in Cen A have previously been carried out by Unger et al. (2000) and Negishi et al. (2001) using the Long Wavelength (LWS) spectrometer on the *Infrared Space Observatory*. Unger et al. (2000) ob-

served Cen A at four pointings along the dust lane and found  $G_0 \sim 10^2$  and  $n \sim 10^3 \text{ cm}^{-3}$ . Using the same observations, Negishi et al. (2001) find  $G_0 = 10^{2.7}$  and  $n \sim 10^{3.1} \text{ cm}^{-3}$ . In samples of galaxies such as those of Malhotra et al. (2001) and Negishi et al. (2001), global values for  $G_0$  range from  $10^2$  to  $10^{4.5}$  and  $n$  ranges between  $10^2$  and  $10^{4.5} \text{ cm}^{-3}$ . In this paper, we look at the PDR characteristics of Cen A on more resolved scales (roughly 260 pc at the  $14''$  resolution of the JCMT) in search of radial variations.

The paper is organised as follows. We describe our data processing for the spectroscopic observations in Section 4.2, and discuss general observational results in Section 4.3. In Sections 4.4 and 4.5 we compare our observations to theoretical models and discuss their implications, and summarize this work in Section 4.6.

## 4.2 *Herschel* Observations

### 4.2.1 PACS spectroscopy

The data for the five fine structure lines observed with the PACS instrument were taken on 2011 July 9 using the unchopping grating scan mode. Each observation consists of a set of  $7 \times 1$  footprints extending eastward along an orientation angle of  $115^\circ$  east of north. One footprint covers a field-of-view of  $43''$  per side and the footprints are separated by  $30''$ . The PACS instrument consists of 25 spatial pixels ('spaxel'), thus we obtain 25 individual spectra per footprint.<sup>1</sup> The basic observational details for each line are summarized in Table 4.1, while outlines of our observations are shown overlaid on a map of the total infrared flux (see below for details) in Figure 4.1.

---

<sup>1</sup>PACS Observer's Manual (hereafter PACS OM; HERSCHEL-HSC-DOC-0832, 2011), available from the ESA *Herschel* Science Centre.

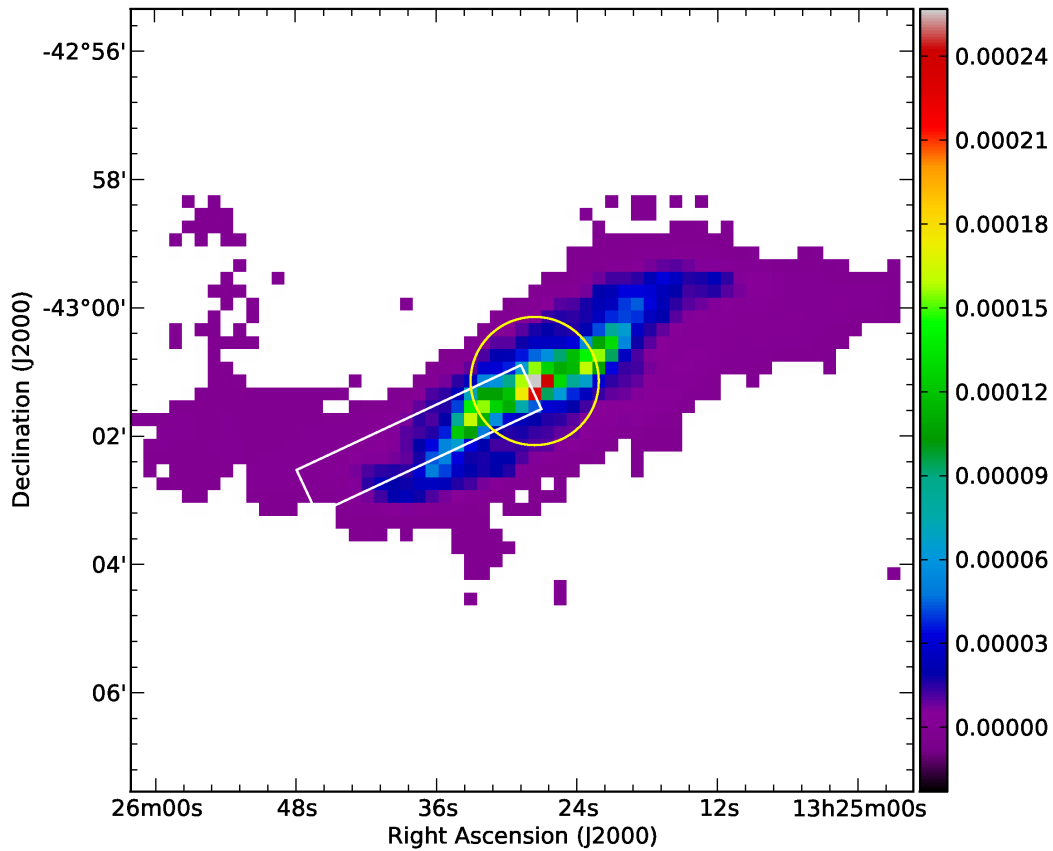


Figure 4.1: The total infrared flux calculated using Equation 4.1 for Cen A. The *Herschel* PACS footprint for our observations is shown as a white rectangle while the yellow circle outlines our SPIRE FTS footprint. Units are in  $\text{W m}^{-2} \text{ sr}^{-1}$ .

From Level 0 to Level 2 the PACS spectroscopic observations are processed with the standard pipeline for unchopped scans using the Herschel Interactive Processing Environment (HIPE; Ott, 2010) version 9.2 with calibration files FM,41. For details of the pipeline see Parkin et al. (2013) or the PACS Data Reduction Guide.<sup>2</sup> Level 1 cubes are exported to PACSman v3.5.2 (Lebouteiller et al., 2012) where each individual spectrum is fit with a second order polynomial and Gaussian function for the baseline and line, respectively. Lastly, we create a map by projecting the rasters onto a common grid with a pixel scale of  $3.133''$ . In Figure 4.2 we

<sup>2</sup>Available for download from the ESA *Herschel* Science Centre. [http://herschel.esac.esa.int/hcss-doc-10.0/index.jsp#pacs-spec:pacs\\_spec](http://herschel.esac.esa.int/hcss-doc-10.0/index.jsp#pacs-spec:pacs_spec)

show the final mosaicked observations for the [C II]<sub>158</sub>, [N II]<sub>122</sub>, [O I]<sub>63</sub>, [O I]<sub>145</sub> and [O III]<sub>88</sub> fine structure lines.

Table 4.1. Basic details of the *Herschel* spectroscopic observations of Centaurus A

Line	Wavelength ( $\mu\text{m}$ )	OBSID	Date of Observation	Map Size ' $\times$ '	FWHM <sup>a</sup> ( $''$ )	Integration Time (s)
[O I]	63.184	1342223819	2011 Jul 9	0.72 $\times$ 4.0	$\sim$ 9.3	1886
[O III]	88.356	1342223817	2011 Jul 9	0.72 $\times$ 4.0	$\sim$ 9.3	3194
[N II]	121.898	1342223818	2011 Jul 9	0.72 $\times$ 4.0	$\sim$ 10	3198
[O I]	145.525	1342223815	2011 Jul 9	0.72 $\times$ 4.0	$\sim$ 11	5840
[C II]	157.741	1342223816	2011 Jul 9	0.72 $\times$ 4.0	$\sim$ 11.5	1886
[N II]	205.178	1342204036	2010 Aug 23	$\sim$ 2' diameter circle	17	17843

<sup>a</sup>Values are from the PACS Observer's Manual and the SPIRE Observers' Manual.

### 4.2.2 SPIRE spectroscopy

The SPIRE Fourier Transform Spectrometer observation of Centaurus A consists of a single pointing with full Nyquist sampling and high spectral resolution. The  $205\ \mu\text{m}$  line comes from observations using the SPIRE short wavelength (SSW) bolometer array, consisting of 37 hexagonally arranged bolometers with a combined total field-of-view of  $2.6'$  (although only bolometers within the central  $\sim 2.0'$  are well calibrated).<sup>3</sup>

We processed the observation using HIPE v11.0 developer's build 2652 and calibration set v10.1 using the standard pipeline (see Parkin et al. (2013) for details), then fit the resulting spectral line in each bolometer with a sinc function. Finally, a map is produced by integrating over each line at a resolution of  $\sim 16''$  and with a  $12''$  pixel scale.

### 4.2.3 Ancillary Data

We also incorporate previously published PACS photometry at  $70$  and  $160\ \mu\text{m}$  (Parkin et al., 2012). These data have been reprocessed using HIPE v9.0 (calibration file set FM,41) and SCANAMORPHOS v21 and were set to a final pixel scale of  $1.4$  and  $2.85''$  for the  $70$  and  $160\ \mu\text{m}$  maps, respectively. From the same paper we also make use of the CO( $J = 3 - 2$ ) observations taken at the JCMT. Lastly, we make use of the *Spitzer* MIPS  $24\ \mu\text{m}$  data, reprocessed as described in (Bendo et al., 2012).

---

<sup>3</sup>Hereafter SPIRE OM. Document HERSCHEL-DOC-0798 version 2.4 (June 2011), is available from the ESA *Herschel* Science Centre.

#### 4.2.4 Final Steps for Analysis

The PACS and SPIRE spectroscopy were convolved to a common resolution matching that of our CO( $J = 3 - 2$ ) observations from the JCMT (14'') using Gaussian kernels. The MIPS 24  $\mu\text{m}$  and PACS 70 and 160  $\mu\text{m}$  maps were convolved to the same resolution using the appropriate kernels from Aniano et al. (2011). All of our maps were resampled onto a pixel scale of 12'', such that each pixel is mostly independent. Lastly, we mask out all detections below  $5\sigma$  in our spectroscopic maps to ensure robust line ratios.

Calibration uncertainties are 4% for the MIPS 24  $\mu\text{m}$  photometry<sup>4</sup>, 5% for the PACS 70 and 160  $\mu\text{m}$  maps (PACS OM). The PACS spectroscopic maps have 30% calibration uncertainties (PACS OM) while the SPIRE FTS map has a 7% calibration uncertainty (SPIRE OM).

### 4.3 Results

#### 4.3.1 Morphological Properties

Figure 4.2 shows our PACS and SPIRE spectroscopic maps at their native resolution and pixel scale. The [C II] emission, tracing both neutral and ionized gas, shows a smooth decrease overall from near the center of the galaxy to the edge of our map. There is a curve in the strongest [C II] emission, which is coincident with the 70  $\mu\text{m}$  emission shown in contours. The peak is at the end of this bend (indicated by the two highest 70  $\mu\text{m}$  contours in black), and is a factor of roughly 100 times higher than the outer part of the map. This peak has also been seen previously in the *Herschel* PACS 160  $\mu\text{m}$  band as well as the three SPIRE photometric bands

---

<sup>4</sup>MIPS Instrument Handbook, available at <http://irsa.ipac.caltech.edu/data/SPITZER/docs/mips/mipsinstrumenthandbook/home/>

at 250, 350 and 500  $\mu\text{m}$  and in CO( $J = 3 - 2$ ) emission (Parkin et al., 2012). Furthermore, Quillen et al. (2006) presented *Spitzer* Infrared Array Camera (IRAC) photometry that demonstrate a parallelogram shaped ring, coincident with our [C II] observations. The total flux in our [C II] map is  $(4.268 \pm 0.002(\text{stat}) \pm 1.280(\text{cal})) \times 10^{-14} \text{ W m}^{-2}$ , over an area of approximately 11200 square arcseconds. Our value is in fairly good agreement with Unger et al. (2000), who found a total flux for their center and south-east pointings (those which overlap our observations) of  $3.83 \times 10^{-14} \text{ W m}^{-2}$  covering a total area of 11100 square arcseconds given ISO's  $70''$  beam. Any disagreement likely is due to the fact that our observations are not entirely spatially coincident with theirs.

The [O I]<sub>63</sub> and [O I]<sub>145</sub> maps reveal the distribution of neutral gas, and they too show a curve downward in emission, as seen in the [C II] emission, with the intensity falling off radially away from the center region. The total flux in these lines is  $(1.171 \pm 0.002(\text{stat}) \pm 0.351(\text{cal})) \times 10^{-14} \text{ W m}^{-2}$  and  $(1.006 \pm 0.003(\text{stat}) \pm 0.302(\text{cal})) \times 10^{-15} \text{ W m}^{-2}$  at 63 and 145  $\mu\text{m}$ , respectively. Interestingly, the strongest emission peaks in the innermost region, unlike the [C II] emission, which shows a weaker enhancement at the center compared to the tip of the curve. Peaked central emission in [O I]<sub>63</sub> has also been observed by Parkin et al. (2013) in the nucleus of M51, where it was attributed to shocks produced by the Seyfert 2 nucleus. Cen A has a strong central active galactic nucleus (AGN), thus it is possible we see the same type of behaviour in the center as in M51. This is further supported by the fact that while our [O I]<sub>145</sub> flux is in good agreement with Unger et al. (2000), who found a total flux of approximately  $1.1 \times 10^{-15} \text{ W m}^{-2}$  in their center pointing with ISO, their [O I]<sub>63</sub> flux is  $1.96 \times 10^{-14} \text{ W m}^{-2}$  in the center alone, with another  $5.1 \times 10^{-15} \text{ W m}^{-2}$  in their south-eastern pointing. Thus, a large fraction of the total [O I]<sub>63</sub> flux likely originates in the nucleus, outside the range of our observations.

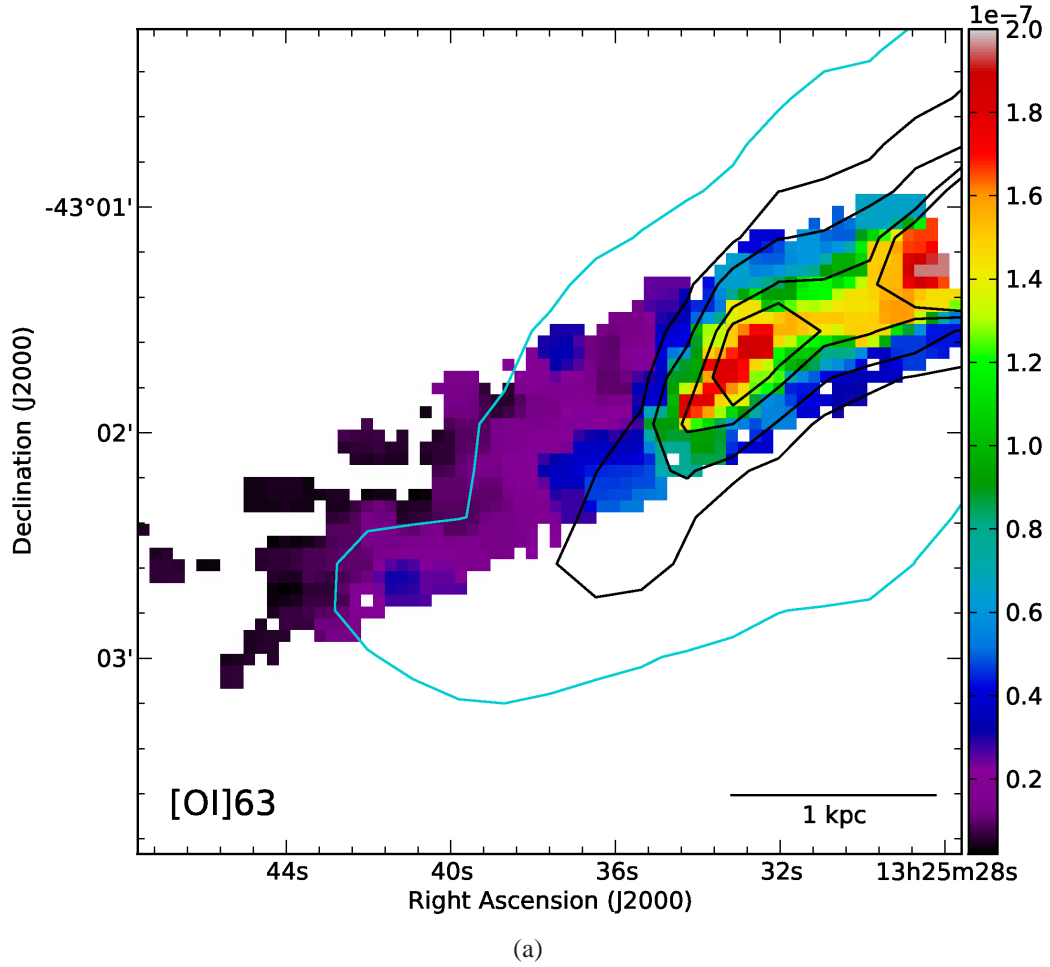
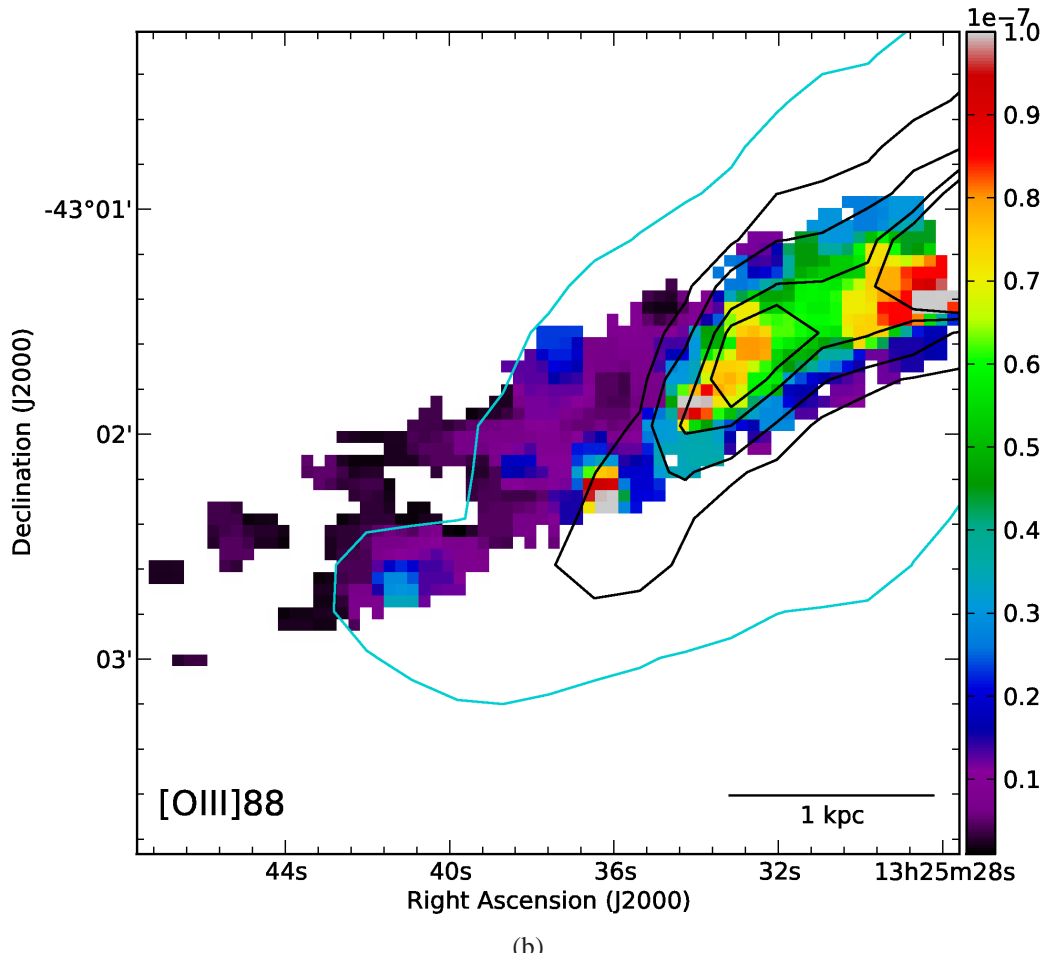
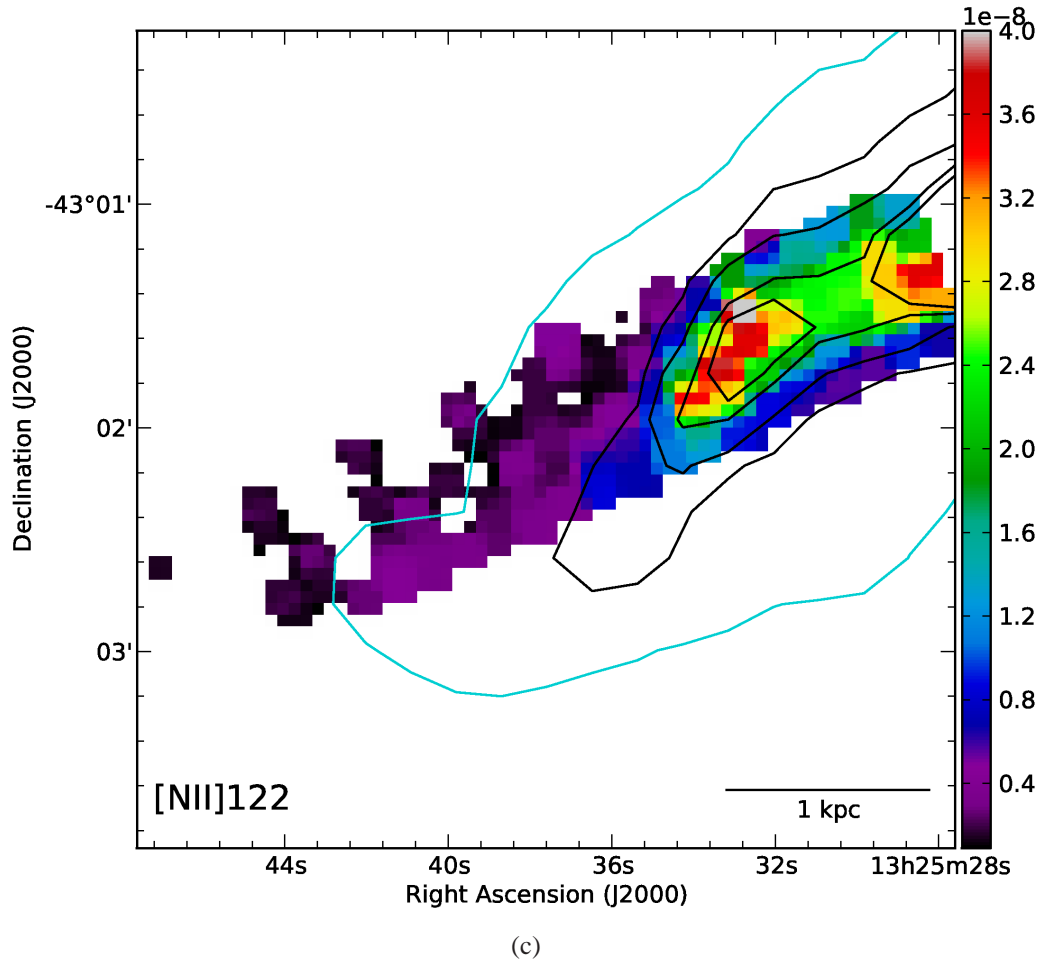


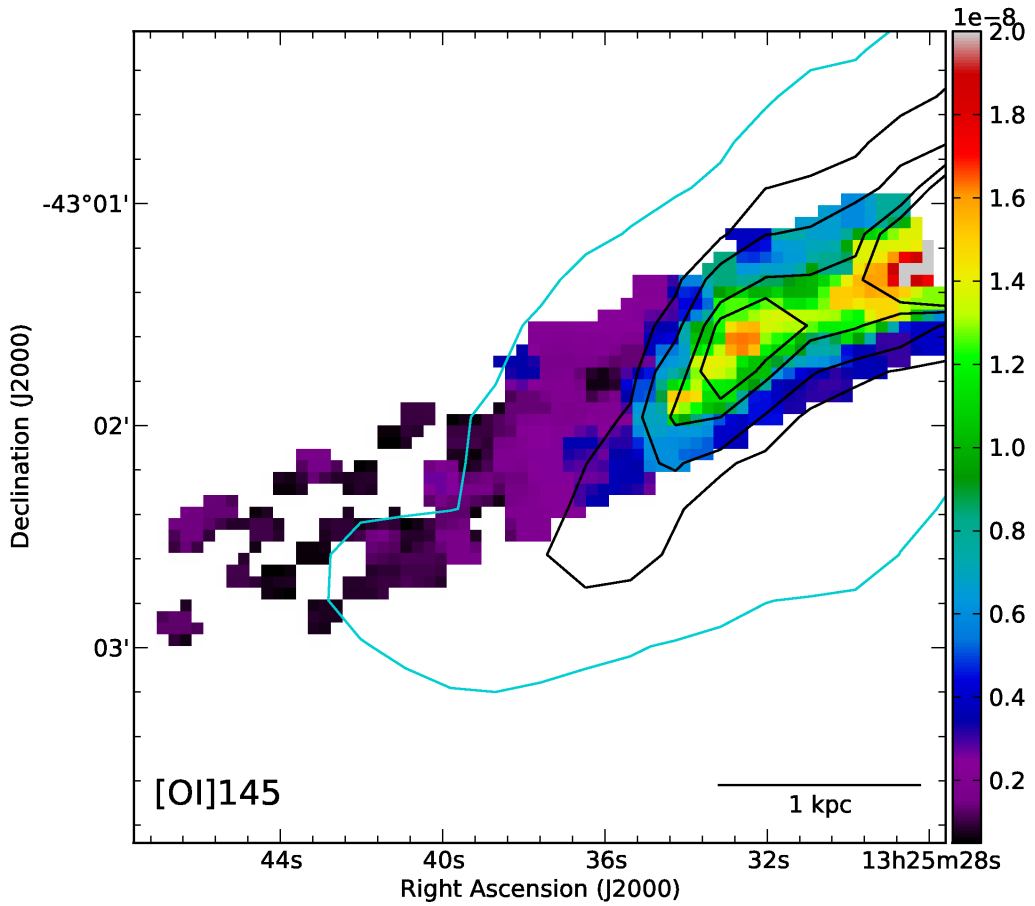
Figure 4.2: The maps of our *Herschel* PACS and SPIRE spectroscopic observations of the far-infrared cooling lines at their native resolution and pixel scale. We have applied a  $3\sigma$  cut to these maps to highlight robust detections. Units in all images are  $\text{W m}^{-2} \text{ sr}^{-1}$ . Contours from the *Herschel* PACS 70  $\mu\text{m}$  photometric map are overlaid on top with the levels corresponding to  $3 \times 10^{-6}$ ,  $1.5 \times 10^{-5}$ ,  $3.0 \times 10^{-5}$ ,  $6.0 \times 10^{-5}$  and  $7.5 \times 10^{-5} \text{ W m}^{-2} \text{ sr}^{-1}$ .

Figure 4.2: *continued*

The  $[\text{N II}]_{122}$ ,  $[\text{N II}]_{205}$  and  $[\text{O III}]$  fine structure lines trace ionized gas. The ionized gas shown by the  $[\text{N II}]_{122}$  and  $[\text{O III}]$  line emission traces the neutral gas and dust emission well in the inner half of the map with sparse detections at greater than a  $3\sigma$  level further out. While there is an enhancement near the center of the galaxy, the peak of the ionized gas as traced by the  $[\text{N II}]_{122}$  emission is at the tip of the curve and is a factor of 2 times greater than the other parts of the inner curve, and an order of magnitude larger than the outer parts of the map. In contrast, the peak emission in  $[\text{O III}]$  is coincident with the peak of the  $[\text{O I}]_{63}$  and

Figure 4.2: *continued*

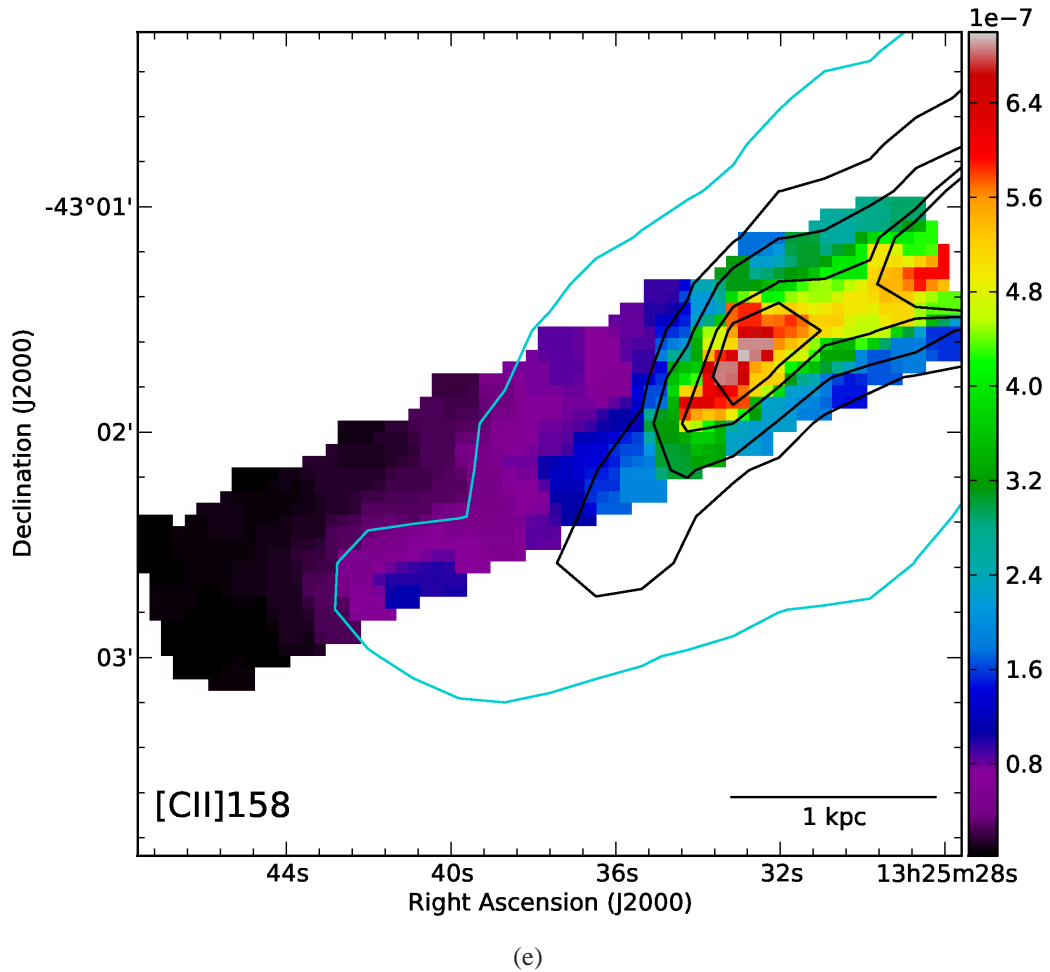
$[\text{O I}]_{145}$ . There are also a few other peaks of emission, one at the tip of the curve and a little pocket in the middle of the strip in the south, which is weakly visible in the  $[\text{N II}]_{122}$ , but not in the maps of neutral gas. The total flux of  $[\text{O III}]$  in our observations is  $(5.50 \pm 0.01(\text{stat}) \pm 1.65(\text{cal})) \times 10^{-15} \text{ W m}^{-2}$ , while the total flux in the  $[\text{N II}]_{122}$  line is  $2.014 \pm 0.004(\text{stat}) \pm 0.604(\text{cal}) \times 10^{-15} \text{ W m}^{-2}$ . Unger et al. (2000) find a flux of  $7.2 \times 10^{-15} \text{ W m}^{-2}$  in  $[\text{O III}]$  for the center pointing, and  $1.5 \times 10^{-15} \text{ W m}^{-2}$  in  $[\text{N II}]_{122}$  for their center pointing, and an upper limit in their south-east pointing of the same flux.



(d)

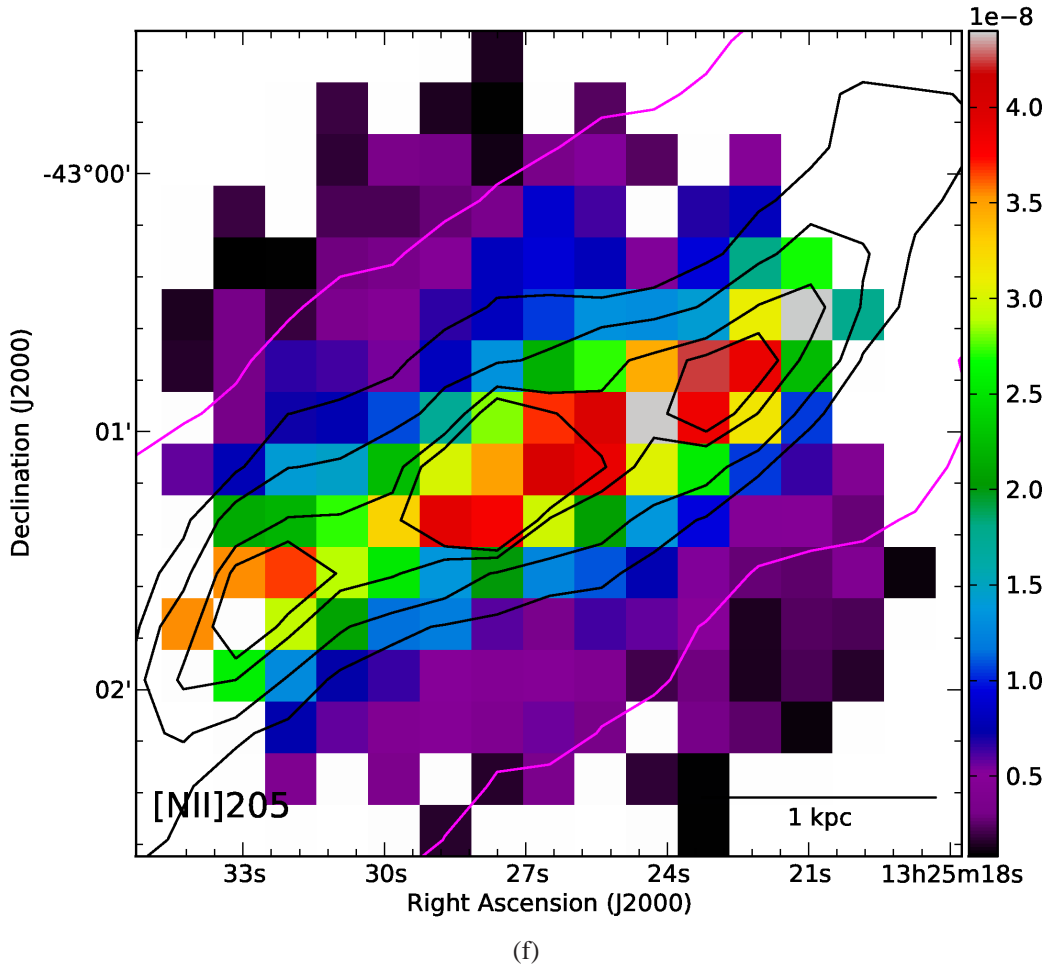
Figure 4.2: *continued*

The area covered by our  $[\text{N II}]_{205}$  map is different than the other five lines we present here, as the observations are centered on the nucleus of the galaxy. We see that there is a strong detection across the disk, with an emission peak that is roughly a factor of 40 larger than emission detected above and below the plane. A comparison between the  $70 \mu\text{m}$  contours and the  $[\text{N II}]_{205}$  shows that the  $70 \mu\text{m}$  peak slightly to the northwest of the center is also detected in the ionized gas, and that the warp in the disk is also visible in the  $[\text{N II}]_{205}$  line. The total flux in this map is  $(6.42 \pm 0.07(\text{stat}) \pm 0.45(\text{cal})) \times 10^{-15} \text{ W m}^{-2}$ .

Figure 4.2: *continued*

Lastly, in Figure 4.1 we show the total infrared flux of Cen A, which is needed for our comparison of observations with the PDR model in Section 4.4. We calculated the total infrared flux using *Spitzer* MIPS 24  $\mu\text{m}$  photometry (Bendo et al., 2012), PACS 70 and 160  $\mu\text{m}$  photometry (Parkin et al., 2012), and the empirically determined equation for the total infrared flux (or luminosity) from Galametz et al. (2013),

$$F_{\text{TIR}} = (2.133 \pm 0.095)\nu_{24}F_{24} + (0.681 \pm 0.028)\nu_{70}F_{70}$$

Figure 4.2: *continued*

$$+(1.125 \pm 0.010)\nu_{160}F_{160}. \quad (4.1)$$

This map covers the entire disk of Cen A; however, we only use the region overlapping with our spectroscopic maps for our analysis.

Table 4.2. Total integrated flux for the PACS cooling lines in Cen A.

Line	$F (10^{-14} \text{ W m}^{-2})^a$	Area <sup>b</sup> ( $\square''$ )
[C II]	$4.268 \pm 0.002$	11232
[N II] <sub>122</sub>	$0.2014 \pm 0.0004$	9792
[O I] <sub>63</sub>	$1.171 \pm 0.002$	11080
[O I] <sub>145</sub>	$0.1006 \pm 0.0003$	10512
[O III]	$0.550 \pm 0.001$	10656
[N II] <sub>205</sub>	$0.642 \pm 0.007$	22752

<sup>a</sup>Total integrated flux of each atomic fine structure line we observed for Cen A. Note that the uncertainties exclude those due to calibrations.

<sup>b</sup>The area in square arcseconds over which each total is calculated. The variations reflect the number of good pixels included in the sum.

### 4.3.2 Line Ratio Diagnostics

#### 4.3.2.1 [C II], [O I]<sub>63</sub> and $F_{\text{TIR}}$

The [C II]/ $F_{\text{TIR}}$  line ratio for Cen A is shown in Figure 4.3 (a). At first glance there does not appear to be any trend with radius; however, when compared with the 70  $\mu\text{m}$  continuum emission overlaid in contours, it appears there is a slight increase with radius ranging from approximately  $3 \times 10^{-3}$  in the center, to  $6 \times 10^{-3}$  in the middle of the strip, and then a decrease in the outermost region of the map, indicating a slight deficit toward the center of the galaxy. The average of this ratio across our strip is  $\sim (5 \pm 1) \times 10^{-3}$ . This ratio is often given by [C II]/ $F_{\text{FIR}}$ , where  $F_{\text{FIR}} = F_{\text{TIR}}/1.3$  (Graciá-Carpio et al., 2008) is the far-infrared flux. Correspondingly, our observations correspond to a range of  $3.9 \times 10^{-3}$  to  $7.8 \times 10^{-3}$  and an average of  $(6.5 \pm 1.3) \times 10^{-3}$  for the [C II]/ $F_{\text{FIR}}$  line ratio.

The  $[\text{C II}]/F_{\text{FIR}}$  line ratio has been probed on resolved scales in other galaxies, including M82 ( $10^{-3} - 10^{-2}$ ; Contursi et al., 2013), NGC 6946 and NGC 1313 ( $8 \times 10^{-3}$ ; Contursi et al., 2002), M51 ( $4 \times 10^{-3}$ ; Parkin et al., 2013) and the Orion Molecular Cloud in the Galaxy ( $3 \times 10^{-3}$ ; Stacey et al., 1993). Our observed line ratio for Cen A is in good agreement with the values in other galaxies as well as a previous determination of this line ratio by Negishi et al. (2001) of  $3.2 \times 10^{-3}$ . On global scales, the  $[\text{C II}]$  deficit appears when comparing ULIRGs to normal galaxies. For example, Luhman et al. (1998) and Luhman et al. (2003) find ULIRGs have a  $[\text{C II}]/F_{\text{FIR}}$  line ratio of less than  $5 \times 10^{-4}$ , which is an order of magnitude lower than in normal galaxies (Crawford et al., 1985; Malhotra et al., 2001; Negishi et al., 2001). Thus, we believe that the deficit observed in Cen A is not of the same degree as in ULIRGs, but is similar to that found in M51 (Parkin et al., 2013).

The line ratio of  $([\text{C II}]+[\text{O I}]_{63})/F_{\text{TIR}}$  (Figure 4.3 (b)) gives us an indication of the heating efficiency in Cen A. The  $[\text{C II}]$  and  $[\text{O I}]_{63}$  lines are the dominant coolants in the neutral gas of PDRs. Thus, their strength tells us how many FUV photons contribute to gas heating, assuming every free electron produced via the photoelectric effect eventually results in the emission of a  $[\text{C II}]$  or  $[\text{O I}]_{63}$  photon. This value is then divided by the total infrared flux, which indicates how many FUV photons result in dust heating if we assume all dust grains irradiated by FUV flux eventually re-emit infrared continuum emission and that nothing else contributes to heating the dust grains. Like the  $[\text{C II}]/F_{\text{TIR}}$  line ratio, the heating efficiency shows a slight increase with radius, with values ranging from  $4 \times 10^{-3}$  to  $8 \times 10^{-3}$  with an average of  $(6 \pm 2) \times 10^{-3}$ . This suggests the heating efficiency is lower toward the center of the galaxy where there is a harder FUV flux as indicated by the  $[\text{O III}]$  emission, which also peaks in the center. Our value for this ratio is consistent with previous measurements in Cen A. Unger et al. (2000) find a value of  $6 \times 10^{-3}$  in

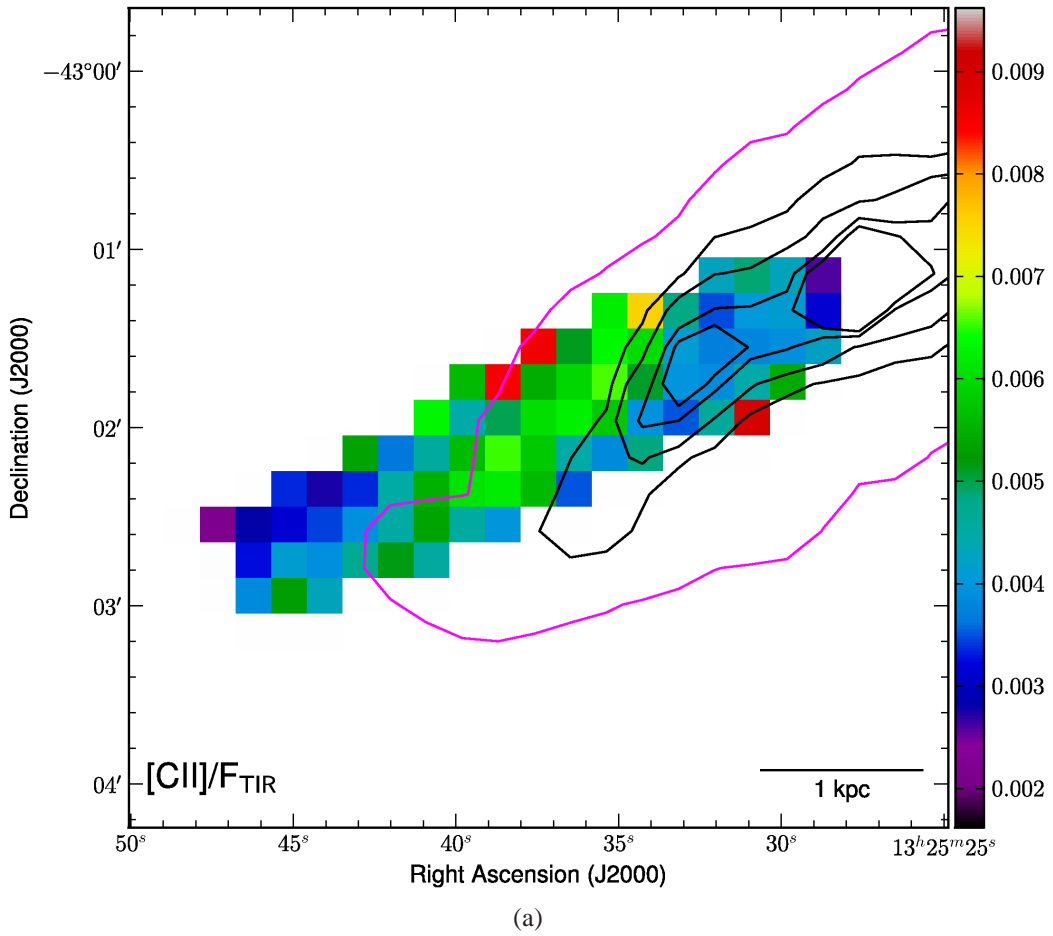
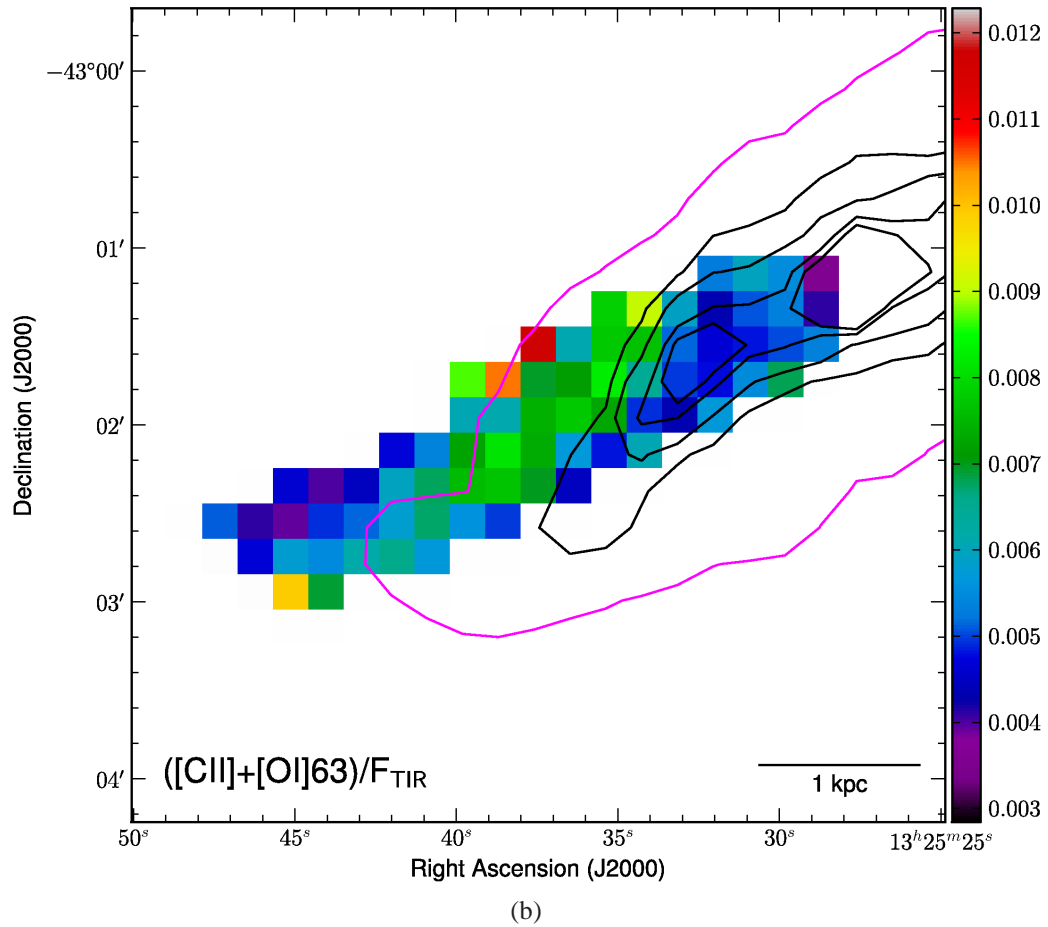


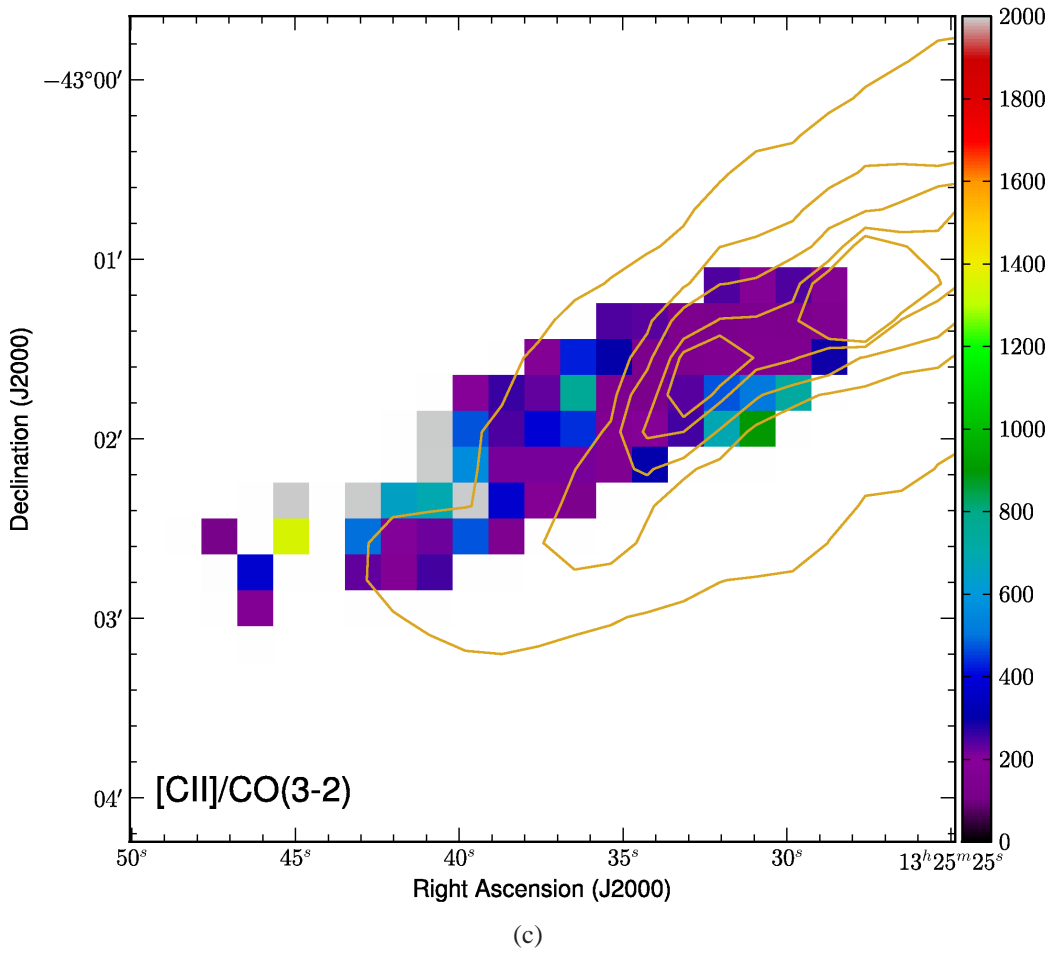
Figure 4.3: Maps of the  $[\text{C II}]/F_{\text{TIR}}$  (a),  $([\text{C II}]+[\text{O I}]_{63})/F_{\text{TIR}}$  (b),  $[\text{C II}]/\text{CO}(J = 3 - 2)$  (c), and  $\text{CO}(J = 3 - 2)/F_{\text{TIR}}$  (d) line ratios for our observed region of Cen A. Contours of the *Herschel* PACS 70  $\mu\text{m}$  emission are overlaid on top, with the same contour levels as in Figure 4.2.

their center and south-east regions, but their 70'' resolution could not identify the radial trend that we see here. In other galaxies this ratio typically varies between  $1.6 \times 10^{-3}$  and  $10^{-2}$ , such as is found by Malhotra et al. (2001), who studied 60 normal, star forming galaxies on global scales.

We can also look at the heating efficiency as a function of infrared color,  $70\mu\text{m}/160\mu\text{m}$  (which indicates dust temperature), as shown in the top panel of Figure 4.4. Here we have divided our strip into eight radial bins as shown by the

Figure 4.3: *continued*

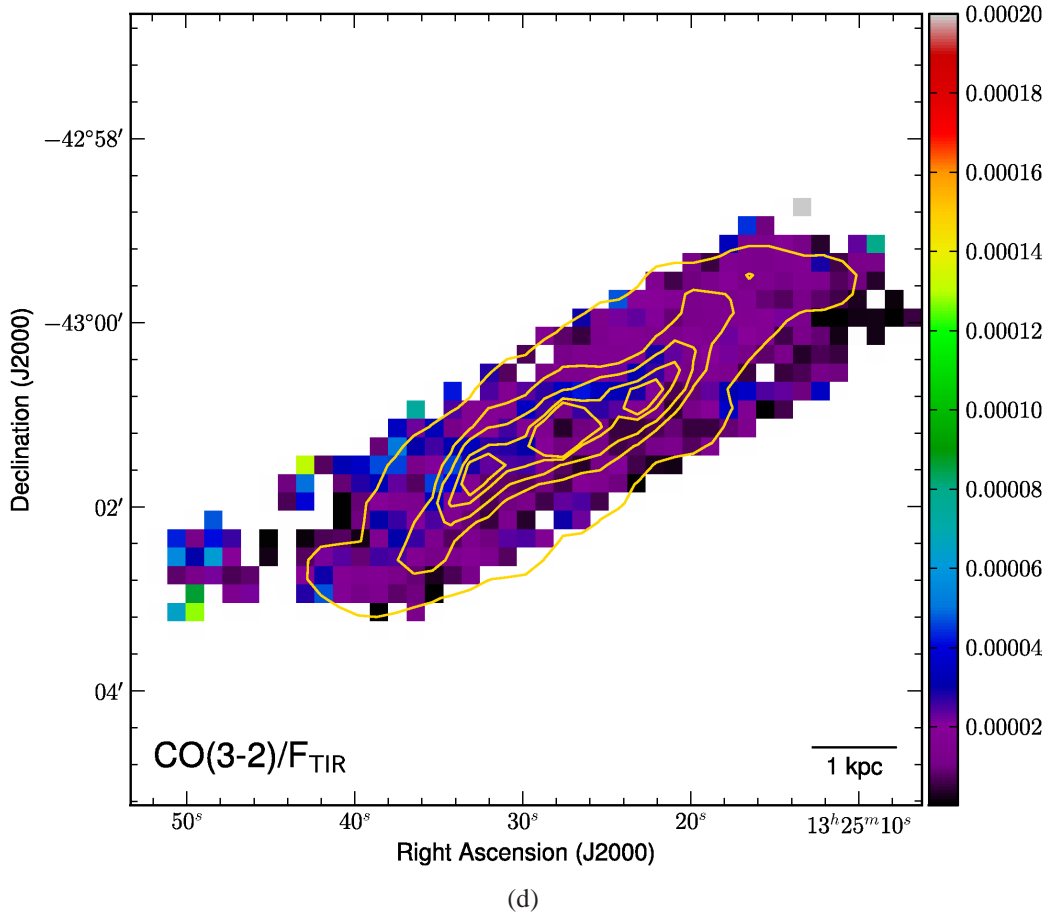
schematic in Figure 4.8 (a), and each point represents the average value in each bin with the standard deviation. The innermost bin (shown in red) has value of  $\sim 5 \times 10^{-3}$ , then we see an increase in the middle bins of up to almost  $8 \times 10^{-3}$  (shown in blue), then a decrease again in the outermost bins. This trend is emphasized in the bottom panel of Figure 4.4, where we show a plot of the heating efficiency as a function of dust temperature, which was determined by Parkin et al. (2012). The innermost bins show the warmest dust. A decrease in heating efficiency with increasing infrared color (and thus dust temperature) has been previously observed within individual galaxies by Lebouteiller et al. (2012) in an H II

Figure 4.3: *continued*

region within the Large Magellanic Cloud, by Croxall et al. (2012) in NGC 1097 and NGC 4559, and by Parkin et al. (2013) in M51.

#### 4.3.2.2 Molecular Gas Cooling

CO can also play a role in the cooling budget, as it too contributes to the cooling via its rotational lines. In Figure 4.3 (d) we show the line ratio  $\text{CO}(J = 3 - 2)/F_{\text{TIR}}$  for Cen A. This ratio is quite weak, varying from roughly  $6.6 \times 10^{-7}$  to  $4.6 \times 10^{-5}$ , with an average of  $(2 \pm 1) \times 10^{-5}$ . There does not appear to be any trend with increasing radius in this line ratio, unlike the other line ratios discussed here. Assuming the

Figure 4.3: *continued*

$\text{CO}(J = 3 - 2)/\text{CO}(J = 1 - 0)$  ratio is 0.3, typical for the diffuse ISM<sup>5</sup> (Wilson et al., 2009), these ratios correspond to a  $\text{CO}(J = 1 - 0)/F_{\text{TIR}}$  ratio of approximately  $8.3 \times 10^{-8}$  to  $5.8 \times 10^{-6}$ . The average value of the  $[\text{C II}]/\text{CO}(J = 1 - 0)$  line ratio is  $(2.1 \pm 1.3) \times 10^3$  across our strip (see Figure 4.3 (c) for a map of the  $[\text{C II}]/\text{CO}(J = 3 - 2)$  line ratio), which is lower than that found for a sample of starburst galaxies and Galactic star forming regions including Cen A, which is 6300 (Stacey et al., 1991). One possible region for such a discrepancy is that the correlation found in Stacey et al. (1991) is for Galactic star forming regions and global values averaged

---

<sup>5</sup>Note this ratio is calculated when the CO integrated intensities are both in units of  $\text{K km s}^{-1}$ . It becomes 8 when the CO fluxes have been converted to units of  $\text{W m}^{-2}$ .

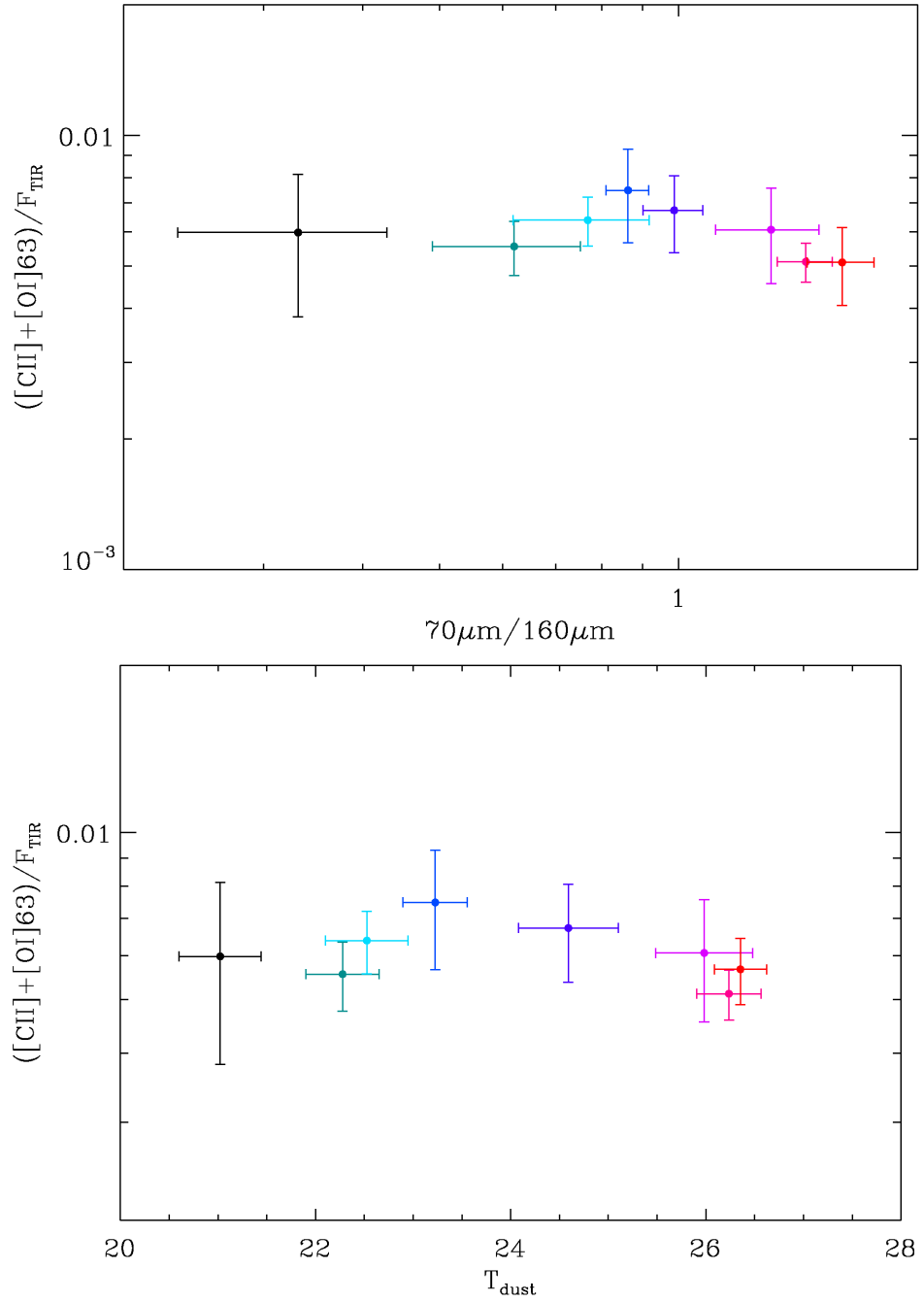


Figure 4.4: The sum of the [C II] and [O I]<sub>63</sub> cooling lines divided by the total infrared flux,  $F_{\text{TIR}}$  for Cen A. Each data point represents the average value within a bin, as described below in Section 4.4. Systematic uncertainties due to calibration are not shown. Top: the  $([\text{CII}]+[\text{OI}]_{63})/F_{\text{TIR}}$  line ratio plotted as a function of the  $70\mu\text{m}/160\mu\text{m}$  color. Bottom: The  $([\text{CII}]+[\text{OI}]_{63})/F_{\text{TIR}}$  line ratio plotted as a function of dust temperature.

over entire galaxies. Our observations fall in between these two scales, and perhaps there is more CO emission on the scale of our strip compared to the [C II] emission.

By converting the CO flux to a molecular hydrogen mass we can compare our various line/ $F_{\text{TIR}}$  ratios with recent results from Graciá-Carpio et al. (2011). These authors investigated the parameter space of line/ $F_{\text{TIR}}$  vs.  $L_{\text{TIR}}/M_{\text{H}_2}$  for a subset of the SHINING sample of galaxies. The ratio  $L_{\text{TIR}}/M_{\text{H}_2}$  loosely represents the number of stars formed per unit mass of molecular gas per unit of time. To convert our CO( $J = 3 - 2$ ) integrated intensity to an H<sub>2</sub> mass, we assume a  $X_{\text{CO}}$  factor of  $(2 \pm 1) \times 10^{20} \text{ cm}^{-2} (\text{K km s}^{-1})^{-1}$ , typical for the Milky Way (Strong et al., 1988), and a CO( $J = 3 - 2$ )/CO( $J = 1 - 0$ ) ratio of 0.3, appropriate for the average ISM (Wilson et al., 2009). Since we do not have global measurements for the various fine structure lines, we opt to instead measure  $L_{\text{TIR}}/M_{\text{H}_2}$  for each of the radial bins (see below) and probe local scales. In Figure 4.5 we plot the line/ $F_{\text{TIR}}$  ratios vs. the  $L_{\text{TIR}}/M_{\text{H}_2}$  for each of the bins in Cen A. Our results are consistent with those from Graciá-Carpio et al. (2011) at the low end of the  $L_{\text{TIR}}/M_{\text{H}_2}$  scale. However, we do not probe to high enough scales to see the deficit take effect at  $L_{\text{TIR}}/M_{\text{H}_2} \gtrsim 80 \text{ L}_{\odot} \text{ M}_{\odot}$  as shown by Graciá-Carpio et al. (2011).

### 4.3.2.3 Ionized Gas Source

The observed [O III]<sub>88</sub>/[N II]<sub>122</sub> line ratio has been used in high redshift sources to interpret either the strength of the ionization parameter,  $U$ , which is the number of ionizing photons divided by the gas density within the narrow line region of an AGN (Abel et al., 2009), or the stellar classification of the youngest stars in an H II region, depending on the type of region one is investigating (Ferkinhoff et al., 2011). We have taken the average observed [O III]/[N II]<sub>122</sub> and plotted it in Figure 4.6 as a black dotted line, with the shaded region outlining the range of values within cal-

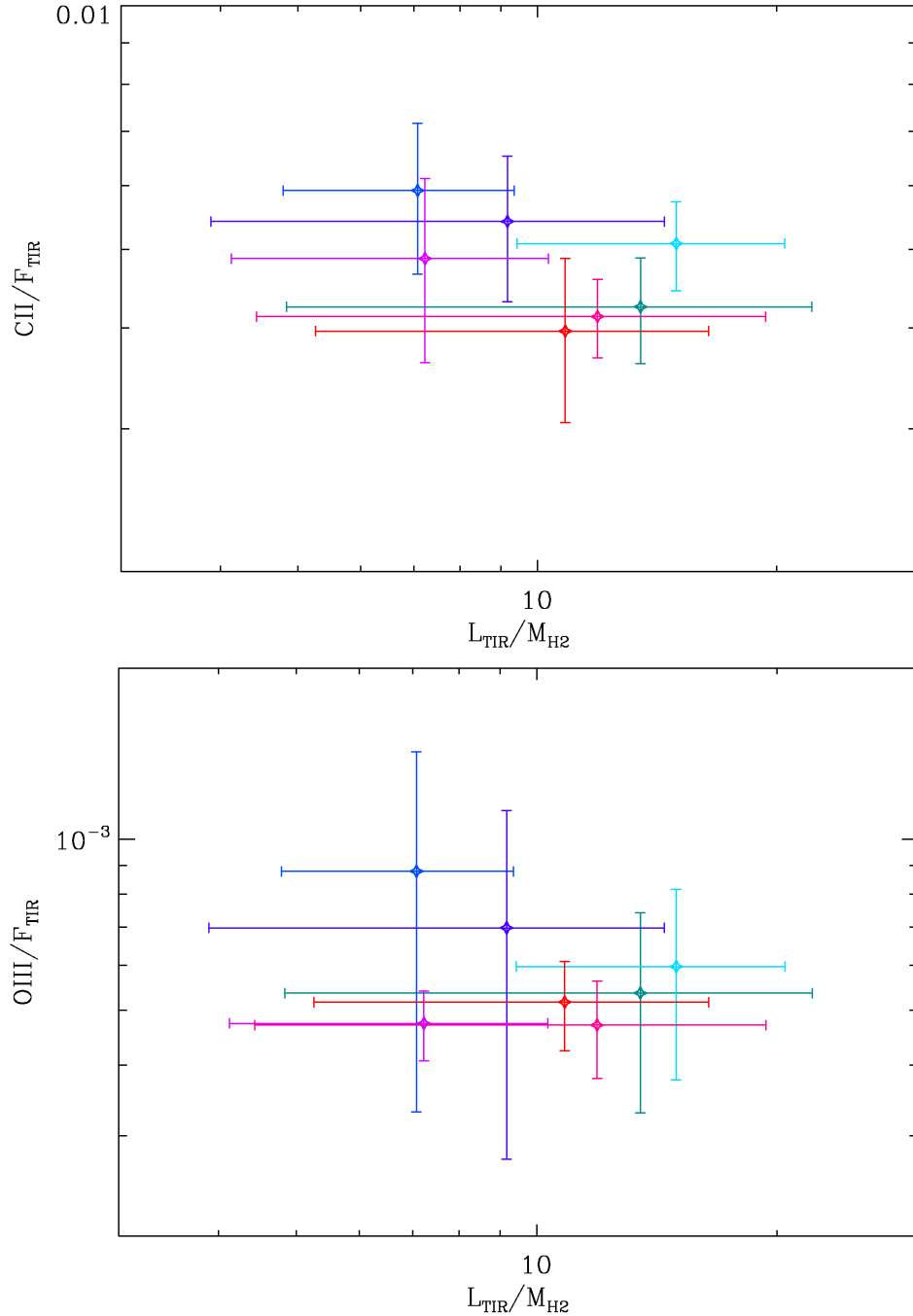


Figure 4.5: The [C II] (top) and [O III] (bottom) line ratios divided by the total infrared flux,  $F_{\text{TIR}}$  for Cen A, plotted as a function of  $L_{\text{TIR}}/M_{\text{H}_2}$ . Each colored data point corresponds to a bin as described in Figure 4.8.

ibration uncertainties. Overlaid on the observed ratio are four predicted line ratios as a function of stellar temperature from the H II region models of Rubin (1985) as shown by the dashed lines. The various colors represent different gas densities. Our results fall within a stellar effective temperature of approximately  $3.45 \times 10^4$  and  $3.62 \times 10^4$  K, which corresponds to stellar classifications of O9.5 or O9 (Vacca et al., 1996). The dash-dotted lines overlaid on the plot represent various narrow line region models from Groves et al. (2004). Comparing the range of our observations to the coinciding models we see that if the central AGN was influencing the surrounding gas out to the limits of our observations, the ionization parameter would range from  $\log U = -4$  to  $-3.2$ , corresponding to a fairly weak AGN. Given that we are not probing the AGN directly, it is more likely the  $[\text{O III}]_{88}/[\text{N II}]_{122}$  line ratio is indicating that stars are producing the H II regions within our observations, or perhaps both the AGN and the stars. If the AGN were to contribute partially to the observed emission it might explain why our observed  $[\text{O III}]_{88}/[\text{N II}]_{122}$  line ratio is higher (and thus the stellar classification is earlier) than is observed in M51 (Parkin et al., 2013).

### 4.3.3 The contribution of ionized gas to the [C II] emission

The emission in the  $[\text{C II}]_{158}$  line comes from three sources: dense neutral gas, ionized gas, and diffuse neutral gas. For us to properly utilize the photodissociation region model in Section 4.4 to interpret our diagnostic far-infrared spectral lines, we need to isolate the  $[\text{C II}]_{158}$  emission from the dense neutral gas found in PDRs. The ionized gas contribution can be determined by comparing two observed line ratios, namely the  $[\text{N II}]_{122}/[\text{N II}]_{205}$  and  $[\text{C II}]_{158}/[\text{N II}]_{205}$  ratios to a theoretical prediction for each line as a function of electron density in an H II region (e.g.

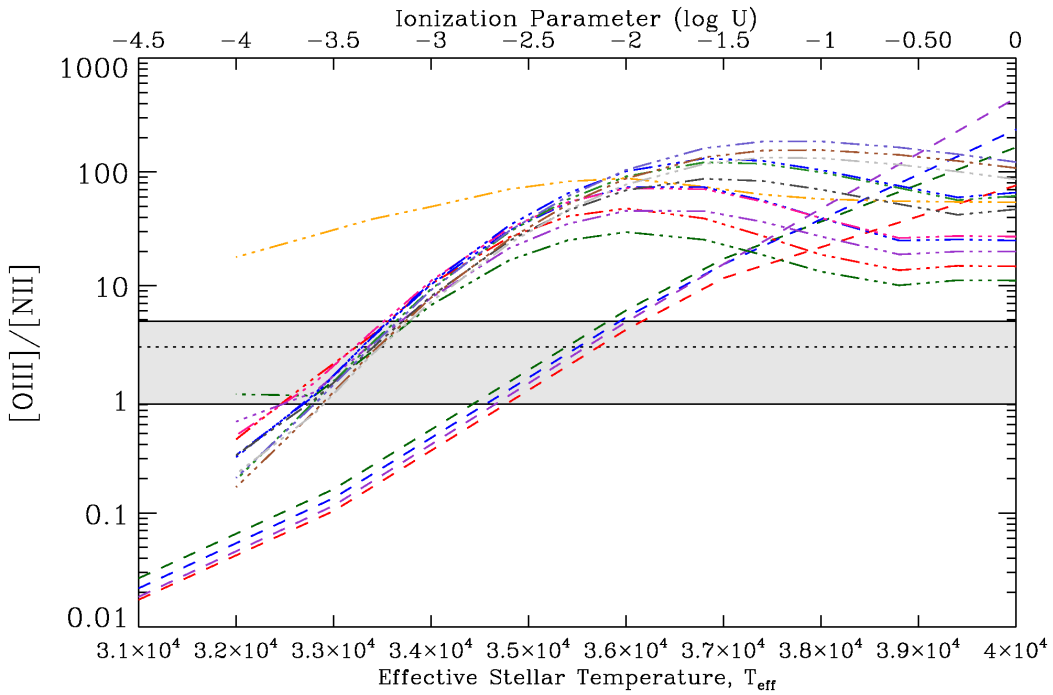


Figure 4.6: A comparison of the average observed  $[\text{O III}]_{88}/[\text{N II}]_{122}$  line ratio for Cen A to predicted line ratios for models of an H II region as well as a narrow line region AGN model. The black dotted line represents the global average over our observed line ratio, while the shaded region encompasses the range of values within uncertainty. The dashed lines show the predicted line ratio as a function of effective stellar temperature (bottom axis) for various gas densities using the H II region model of Rubin (1985). The dash-dotted lines represent the predicted line ratios for the NLR regions as a function of the log of the ionization parameter  $U$  (top axis) for various gas densities and power law indices using the model of Groves et al. (2004).

Oberst et al., 2006; Parkin et al., 2013). To calculate the level populations (and thus the predicted fluxes) for the two  $[\text{N II}]$  transitions we employ the Einstein coefficients from Galavis et al. (1997) and collision strengths from Hudson & Bell (2004). For the  $[\text{C II}]_{158}$  line level populations we use the Einstein coefficients of Galavis et al. (1998) and collisions strengths of Blum & Pradhan (1992). Due to the lack of accurate measurements of the gas phase abundances of C or N, as well as the metallicity in Cen A, we adopt Solar gas phase abundances and assume

no metallicity gradient within the region we are investigating. The abundances we choose are from Savage & Sembach (1996), and are  $\text{C}/\text{H} = 1.4 \times 10^{-4}$  and  $\text{N}/\text{H} = 7.9 \times 10^{-5}$ .

Our observed  $[\text{N II}]_{122}/[\text{N II}]_{205}$  line ratio is initially calculated for the small region of overlap between the observations of the two lines. We convolve the  $[\text{N II}]_{122}$  to the resolution of the  $[\text{N II}]_{205}$  ( $17''$ ) and align the two maps and re-grid to a common pixel scale. Next, we convert the units of the  $[\text{N II}]_{122}$  map to match those of the  $[\text{N II}]_{205}$ ,  $\text{Jy beam}^{-1}$ , and then calculate the line ratio in each of the overlapping pixels. We follow the same steps in producing the  $[\text{C II}]_{158}/[\text{N II}]_{205}$  line ratio.

Using theoretical curves of the line ratios as a function of electron density for an H II region, we determine the electron density at which our observed  $[\text{N II}]_{122}/[\text{N II}]_{205}$  ratio matches that of the theoretical prediction for each pixel. We find a mean electron density of  $6.3 \text{ cm}^{-3}$  with lower and upper limits of 0.8 and  $12.3 \text{ cm}^{-3}$ . Given that there is little overlap between our  $[\text{N II}]_{205}$  map and our  $[\text{N II}]_{122}$  map, we choose to take the mean observed ratio and standard deviation as the adopted  $[\text{N II}]_{122}/[\text{N II}]_{205}$  measurement for the full area of our PACS observations. Thus, we find  $[\text{N II}]_{122}/[\text{N II}]_{205} = 0.8 \pm 0.2$ , and create an  $[\text{N II}]_{205}$  map that we can then, in turn, use to create an observed  $[\text{C II}]_{158}/[\text{N II}]_{205}$  map.

With the electron density known, we then determine the theoretical prediction for the  $[\text{C II}]_{158}/[\text{N II}]_{205}$  ratio in the ionized gas. Dividing the predicted ratio map by our observed ratio map provides us with the fraction of [C II] emission originating in H II regions. This is then subtracted from our  $[\text{C II}]_{158}$  map. In Figure 4.7 we show the fraction of  $[\text{C II}]_{158}$  emission coming from ionized gas along the disk of Cen A covered by our observations.

For comparison with the PDR model in Section 4.4, we remove the fraction

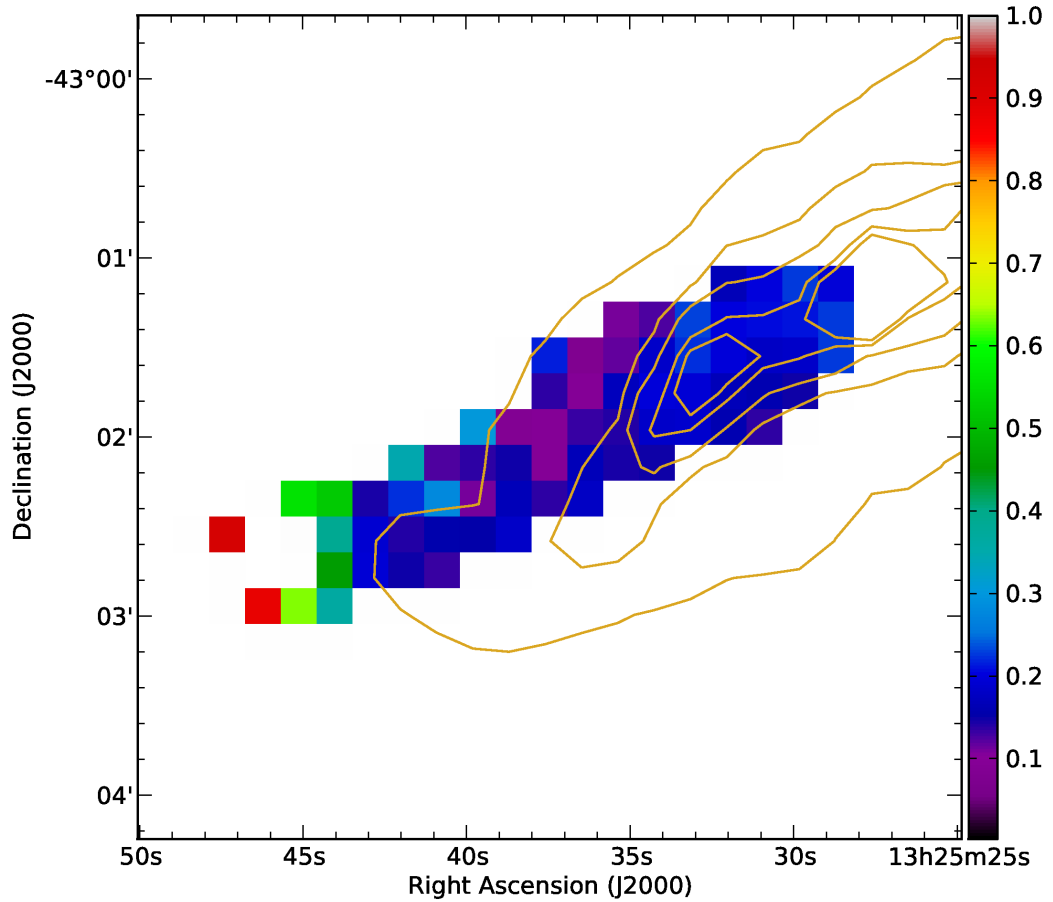


Figure 4.7: The fraction of  $[\text{C II}]_{158}$  emission originating from ionized gas for the eastern half of the disk of Centaurus A.

of  $[\text{C II}]_{158}$  emission coming from ionized gas, which in general is quite low. The majority of our map demonstrates a contribution of roughly 10 to 20%, with the pixels showing the highest ionized gas contribution falling at the edge of the map farthest from the center of the galaxy, where the signal-to-noise is lower.

## 4.4 PDR modelling

A comparison between observed line ratios and a PDR model allows us to diagnose the physical properties of the molecular clouds from which the fine structure line

emission originates. Here we choose to use the PDR model of Kaufman et al. (1999, 2006), which has been updated and expanded from the model of Tielens & Hollenbach (1985). This particular model assumes the PDR is a plane-parallel, semi-infinite slab and is only parameterized by two free variables: the hydrogen gas density,  $n$ , and the strength of the impeding far-ultraviolet (FUV) radiation field normalized to the Habing field ( $1.6 \times 10^{-3}$  erg cm $^{-2}$  s $^{-1}$ ; Habing, 1968),  $G_0$ . The model simultaneously treats the thermal balance, chemical network and radiative transfer and produces a grid of predicted fine structure line strengths as a function of  $n$  and  $G_0$ . By comparing observed line ratios to the predicted ones we can extract the corresponding  $n$  and  $G_0$ .

For our investigation we choose to utilize the line ratio parameter space of  $[\text{C II}]_{158}/[\text{O I}]_{63}$  vs.  $[\text{C II}]_{158} + [\text{O I}]_{63})/F_{\text{TIR}}$ . In order to search for radial variations in the disk of Cen A we have divided our observed line ratio maps into eight bins of pixels to measure  $n$  and  $G_0$ . The area of our line ratio maps is displayed in Figure 4.8 (a), where the bins are color-coded and labelled. The average observed values in each bin are overlaid on the PDR model grid in Figure 4.8 (b), with the error bars incorporating both the measurement and calibration uncertainties of the observations as well as the standard deviation of the data in each bin. We note here that the total infrared flux,  $F_{\text{TIR}}$ , has been reduced by a factor of two as recommended by Kaufman et al. (1999) to accommodate the fact that the observed total flux emits from both the near and far sides of the cloud(s) because it is optically thin; however, the model assumes it only emits from the side exposed to the source of FUV flux. The resulting values of  $n$ ,  $G_0$  and the temperature at the surface of the PDR,  $T$ , are presented in Table 4.3 under the “Uncorrected” heading.

The PDR model assumes the  $[\text{C II}]_{158}$  emission originates only in neutral gas, but as described in Section 4.3.3,  $[\text{C II}]_{158}$  emission can be produced in both

neutral and ionized gas. Thus, to properly compare our observations to the model we need to remove the contribution from the ionized gas. We also need to make a correction to the  $[\text{O I}]_{63}$  observations that stems from geometrical effects of many PDRs in a given observation for extragalactic sources. We see PDRs at all orientations with respect to our line of sight, but observed emission only escapes from the lit side of the PDR when the line is optically thick, as is the case for the  $[\text{O I}]_{63}$  line. Kaufman et al. (1999) state that as a result of the optically thick line and various PDR orientations, we only observe about half of the total  $[\text{O I}]_{63}$  emission produced, while the remaining half radiates away from the line of sight. Thus, we opt to follow this advice and increase our observed  $[\text{O I}]_{63}$  flux by a factor of 2, as we have previously done with M51 (Parkin et al., 2013). We show the fully corrected line ratios compared to the PDR model in Figure 4.8 (c) and tabulate the results in Table 4.3. We see that with these changes the data points shift down and slightly to the right, corresponding to increases in both  $G_0$  and  $n$ .

As a consistency check, in Figure 4.8 (d) we also show a comparison of our observations with the PDR model parameter space  $[\text{C II}]/[\text{O I}]_{145}$  vs.  $([\text{C II}] + [\text{O I}]_{63})/F_{\text{TIR}}$ , which has the advantage of the optically thin  $[\text{O I}]_{145}$  line. We find that this parameter space gives consistent solutions for  $n$  and  $G_0$  as those derived from the plot in the bottom left panel of the same figure. This reassures us that our assumption that the  $[\text{O I}]_{63}$  line is optically thick is valid.

We note here that there is a second solution in this parameter space which diagnoses the molecular clouds with a weaker  $G_0$  ( $\sim 10^0 - 10^{0.75}$ ) and higher  $n$  ( $\sim 10^{3.5} - 10^{4.25}$ ). However, comparing our observed  $[\text{C II}]$  integrated intensity to that predicted by the PDR model based on the second solution, the second solution would suggest that there are up to a few thousand PDRs along each line of sight, which, despite the fact that Cen A is almost edge on, seems unlikely within a  $14''$

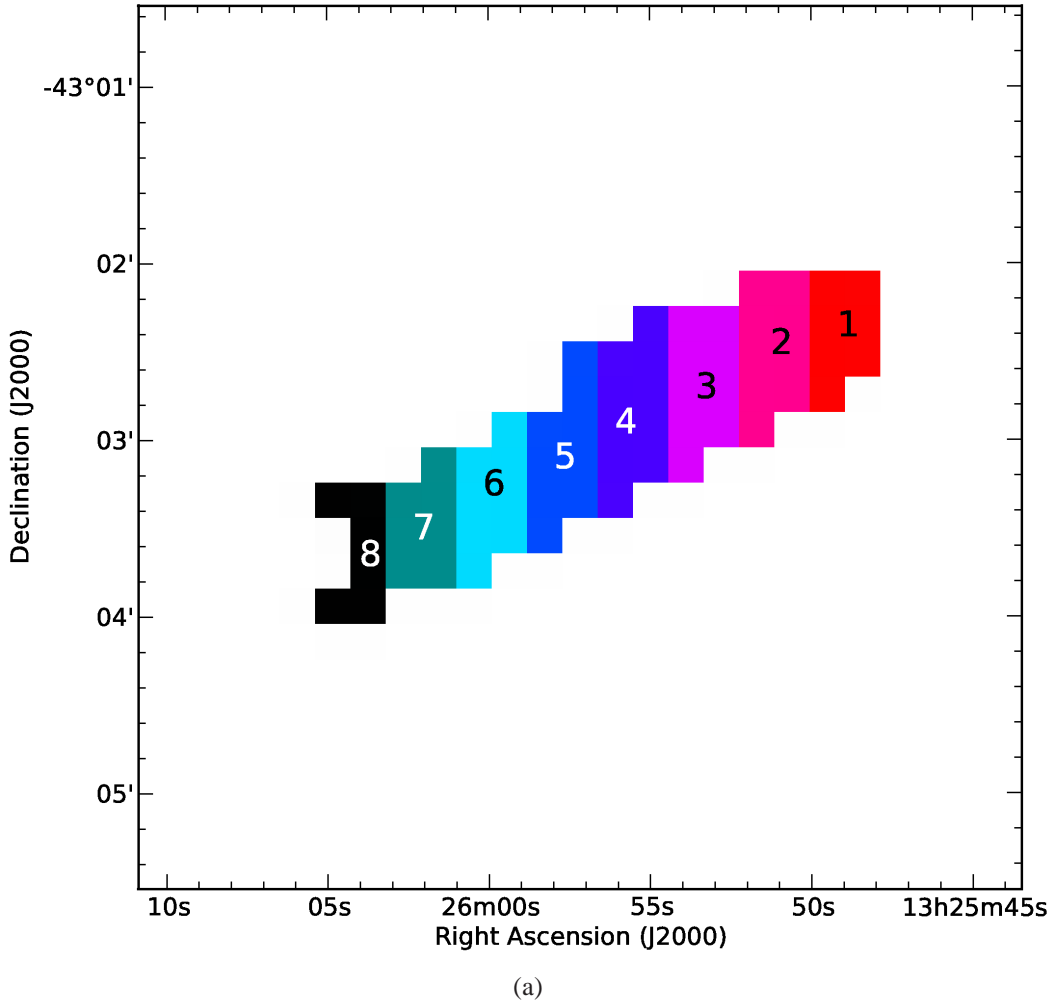


Figure 4.8: (a): A schematic of the radial bins we divide our observed line ratio maps into. The colors in this image correspond to the data points in the other three panels of this figure. (b): A comparison of our observed (and uncorrected)  $[\text{C II}]/[\text{O I}]_{63}$  and  $([\text{C II}]+[\text{O I}]_{63})/F_{\text{TIR}}$  line ratios to the PDR model of Kaufman et al. (1999) for the eastern half of Centaurus A. The data points represent our observations, each color corresponding to a radial bin as shown in the top left panel. The solid lines represent contours of constant  $\log G_0$  while the dotted lines represent curves of constant  $\log n$ . (c): The same plot as in the top right panel, but here the  $[\text{C II}]$  and  $[\text{O I}]_{63}$  have been corrected as described in the text. (d): Our observed  $[\text{C II}]/[\text{O I}]_{145}$  and  $([\text{C II}]+[\text{O I}]_{63})/F_{\text{TIR}}$  line ratios compared to the PDR model. The lines and data points are the same as in the top right and bottom left panels.

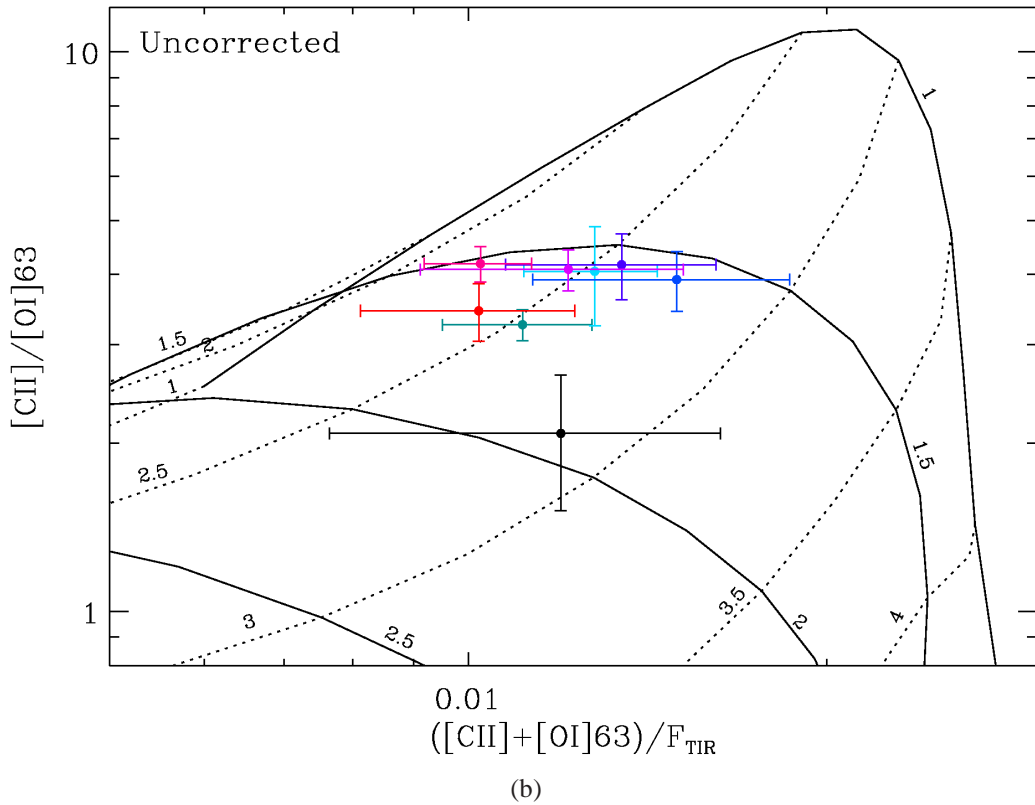
Table 4.3. Properties of the gas derived from the PDR model

Case	Bin	$\log(n/\text{cm}^{-3})$	$\log G_0$	$T (\text{K})$
uncorrected <sup>a</sup>	1	(2.25–2.5) <sub>-0.75</sub> <sup>+0.5</sup>	(1.5–1.75) <sub>-0.25</sub> <sup>+0.5</sup>	(120–170) <sub>-40</sub> <sup>+655</sup>
	2	(2.0–2.25) <sub>-0.5</sub> <sup>+0.5</sup>	(1.5–1.75) <sub>-0.5</sub> <sup>+0.25</sup>	(140–210) <sub>-70</sub> <sup>+410</sup>
	3	(2.25–2.5) <sub>-0.75</sub> <sup>+0.5</sup>	(1.5–1.75) <sub>-0.25</sub> <sup>+0.25</sup>	(120–170) <sub>-40</sub> <sup>+450</sup>
	4	(2.5–2.75) <sub>-1.0</sub> <sup>+0.5</sup>	(1.5–1.75) <sub>-0.25</sub> <sup>+0.25</sup>	(110–150) <sub>-35</sub> <sup>+470</sup>
	5	(2.5–2.75) <sub>-1.0</sub> <sup>+0.5</sup>	(1.5–1.75) <sub>-0.25</sub> <sup>+0.25</sup>	(110–150) <sub>-35</sub> <sup>+470</sup>
	6	(2.5–2.75) <sub>-1.0</sub> <sup>+0.25</sup>	(1.5–1.75) <sub>-0.25</sub> <sup>+0.25</sup>	(110–150) <sub>-30</sub> <sup>+470</sup>
	7	(2.5–2.75) <sub>-1.0</sub> <sup>+0.25</sup>	(1.5–1.75) <sub>-0.25</sub> <sup>+0.25</sup>	(110–150) <sub>-30</sub> <sup>+470</sup>
	8	(2.75–3.0) <sub>-0.5</sub> <sup>+0.5</sup>	(1.75–2.0) <sub>-0.25</sub> <sup>+0.25</sup>	(130–170) <sub>-40</sub> <sup>+85</sup>
corrected <sup>b</sup>	1	(3.0–3.25) <sub>-0.5</sub> <sup>+0.25</sup>	(2.0–2.25) <sub>-0.25</sub> <sup>+0.25</sup>	(155–200) <sub>-40</sub> <sup>+70</sup>
	2	(2.75–3.0) <sub>-0.25</sub> <sup>+0.25</sup>	(2.0–2.25) <sub>-0.25</sub> <sup>+0.25</sup>	(160–200) <sub>-35</sub> <sup>+70</sup>
	3	(3.0–3.25) <sub>-0.5</sub> <sup>+0.25</sup>	(2.0–2.25) <sub>-0.25</sub> <sup>+0.25</sup>	(155–200) <sub>-40</sub> <sup>+70</sup>
	4	(3.0–3.25) <sub>-0.5</sub> <sup>+0.5</sup>	(1.75–2.0) <sub>-0.25</sub> <sup>+0.25</sup>	(125–160) <sub>-45</sub> <sup>+60</sup>
	5	(3.0–3.25) <sub>-0.25</sub> <sup>+0.5</sup>	(1.75–2.0) <sub>-0.5</sub> <sup>+0.25</sup>	(125–160) <sub>-55</sub> <sup>+40</sup>
	6	(3.0–3.25) <sub>-0.5</sub> <sup>+0.25</sup>	(1.75–2.0) <sub>-0.0</sub> <sup>+0.25</sup>	(125–160) <sub>-10</sub> <sup>+60</sup>
	7	(3.0–3.25) <sub>-0.25</sub> <sup>+0.25</sup>	(2.0–2.25) <sub>-0.25</sub> <sup>+0.25</sup>	(155–200) <sub>-40</sub> <sup>+50</sup>
	8	(3.5–3.75) <sub>-0.5</sub> <sup>+0.25</sup>	(2.5–2.75) <sub>-0.5</sub> <sup>+0.5</sup>	(200–260) <sub>-90</sub> <sup>+110</sup>

Note. — The values reported for  $\log G_0$ ,  $\log(n/\text{cm}^{-3})$ , and  $T$  show the best fitting range from the model grid in brackets. The lower limits on these values are calculated by subtracting the lower uncertainty from the lower end of the best fitting range, while the upper limits should be calculated by adding the upper uncertainty to the upper end of the best fitting range.

<sup>a</sup>The uncorrected results include all of the observed [C II] emission.

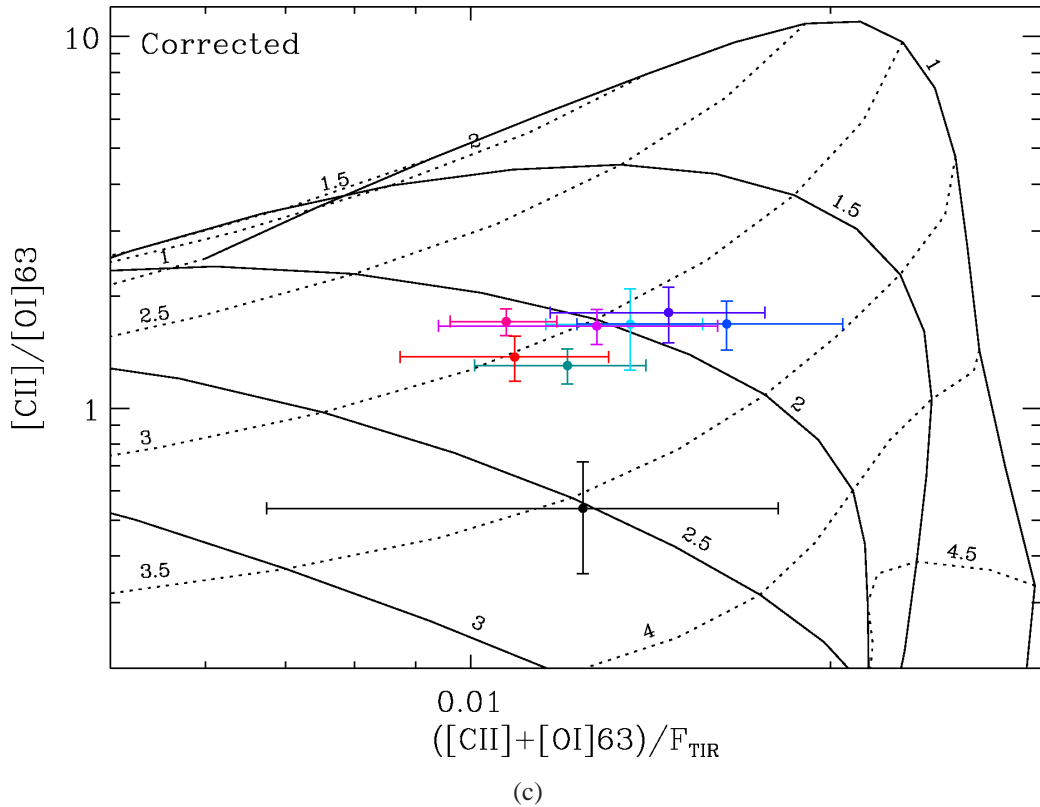
<sup>b</sup>The corrected results include only [C II] emission from neutral gas, and the [O I]63 has been increased by a factor of two to account for multiple PDRs.

Figure 4.8: *continued*

beam. A similar argument has been used by Kramer et al. (2005) and Parkin et al. (2013) to infer that this solution is invalid. Thus, we eliminate this solution for the discussion aspects of this paper.

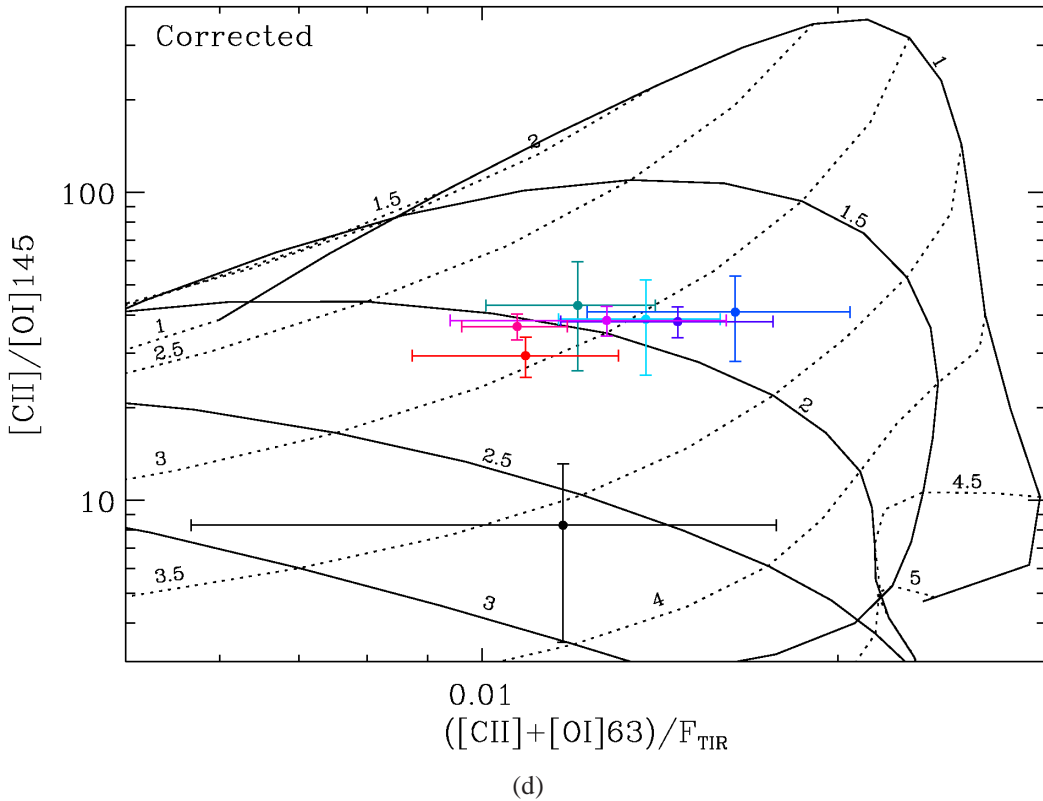
## 4.5 Discussion

The heating efficiency and  $[C\,II]/F_{TIR}$  line ratios found along the strip of Cen A are consistent with values found in normal, star-forming spiral galaxies as was discussed above in Section 4.3.2, with average values of  $(6 \pm 2) \times 10^{-3}$  and  $\sim (5 \pm 1) \times 10^{-3}$ , respectively. We also see, for the first time, a slight decrease in efficiency toward the center of the galaxy, which tells us the dust grains and PAHs

Figure 4.8: *continued*

that provide the free electrons for gas heating are likely becoming too positively charged for the photoelectric effect to take place efficiently. The most likely cause of the heating deficiency is the AGN itself, as it generates a hard radiation field. We do see support for this in Figure 4.2 in the [O III] and [N II]<sub>122</sub> lines, which show peaked emission near the edge of our observations toward the center of the galaxy. We also see strong [N II]<sub>205</sub> emission in the nucleus of the galaxy. In contrast, we also see the strongest [O I]<sub>63</sub> emission toward the center of the galaxy, indicating the presence of neutral gas. However, this line can also be indicative of gas heating via shocks (Hollenbach & McKee, 1989).

In Parkin et al. (2012) a radially decreasing trend in both the dust temperature and the gas-to-dust mass ratio was reported, implying some influence on the

Figure 4.8: *continued*

surrounding ISM by the central AGN in Cen A. Interestingly, we do not see a radial trend in the density of hydrogen nuclei,  $n$  nor the strength of the interstellar radiation field impeding onto the molecular cloud surfaces  $G_0$ , within the combined statistical plus calibration uncertainties (calibration uncertainties not shown in Figure 4.8). Even within one standard deviation of the mean value in each bin, there is little trend with increasing radius from the center (only the outermost bin shows a significant deviation from the other bins; however, this may be due to the low signal-to-noise in the pixels). Correspondingly, the surface temperature of the clouds also does not show a radial trend, in contrast to the dust temperature. These results suggest that the physical properties of the molecular clouds nearest the center in our observations are not being affected strongly by the AGN.

One possible explanation for this might be the high inclination of Cen A with respect to the line of sight. Cen A has an inclination of roughly  $75^\circ$  (Quillen et al., 2006) so it is nearly edge on. If we were only diagnosing the characteristics of clouds from the nearest side of the galaxy, we might not observe any effects of the AGN on the surrounding clouds. However, while we believe the [O I]<sub>63</sub> line is optically thick, [O I]<sub>145</sub> is not, and it is unlikely the [C II], and  $F_{\text{TIR}}$  are optically thick as well. Thus, it is more likely that any effects the AGN might have on the surrounding gas are diluted because we are integrating emission over clouds through the arm and interarm regions as well as any in the vicinity of the AGN along our line of sight.

Another possibility to explain why the dust, tracing the inner parts of giant molecular clouds (GMCs) and the diffuse ISM, is affected by the AGN but not the PDR gas, is that the AGN is affecting these regions of the ISM more so than around the edges of GMCs, where warm PDRs tend to exist due to recent massive star formation. This might be plausible if the X-rays produced by the AGN are affecting the diffuse ISM more than the PDRs, and an appreciable fraction of the observed dust continuum is from the diffuse ISM.

We also note that the dust temperatures are colder (20–30 K) than those in the gas (roughly 100–300 K). This may not be surprising, as the far-infrared continuum is optically thin and thus we are probing deeper into the cloud, whereas the PDR model only provides us with the temperature of the gas at the surface. Furthermore, Parkin et al. (2012) fit the dust SED between 70 and 500  $\mu\text{m}$  where the dust grains are more likely to be in thermal equilibrium with their surroundings, while the hotter dust grains would be better represented by mid-infrared continuum, such as at 24  $\mu\text{m}$  map, which is often used as an obscured star formation tracer (Wu et al., 2005; Calzetti et al., 2007, 2010; Kennicutt et al., 2009).

### 4.5.1 Inferred Physical Conditions from PDR Modelling

In Section 4.4 we found that the average values of  $G_0$  and  $n$  across the disk ranged from  $\sim 10^{1.75}$ – $10^{2.75}$  and  $\sim 10^{2.75}$ – $10^{3.75}$  cm $^{-3}$ , respectively. These results are consistent with those previously published by Unger et al. (2000), who found  $G_0 \sim 10^2$  and  $n \sim 10^3$  cm $^{-3}$ , as well as by Negishi et al. (2001) who found  $G_0 = 10^{2.7}$  and  $n = 10^{3.1}$  cm $^{-3}$  for Cen A. The properties of the molecular clouds are also consistent with those found by large surveys on global scales. The 60 galaxies in the Malhotra et al. (2001) sample show  $10^2 \leq G_0 \leq 10^{4.5}$  and  $10^2$  cm $^{-3} \leq n \leq 10^{4.5}$  cm $^{-3}$ , while the full sample of Negishi et al. (2001) shows a range of  $10^2$  to  $10^4$  for both  $n$  and  $G_0$ , where  $n$  is in units of cm $^{-3}$ .

We also compare our results to those found for other individual galaxies. Contursi et al. (2013) investigated the PDR characteristics within four regions of the starburst M82. They found that within their central starburst and disk components,  $G_0 = 2500$ ,  $n = 900$  cm $^{-3}$ , and  $G_0 = 450$ ,  $n = 220$  cm $^{-3}$ , respectively, consistent with the results for Cen A. Croxall et al. (2012) found values for  $G_0$  and  $n$  of  $10^{1.7}$ – $10^{3.0}$  and  $10^{2.5}$ – $10^{3.0}$  cm $^{-3}$  for the Seyfert 1 galaxy NGC 1097 and the spiral galaxy NGC 4559, while Contursi et al. (2002) found values of  $G_0$  and  $n$  of  $10^{2.0}$ – $10^{4.0}$  and  $10^{2.0}$ – $10^{4.0}$  cm $^{-3}$  for the two spiral galaxies NGC 6946 and NGC 1313. Lastly, in M33, a nearby spiral, Mookerjea et al. (2011) find  $G_0 = 32$  and  $n = 320$  cm $^{-3}$ . Thus, Cen A has a lower value for  $G_0$  for M82, but a higher value for  $G_0$  than M33, and is in fairly good agreement with the range of values of  $G_0$  and  $n$  found in other sources.

In contrast to the values for  $G_0$  and  $n$  found in normal or starbursting galaxies, Wilson et al. (2013) investigated the elliptical galaxy NGC 4125 and found that the [C II]/[O I] $_{63}$  line ratio is greater than 3–4 (including calibration uncertainties)

and  $([C\text{ II}]+[\text{O I}]_{63})/F_{\text{TIR}}$  is greater than  $1.3 \times 10^{-3}$ . These values would place it left and upwards in the parameter space in Figure 4.8(b), in a region where only the low  $G_0$ , high  $n$  solutions lie (not shown in the figure). We choose to compare these line ratios for NGC 4125 with our uncorrected results for Cen A because the [C II] emission from NGC 4125 was not corrected for ionized gas. In fact, it is likely that NGC 4125 is ionized gas dominated given that only an upper limit for  $[\text{O I}]_{63}$  is determined but there are significant detections in  $[\text{N II}]_{122}$  and [C II]. Furthermore, Welch et al. (2010) find only an upper limit in CO emission for NGC4125.

Crocker et al. (2011) studied 12 early type galaxies and found their star forming properties to be similar to other star forming galaxies. Crocker et al. (2012) studied a subsample of early type galaxies from the ATLAS<sup>3D</sup> survey (Young et al., 2011) and found diagnostic CO line ratios in many of these galaxies that were consistent with those of typical spiral galaxies. Thus, Cen A likely has a more normal ISM than NGC 4125 when compared to samples of elliptical and lenticular galaxies, as well as spiral galaxies.

### 4.5.2 Potential Non-PDR contributions to observed lines

We note that there is a possibility that of the [C II] emission stemming from neutral gas, some may come from the diffuse ISM rather than from PDRs. If this were the case, the data points in Figure 4.8 would shift downward and to the left. However, Unger et al. (2000) looked into this possibility and concluded that less than 5% of the [C II] emission originated in non-PDR gas within their ISO observations of Cen A. Furthermore, we calculate the ratio of H<sub>2</sub>/H I using the maps from Parkin et al. (2012) and find an average value of roughly 5 through the area covered by our spectroscopic strips, suggesting that the gas is molecular H<sub>2</sub> dominated.

In addition, it is possible that not all of the observed  $F_{\text{TIR}}$  emission stems from PDRs as well; for example, it could come from H II regions. Looking at the right panel of Figure 4.8 we see that we can reduce the  $F_{\text{TIR}}$  by roughly a factor of 3 before our data become inconsistent with the PDR model. Thus, at least 1/6 (the extra factor of two comes from the fact that we have already reduced the observed flux for comparison with the PDR) of the observed  $F_{\text{TIR}}$  emission in Cen A comes from PDR gas.

### 4.5.3 Comparison to M51

Parkin et al. (2013) investigated the same atomic fine structure lines in central  $\sim 2.5'$  of M51 by dividing the galaxy into four distinct regions: the nucleus, center, arm and interarm regions. They discovered a radial trend in both the fraction of ionized gas (from about 80% in the central region of the galaxy down to 50% in spiral arm and interarm regions) as well as in the properties of the molecular clouds,  $n$ ,  $G_0$  and  $T$ . However, they also discovered that in addition to the radial trend, the molecular clouds in the arm and interarm regions displayed the same physical characteristics, despite differing star formation rate surface densities. We now discuss the similarities and differences between the properties of the gas in both M51 and Cen A.

To give any meaning to this comparison we first need to consider the star formation rate (SFR) and star formation rate surface density (SFRD),  $\Sigma(70)$ . We estimate the SFR of Cen A by using the equation derived empirically by Li et al. (2013) that uses the luminosity of the *Herschel* PACS 70  $\mu\text{m}$  map (their equation (4), with the calibration constant determined for their combined dataset as listed in their Ta-

ble 5):

$$\text{SFR}(70) = 1.18 \times 10^{-43} L(70), \quad (4.2)$$

where the SFR rate is given in  $M_{\odot} \text{ yr}^{-1}$  and the luminosity at 70  $\mu\text{m}$  is given in  $\text{erg s}^{-1}$ . With this equation we obtain a total SFR in the region covered by our 70  $\mu\text{m}$  map of approximately  $3.7 M_{\odot} \text{ yr}^{-1}$ . Li et al. (2013) caution that the SFR determined with this equation for regions larger than approximately 200 pc may be overestimated by up to 50% because Equation 4.2 assumes that  $L(70)$  is entirely associated with recent star formation activity. However, on scales larger than 200 pc diffuse 70  $\mu\text{m}$  emission may account for half of the observed luminosity. Each pixel in our 70  $\mu\text{m}$  map has a 12'' scale, corresponding to a physical size of roughly 220 pc, at the limit of scale the equation is valid for. However, since we are summing over the disk to obtain the total SFR, we will conservatively assume half of the 70  $\mu\text{m}$  is not associated with current star formation, reducing the observed SFR to  $\sim 1.85 M_{\odot} \text{ yr}^{-1}$ .

Next we need to estimate the SFRD for Cen A. Since it is edge on, while M51 is face on, we want to determine the area of the disk of Cen A if it were face-on, as well. For simplicity, we assume the disk is circular and take the radius to be that of the edge-on disk. Given the warped nature of the disk we take two radius measurements as lower and upper bounds (3.5–6'), corresponding to upper and lower limits on the SFRD of  $\Sigma(70) = 0.014\text{--}0.04 M_{\odot} \text{ yr}^{-1} \text{ kpc}^{-2}$ . For consistency, we apply the same equation to M51 using only the area covered by the fine structure line observations in Parkin et al. (2013), which is roughly 49  $\text{kpc}^2$ . We obtain a value for the SFR in this region of  $M_{\odot} \text{ yr}^{-1}$ , thus a star formation rate surface density of  $\sim 0.05 M_{\odot} \text{ yr}^{-1} \text{ kpc}^{-2}$  (again assuming 50% of the 70  $\mu\text{m}$  is from recent star formation). In comparison, Kennicutt (1998) reports a global

mean SFR density of approximately  $0.02 \text{ M}_\odot \text{ yr}^{-1} \text{ kpc}^{-2}$  for M51, while Kennicutt et al. (2007) find a range of SFR densities between  $0.001$  and  $0.4 \text{ M}_\odot \text{ yr}^{-1} \text{ kpc}^{-2}$  for 257 apertures centred on H II regions within M51. Thus, the range of values for the SFR density in Cen A is roughly consistent with those found in M51.

With the SFRDs of both galaxies in mind, we can first compare the heating efficiency as a function of the  $70 \mu\text{m}/160 \mu\text{m}$  ratio between the two galaxies. In Parkin et al. (2013) it was shown that the average value for the heating efficiency was about  $5 \times 10^{-3}$  in the arm and interarm regions of M51, then decreased to  $3 \times 10^{-3}$  in the nucleus. In Figure 4.4 we see that this ratio is slightly higher in Cen A than in M51, with a value of  $5 \times 10^{-3}$  in the bins closest to the AGN, a peak of  $7.5 \times 10^{-3}$  in the middle of the strip, and a value of  $6 \times 10^{-3}$  in the outermost bins. This implies that M51 has a higher content of charged dust grains and PAHs than in Cen A, which is consistent with the presence of the significant amount of ionized gas observed in the central region of M51.

Next, we compare the mean values of the  $[\text{C II}]/[\text{O I}]_{63}$  and  $([\text{C II}]+[\text{O I}]_{63})/F_{\text{TIR}}$  line ratios for each of the four regions of M51 with those from each of the radial bins of Cen A on the PDR model  $[\text{C II}]/[\text{O I}]_{63}$  versus  $([\text{C II}]+[\text{O I}]_{63})/F_{\text{TIR}}$  parameter space in Figure 4.9. The values for  $n$  and  $G_0$  in Cen A are consistent with those of the arm and interarm regions of M51 within uncertainties, even for the innermost bins in our observations. However, the nuclear and center regions of M51 have slightly higher values for  $n$  and  $G_0$  and a higher ionized gas fraction. This is an interesting result because both galaxies have active centers, with M51 containing a Seyfert 2 nucleus (Ho et al., 1997); thus, we might expect similar properties in their central regions. We note that we do not have observations directly of the nucleus of Cen A; however, the result stands even if we ignore the nucleus region of M51 because the center region contains molecular clouds with higher density that are ex-

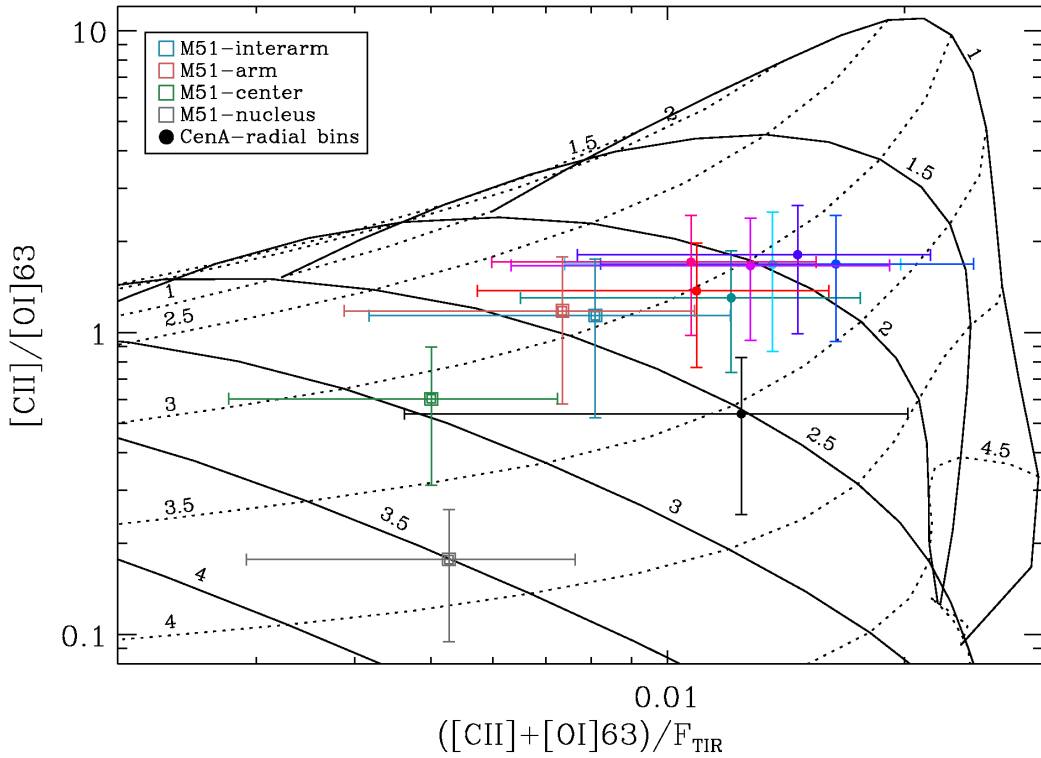


Figure 4.9: A comparison of the PDR model results for the radial bins of Cen A with the PDR model results for the four regions in the inner region of M51 from Parkin et al. (2013).

posed to a stronger radiation field than those in Cen A. The difference might also be due to the higher fraction of ionized gas in M51 than in Cen A. If M51 has a larger population of massive young stars, they would produce more FUV radiation and more H II regions. Alternatively, the difference could be another consequence of the high inclination of Cen A. If there is a stronger radiation field affecting clouds near the center of the galaxy, it may be diluted by the weaker fields contributing along the line of sight. Investigating additional galaxies with active nuclei could confirm which is the more likely scenario.

The  $[O\ III]/[N\ II]_{122}$  line ratio indicates that the youngest stars in Cen A are hotter (O9.5 or O9) than in M51 (B0; Parkin et al., 2013) based on the stellar

classifications from Vacca et al. (1996). This apparent discrepancy may be due to lower signal-to-noise in the M51 observations of the [O III] line than in Cen A, which would indicate that the observed [O III]/[N II]<sub>122</sub> ratio in M51 from Parkin et al. (2013) is a lower limit, bringing the ratio closer to that observed in Cen A. It is also possible that the observed ratio is a combined effect of stars and the stronger AGN in Cen A, thus making the apparent stellar classification earlier than it really is.

## 4.6 Conclusions

We have presented new spectroscopic observations of the unusual elliptical galaxy Centaurus A from the *Herschel* PACS instrument. These observations focus on important atomic cooling lines originating from both neutral ([C II](158  $\mu\text{m}$ ), [O I](63 and 145  $\mu\text{m}$ )) and ionized gas ([N II](122 and 205  $\mu\text{m}$ ) and [O III](88  $\mu\text{m}$ )) covering a radial strip on the eastern side of the nucleus of the galaxy (or a central aperture for the 205  $\mu\text{m}$  line). We divide our observational strip into eight bins radially to search for variations in the heating and cooling properties of the gas, as well as the characteristics of the PDR regions in the disk.

We find that the heating efficiency in the disk, represented by the  $([\text{C II}] + [\text{O I}]_{63})/F_{\text{TIR}}$  line ratio, shows a slight increase with increasing radius from  $4 \times 10^{-3}$  to  $8 \times 10^{-3}$ , consistent with values determined in galaxies on global scales, as well as on resolved scales in other individual galaxies. Furthermore, the slightly suppressed heating efficiency suggests a harder radiation field in the region, likely from the AGN at the center.

A comparison between a PDR model and our observations reveals that the strength of the FUV radiation field incident on the PDR surfaces ranges from  $\sim$

$10^{1.75}\text{--}10^{2.75}$  and the hydrogen gas density ranges from  $\sim 10^{2.75}\text{--}10^{3.75}$  cm $^{-3}$ , in agreement with typical values in other star forming galaxies (including M82, which has a central starburst) and distinct from the elliptical galaxy NGC 4125. However, we do not see a significant radial trend in either  $n$  or  $G_0$ , in contrast to M51. Furthermore, while the results from the PDR modelling for Cen A agree with those for the arm and interarm regions in M51, the central region of M51 shows higher values for  $n$  and  $G_0$ . Observations of the nucleus of Cen A in the important fine structure lines may reveal a similar trend; however, we point out that in the central region of M51 up to 70% of the [C II] emission originates in diffuse ionized gas while in Cen A this fraction is only 10–20%, thus this may partially explain the differences between the two galaxies. The differences may also arise as a result of the high inclination of Cen A diluting any effects the AGN may have on the surrounding ISM.

We conclude that the disk of Cen A exhibits properties in its molecular clouds that are similar to other normal disk galaxies, despite its unusual morphological characteristics.

## Acknowledgments

The research of C. D. W. is supported by the Natural Sciences and Engineering Research Council of Canada and the Canadian Space Agency. PACS has been developed by a consortium of institutes led by MPE (Germany) and including UVIE (Austria); KU Leuven, CSL, IMEC (Belgium); CEA, LAM (France); MPIA (Germany); INAF-IFSI/OAA/OAP/OAT, LENS, SISSA (Italy); IAC (Spain). This development has been supported by the funding agencies BMVIT (Austria), ESA-PRODEX (Belgium), CEA/CNES (France), DLR (Germany), ASI/INAF (Italy),

and CICYT/MCYT (Spain). SPIRE has been developed by a consortium of institutes led by Cardiff University (UK) and including Univ. Lethbridge (Canada); NAOC (China); CEA, LAM (France); IFSI, Univ. Padua (Italy); IAC (Spain); Stockholm Observatory (Sweden); Imperial College London, RAL, UCL-MSSL, UKATC, Univ. Sussex (UK); and Caltech, JPL, NHSC, Univ. Colorado (USA). This development has been supported by national funding agencies: CSA (Canada); NAOC (China); CEA, CNES, CNRS (France); ASI (Italy); MCINN (Spain); SNSB (Sweden); STFC and UKSA (UK); and NASA (USA). HIPE is a joint development by the Herschel Science Ground Segment Consortium, consisting of ESA, the NASA Herschel Science Center, and the HIFI, PACS and SPIRE consortia. The James Clerk Maxwell Telescope is operated by The Joint Astronomy Centre on behalf of the Science and Technology Facilities Council of the United Kingdom, the Netherlands Organisation for Scientific Research, and the National Research Council of Canada. This research has made use of the NASA/IPAC Extragalactic Database (NED) which is operated by the Jet Propulsion Laboratory, California Institute of Technology, under contract with the National Aeronautics and Space Administration. This research made use of APLpy, an open-source plotting package for Python hosted at <http://aplpy.github.com>.

# Bibliography

- Abel, N. P., Dudley, C., Fischer, J., Satyapal, S., & van Hoof, P. A. M. 2009, ApJ, 701, 1147
- Aniano, G., Draine, B. T., Gordon, K. D., & Sandstrom, K. 2011, PASP, 123, 1218
- Bendo, G. J., Galliano, F., & Madden, S. C. 2012, MNRAS, 423, 197
- Blum, R. D., & Pradhan, A. K. 1992, ApJS, 80, 425
- Braine, J., Gratier, P., Kramer, C., et al. 2012, A&A, 544, A55
- Brauher, J. R., Dale, D. A., & Helou, G. 2008, ApJS, 178, 280
- Calzetti, D., Kennicutt, R. C., Engelbracht, C. W., et al. 2007, ApJ, 666, 870
- Calzetti, D., Wu, S.-Y., Hong, S., et al. 2010, ApJ, 714, 1256
- Combi, J. A., & Romero, G. E. 1997, A&AS, 121, 11
- Contursi, A., Kaufman, M. J., Helou, G., et al. 2002, AJ, 124, 751
- Contursi, A., Poglitsch, A., Grácia Carpio, J., et al. 2013, A&A, 549, A118
- Crawford, M. K., Genzel, R., Townes, C. H., & Watson, D. M. 1985, ApJ, 291, 755

- Crocker, A., Krips, M., Bureau, M., et al. 2012, MNRAS, 421, 1298
- Crocker, A. F., Bureau, M., Young, L. M., & Combes, F. 2011, MNRAS, 410, 1197
- Croxall, K. V., Smith, J. D., Wolfire, M. G., et al. 2012, ApJ, 747, 81
- Eckart, A., Cameron, M., Rothermel, H., et al. 1990, ApJ, 363, 451
- Ferkinhoff, C., Brisbin, D., Nikola, T., et al. 2011, ApJ, 740, L29
- Galametz, M., Kennicutt, R. C., Calzetti, D., et al. 2013, MNRAS, 431, 1956
- Galavis, M. E., Mendoza, C., & Zeippen, C. J. 1997, A&AS, 123, 159
- . 1998, A&AS, 131, 499
- Graciá-Carpio, J., García-Burillo, S., Planesas, P., Fuente, A., & Usero, A. 2008, A&A, 479, 703
- Graciá-Carpio, J., Sturm, E., Hailey-Dunsheath, S., et al. 2011, ApJ, 728, L7
- Griffin, M. J., et al. 2010, A&A, 518, L3
- Groves, B. A., Dopita, M. A., & Sutherland, R. S. 2004, ApJS, 153, 9
- Habing, H. J. 1968, Bull. Astron. Inst. Netherlands, 19, 421
- Harris, G. L. H., Rejkuba, M., & Harris, W. E. 2010, PASA, 27, 457
- Ho, L. C., Filippenko, A. V., & Sargent, W. L. W. 1997, ApJS, 112, 315
- Hollenbach, D., & McKee, C. F. 1989, ApJ, 342, 306
- Hollenbach, D. J., Takahashi, T., & Tielens, A. G. G. M. 1991, ApJ, 377, 192
- Hudson, C. E., & Bell, K. L. 2004, MNRAS, 348, 1275

Israel, F. P. 1998, A&A Rev., 8, 237

Kaufman, M. J., Wolfire, M. G., & Hollenbach, D. J. 2006, ApJ, 644, 283

Kaufman, M. J., Wolfire, M. G., Hollenbach, D. J., & Luhman, M. L. 1999, ApJ, 527, 795

Kennicutt, Jr., R. C. 1998, ApJ, 498, 541

Kennicutt, Jr., R. C., Calzetti, D., Walter, F., et al. 2007, ApJ, 671, 333

Kennicutt, Jr., R. C., Hao, C.-N., Calzetti, D., et al. 2009, ApJ, 703, 1672

Kramer, C., Mookerjea, B., Bayet, E., et al. 2005, A&A, 441, 961

Le Petit, F., Nehmé, C., Le Bourlot, J., & Roueff, E. 2006, ApJS, 164, 506

Lebouteiller, V., Cormier, D., Madden, S. C., et al. 2012, A&A, 548, A91

Leeuw, L. L., Hawarden, T. G., Matthews, H. E., Robson, E. I., & Eckart, A. 2002, ApJ, 565, 131

Li, Y., Crocker, A. F., Calzetti, D., et al. 2013, ApJ, 768, 180

Luhman, M. L., Jaffe, D. T., Sternberg, A., Herrmann, F., & Poglitsch, A. 1997, ApJ, 482, 298

Luhman, M. L., Satyapal, S., Fischer, J., et al. 2003, ApJ, 594, 758

—. 1998, ApJ, 504, L11

Malhotra, S., Kaufman, M. J., Hollenbach, D., et al. 2001, ApJ, 561, 766

Mookerjea, B., Kramer, C., Buchbender, C., et al. 2011, A&A, 532, A152

Morganti, R. 2010, PASA, 27, 463

Morganti, R., Oosterloo, T., Struve, C., & Saripalli, L. 2008, A&A, 485, L5

Negishi, T., Onaka, T., Chan, K.-W., & Roellig, T. L. 2001, A&A, 375, 566

Oberst, T. E., Parshley, S. C., Stacey, G. J., et al. 2006, ApJ, 652, L125

Ott, S. 2010, in Astronomical Society of the Pacific Conference Series, Vol. 434, Astronomical Data Analysis Software and Systems XIX, ed. Y. Mizumoto, K.-I. Morita, & M. Ohishi, 139–+

Parkin, T. J., Wilson, C. D., Foyle, K., et al. 2012, MNRAS, 422, 2291

Parkin, T. J., et al. 2013, ApJ, in press

Phillips, T. G., Ellison, B. N., Keene, J. B., et al. 1987, ApJ, 322, L73

Pilbratt, G. L., et al. 2010, A&A, 518, L1

Poglitsch, A., et al. 2010, A&A, 518, L2

Quillen, A. C., Brookes, M. H., Keene, J., et al. 2006, ApJ, 645, 1092

Quillen, A. C., de Zeeuw, P. T., Phinney, E. S., & Phillips, T. G. 1992, ApJ, 391, 121

Röllig, M., Ossenkopf, V., Jeyakumar, S., Stutzki, J., & Sternberg, A. 2006, A&A, 451, 917

Rubin, R. H. 1985, ApJS, 57, 349

Rydbeck, G., Wiklind, T., Cameron, M., et al. 1993, A&A, 270, L13

Savage, B. D., & Sembach, K. R. 1996, ARA&A, 34, 279

Stacey, G. J., Geis, N., Genzel, R., et al. 1991, ApJ, 373, 423

Stacey, G. J., Jaffe, D. T., Geis, N., et al. 1993, ApJ, 404, 219

Stacey, G. J., Viscuso, P. J., Fuller, C. E., & Kurtz, N. T. 1985, ApJ, 289, 803

Sternberg, A., & Dalgarno, A. 1989, ApJ, 338, 197

—. 1995, ApJS, 99, 565

Störzer, H., Zielinsky, M., Stutzki, J., & Sternberg, A. 2000, A&A, 358, 682

Strong, A. W., Bloemen, J. B. G. M., Dame, T. M., et al. 1988, A&A, 207, 1

Struve, C., Oosterloo, T. A., Morganti, R., & Saripalli, L. 2010, A&A, 515, A67+

Tielens, A. G. G. M., & Hollenbach, D. 1985, ApJ, 291, 722

Tubbs, A. D. 1980, ApJ, 241, 969

Unger, S. J., Clegg, P. E., Stacey, G. J., et al. 2000, A&A, 355, 885

Vacca, W. D., Garmany, C. D., & Shull, J. M. 1996, ApJ, 460, 914

van Dishoeck, E. F., & Black, J. H. 1986, ApJS, 62, 109

—. 1988, ApJ, 334, 771

Weiß, A., Kovács, A., Güsten, R., et al. 2008, A&A, 490, 77

Welch, G. A., Sage, L. J., & Young, L. M. 2010, ApJ, 725, 100

Wilson, C. D., et al. 2009, ApJ, 693, 1736

Wilson, C. D., et al. 2013, ApJ, in press

Wolfire, M. G., Tielens, A. G. G. M., & Hollenbach, D. 1990, ApJ, 358, 116

Wu, H., Cao, C., Hao, C.-N., et al. 2005, ApJ, 632, L79

Young, L. M., et al. 2011, MNRAS, 414, 940

Chapter **5**

## Summary & Future Work

In this thesis I have utilised the unprecedented sensitivity and resolution of the *Herschel Space Observatory*, designed to probe the cold interstellar medium (ISM) from roughly 55 to 672  $\mu\text{m}$  using both photometric and spectroscopic instruments. Our goal was to search for local variations within the ISM of two contrasting environments, namely the nearby galaxies Centaurus A (Cen A) and M51. In addition, I strived to contribute to the overall understanding of the effects of an active galactic nucleus (AGN) to the neighbouring ISM. Lastly, I wanted to characterise the nature of the disk of Cen A to establish if it warrants the ‘peculiar’ designation it has received in its morphological classification.

In Chapter 2 I focused on the cold gas and dust in Cen A using *Herschel* PACS and SPIRE observations of the dust continuum at 70, 160, 250, 350 and 500  $\mu\text{m}$ . I combined these data with observations of the CO( $J = 3 - 2$ ) transition from the HARP-B instrument on the James Clerk Maxwell Telescope to obtain measurements of the molecular gas content of the warped disk. Using a modified blackbody I modelled the dust spectral energy distribution (SED) on a pixel-by-pixel basis with the *Herschel* photometry and found a radial decrease in both the

dust temperature, varying from 30 K down to 20 K, as well as the dust mass distribution. Furthermore, I found a similar radial distribution in the total gas distribution. Most interestingly, however, when I created a map of the gas-to-dust mass ratio I found a radial trend in this as well. While the average value I found of  $103 \pm 8$  is consistent with that of the Milky Way, the region in the vicinity of the AGN had a gas-to-dust ratio of almost 275. Eliminating a gradient in the metallicity or the  $\text{CO}(J = 3 - 2)/\text{CO}(J = 1 - 0)$  ratio as possible explanations for this trend, I concluded that the AGN is removing dust from the surrounding ISM via dust sputtering by a hard X-ray radiation field or dust expulsion by the jets. Thus, in the case of Cen A I have found that indeed the AGN does have an effect on the neighbouring regions.

Next, I turned to the grand-design spiral galaxy M51 and presented *Herschel* spectroscopy of the central  $2.5' \times 2.5'$  of the disk in Chapter 3. These observations targeted the important far-infrared fine-structure lines  $[\text{C II}](158 \mu\text{m})$ ,  $[\text{N II}](122 \& 205 \mu\text{m})$ ,  $[\text{O I}](63 \& 145 \mu\text{m})$  and  $[\text{O III}](88 \mu\text{m})$ , which are the dominant contributors to the global gas cooling budget in both neutral and ionised phases, particularly in photon dominated (photodissociation) regions (PDRs) and H II regions. I subdivided our maps into four distinct regions, namely the nucleus (which contains a Seyfert 2 nucleus), centre, arm and interarm regions, to search for trends in the physical characteristics of the gas. I determined for the first time that there is a radial trend in the contribution to the  $[\text{C II}](158 \mu\text{m})$  emission from ionised gas, from 80% in the nucleus down to about 50% in the arm and interarm regions. Furthermore, I found a slight suppression in the heating efficiency in the nucleus compared to the other regions, as shown by a decrease in the  $([\text{C II}](158 \mu\text{m}) + [\text{O I}](63 \mu\text{m})) / F_{\text{TIR}}$  ratio with increasing  $70 \mu\text{m}/160 \mu\text{m}$  colour. A comparison between our spectroscopy and a PDR model revealed a decreasing trend in the strength of the far-ultraviolet

radiation field,  $G_0$  and density of hydrogen nuclei,  $n$ , as a function of increasing radius (or region). For the first time I also show that there is no difference in  $G_0$  and  $n$  between the arm and interarm regions, despite having different star formation rate densities. This in turn, indicates that there is no difference in the molecular cloud properties between those in the spiral arms of M51, and those in the interarm regions. Again I have shown that an active nucleus affects the ISM in the surrounding region.

Lastly, in Chapter 4 I examine a radial strip of the eastern half of the disk in Cen A in the same cooling lines I investigated in M51. I divided the strip into eight bins to deduce any radial trends in the gas component of the ISM, as I found in M51 in Chapter 2. I found that there is a slight trend with increasing radius in the heating efficiency, as it is reduced near the nucleus by about a factor of two compared to larger radii. I also determined that, unlike M51, the majority of the [C II](158  $\mu\text{m}$ ) emission originates in neutral gas. Furthermore, I also do not observe any significant radial changes in the values of  $G_0$  and  $n$ . However, the most significant result of this investigation is that the values of  $G_0$  and  $n$  are more consistent with normal spiral galaxies than elliptical galaxies. Thus, while Cen A is a typical elliptical galaxy on global scales, its disk exhibits properties of a spiral galaxy with an active nucleus.

There are a few implications of the results of this thesis on the evolution of the ISM in general. A reduction in the heating efficiency has been attributed to the dust grains and polycyclic aromatic hydrocarbons becoming too positively charged to efficiently free electrons, which in turn, contribute to gas heating (Tielens & Hollenbach, 1985; Croxall et al., 2012; Lebouteiller et al., 2012). I observe such a decrease in the nuclei of both M51 and Cen A, though in Cen A it is slightly less obvious. This would imply that the active nuclei of both sources are impacting the heating and cooling processes in the gas, which ultimately will lead to a reduction

in the gas's ability to cool enough to form molecular cores and the next generation of stars.

My results in Chapter 3 and Chapter 4 demonstrate that molecular clouds possess similar properties regardless of whether they are in the arms or interarm regions. Ultimately, this result would imply that the reason the spiral arms appear more prominent in disk galaxies is simply due to an increase in the number of molecular clouds producing young stars that, in turn, contribute to heating the gas and dust. Perhaps molecular clouds are also very similar in nature in all galaxies producing stars, and this is something I can look into by studying other nearby galaxies.

### 5.0.1 Future Work

To further solidify our conclusions that active galactic nuclei directly affect the surrounding ISM, I would like to extend our investigation to other nearby galaxies. In particular, it would be ideal to probe sources with varying AGN luminosities to see if their impact on the ISM changes with luminosity. A couple of potential options are NGC 4151 and NGC 1068. Both of these galaxies have been observed with *Herschel* as part of the Very Nearby Galaxies Survey. In addition, I have obtained CO( $J = 3 - 2$ ) observations from the JCMT, revealing detections in CO( $J = 3 - 2$ ) for NGC 1068, but interestingly, I only determined an upper limit for NGC 4151. A previous study of NGC 1068 by Spinoglio et al. (2012) used the SPIRE FTS instrument to study the CO ladder and determined there is an X-ray dominated region likely influenced by the AGN. We can expand on this work to fully probe the surrounding ISM. NGC 4151 is an interesting target because we do not observe CO( $J = 3 - 2$ ), thus suggesting there is very little warm molecular gas in it; how-

ever, it has been detected in CO( $J = 1 - 0$ ) (Dumas et al., 2010). It has a Seyfert 1 nucleus (Ulrich, 2000) and is classified as a barred spiral (de Vaucouleurs et al., 1991). Thus, this galaxy would give us yet another unique perspective on AGN impact on the ISM.

Another potential direction we can take is to expand our PDR region modelling to other galaxies to further characterise the molecular cloud properties. One way to definitively explain the subtle differences we see between Cen A and M51 is to investigate a target that is fully edge on, such as NGC 891. This galaxy is classified as an SAb morphological type (de Vaucouleurs et al., 1991), and is located about 9.6 Mpc away (Strickland et al., 2004), giving us the same spatial resolution as M51. It is believed to be a close analogue to the Milky Way, and its orientation allows for in-depth studies of the disk and the halo (van der Kruit, 1984; Scoville et al., 1993; Whaley et al., 2009). It has also been well studied at numerous wavelengths (e.g. Scoville et al., 1993; Whaley et al., 2009; Bianchi & Xilouris, 2011; Hodges-Kluck & Bregman, 2013). Recently, Bregman et al. (2013) studied the gas in the halo 5 kpc above the plane and determined from its metallicity that it was from the disk via a galactic fountain. These properties make it an interesting target for conducting further PDR analysis.

We have spectroscopic observations of a radial strip along one half of the disk of NGC 891 in the same important cooling lines as we have just presented for M51 and Cen A from PACS and SPIRE. A similar analysis into NGC 891 could aid in interpreting our results in Chapters 3 and 4, and determine if the slight difference in  $G_0$  and  $n$  between the two galaxies is an inclination effect.

Lastly, I can propose to observe Cen A with the Atacama Large Millimetre Array (ALMA) to aid in constraining our PDR model results. ALMA will be able to observe Cen A at unprecedented resolution in the submillimetre, giving us access

to the CO( $J = 3 - 2$ ) line and its adjacent dust continuum on spatial scales of less than 1.0–1.4'' (ALMA Primer, 2012), corresponding to physical scales of less than approximately 26 pc at the distance of Cen A. At these scales, we can resolve individual giant molecular clouds with masses larger than roughly  $10^4 M_{\odot}$ , and possibly resolve the nucleus, which is still point-source like in a  $2.4'' \times 6''$  beam (Espada et al., 2009).

It is crucial to take advantage of infrared and submillimetre observations of nearby galaxies to help us fully understand the life cycle of the ISM and the impact of star formation on its host molecular cloud. Now that the *Herschel Space Observatory* has ended its observing lifetime, we need to fully exploit the data it has produced and continue to probe the local properties of the dust and gas in nearby galaxies. If we can understand the evolution of the ISM we can improve our understanding on galaxy evolution as a whole. This thesis has presented important results that aid in bringing us closer to this goal.

# Bibliography

- Bianchi, S., & Xilouris, E. M. 2011, A&A, 531, L11
- Bregman, J. N., Miller, E. D., Seitzer, P., Cowley, C. R., & Miller, M. J. 2013, ApJ, 766, 57
- Croxall, K. V., Smith, J. D., Wolfire, M. G., et al. 2012, ApJ, 747, 81
- de Vaucouleurs, G., de Vaucouleurs, A., Corwin, Jr., H. G., et al. 1991, Third Reference Catalogue of Bright Galaxies (Springer-Verlag, New York)
- Dumas, G., Schinnerer, E., & Mundell, C. G. 2010, ApJ, 721, 911
- Espada, D., Matsushita, S., Peck, A., et al. 2009, ApJ, 695, 116
- Hodges-Kluck, E. J., & Bregman, J. N. 2013, ApJ, 762, 12
- Lebouteiller, V., Cormier, D., Madden, S. C., et al. 2012, A&A, 548, A91
- Schieven, G., ed., 2012, Observing with ALMA: A Primer for Early Science, ALMA Doc. 1.1, ver. 1.1
- Scoville, N. Z., Thakkar, D., Carlstrom, J. E., & Sargent, A. I. 1993, ApJ, 404, L59

Spinoglio, L., Pereira-Santaella, M., Busquet, G., et al. 2012, ApJ, 758, 108

Strickland, D. K., Heckman, T. M., Colbert, E. J. M., Hoopes, C. G., & Weaver, K. A. 2004, ApJS, 151, 193

Struve, C., Oosterloo, T. A., Morganti, R., & Saripalli, L. 2010, A&A, 515, A67+

Tielens, A. G. G. M., & Hollenbach, D. 1985, ApJ, 291, 722

Ulrich, M.-H. 2000, A&A Rev., 10, 135

van der Kruit, P. C. 1984, A&A, 140, 470

Whaley, C. H., Irwin, J. A., Madden, S. C., Galliano, F., & Bendo, G. J. 2009, MNRAS, 395, 97